Research & Development

2021

Mechanical Engineering Letters – 2021

Annual Technical-Scientific Journal of the Mechanical Engineering Faculty,
Szent István University, Gödöllő, Hungary / Institute of Technology,
Hungarian University of Agriculture and Life Sciences (MATE)

HU ISSN 2060-3789

Páter K. u. 1., Gödöllő, H-2103 Hungary
Volume 21 (2021)

Contents

Matlab/simulink based modeling of grid-connected PV systems

Teklebrhan NEGASH[1], István SERES[2], István FARKAS[3]
[1]Doctoral School of Mechanical Engineering,
[2]Institute of Mathematics and Basic Science,
Hungarian University of Agriculture and Life Sciences (MATE)
[3]Institute of Technology, Hungarian University of Agriculture and Life Sciences (MATE)

Abstract

In this paper, modeling and simulation of a three-phase two-stage grid-connected PV system is presented. The simulation was conducted in MATLAB/Simulink environment. The I-V and P-V characteristics of the solar array was analyzed under different operating temperature and irradiance. The system is modeled and designed to work at the unity power factor. An MPPT control system based on P&O algorithm was employed to control the DC-DC converter. The simulation results show that the variation in power output and current due to gradual change in solar irradiation and sudden cloud transient was satisfactorily regulated by the MPPT control system.

Keywords

PV-array, DC-DC converter, inverter, MPPT, grid-connect PV

1. Introduction

The utilization of renewable energy has long been identified to have several potential solutions to environmental problems caused by the deployment of traditional electricity generation systems. It is this fact that the interest in renewable energy in general and grid-connected PV systems, in particular, is rapidly increasing around the globe. Several state-of-the-art types of research are conducted in different sectors to come up with technical solutions to integrate renewable energy into the grid in a safe and reliable manner (Arafa et al., 2017).

For example, Atsu et al. (2021) studied the performance of different grid-connected PV technologies in Hungary. For their remarkable environmental, technical, and economic benefits grid-connected PV systems reach a record-high level of integration in recent decades (Abdmouleh et al., 2017). Moreover, a much higher deployment of renewable energy is expected for a future grid that provides more flexibility and reliability of power systems. This in turn calls for a continuous upgrade of grid standards and guidelines for hosting more energy in the future grid. It is the grid codes and standards that determine the continuous operation range of power plants by specifying the electrical limits and requirements.

Grid-connected PV systems have numerous advantages over the stand-alone system as they eliminate the need for storage systems. Moreover, grid-connected PV system controls the flow of power from the PV system to the utility grid by employing different power conditioning units. The power conditioning units collectively maximize the PV power output irrespective of the environmental conditions so as to increase the overall efficiency of the PV system (Subrahmanya and Rajkiran, 2017).

The key component of a grid-connected PV system is the grid-inverter, these devices act as an effective interface unit for distributed renewable energy resources. The main function of PV inverter is to harvest the possible available energy from solar PV and to integrate it with the utility grid. The Maximum Power Point Tracking (MPPT) algorithm within the DC-DC converter plays a crucial role in maximizing the power obtained from the PV module (Kabalcı, 2020; Zeb et al., 2018). The boost converter is used to boost the module (array) voltage and acts as a link between the DC source and the AC side (Majhrul and Ashok, 2017). Before the inverter voltage and current are fed to the utility grid it is filtered by using RLC filters to remove the harmonics and ripples.

In this paper, the behavior of grid-connected PV systems under varying operating conditions is investigated using MATLAB/Simulink software. Moreover, the effectiveness of MPPT control algorithm is demonstrated for varying irradiance and cloud transients.

2. Analysis methodology

System configuration

The components of the conventional grid-connected PV system are given in Fig. 1. As shown in the figure DC current generated from PV array is transformed and transferred via various interfacing devices to the grid. Optional components such as the DC-DC converter boosts the voltage to a certain value if required and decouples the PV system from the grid-connected inverter. The low-frequency transformer is an optional device that is integrated into the system depending on the system topology and regulation. Other elements such as grid connection filter and grid monitor unit are also incorporated into the system to provide safety features such as synchronization and anti-islanding detection (Kouro et al., 2015).

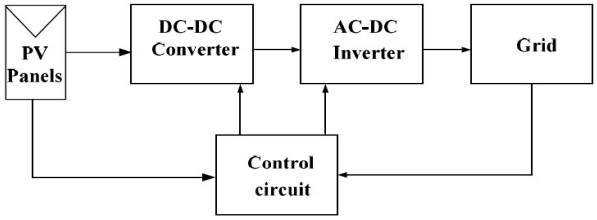

Figure 1. Schematic representation of grid-connected PV system (Deshpande and Bhasme, 2017)

The overall performance and efficiency of a grid-connected PV system are a combined result of all the above-shown components. The efficiency of the PV panel ranges between 8-15% and the efficiency of the inverter is around 95-98%. The improvement of these technologies is under intense research from different dimensions (Jain et al., 2015). The most important component the so-called Maximum Power Point Tracking (MPPT) is the focus of many researchers and special focus is given in this paper to increase the overall performance of the system.

MATLAB/Simulink modeling and control of grid-connected PV systems

In this section, a detailed MATLAB-based grid-connected PV system is presented. The performance of the grid-connected PV system is analyzed using the graphical-oriented Simulink tool. The structure of the model is given in Fig. 2. The model components are

- PV array of maximum capacity 100 kW at 25^{o}C and 1000 W/m^2
- DC-DC boost converter
- Grid inverter and power filter
- Three-phase grid AC source

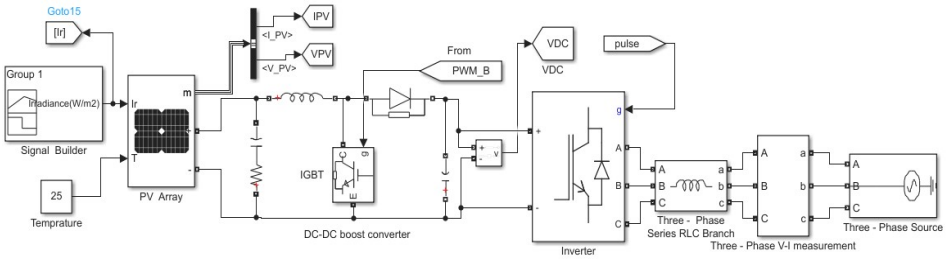

Figure 2. Part of the simulation diagram developed in MATLAB/Simulink environment

The PV array consists of 325 modules of type SunTech Power (STP-310-24/Ver) of rated power 310.156 W each. The array is configured with 25 strings of modules connected in parallel with each string having 13 modules in series (25*13*310.156=100.8 kW).

The power generated from the PV array is transferred to the grid through the DC-DC converter, inverter, and power filters. The DC-DC boost converter is used to increase the array voltage to the required level depending on the system requirement. The IGBT-based DC-DC boost converter has a switching frequency of 5 kHz. The switching of the converter is controlled using the duty cycle of the MPPT controller as shown in Fig. 3. The MPPT varies the duty cycle and the output of the DC-DC boost converter to extract maximum power. Different algorithms are developed to control the MPPT controller in this work the perturb and observe (P&O) algorithm is used to control the reference current.

It is a common practice to use low-pass passive filters to minimize current harmonics and the ripples in the output voltage. For example, Naki and Erdal

(2019) studied the control mechanism of grid-connected inverters using MPPT based predictive modeling and the values of the inductor filter and capacitive filter used in this paper are computed from the formulas given in their work.

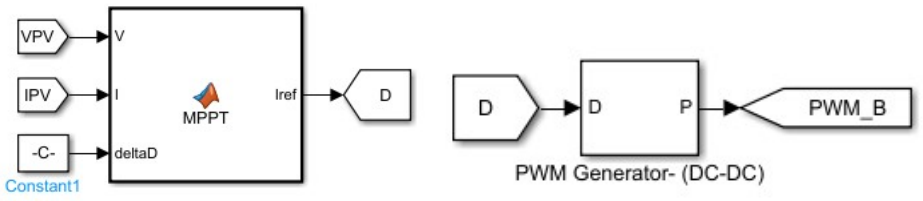

Figure 3. MPPT controller - Simulink model

3. Simulation results and discussion

In this study, the behavior and characteristics of a grid-connected PV system are investigated under varying operating conditions. The effect of environmental factors such as irradiation and temperatures on the I-V and P-V characteristics of a PV module is investigated. Fig. 4 and Fig. 5 show the irradiation and temperature effect on P-V, and I-V characteristics of a SunTech Power (STP-310-24/Ver) module respectively. The operating parameters of the PV module are given in Table 1.

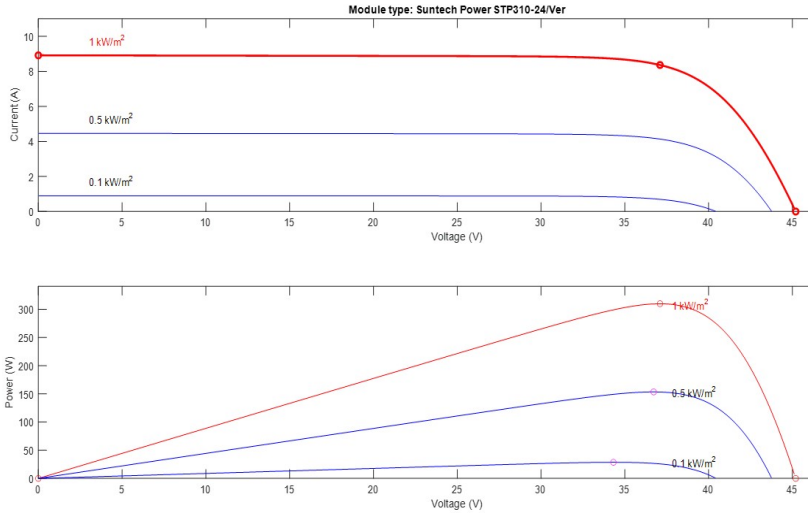

Figure 4. Irradiation effect on I-V and P-V characteristics of a single SunTech Power -STP-310-24/Ver module

The power generated from the PV array is mainly dependent on solar irradiation, and other environmental factors such as temperature have a

significant effect on the generated power as shown in Fig. 5. The voltage and power produced at constant irradiance increase with decreasing temperature. In the current study, at normal operating conditions when the temperature is kept at 25 ^{o}C the PV array generates 100.8 kW of power. As the temperature decreases the generated power further increases as shown in Fig. 5.

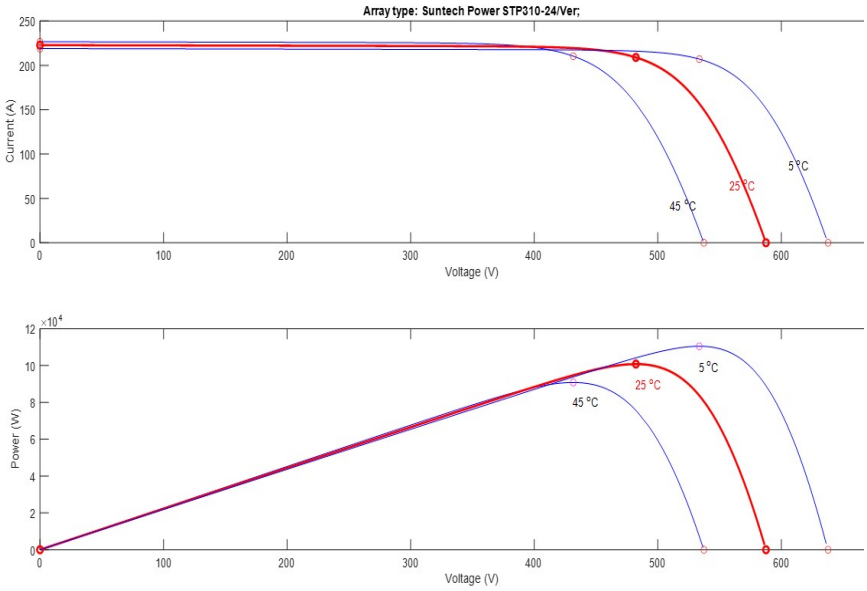

Figure 5. The effect of temperature on the I-V and P-V characteristics of the PV array

Table 1. Module (SunTech Power -STP-310-24/Ver) parameters

Operating variables	Maximum value
Maximum power (W)	310.156
Short circuit current Isc(A)	45.2
Voltage at maximum power point Vmp (V)	8.91
Voltage at maximum power point Vmp (V)	37.1
Current at maximum power point Imp (A)	8.36

First, the irradiation curve was developed using a signal builder block from the Simulink library. The irradiation data was approximated for a summer day in a typical tropical region. The irradiation profile was seen to be zero at night and gradually increased from 6 AM up to noon and again gradually dropping up to 6 PM. A sudden drop of irradiation appeared at 10 AM and again rose to its maximum level at 12 PM. Thus, the nature of the data set was selected to enable us to investigate the PV system under varying irradiation conditions and cloud transients. The signal builder is connected to the PV array. The signal of the

irradiation data developed on the signal builder block of the Simulink tool is given in Fig. 6. To examine the behavior of the collective data profile at each data point the run time of the MATLAB simulation was set to 24 s. All the simulation results were, however, conducted for a constant temperature of 25 ^{o}C.

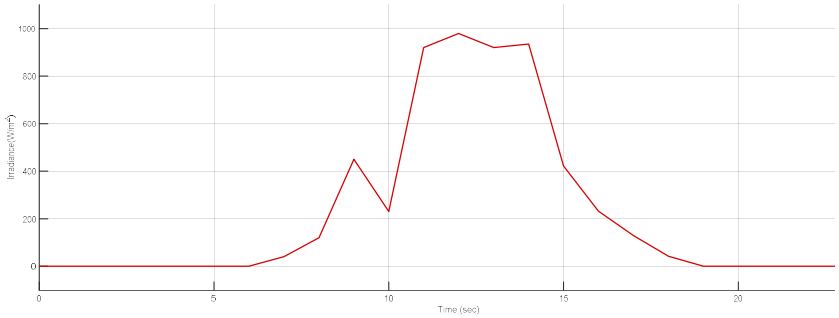

Figure 6. Irradiation profile fed to the PV array

The three-phase two-stage 100 kW PV system is connected to the grid via the DC-DC boost converter and the grid inverter. P&O algorithm is used in the MPPT tracker of the DC-DC converter to control the reference current. The waveforms of the grid current and voltage are given in Fig. 7. The voltage and current are in phase. As shown in the figure the current waveform responds to the change of irradiation while the voltage remains constant. The Grid inverter along with three-phase RLC filter was employed to convert the DC values to pure sinusoidal grid current and voltage. Pulse width modulation signals were used to generate reference signals for switching the inverter on and off.

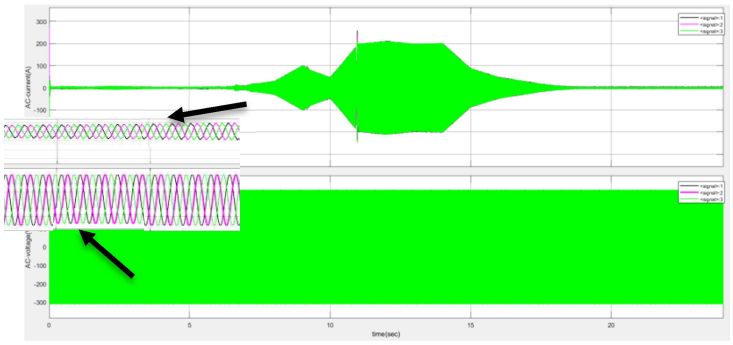

Figure 7. Three-phase wave current and voltage along with zoomed-view of grid voltage and current

The zoomed-view of voltage and current injected into the grid can be seen from Fig. 7. The figure clearly shows that there is no phase leading between the AC voltage and current. They are pure waveforms and in phase.

The DC current and the DC power output of the PV array are given in Fig. 8. As shown in the figure the current and DC power generated from the PV system changes with the irradiation signal. The MPPT controller works to regulate the variation of the power output while tracking the maximum operating point. The control system regulated the DC-bus voltage and the active and reactive current components. The reference reactive current value is set to zero in order to keep the power factor unity. The DC-bus voltage is the balancing part, if the DC-bus voltage is maintained constant the system is balanced. In this case, the PI controller maintained the DC-link voltage to the optimum level. The power produced is then a function of the generating current.

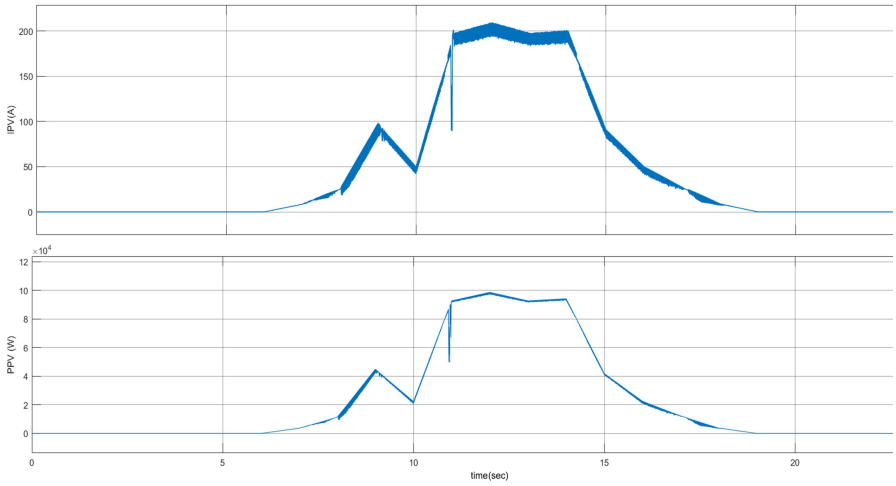

Figure 8. PV array current and DC-power generated from the PV system

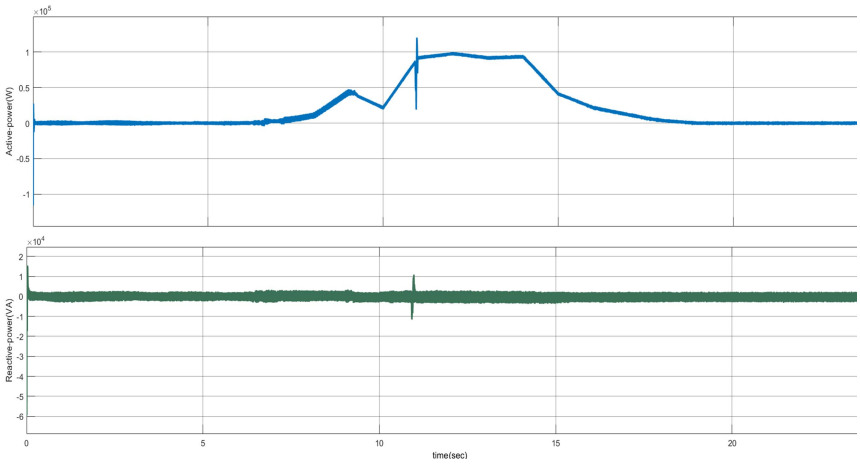

Figure 9. Active and reactive power component of the grid-connected PV-system

The performance of the grid-connected system under variable irradiation level is shown in Fig. 9. The controller is able to maintain and control the DC-bus voltage and power factor at the required level under all irradiation levels. As shown in the figure the active power varies proportionally with the irradiation profile while the reactive power remains minimal around the zero level.

Conclusions

In the current study, a MATLAB/Simulink-based simulation of a three-phase two-stage grid-connected PV system was conducted. The component of the PV system was modeled using interactive Simulink blocks and supporting algorithms and programming codes. The detailed design of the main components used in the system was presented. The solar curve was generated from a signal builder and fed to the PV array. The I-V and P-V characteristics of the PV array were then analyzed under different operating temperatures and irradiance levels. The effect of irradiance was found to be profound compared to the temperature effect. The DC-DC boost converter equipped with MPPT controller and signal generator (PWM) is employed to extract maximum power from the PV array. The MPPT control unit with P&O algorithm was used to regulate and maximize the power flow to the DC-link. The low bypass filters were used to remove the current harmonics and voltage ripples. The grid inverter along with other power conditioning units is then used to inject the PV current into the grid at unity power factor. More detailed studies will be conducted in future work to analyze and address more power quality parameters such as total harmonic distortion and voltage ripples of the injected current and voltage. Moreover, more details in power quality improvement techniques such as active and passive power filters and UPQC techniques with their detailed controlling mechanism will be studied.

Acknowledgements

This work was supported by the Stipendium Hungaricum Programme and by the Mechanical Engineering Doctoral School, Hungarian University of Agriculture and Life Sciences, Gödöllő, Hungary.

References

[1] Abdmouleh, Z., Gastli, A., Ben-Brahim, L., Haouari, M., Al-Emadi, N.A., 2017. Review of optimization techniques applied for the integration of distributed generation from renewable energy sources. Renewable Energy. https://doi.org/10.1016/j.renene.2017.05.087

[2] Arafa, O.M., Mansour, A.A., Sakkoury, K.S., Atia, Y.A., Salem, M.M., 2017. Realization of single-phase single-stage grid-connected PV system.

Journal of Electrical Systems and Information Technology 4, 1–9. https://doi.org/10.1016/j.jesit.2016.08.004

[3] Atsu, D., Seres, I., Farkas, I., 2021. The state of solar PV and performance analysis of different PV technologies grid-connected installations in Hungary. Renewable and Sustainable Energy Reviews 141. https://doi.org/10.1016/j.rser.2021.110808

[4] Deshpande, S., Bhasme, N.R., 2017. A Review of Topologies of Inverter for Grid Connected PV Systems, in: International Conference on Innovations in Power and Advanced Computing Technologies.

[5] Jain, S., Vaibhav, A., Goyal, L., 2015. Comparative analysis of MPPT techniques for PV in domestic applications. Institute of Electrical and Electronics Engineers (IEEE), pp. 1–6. https://doi.org/10.1109/poweri.2014.7117636

[6] Kabalcı, E., 2020. Review on novel single-phase grid-connected solar inverters: Circuits and control methods. Solar Energy. https://doi.org/10.1016/j.solener.2020.01.063

[7] Kouro, S., Leon, J.I., Vinnikov, D., Franquelo, L.G., 2015. Grid-connected photovoltaic systems: An overview of recent research and emerging PV converter technology. IEEE Industrial Electronics Magazine 9, 47–61. https://doi.org/10.1109/MIE.2014.2376976

[8] Majhrul, I., Ashok, K., 2017. Modeling and Control of Utility Grid Connected Solar Photovoltaic Array Integrated System Using MATLAB, in: 2017 International Conference on Computation of Power, Energy, Information and Communication (ICCPEIC). IEEE.

[9] Naki, G., Erdal, I., 2019. MPPT Based Model Predictive Control of Grid Connected Inverter for PV Systems, in: 8th International Conference on Renewable Energy Research and Applications. IEEE, Brasov, ROMANIA.

[10] Subrahmanya, B., Rajkiran, Ballal.I., 2017. MATLAB/Simulink based Design & Dovelopment of 5kW Solar PV-Grid Connected Power Sytsem; Trends and Challenges, in: 2017 International Conference on Circuits Power and Computing Technologies [ICCPCT].

[11] Zeb, K., Uddin, W., Khan, M.A., Ali, Z., Ali, M.U., Christofides, N., Kim, H.J., 2018. A comprehensive review on inverter topologies and control strategies for grid-connected photovoltaic system. Renewable and Sustainable Energy Reviews. https://doi.org/10.1016/j.rser.2018.06.053

Color analysing of ipa brewing phases, including daily measuring of fermentation process

András BARCZI[1] , Dorottya SZABÓ[1], Péter MAGYARI[2], Gábor GÉCZI[1]
[1]Department of Environmental Technology, Institute of Environmental Sciences, Hungarian University of Agriculture and Life Sciences (MATE)
[2]Private homebrewer

Abstract

One of the most popular ALE-type beers is the Indian Pale Ale (IPA), which, due to its hop content, gives the beer a completely fruity-citrus flavor. It is especially popular with novice brewers as it has no enormous machine requirements compared to LAGER type beers. In the study, we made our already known and popular recipe, a New England IPA, in a 30-liter brewing pot. This type requires only one type of malt, however, we added barley flakes, oat flakes, and wheat flakes to enhance the flavor. Hops are very dominant in the taste of this type of beer, five of which were used during brewing and later at "dry hopping" during fermentation. ALE beer types are also characterized by a simple thermal step; simultaneous activation of alpha and beta amylases followed by simultaneous cessation of activity. Sampling was performed every minute during mashing, brewing, hopping, cooling, and yeasting with a calibrated NIX-type measuring device, with repetition to avoid measurement errors. During the fermentation stage, the color change was observed by daily sampling. The aim of the study is to be able to separate the stages of brewing by color and to identify the stages of the already known biological and chemical activities by color. Learning about colors can even help large-scale companies to identify chemical and biological parameters based on colors, so they can get an accurate and immediate data of the condition of their product with chemical-free sampling. This study is the first part of a longer series of experiments where we will perform similar experiments on several types of beer (LAGER, STOUT, APA, WHEAT, RED, etc.). We would also like to know about the possible effect of carbonization on color, the possible effect of storage in a bottle on color, and possible deviations from a similar decoction.

Keywords

brewing, IPA, color, color analysation, color measuring

1. Introduction

Malting, mashing, brewing, fermentation, and bottling are usually mentioned among the beer brewing operational steps. All brew phases are essential,

including mashing, when the grinded malt is mixing with water and slowly heated up, boiling when biological activation is eliminated, and hops (or part of the hops) are added, the cooling down or chilling, when particles are settling down. (Tóth et al., 2013; Goode et al., 2005). The purpose of brew-mashing is that the useful substances, proteins and still in soluble phase existing starch shall be dissolved to the highest possible extent and be transformed into sugar. Mashing in the major breweries mostly run by decoction method. Characteristic for this decoction procedure is, that 1/3 portion of the mash from the mash tun is led into a brewing kettle, there it is gradually boiled and then pumped back into the mash tun to mix it up again with the rest of the mash. This step is repeated twice or three times thus reaching the final temperature of 62-79 °C of mashing. During microbrewing or home breweries, infusion-method is more commonly used; here the entire content of mash tun is gradually heated up to the desired temperature, applying necessary multiple pause periods. While this study focuses on microbrewing, we are going to focus on this infusion method. According to infusion method, after reaching the desired mashing temperature, mash is stirred until transformation of starch into fermentable sugars terminates.

Spreading and popularity of micro- breweries varies country by country and era by era, but from 2010 most countries (where there is no anti-alcohol laws) reports definitive increasing. Even in a micro-brewing technology, brewing the beer starts with grinding the barley or malt (Figure 1.). Grinding the malt is in fact a process executed among cylinders which is of vital importance from the perspective of chemical-biological transformations executed while mashing, qualitative composition and extraction of wort, furthermore yield (Korzenszky, 2007; Korzenszky and Judák, 2009). Grinding the malt is milling, executed between rollers, which is of vital importance from the aspects of chemical-biological transformations during mashing.

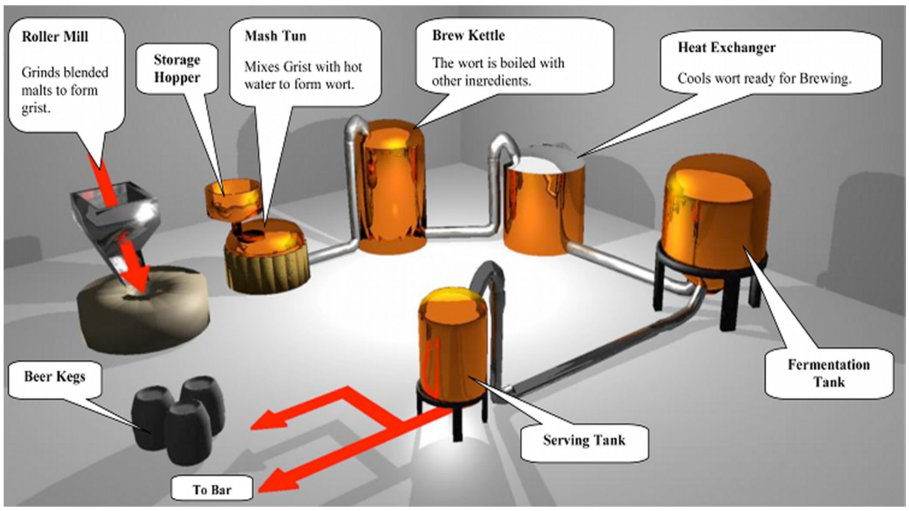

Figure 1. Brewing technology (http1)

Checking the malt grist in small scale production-routine takes place by visual control, but by means of using sieves-series it is possible to acquire quantified evaluation. With the sieve-series, structure of grist can be established, distribution of grain-size is easy to depict in graphs and average grain size which is characteristic for the grist might also be determined (*Frančáková et al, 2011;* Ivanišová et al., 2011; Korzenszky, 2012; Miller, n.a.; Mousia, 2004; Reilly et. al., 2004; Warpala and Pandiella, 2000). Further technological step is the above-mentioned mashing during which the grist of malt is mixed with water while slow heating. Aim of the process is that useful substances in the grist of malt like proteins, still soluble starch shall be dissolved at as high ratio as possible and be transformed into sugar. In smaller facilities, home breweries the content of mashing tank is gradually heated to the wished 62-75°C temperature, applying more pauses as and when necessary. Mashing is accomplished with starch transforming into sugar which can be checked by using iodine test. (Briggs, 1998; Fix 2000; Géczi 1994; Narziss, 1981) For quick determining the extract produced during the mashing is carried out by using Balling-grade [°B] or Brix-grade [°Bx] measurement unit, in laboratories the extract- and dry substance content of wort might be determined by analytical means as well (Bamforth, 2006; Fix and Fix, 1997).

Methods of brewing and later hop-boiling (electrical, gas-operated, etc.) determine beer brewing from both economic and environmental aspects. Lately the technologies are deemed as environmental-conscious where energy-consumption is reduced, water-consumption is reduced, or the amount of waste is reduced. Restructuring the technologies and taking the possibilities repeatedly into consideration may result in solutions which can reduce the energy demand of the given production process by recycling a specific waste/byproduct which was produced during a technology phase. (Korzenszky et al., 2014). Beside that all, micro-scale practice uses electric energy for grinding, circulating the liquids and cooling, but in many cases mashing and hop boiling is also carried out by using electric heating elements. From this perspective it is worth examining the grinding process from the beer production technological steps. While iodine test is accurate and could be replaced by Balling-grade [°B] or Brix-grade [°Bx] measurement unit, those methods need sampling, calibration and automatization mechanization is almost impossible, color chart comparison is a great alternative when same recipe is followed. Sampling is easier, needs less amount of sample, in addition it doesn't need any chemicals.

2. Experimental

The aim of the study is, to repeatedly measure the color, and the color saturation of the brewing liquid from the start of the mashing, till the consumption, while Brix-grade [°Bx] and temperature [°C] is by-measured as a reference by a calibrated refractometer (calibration was performed with distilled water, few minutes before the measuring campaign). As a first step of this long-term, multi-

stage performed measurement campaign, we decided to go for a brew with simple heat-steps, while color change is predictable. According to this reason, the research went for New England Indian Pale Ale (NEIPA), with dry hopping. NEIPA has a hazy, cloudy beer appearance, the saturation is higher than a settled, clear lager; NEIPA is a great initial measuring ale-liquid.

Yield was calculated for 26 liters, we mashed 4.5 kg ALE type barley malt, 0.7 kg of barley flake, 0.7 kg of oat flake, 0.4 kg of wheat flake, and 1 liter of rice hulls. Rice hulls is used for supporting the settling during chilling, as we know, it doesn't add any flavor, odor, or color.

While water has a great impact on the taste of beers and ales, we would like to repeat the measuring campaign, so we used distilled water, to avoid the varying by the water. The pot was automatized for heat steps, so there was no latency during mashing. After reaching 53 °C, the malt mixture (barley malt, barley flake, oat flake, wheat flake and rice hull) was loaded into the pot, and water was heated further to 67 °C. This temperature is activating equally the beta-, and the alpha-amylase for hydrolysis starch. We let the liquid on 67 °C for 60 minutes. After we eliminated the biological activity (increasing the temperature to 78 °C, for 15 minutes), we started the rinse the removed malt mixture with heated distilled water (90 °C) and room temperature distilled water (22 °C) and let the malt mixture drips off.

Temperature was increased to boiling (100 °C) for 60 minutes. Evaporating water was replaced by distilled hot water, we kept the Brix grade at 14 °Bx. At 45 minutes first portion of hops were added: 50 g of Amarillo pellets were placed into the liquid, using spider-hop (instead of hop-sack) for better dissolving. When 60 minutes of boiling has ended we placed the next portion of hops, and it was in the wort till the transfer into the fermenter. The second mixture of the hops (all pellets) were the following: Citra 30 g, Galaxy 30 g, Mosaic 30 g, Villamette 20 g. NEIPA brews always incudes high amount of hops.

Before we eliminated biological activity, we gathered 500 ml of the wort, into a 2-liter flask (sterilized alembic), and after cooling it down to room temperature (22 °C), we created a starter liquid with the yeast. We dissolved 10 g of Brew Ar Tech New England yeast for fermentation. While 10 g of yeast is only enough for 20-25 liters of wort, with this starter-liquid it is decent amount for 30 liters of wort to ferment. Before we transferred the wort into the fermenter cask, we let it settling for 60 minutes, so "floaties" (small chunks of coagulated protein that have fallen out of the solution of the liquid beer) were settled. This part is not necessary, but the ale appearance is better when it is applied.

After the transfer to the fermenter cask, we mixed in the starter yeast mixture, closed the fermenter, and shook the fermenter for 30 seconds, to increase the DO (dissolved oxygen) level for better fermentation. The fermenter was installed in a room with constant 20 °C.

After 3 days the fermenting wort received the first dry hop dose (all pellets): Citra 60 g, Galaxy 30 g, Mosaic 30 g, Villamatte 10 g. This time sterilized hop sack was applied. After 4 days (7 days after fermentation started) the wort received the second dose of dry hop (pellets): Azzacca 50 g.

After 7 more days the wort was ready for bottling. Avoiding the oxygen dissolving, we used long-neck loader into the bottles, 5 g of sugar were added to each bottle (for carbonization), and then all bottles (78 bottles - around 25.74 liters) were capped, carbonization process began.

For measuring we used NIX COLOR PRO handheld measurer, with its own calibrated white background. We always took 10 ml sample of the wort and sampled it with any eyedropper. During the mashing, the rinsing, the boiling, warm hoping, cooling and settling: samples were took in every 60 seconds. During fermentation, dry hoping, and carbonization samples were taken daily. We repeated every measuring 3 times (individual drops from the 10 ml shook sample), calculated the average, so every minute shows an average data. If a scatter of a sample was over 5%, we repeated the measuring with new drop (happened only 2 times).

NIX COLOR PRO uses its own light and sensor system, so outer light sources were not influencing the measuring. Many color profiles were recorded, but in this study, we focused on RGB, while it is the easiest way to follow. We sampled the wort (and the ale) 267 times, according to Table 1.

Table 1. Table of the quantity of samples

Process name	**Collected samples**
Increasing temperature	15
Mashing	61
Eliminate biological activity and rinsing	26
Boiling	62
Cooling	18
Settling	55
Fermentation and dry hopping	15
Carbonization period	14
Finished ale	1
SUM	267

Heat makes no difference on the color measuring, as our previous applying has proven it, so sampling heat was not considered.

In Excel we collected all measured data and made a comparison. NIX COLOR PRO software calculates in HEX-decimal code, but it calculates red, green, and blue (RGB) channel separately (0-255), so no further data exchange was applied.

Color changing could not be described as linear or logarithmical (because of the large scattering) visual appearance was not available by using linear or logarithmical gradients. Applying 60 or more color bars is hardly interpretable, so while the chart data is accurate, the appeared colors has only representative purpose of the study: from starting point to finish point gradient.

3. Results and discussion

Figure 2 presents the color changing during the brewing process of the subjected NEIPA brew, without color visualization. Vertical values are set between 0 and 255 as it is usually at RGB values. Horizontal values are set per sample, without time quantation. The whole chart is presented without any kind of border signs, however all phases are easily separable. On RGB mixing RED channel mixed to GREEN channel gives the yellow color, and while IPA style Ale's are usually close to yellow, as Figure 2 demonstrates: RED and GREEN channels are always reach higher values, and usually RED channel reach even higher, so the tone transfer into orange-like color.

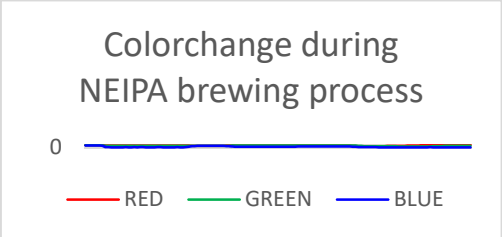

Figure 2. Color change during NEIPA brewing process

Figure 2 presents however three increases of the BLUE channel. The first increase is when biological activity has been eliminated, but maybe this is only the huge amount of foam, that distorts the values, the color is closer to white-grey with a hint yellow. The second is at the end of the boiling phase, when hops were added to the wort. Even though hop pellets are green, the GREEN channel was not increased significantly, while BLUE channel shows increasing. The third smaller phenomenon is two minor spikes in the fermentation phase, when dry hopping was done, but it was just two negligible spikes.

Figure 2 demonstrates, that during the heat transfer phases (heating, mashing, boiling) RED channel stagnates, the scattering is under 10%. The rinsing phase presents a smaller drop, but it can be caused by the foaming. Despite of a huge drop at the settling phase, it is increasing back rapidly, mostly because GREEN channel decreases even more. This phenomenon can be explained by the settling of floaties, and many hop and malt particles. On the RED channel two negative spikes is detectable, on the time when dry hopping process happens.

On Figure 3, all color changes are represented visually, using grades. Grades were set on the starting and ending values of each process, but there is no time quantizing here, every phase is presented on the same size.

Figure 3. Color changing visualization , without time quantation

On Figure 3 we can see a white-grey area on the third phase, this is the phase, when RED channel drops, and BLUE channel increases simultaneously. As it was mentioned above, this phenomenon is may caused by foaming. An almost red-ish color is detectable on Figure 3, but it is a short period in time, this is the end of the settling, when floaties were settling down, making a decrease on the GREEN channel, which was increasing steadily during the fermentation and dry hoping process.

On Figure 4, we can see a time quantized color visualization layered on the RGB chart, however as in the last two phase was sampled daily instead of per minute, it is a bit confusing, but it makes no sense, to quantize them in real time, because the first six phase took less than five hours, but the last two phases took four weeks.

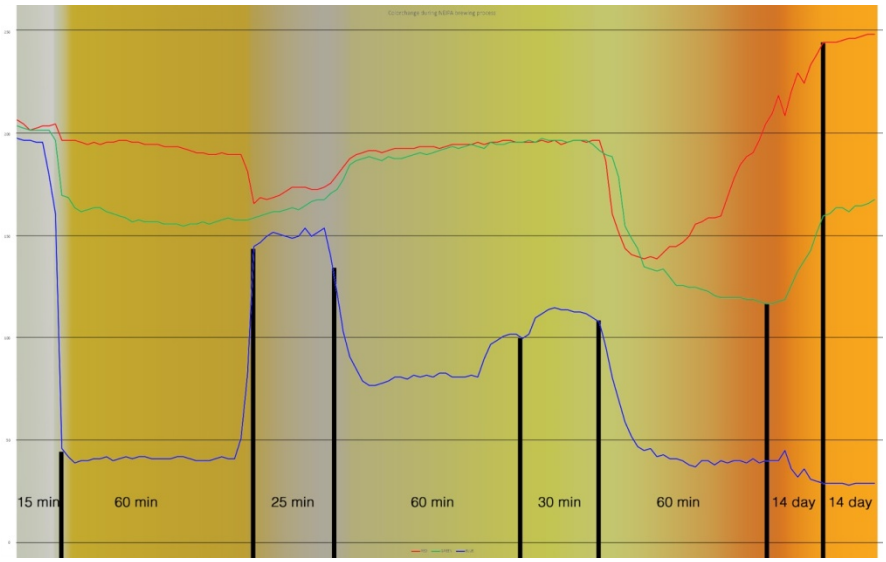

Figure 4. Time quantized color visualization on the RGB chart, with time quantizing labeling

Conclusions

- This study is the first step in a long and intensive measuring campaign. After understanding the color changing, it is now recommended, repeat the brewing processes, with the same measuring method, and search for physical or chemical parameters and some presumably correlation between them.
- However temperature and Brix grade were recorded, this study focuses only on the colors alone in itself, as a flagship to this long project.
- The study demonstrates, that variation of the colors is detectable, and every process could be described by a gradient. These color gradients are easily separable, so are the brewing process phases.

Acknowledgements

No relevant acknowledgments here.

References

[1] Bamforth C. W. 2006. Scientific Principles of Malting and Brewing American Society of Brewing Chemists, 246p.
[2] Briggs, D. E. 1998. Malts and Malting. Blackie Academic & Professional, London, 796p.
[3] Fix G. J., Fix L. A. 1997. An Analysis of Brewing Techniques. Brewers Publications, 192p.
[4] Géczi G. 1994- Házi sörfőzési technológia tervezése. (Planning of small-scale brewing technology, in hungarian) Diplomaterv, Gödöllő Agrártudományi Egyetem, Mezőgazdasági Gépészmérnöki Kar, 69p.
[5] Frančáková, H., Líšková, M., Bojňanská, T., Mareček, J. 2011. Effect of Milling Softness on Basic Technological Parameters of Wort (in Slovakian) Potravinarstvo, 5, (1) 39-42. doi:10.5219/111
[6] Ivanišová, E., Ondrejovič, M., Drapp, Š., Tokár, M. 2011. The Evaluation of Antioxidant Activity of Milling Fractions of Selected Cereals Grown int he Year 2010 Potravinarstvo, Vol.5, (4), 28-33. doi:10.5219/163
[7] Narziss L. 1981. A sörgyártás. (The Beer Production, in hungarian) Mezőgazda kiadó, Budapest, 346p.
[8] Goode, D. L., Papp, L., Schober T. J., Ulmer H. M., Arendt E. K. 2005. Development of a new rheological laboratory method for mash systems : Its application in the characterization of grain modification levels J. Inst. Brew. 111(2), 165–175.
[9] http1: http://www.cerealsdb.uk.net/cerealgenomics/WheatBP/Documents/DOC_Baking.php
[10] Korzenszky, P. 2007. Effect of Hammer Speed on Particle Size Distribution in Hammer Mills HUNGARIAN AGRICULTURAL ENGINEERING Vol 20. 51-52.
[11] Korzenszky, P., Judák, E. 2009. New technological possibilities for modifying particle size in feed production HUNGARIAN AGRICULTURAL RESEARCH Vol 3-4. 13-16.
[12] Korzenszky, P. 2012. Examination of grinding operation in the food chain Xenobiotics: Soil, Food and Human Health Interactions 123-131.
[13] Korzenszky, P., Puskás, J., Mozsgai, K., Lányi, K., Mák, Z. 2014. Innovation possibilities of a thermolysis plant to be established in Hungary, 20th International Symposium on Analytical & Applied Pyrolysis: Pyro2014., Birmingham, UnitedKingdom, 2014.05.19-2014.05.23.Paper B143.
[14] Miller D. (n.a.): Mills and Milling available: http://brewlikeapro.net/maltmilling.html download: 2013.12.10
[15] Mousia, Z., Balkin, R. C., Pandiella S. S., Webb C. 2004. The effect of milling parameters on starch hydrolysis of milled malt in the brewing process

Process Biochemistry39 (12), 2213-2219.
[16] Reilly, D. I., O'Cleirigh, C., and Walsh, P. K.: 2004. Laboratory-Scale Production of High-Gravity Wort Suitable for a Broad Variety of Research Applications J. Am. Soc. Brew. Chem. 62(1):23-28.
[17] Tóth, Ž., Frančáková, H., Solgajová, M., Dráb, Š. 2013. Water Hardness as an Important Parameter of pH. JMBFS vol 2(Special issue 1), 2043-2051.
[18] Warpala I. W. S., Pandiella S. S. 2000. Shorter Communication: Grist Fractionation and Starch Modification During the Milling of Malt. Elservier, Food and Bioproducts Processing 78 (2), 85-89.

Laboratory tests of plastic recyclings for 3D printing utilisation

Alaeddine OUSSAI [1], László KÁTAI[1], István SZALKAI[3], Zoltán BÁRTFAI[2]

[1]Department of Mechanical Engineering, Institute of Technology, Hungarian University of Agriculture and Life Sciences (MATE)

[2]Department of Agriculture and Food Machinery, Institute of Technology, Hungarian University of Agriculture and Life Sciences (MATE)

[3]Budapest Public Utilities Ltd.

Abstract

Fused Deposition Modelling (FDM) is the most common 3D printing technology. In an additive process, an object is created by successive layering of material until the entire object is created so those process with different settings is important. Tensile test specimens of two types of printed Polyethylene terephthalate have been carried out to examine the main mechanical properties. Virgin polyethylene Terephthalate (PET) and recycled PET are the used materials for this research. A total of forty test pieces of the two types were evaluated. The differences in stress-strain curves, tensile strength values and, elongation at break were compared among the tested samples. Our hypothesis was there is no significant difference between the mechanical properties of the recycled and virgin materials used for 3D printing. The test results have shown the hypothesis.

Keywords

3D printing, recycling, mechanical proprieties, filament.

1. Introduction

The 3D printing thermoplastic causes a release of gases at high temperatures. This occurs in the context with the ABS where there have been emissions noticed for carbon monoxide, hydrogen cyanide, and many volatile organics. (I. Anderson 2017) The ultrafine particle emission with the ABS was higher compared to the PET filament causing potential health hazards. This has been mainly because of the contaminates associated with the poor health risks. Such risks should be considered before further investigation is done. Hence, there is a need for maintaining a safe ventilation system during the 3D printing process. A fine example is the use of HEPA filters associated with desktops which are now in market and being considered for future 3D printers to prevent the health risks. (Perkins, L.; Lobo and H. Cornell)

A 30% global requirement is met by 60% of plastic material derived from synthetic fibers. In textile industries, PET is also referred to as polyester that covers 18% of world polymer production and is the third-largest usable polymer after polyethene (PE) and polypropylene (P.P) (Rutkowski Joseph, V.; Barbara, C. Levin) The first PET bottle was taken out of patent by Nathaniel Wyeth in 1973. PET is also used in making a thin film and solar cells.

The objective of this paper is to examine the mechanical properties (tensile, shear, and hardness characteristics) of specimens formed from the virgin PET filament. The obtained results are compared with the samples fabricated from the PET filament that is generated from recycling of the original printed 3D specimens. The reason for selecting PET over other plastic polymers is its pliability for recycling purposes. (Stephens, B.; Azimi, P.; Orch, Z.; Ramos, T)

2. Experimental

Polyethylene terephthalate waste management and collection

The waste aggregated of PET plastic was prepared via griding the plastic PET bottles. The grinding of PET plastic aggregate is carried out in three main steps: Collection of the plastic waste, drying of bottles and shredding and grinding of bottles to the specified particle size (ASTM.ORG) The process of grinding was conducted at the Budapest Public Utilities Ltd, Hungary. Table 1. shows the different types of selective waste recycled in the last years by the company. The statistics are based on the monthly sorting of incoming waste material.

Table 1. Types and ratio of the collected selective waste during first trimester 2018

2018		January		February		March	
		103Kg	m/m%	103Kg	m/m%	103Kg	m/m%
PET	Clean	30,4	12,2	27,0	10,6	30,2	11,9
	Blue	38,5	15,4	30,4	11,9	32,6	12,8
	Coloured	10,9	4,4	16,0	6,3	18,9	7,4
Foil	Dyed	6,3	2,5	8,6	3,4	5,6	2,2
	Natural	4,1	1,6	7,3	2,9	5,0	2,0
Flacon		36,5	14,6	25,4	10,0	22,4	8,8
Hungarocell		0,3	0,1	1,0	0,4	1,4	0,6
Metal	Tinned metal	6,0	2,4	6,2	2,4	3,0	1,2
	Aluminium	6,1	2,4	6,4	2,5	3,3	1,3
Other Waste		111,1	44,4	126,3	49,6	131,8	51,8
Altogether		250,2	100,0	254,6	100,0	254,2	100,0
Recyclable		138,8	55,5	127,3	50,0	121,0	47,6
Non-Recyclable		111,4	44,5	127,3	50,0	133,2	52,4

The clean and coloured PET material was selected for the experimental work. The mechanical strength testing of 3D printed components was performed at the Institute of Technology, MATE (former Szent István University). Initially, the specimen was dried before the extrusion process.

Table 2. Thermal properties for PET

Material	Polyethylene Terephthalate
Melting point [°C].	225
Drying time [hours].	4-5
Drying temperature [°C].	160

The test was done in the laboratory of Department of Material Sciences and Industrial Processes (former Szent István University) following receiving the specimens from the 3D printing Free Dee printing solutions.

For specimen preparation the PET was first dried for extrusion, this was followed by the shredding of the material and drying. After properly drying the material was ready for extrusion. The next filament extruder was used for the extrusion of the PET.

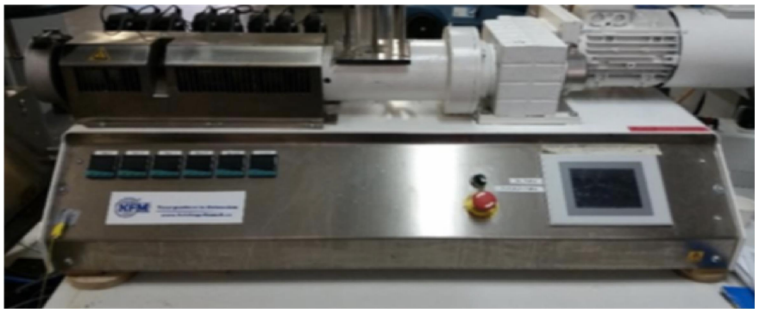

Figure 1. Sample of extrusion machine during the preparation of the specimens.

Table 3. Setting and parameters using during the preparation

TEST	Diameter of shredded material(mm)	Temperature range[°C]	Filament fan speed (%) - extruder(rpm)
1	2,85	240-245	80-5
2	2	240-245	80-5
3	1,75	240-245	80-5

There were 3 different diameters used for the shredding of the material being maintained at a constant heat temperature range along with the speed of the fan.

The measurement was ready after 3 tests. The table 3 below shows the setting for the everyday test.

Experiments and mechanical tests
The tests start by studying the filament quality control by measuring the diameter of the recycled PET and the filaments in intervals of 1 meter. This is followed by testing the surface and the cross-sections of the materials and finding out the melting points allowing us to study the thermal properties. The second test will be studying the tensile testing for the raw materials.

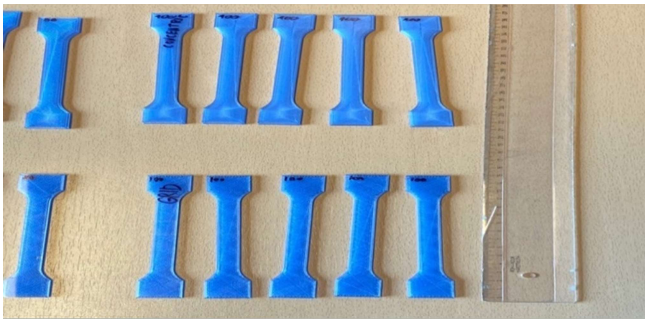

Figure 2. Testing materials standard for the specimens [10]

The initial test specimens were manufactured using the virgin PET filament with a nominal diameter of 1.75 mm. The specimens were produced at 210 ºC with a 0.4 mm nozzle, thickness and width of specimens were measured using a digital micrometer with 0,01 mm accuracy Tensile testing were performed on Testometric Zwick/Roel Z100 with a head travel speed of 5 mm/min (Figure 3). The tensile specimens were prepared according to the American Society of Testing Materials (ASTM) standard Iso 527-1:2012 as in Figure 2.

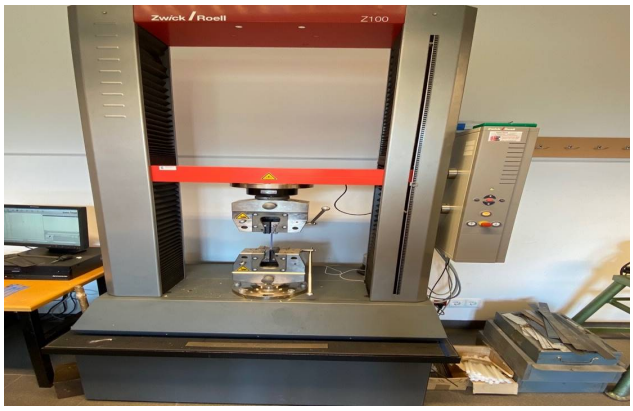

Figure 3. Tensile testing at the MATE labororatory

Table 4. Tensile properties ofVirgin versus recycled polyethylene terephthalate 3D printed specimens

	Virgin	recycled
Number of specimens	20	20
Average tensile yield strength (MPa)	34.871	29.742
Standard deviation	1.593	2.778
Average tensile modulus of elasticity (MPa)	3670	3346
Standard deviation	224	413

3. Results and discussion

Tensile properties for virgin and recycled Polyethylene Terephthalate

Extensometers for polyethylene material were not needed as the extension/strain ratio was sufficient to estimate strain [15]. The PET tensile specimens' strain/extension ratio was 0.243 after plotting the strain from extensometers against the crosshead extension. The strain from the crosshead extension, which form part of the modulus calculations, were estimated via the aforementioned method.

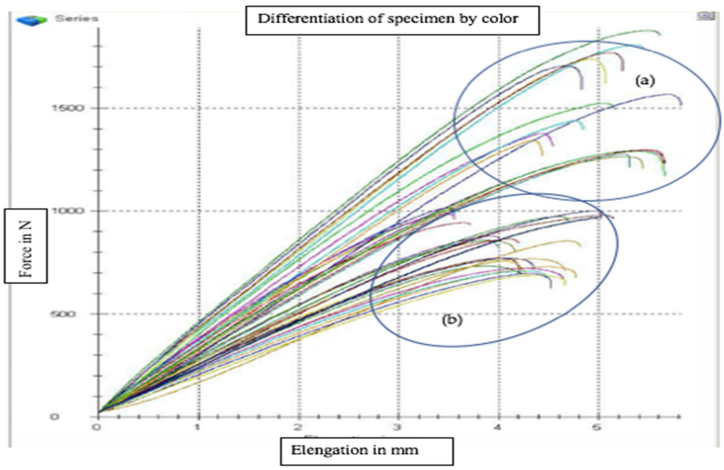

Figure 4. Tensile elongation of a recycled (a) and Virgin (b) 3D printed PET.

As afore-mentioned, with the Stress-Strain diagrams it is also possible to determine the desired properties, such as the Young Modulus, Yield Strength and Tensile Strength. In the following analysis, it will be presented, for each material, the Stress-Strain curves as well as the tables representing the mechanical properties analysed from the three trials performed, at each printing

temperature. Starting by the ABS samples, in Figure 5 it is presented the Stress-Strain curve correspondent to the average of values collected, for each printing temperature.

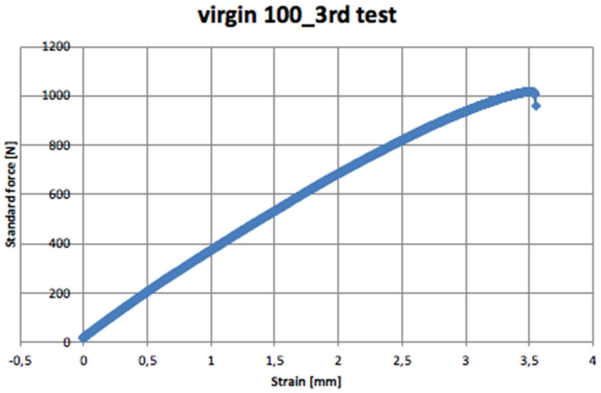

Figure 5. Strain force curve of 3rd sample test of 100% virgin 3D printed PET.

Tensile strength and hardness properties of virgin and recycled material

The PET samples revealed to have similar Strain-Stress curves, independently of the printing temperature. This can traduce similar values for the three properties in study. It is important to refer that all the PET specimens fractured almost immediately after their maximum Tensile Strength values. The PET mechanical properties obtained from the tensile test are presented in table 5 and 6, at each percentage.

Table 5. Tensile strength of Virgin PET Filament

Virgin PET	Test numbers	Average tensile strength (MPa)
100%	5	25,26
80%	5	21,34
60%	5	23,92
40%	5	18,10

Table 6. Tensile strength of Recycled PET Filament

Recycled PET	Test numbers	Average tensile strength (MPa)
100%	5	43,15
80%	5	34,214
60%	5	37,80
40%	5	24,33

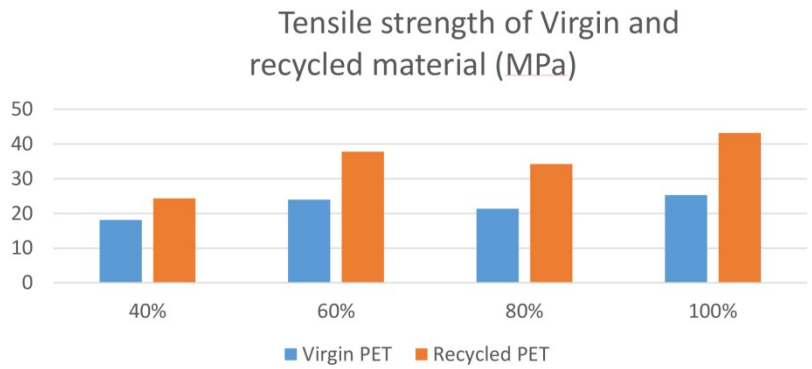

Figure 6. Tensile strength of a recycled and virgin 3D printed PET.

The test results were generated both with the virgin and the recycled test specimens studying the same parameters: tensile, shear, and hardness properties. 40 samples each from the virgins and the recycled were tested for the yield strength and the tensile modulus of the elasticity. The overall summary of the results is shown in table 5,6,7 and 8.

The yield point was studied by setting an offset value of 0.11 mm. The tensile modulus was measured by using a pre-set relationship between the crosshead extension and the strain using the tensile specimens. Using the reference, the extension to the strain ratio can be studied to estimate the strain without using the extensometers for the same materials.

Table 7. Shear strength of virgin versus recycled Polyethylene Terephthalate 3D printed specimens

	virgin	recycled
Number of specimens	20	20
Average shear yield strength (MPa)	28,448	29,253
Standard deviation	0.69	2.00

Table 8. The hardness of virgin versus recycled Polyethylene Terephtalate 3D printed specimens

	virgin	recycled
Number of specimens	20	20
Average hardness (shore D)	73,10	68,71
Standard deviation	0.725	2

These results are highly encouraged in nature. Although, there were differences between the original and the recycled. But the average mechanical properties of the recycled specimens were lower than those of the virgin specimens by about 3 to 9 %. Also, to highlight the fact was an increase in the variability of the results of the recycled material as shown by the increased standard deviation.

The current research demands a more sustainable method of chemical recycling; with lesser energy demands and computability for mixing plastic wastes. There should be less need for sorting and expanding the technology towards using non-recyclable polymers. Based on the literature review it was found that mechanical recycling is the only available technique for the recycling of plastic solid waste. The main procedure is the removal of the organic residue by washing followed by shredding, melting, and re-molding of the polymer to produce a material that is compatible with virgin plastic to blend and create a material that is suitable for manufacturing. The current technologies that are being used beyond the traditional mechanical recycling involve using pyrolysis for the selective production of gases, fuels, or waxes via the use of the catalysts; hereby being referred to as chemical recycling. Although due to high energy cost requirements it is not widely used. Another alternative option is incineration i.e. the collection of energy in the form of heat via the burning of the materials. This method is convenient for the treatment of mixed waste as it avoids the need for sorting out but does not help in many recapitalizations of the recovery and reuse of the components due to them being burned. As well it is not an energy-efficient method like recycling.

Conclusions

In the frame of the research project the laboratory tests were done in co-operation with the Budapest Public Utilities Ltd. This company works in strong partnership with the Institute of Technology. They also have a well-equipped laboratory for testing recycled plastic waste. A previous test has shown that the conductive antistatic ABS has many advantages like excellent mechanical strength, impact resistance with dimensional stability along with the high flow creep resistance and excellent heat and low-temperature resistance. The PET filament was found better. The main problem associated with the rPET extrusion is the stoppage of the material flow. During the middle of the extrusion the extrudate eventually stopping coming out of the die causing the HDPE filament to thin and then break. The pristine HDPE extrusion did not proceed without any complications.

There was a decrease found in the properties such as the tensile strength, hardness because of several factors. This could be because of the degradation in the properties of the recycled filament itself or because of the problems arising from the 3D print such as the extrusion interruptions or to the limit in the inter-layer adhesion. The individual filament properties could not be studied hence these were not included in

the study. There was some issue associated with the recycled filament like nozzles clogging, along with the issues in the printing and can lead to defects in the specimens. The main issue associated with the filament re-extrusion was it done without using a filter hence there could be some microscopic.

The p-value was significantly lower than 0.003. Due to the presence of the clogging impurities, there were some differences present in the printing process with the recycled filaments, as the filtering was not done in the extrusion process well. The main source for this increase in variation was the variation present in the recycled filament because of the difficulties described above. The study provided new data on the field of 3D recycling as well as on recycled 3D printed PET with the final inference that there is no significant difference in properties between the recycled and the virgin after comparing mechanical properties of Polyethylene terephthalate material. Hence it helps in providing a sustainable environment where one can recycle plastic and reduce the emission of CO_2. Getting the 0.003 significant value show the main achievement and the validity of this hypothesis.

The results are supporting and encouraging overall with the further development of the recycling technology for 3D printing as well as the potential for the home and small business recycling of the 3D printed waste. This technique has certain benefits but not without potential health hazards. These include lower carbon dioxide production along with the recycling of the filament with a decrease in landfill usage. There is also a scope of reducing the costs by recycling locally by engaging people in small groups, a business where they can produce recycling equipment by investing in the range of $3000. Such an investment can be recovered following the production of about one hundred pools of filament. There are many benefits associated with risks of recycling the filament-like nozzle clogs, mechanical property degradation, and an increased particle release. The clogging of the nozzle can be reduced by reducing the contamination with the help of further research into the use of large nozzles and high forming temperatures.

Such good results on the performance of the parts with the recycled PET filament should be done along with kinds of plastics such as ABS to show their viability along with the benefits of filament recycling like the 3D printing industry.

Acknowledgements

This research was supported by the Hungarian University of Agriculture and Life Sciences (MATE)

References

[1] Anderson, I. Mechanical properties of specimens 3D printed with virgin and recycled Polyactic Acid. 3D Print. Addit. Manuf. 2017,

[2] ASTM D638-14. Standard Test Method for Tensile Properties of Plastics;

ASTM International: West Conshohocken, PA, USA, 2014; Available online: www.astm.org (accessed on 25 March 2020).
[3] Oussai A.; Kátai L.; Bártfai Z.: Development of 3D printing row materials from plastic waste
Hungarian Agricultural Engineering. 2020, 37, 34-40
[4] Perkins, L.; Lobo, H. Cornell University and Datapoint Labs. A Novel Technique to Measure Tensile Properties of Plastics at High Strain Rates. Available online: www.datapointlabs.com/testpaks/antec2005.htm
[5] Rutkowski Joseph, V.; Barbara, C. Levin. Acrylonitrile- Butadiene-Styrene Copolymers (ABS): Pyrolysis and combustion products and their toxicity–A review of the literature. Fire Mater. 1986, 10, 93–105
[6] Stephens, B.; Azimi, P.; Orch, Z.; Ramos, T. Ultrafine particle emissions from desktop 3D printers. Atmos. Environ. 2013, 79, 334–339.

An overview on 3D printing Polymers and bio-based polymers

Rawabe F FAIDALLAH[1], Zoltán SZAKÁL[2], István OLDAL[2]
[1]Doctoral School of Mechanical Engineering (MATE)
[2]Institute of Mechanical Engineering -
Hungarian University of Agriculture and Life Sciences (MATE)

Abstract

Companies and researchers are increasingly interested in biodegradable polymers and composites because they are environmentally friendly, eco-friendly, and suitable for a variety of applications. To achieve better compatibility for customized and enhanced material characteristics, a variety of ways have been used. Three-dimensional (3D) printing is a flexible technique that has attracted increasing interest in recent years. In many fields such as (tissue engineering, morphological design, drug delivery), aerospace, military, automotive, environment and energy, sports, and acoustic applications. 3D printing has powerful biodegradable materials that are important for environmental protection and emergencies such as COVID -19. Fused Deposition Modelling (FDM) one of the common technologies in 3D printing methods, has many advantages, such as low cost and a wide range of materials. It offers in the production of composite materials, including high precision, cost efficiency, and customized geometry. This article provides an overview of biodegradable polymer composites, as well as their use of it in 3D printed composite manufacturing.

Keywords

3D printing, FDM, polymer, polymer composites, biomaterial, biodegradable.

1. Introduction

Polymers have become a very important material in our daily lives. They're used in various fields such as food, industry, medicine, and the automotive industry. newly, polymers have begun to replace advanced materials due to their superior properties. However, disposable materials account for more than one-third of plastic production, resulting in environmental problems because of waste and plastic emissions [1]. A renewed interest in the research of degradable polymers has been inspired by greater awareness of the pollution problem and its effect on the environment. Because of environmental issues, researchers resort to developing materials that do not have a harmful effect and are environmentally friendly. Most biodegradable polymers belong to thermoplastics (poly (lactic

acid), poly (vinyl alcohol, poly hydroxyl alkanoate), or plant polymers (e.g. starch and cellulose). Thermoplastics made from polyolefins aren't biodegradable, although some of them contain pro-oxidant additives that make them photodegradable and term degradable. The use of non-biodegradable polyethylene films (PE) on green spaces or soils has caused serious problems in Southeast Asia [2]. Non-biodegradable polymers such as polypropylene (PP), polyethylene (PE), poly (ethylene terephthalate), polystyrene ethylene vinyl alcohol, expanded polystyrene, polyurethane, polyamides, and poly (vinyl chloride) have become widely used in the packaging industry due to their good physical and mechanical properties. polymers are commonly utilized in 3D printing, but the raw materials used for 3D printing nowadays consist of different polymer composites to get the desired qualities of the end product [3]. The time it takes for a printer to manufacture a final product is typically a few hours; however, the period varies on the size of the item to be made and the type of printer used for 3D printing [4].

3D Technologies' stereolithography (SLA) was the first commercial application of AM in 1987 [5]. Since then, the AM has evolved very rapidly, particularly in the last decade. There are different methods of this technologies: laminated object manufacturing (LOM) based on Plastic lamination [6], stereolithography apparatus (SLA) based on photopolymerization [7], selective laser sintering (SLS) [8], and Fused Deposition Modelling (FDM) [9] based on the Melting of Plastic filaments.

The FDM process is worked by extruding thermoplastic material, which has heated up to its melting point through a nozzle, then depositing the extruded layers of materials on top of each other. Currently, FDM considers the most widely used technology of all types of 3DP technology around the globe due to the low cost of the printer device, sim PLA [10], PVA (polyvinyl alcohol) [11], TPU (thermoplastic polyurethane) [12], nylon [13] It can be considered as one of the most widely used materials in 3D printing technologies, and a variety of cheap filaments [14]. platform temperature, nozzle size, layer thickness, printing direction, nozzle head temperature, printing speed, and raster angle are parameters that could be Controlled it improves the print quality. Other researchers looked at the details of many processing parameters. According to the research, a suitable bed temperature and regulated convective heat transfer conditions can increase the bonding strength of successive layers, improving the mechanical properties of printed objects [15]. FDM technologies are widely used in different applications like aeronautics, automotive, construction, aerospace, and medicine. Various thermoplastic polymers like acrylonitrile butadiene styrene (ABS), polylactic acid (PLA), and polyimide are used as the material of FDM technologies in the shape of filament. ABS material has better elongation, ductility, and flexural strength compared with PLA material, but it has emitted gas in the printing process. in the other hand, PLA material is more environmentally friendly material compared with ABS material because of degrades faster than ABS material and is produced from renewable resources. in addition, is a biodegradable thermoplastic polymer compound. It's a non-toxic,

ecologically friendly aliphatic polyester made from lactic acid (derived from animals and plants) that's used to make films, textiles, and bottles. PLA has excellent mechanical qualities and, because of its biodegradability, can be used to replace petroleum-based polymers [16].

The use of 3D printing throughout the production process of a product has decreased the extra costs experienced. Furthermore, because of its cheap cost, additive manufacturing can produce a large number of customized products [16]. Furthermore, 3D printed items have improved in terms of resolution, accuracy, usefulness, and reproducibility throughout time. The cost of manufacturing has decreased as a consequence of the growing number of 3D printers and easy access to applications [17].

2. Fused Deposition Modelling (FDM) based on the Melting of plastic

The FDM process is worked by extruding thermoplastic material, which uses thermoplastic filament as feedstock, the filament has heated up to its melting point, then is extruded through a nozzle in the XY plane creating a layer of solid material on the build plate. Creating a model can be done by depositing a layer contour, The material is then extruded in the XY plane by a nozzle, forming a solid layer on the build plate. By depositing a layer contour and then filling the interior with plasticized material with zigzag head movements, a model could be created. The head moves along the Z-axis after manufacturing one layer, starting the build-up of the next layer. We can make various forms using this method with a minimum of previous step. The manufacturing process begins with the creation of a model in a CAD program then its transfer to software like (Ultra-software) that could control of process parameters such as head movement, feed rate, layer thickness, infill, head and table temperatures, slicing, support application, etc. Then the software creates G-code, which can then be transferred to a 3D printer to create an actual model. The model that was taken from the printer may need requires finishing machining to delete the supports and flaws. [18, 19]. Currently, FDM considers the most widely used technology of all types of 3DP technology around the globe due to its low cost of the printer device, simplicity, and variety of inexpensive filaments. Figure 1 shows a schematic of the 3D printing process using the FDM technology.

Figure 1. The procedure of FDM printing

For some designs, the support materials can be easily removed, but when it comes to complex structures, removing the support materials presents some

difficulties. Ultimaker has developed a water-soluble support material that leaves no trace in the supporting parts and creates a clear part. Dynamic structures may be easily created with this type of support material. The accuracy of the part that had been created depends on the movement of the extruder, the temperature, the speed, and the flow rate of the material during the nozzle. The FDM (Figure 2) is widely used for creating anatomical models in dentistry and surgical exercises [20].

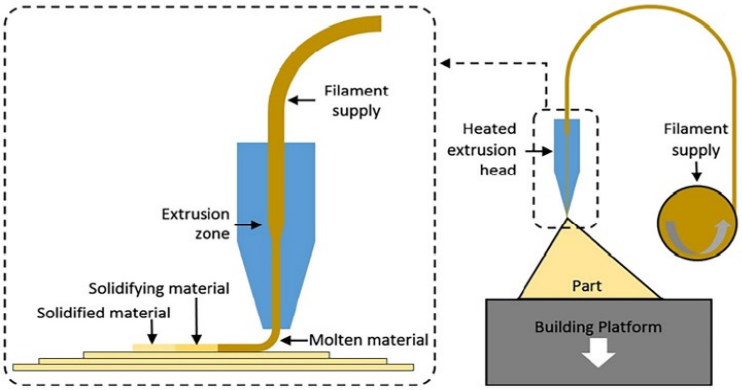

Figure 2. Fusion deposition Modelling (FDM)

3. Thermoplastics as feedstock materials for FDM

To choose the suitable polymer for the final product, we must first understand the qualities (mechanical and physical properties) and printability of the material. The most prevalent types of thermoplastics are classified by performance in Figure 3a, and their printability, optical quality, and mechanical qualities are shown in Figure 3b. In Figure 3b, impact resistance, heat resistance, and elongation at break are the chemical and mechanical properties that resist higher temperatures, impact energy, and longitudinal deformation before breakage. The simplicity of printing means how easy it's to print a base material in terms of print bed adhesion, maximum print speed, ease of feeding to the printer, and frequency of print defects. These considerations are helpful when selecting materials for FDM [21].

The most common thermoplastics for filaments in 3D printing (PLA, ABS, nylon, and PEEK) are discussed in the next section, and Table 1 compares them in terms of physical and mechanical characteristics, as well as printing circumstances. Heat deflection temperature is a measurement of a polymer's resistance to distortion under a particular load at a higher temperature, and it may be used to figure out what temperature the polymer should be employed at. In table 1, heat deflection temperature refers to the temperature at which a certain material specimen bends 0.25 mm under a given strain.

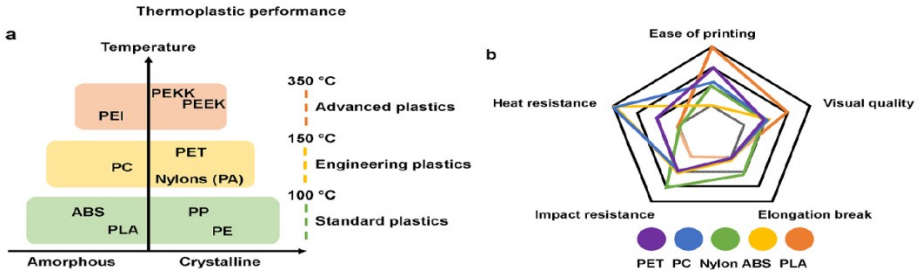

Figure 3. Thermoplastics as feedstock materials for FDM.
(a) Standard thermoplastics (acrylonitrile butadiene styrene (ABS), polylactic acid (PLA), polypropylene (PP), and polyethylene (PE)) are utilized for ordinary parts that are subjected to minimal stress. Engineering plastics (Polycarbonate (PC), polyethylene terephthalate (PET), and nylon (PA)) are used in structural elements because they have better wear resistance than conventional plastics. Advanced polymers (Polyethyleneimine (PEI), polyether-ether-ketone (PEEK)) are resistant to high temperatures, wear, and chemicals. (b) A Rader plot graph demonstrating polymer attributes such as printing ease, visual quality, elongation break, impact resistance, and heat resistance.

Polyether ether ketone (PEEK)

It has high mechanical strength, is lightweight, chemical, and heat resistant [7]. PEEK has a rather high printing temperature, about 340 °C [12]. It has a glass transition temperature of about 143 °C. Furthermore, it has many advantages, such as excellent mechanical and chemical resistance properties (high resistance to biodegradation and thermal degradation), enable it to be used in extreme environments requiring high service temperatures or mechanical properties, such as piston parts, bone, bearings, vehicles, and aircraft [22]. PEEK is a good option alternative feedstock for FDM since it can be handled similarly to an amorphous polymer, resulting in dimensional stability and good layer adhesion.

Acrylonitrile butadiene styrene (ABS)

ABS is made by the polymerization of styrene and acrylonitrile in the presence of polybutadiene and is amorphous. ABS is more suitable for use in FDM because it has higher toughness and strength than PLA, as well as better resistance to corrosive chemicals. [23]. However, it is somewhat difficult to print on because it tends to warp, which is due to a high shrinkage factor. ABS can produce chemical vapours that affect people with chemical sensitivity. The melting point of ABS is usually between 200-250 °C [24]. The automotive, healthcare and aerospace industries have employed ABS to fabricate a few functional components [25].

Polyethylene terephthalate (PET)

PET is a polymer that is semi-crystalline and belongs to the polyester family. Rather than raw PET, glycol-modified polyethylene terephthalate (PETG) is more popular in 3D printing filament owing to being less brittle and easy to use. PETG has better printability compared to ABS and enables the production of 3D

products with a smooth surface finish and excellent impact resistance, but PETG has a high absorbability of moisture from the air [26].

Nylon 6

Nylon 6 is known for its heat resistance, flexibility, and impact strength. It's good toughness values and is also durable. However, as a hygroscopic material, it absorbs a lot of moisture, which reduces its overall quality [27]. Like ABS, nylon tends to warp. The warping effect can be reduced by keeping the bed temperature at about 75 °C. However, it's sensitive to moisture and should be stored in a cool, dry place to maintain high-quality products [28].

Table 1. Comparison of the physical and mechanical properties, and printing conditions of ABS, Nylon, PET, and PEEK for FDM.

	ABS	Nylon 6	PEEK	PETG
Glass transition temperature (°C)	102–115	47–57	137–152	70-80
Melting temperature (°C)	-	220	335–343	-
Heat deflection temperature (°C)	100	190	160	71
Modulus (GPa)	1.8–2.39	2.8–3.1	3.56	0.9-1.1
Tensile strength (MPa)	25–65	79	92	55
Printing temperature (°C)	220–250	220–270	360–450	250
Bed temperature (°C)	95–110	70–90	360–450	75-90
Ref.	[26]	[29]	[29]	[26, 30]

4. Bio-degradable polymer

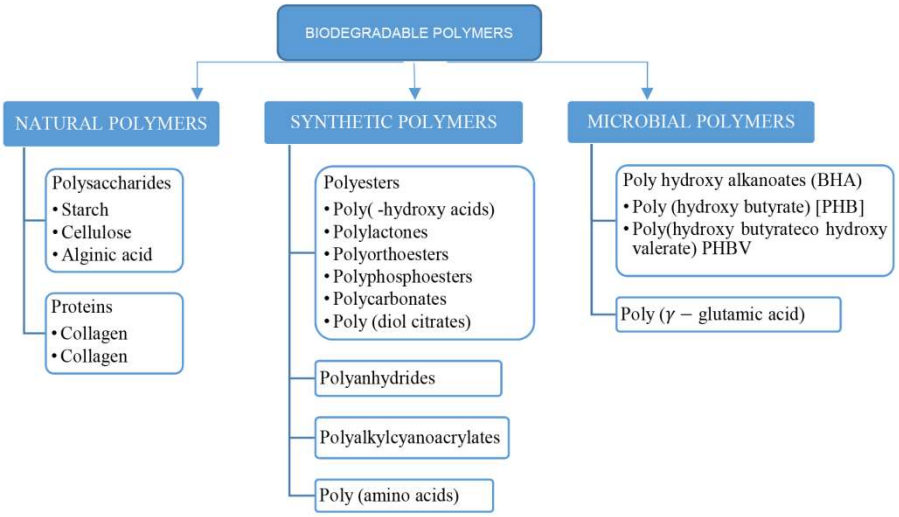

Figure 4. Classification of Biodegradable polymers.

Depending on their origin, biodegradable polymers are categorized into two categories: natural and synthetic. Synthetic polymers have an advantage over natural polymers in that they are more adaptable, have adjustable mechanical characteristics, and can vary the rate of deterioration as needed. Natural polymers, on the other hand, appear appealing due to their outstanding biocompatibility, but they haven't been completely studied due to undesired features including antigenicity and batch fluctuation [31]. Many fascinating uses for biodegradable polymers exist, including drug administration, tissue engineering, gene therapy, regenerative medicine, temporarily implanted devices, implant coatings, etc. [32, 33]. The basic criteria for selecting a polymer as a degradable biomaterial are matching the mechanical properties and degradation rate to the application requirements, nontoxic degradation products, biocompatibility, durability/stability, processability, and cost [31, 34]. Mechanical properties should be matched to the application to maintain adequate strength until the surrounding tissue has healed [35]. There are many Biodegradable polymers available for different applications (Figure 4), and the choice of the polymer depends on the requirements placed on a particular biomaterial.

Table 2. Bio-degradable materials for Fused deposition modeling machine.

Material	Produced from	Extrusion temperature	Properties
PLA	Plants starch	160 - 222 ℃	Tough, strong, bio-plastic, nontoxic, odorless, low-warp, Low heat resistance, brittle
PHA	Sugar with biosynthesis	160℃	UV-stable, stiffness, Elasticity ,brittle
HIPS	Petroleum	190 - 210 ℃	High impact resistance, soluble in limonene
PVA	Petroleum	190 - 210 ℃	Water-soluble, good barrier, biodegradable, recyclable, nontoxic, Expensive, deteriorates with moisture, special storage
PCL	Crystalline	100 - 140	non-toxic slow degradation good resistance to water and oil
High-density polyethylene	Ethylene monomer	180-205 ℃	Biodegradable, stronger intermolecular forces and tensile strength, Expensive

On the market, bio-composite filaments consist of a biologically degradable polymer matrix and bio-fillers. The additives are capable of fibers or particles. The percentage of filaments varies from a very small percentage to 40 percent of the amount. The most commonly used thermoplastic is polylactic acid, and

sawdust, cellulose fibers, or other natural fibers can be used as fillers. Filament manufacturers use different types of fibers: plum, seaweed, maple, hazelnut, bamboo, wick, mahogany, cedar, walnut, and willow. These are used to give a wood-like feel to the esthetic components [36]. The influenced thermoplastic cellulose derivatives are used on an FDM computer. Additive manufacturing as a key technology will push the design boundaries to more robust elements without the need for an additional cost or process specifications. It makes it especially appropriate for personalized parts and components sized in small batches. However, despite certain AM machine tools for small scale and low external specifications, it can co-locate development and use case venue, reducing the transportation and transport needs. Although FFF devices are being adopted by many consumers and manufacturers because of their minimal cost and effortless application, certain innovations of additive manufacturing shouldn't be overlooked [37]. Table 2 shows biodegradable which is used in FDM manufacturing.

PHA can be used as such or in a blend with polylactic acid. PVA is a biodegradable and water-soluble polymer that is used to support constructions. Duran et al [38] PVA is printed as support structure for ABS. They found that PVA is printable for up to 45 minutes when dried before it absorbs moisture from the air and becomes unprintable. High-impact polystyrene (HIPS) is similar to ABS with good mechanical properties and extrusion temperature. It's used as a substrate for ABS because it dissolves in limonene, but ABS doesn't. In biocompatible and medical applications, 3D printing filaments are made from polymers with low melting temperatures. These materials can be used in the FDM process to fabricate parts that blend into human tissue, such as scaffolds. Chia et al.[39] and Serra et al. [40] list some of these materials. Pietrzak et al. [41] and Melocchi et al [42] were developed capsules for drug delivery systems by using Biodegradable 3D-printed hollow hydroxypropyl cellulose (HPC) These capsules are taken orally and the degradation of the capsule in the stomach releases the drugs concealed in it.

Polylactic acid (PLA)

PLA is a common thermoplastic known for its biodegradability but also known for its sensitivity to humidity over 60 °C. PLA has a relatively low melt point around 145–186 ◦C and can be easily formed into filament with a temperature over 185–190 ◦C [43]. Biocompatibility and good mechanical properties (relatively high strength and modulus). The constructed by PLA parts have been observed to have lower distortions while printing than ABS, However they are less resistant and thermally conductive [44, 45]. PLA construct are most commonly utilized in practical applications that demand a certain level of aesthetics [46, 47]. it is extracted from renewable energy sources like maize starch or cane sugar. It may be produced using existing production equipment (the ones created and utilized in the oil and gas industry for materials). As a result, production process is quite inexpensive. PLA, therefore, has the second biggest production capacity of every bioplastic (most usually referred to as

polymer protein) [48]. Polylactic acid has a wide range of applications. Some of the most common applications are ecofriendly medical equipment, disposable films, and containers. PLA is excellent for use as a shrink wrap sheet because it binds when heated. Furthermore, the ease with which polylactic acid fuses lends itself to some intriguing applications for printing technology [49].

Polyvinyl alcohol (PVA)

The extent of hydrolysis and content of the acetate group affect the crystallinity and solubility of the polymer. The melting point for fully hydrolyzed PVA is 230 _C and 180–190 ℃ for partial hydrolysis. PVA biodegrades slowly, but decomposes quickly over 200 °C [50]. It has become a more suitable material to create structures and in other construction works owing to its durability, compatibility with natural fibers, chemical, lower cost, and flame resistance. vinyl polymer materials are formed by polymerizing the corresponding monomers. PVA endures either partial or full thermal decomposition of this polyvinyl acetate to extract acetate groups. PVA is used as innovative inks for additive manufacturing of objects of various sizes utilizing a layer-by-layer additive fabrication process.

Poly(ε-caprolactone) (PCL)

Poly(caprolactone) (PCL) is the most widely studied in this family [51, 52]. PCL is considered a non-toxic and tissue-compatible material and a semicrystalline polymer with a glass transition temperature of about -60ºC. The polymer has a low melting temperature (59 to 64ºC) and is compatible with a range of other polymers. PCL PCL is a valuable base polymer for developing long-term, implanted drug delivery devices since it degrades at a considerably slower pace than PLA. PCL is regarded as a non-toxic and tissue-compatible chemical [53]. PCL has been investigated as a vehicle for the long-term introduction of drugs/vaccines (Capronor®) and cell-based treatments due to its delayed degradation feature. Capronor® is long-acting contraception that contains the hormone levonorgestrel [54]. PCL has a modest tensile strength (about 23 MPa) and a very high elongation at breakage (>700%) [55]. PCL is well suited for fused deposition modeling (3D melt printing) and it has been used to prepare a variety of 3D scaffolds for tissue engineering [56].

Polyhydroxyalkanoates (PHA)

PHA consists of a class of natural-based polyesters synthesized using microbial fermentation of carbon-based feedstock; which are biodegradable and readily compostable thermoplastics, [57]. The polymer shows a glass transition temperature in the range of −5 to 20 °C. PHA are both bio-based and biodegradable, with physical and chemical properties similar to polypropylene, thereby making it a good alternative to PLA in biopolymer system developments. PHA is generally known to be:

- Although resistant to UV radiation, it is weak toward acids and bases.

- Biocompatible and non-toxic, thereby making it suitable for biomedical and food packaging applications [57].
- Insoluble in water, and relatively resistant to hydrolytic degradation

Its biocompatibility and biodegradability by simple hydrolysis of ester bonds in aerobic conditions and piezoelectric properties make them suitable for drug delivery, tissue engineering, and orthopedic applications.

High impact polystyrene (HIPS)

HIPS is a biodegradable thermoplastic with low strength and good process technology .The excellent flow characteristics, inexpensive cos, and impact resistance of this FFF filament are all benefits [44]. However, it is prone to wear and requires a high printing temperature and a hot build platform. HIPS has qualities that are comparable to ABS, however it is less thick. HIPS is preferable for support structures because it dissolves with chemicals such as limonene [58].

High-density polyethylene

Polyolefin thermoplastics such as high-density polyethylene (HDPE) are the world's leading manufacturers of plastics, environmentally friendly polymerization processes, recycling, and sustainability. HDPE is an ethylene monomer material made of thermoplastics. When used as HDPE pipe, it is sometimes called " polyethylene" or "alkathene" Higher density polyethylene is used to make high density plastic water bottles, plastic lumber, abrasion resistant containers, and geomembranes. An evaluation of the mechanical reusability of HDPE, a raw material widely used for open additive manufacturing, to assess the feasibility of using this recycled plastic in open 3D additive manufacturing [59].

Cellulose and nanocellulose

Cellulose is an inexhaustible and sustainable polymer. This highly innovative polymeric material is synthesized by numerous living organisms and used extensively in the pharmaceutical and food industries [60]. Its abundance is a consequence of the constant photosynthetic cycles occurring within the cells of plants, which can synthesize several tons a year [60]. They can be obtained from plants or agricultural waste; from husk fiber, bamboo, wood, and sugar cane bagasse [60]. The main characteristics of cellulose include its biodegradability, hydrophilicity, chirality, broad chemical modifying capacity, and capability of forming versatile semicrystalline fiber morphologies [61]. Most importantly, in the context of this review, it has the potential to encounter the cumulative demand for environmentally friendly, lightweight products but, similar to lignin, it can be limited by its poor mechanical properties [62].

5. Biodegradables in 3D printing manufacturing

PLA is widely used as a filament for 3D printing. PLA and other biodegradable polymer filaments can be processed with nanoparticles or nanofillers to form a

blend or composite to improve the properties of the filament and the final printed object. 3D printing is primarily used in the fabrication of scaffolds and other tissue engineering applications. Since the scaffolds are made of biodegradable polymer filaments, they're biocompatible and biodegradable under enzymatic action [63, 64]. PLA is the most commonly used bioplastic for FFF filaments. PLA is a biodegradable and biocompatible plastic derived from the fermented starch of plants such as corn, sugar beets, and sugar cane. It also doesn't emit toxic gases when printed. Polyhydroxyalkanoate (PHA) is a bioplastic produced by the bacterial fermentation of sugars or lipids. Like PLA, PHA is also a thermoplastic aliphatic polyester. The two most frequently used and widely available of PHAs are poly (3-hydroxybutyrate-co-3-hydroxy valerate) (PHBV) and poly(3-hydroxybutyrate) (PHB). PHB has more fracture toughness, strength, and rigidity than PHBV, which is ductile.

A novel electro-hydrodynamic jet printing with FDM technique (E-FDM) was employed by Zhang et al. to prepare 3D printed tissue regeneration scaffolds using poly (lactic acid) PLA filaments with different structure sizes. The 3D printing technique gave high speed and high-resolution prints i.e. up to submicron level and directly used PLA filament [65].

FDM 3D printing carried out using graphene incorporated PLA filament also produced patient-specific implants and orthopedic scaffolds with graded porosity and optimum density as reported by Bustillos et al. The polymeric chains were restricted by graphene giving a reduction in crystallinity, enhancement in the creep resistance, and other mechanical properties. The 3D sample prepared from these composites exhibited superior wear and creep resistance as compared to that prepared using pure PLA filaments [66].

Foresti et al. [67]. used the FFF process to produce respirators to support COVID -19 pandemic response by providing safety protection devices. For printing masks utilizing the FFF method, several health-related considerations such as health, consumer safety, virus prevention, regulatory requirements, reusability, and disinfect ability are crucial. Polylactic acid (PLA), advanced polyolefins, and styrene-ethyl butylene-styrene are used in the research work to produce flexible and adaptable masks. Application of continuous fiber-reinforced thermoplastic composites (CFRTPCs) in printing 3D samples which could be used in aviation and aerospace applications was carried out by Tian et al.

The developed 3D printed samples were lightweight and an efficiently performing alternative to conventional materials. These CFRTPCs were formulated using a polymer matrix of poly (lactic acid) (PLA) filament and reinforcement of continuous carbon fibers which were fed to fused deposition modeling (FDM) 3D printers simultaneously. The fiber content of 27% gave optimum mechanical properties to the composite. The layer thickness of 0.4 mm to 0.6 mm exhibited optimum bonding between the layers [68].

Ferreira et al. [69] investigated the characteristics of PLA composites with pure PLA using short carbon fibres with an average length of 60 μm as reinforcing material. An experimental investigation showed that the tensile modulus, stiffness, Poisson's ratio, and shear modulus of the composite parts

increased significantly. In contrast, there were no significant changes in tensile and shear strength. This indicates that the matrix material was stressed during loading and the adhesion between PLA and carbon fibres was insufficient.

Hollander et al. employed PCL filaments using a model drug indomethacin in 3 concentrations using the hot-melt extrusion technique. These modified filaments were used to print T-shaped prototypes of the intrauterine system using the FDM 3D printing technique. The morphology and other properties of the filament and printed samples were dependent on the amount of drug-loaded in the sample [70].

Rymansaib et al. [71] used carbon nanotube and graphite flakes as reinforcements at different proportions with different thermoplastics such as PLA, graphene-PLA, ABS, PCL, and HIPS to identify the best material for FFF electrode production. Owing to its improved surface properties and electrical conductivity, HIPS with 10% carbon nanotubes and 10% graphite flakes has been the most suited combination for electrode production, according to different composite compositions.

Many industrial sectors should consider PLA and Poly (3-hydroxybutyrate (PHB) to be biodegradable and biocompatible alternatives to traditional polymers, but both PLA and PHB have drawbacks. PHB has poor processing qualities and is hard, fragile, and brittle. It is recommended that PHB be blended with an amorphous polymer, such as poly(-lactic acid), to minimize its crystallinity and so increase its applicability [72]. Despite this blending, these pure PHB/PLA blends remain brittle and stiff, with poor mechanical characteristics and thermal degradation around the melting point, limiting their processability. The poor ductile properties can be improved by the addition of plasticizers [73].

To investigate the mechanical characteristics of composite components Kaygusuz and Özerinç [74], mixed 12 wt% PHA with PLA for FFF filaments. When compared to PLA-only components, the ductility improved by around 160 %, while the tensile strength reduced by about 25 %. It was suggested that the printing temperature be regulated between 210 and 240°C. Plasticizers such as acetyl tributyl citrate and tributyl citrate can help improve the bonding between PHA and PLA [75].

Ausejo et al. [76] also produced parts by the FFF process from PLA/PHA composites at horizontal and vertical build orientations. It was concluded that the build orientation is a significant process parameter for tensile properties, morphology, structure, and surface properties of the composite build parts. The PLA/PHA composite is a potential filament material for bone scaffolds as it is nontoxic and biocompatible.

Chen et al. [77] for tissue engineering applications researchers adopted the FFF technique. The filament material is a polymer matrix composite comprising PVA and β-TCP. PVA has the bone-bonding ability and mechanical performance are boosted by the inclusion of β-TCP as reinforcement, in addition to its nontoxicity, tunable hydrophilicity, facile modifiability, and superior biocompatibility. In the creation of composite filaments for the manufacture of

porous structures using the FFF technique, micrometer-sized HA was utilized as reinforcement particles with the PLA matrix[78]. In the PLA-HA composite, several quantities of HA were employed, with the highest proportion of HA being 50%. In comparison to PLA-only composite components, PLA-HA composite parts have high porosity, high surface roughness, high cell adhesion, and poor stiffness. compared to pure PLA parts.

other researchers, such as Wu et al. [79] have employed PHA composites in the FFF method for filament preparation. Complex shaped items and food-grade packaging may be made with PHA matrix composites[80]. Plasticizers and other additives can be added to composites to increase particular attributes including interlayer bonding and tensile strength.

Wang et al. [22], compared a composite of cellulose nanofibers and P LA using polyethylene glycol 600 (PEG600) as a plasticizer to pure PLA in their investigation. With a fiber concentration of 2.5 wt.%, thermal stability, tensile strength, and elongation at the break all increased considerably.

Conclusion

The three most well-known polymer materials for pure thermoplastic FFF filaments and composite FFF filaments are PLA, ABS, and nylon. Other polymers have been utilized as FFF filament, including PEI, PC, PP, HIPS, and PEEK. The use of 3D printing technology in biomedical applications has expanded the usage of biodegradable polymers in the form of tailored scaffolds and grafts. These polymers may be used in a variety of additional ways, such as fibers and textiles for eco-friendly packaging and in the textile industry. As a result, there is extensive scope for more academic and industry research into understanding and commercializing diverse products made from these polymers that are ideal for various uses. However, research into producing composite filament from these polymers is currently restricted.

References

[1] Negrin M, Macerata E, Consolati G, Quasso F, Genovese L, Soccio M, Giola M, Lotti N, Munari A, Mariani M (2018) Gamma radiation effects on random copolymers based on poly(butylene succinate) for packaging applications. Radiat Phys Chem 142:34–43

[2] Calabia B, Ninomiya F, Yagi H, Oishi A, Taguchi K, Kunioka M, Funabashi M (2013) Biodegradable Poly(butylene succinate) Composites Reinforced by Cotton Fiber with Silane Coupling Agent. Polymers 5:128–141

[3] Boparai KS, Singh R (2018) Thermoplastic composites for fused deposition modeling filament: Challenges and applications

[4] Mohamed OA, Masood SH, Bhowmik JL, Somers AE (2017) Investigation on the tribological behavior and wear mechanism of parts processed by fused deposition additive manufacturing process. J Manuf Process 29:149–159

[5] Wohlers T, Gornet T (2014) History of additive manufacturing. Wohlers Rep 24:118
[6] Ahn D, Kweon J-H, Choi J, Lee S (2012) Quantification of surface roughness of parts processed by laminated object manufacturing. J Mater Process Technol 212:339–346
[7] Wang J, Goyanes A, Gaisford S, Basit AW (2016) Stereolithographic (SLA) 3D printing of oral modified-release dosage forms. Int J Pharm 503:207–212
[8] D. Slavko and K. Matic, (2010) Selective laser sintering of composite materials technologies. Annals of DAAAM & Proceedings, Bd. 21
[9] N. Turner B, Strong R, A. Gold S (2014) A review of melt extrusion additive manufacturing processes: I. Process design and modeling. Rapid Prototyp J 20:192–204
[10] Cuiffo MA, Snyder J, Elliott AM, Romero N, Kannan S, Halada GP (2017) Impact of the Fused Deposition (FDM) Printing Process on Polylactic Acid (PLA) Chemistry and Structure. Appl Sci 7:579
[11] Ni F, Wang G, Zhao H (2017) Fabrication of water-soluble poly(vinyl alcohol)-based composites with improved thermal behavior for potential three-dimensional printing application: ARTICLE. J Appl Polym Sci 134
[12] Xiao J, Gao Y (2017) The manufacture of 3D printing of medical grade TPU. Prog Addit Manuf 2:117–123
[13] Chunze Y, Yusheng S, Jinsong Y, Jinhui L (2009) A Nanosilica/Nylon-12 Composite Powder for Selective Laser Sintering. J Reinf Plast Compos 28:2889–2902
[14] Liu Z, Wang Y, Wu B, Cui C, Guo Y, Yan C (2019) A critical review of fused deposition modeling 3D printing technology in manufacturing polylactic acid parts. Int J Adv Manuf Technol 102:2877–2889
[15] Sun Q, Rizvi GM, Bellehumeur CT, Gu P (2008) Effect of processing conditions on the bonding quality of FDM polymer filaments. Rapid Prototyp J 14:72–80
[16] Ngo TD, Kashani A, Imbalzano G, Nguyen KTQ, Hui D (2018) Additive manufacturing (3D printing): A review of materials, methods, applications and challenges. Compos Part B Eng 143:172–196
[17] Pu'ad NM, Haq RA, Noh HM, Abdullah HZ, Idris MI, Lee TC (2020) Review on the fabrication of fused deposition modelling (FDM) composite filament for biomedical applications. Mater Today Proc 29:228–232
[18] Bakarich SE, Gorkin R, in het Panhuis M, Spinks GM (2014) Three-Dimensional Printing Fiber Reinforced Hydrogel Composites. ACS Appl Mater Interfaces 6:15998–16006
[19] Dudek P (2013) FDM 3D Printing Technology in Manufacturing Composite Elements. Arch Metall Mater 58:1415–1418
[20] Mostafa N, Syed HM, Igor S, Andrew G (2009) A study of melt flow analysis of an ABS-Iron composite in fused deposition modelling process. Tsinghua Sci Technol 14:29–37
[21] Park S, Fu K (Kelvin) (2021) Polymer-based filament feedstock for additive manufacturing. Compos Sci Technol 213:108876

[22] Wang Q, Ji C, Sun L, Sun J, Liu J (2020) Cellulose Nanofibrils Filled Poly(Lactic Acid) Biocomposite Filament for FDM 3D Printing. Molecules 25:2319
[23] Kuo C-C, Liu L-C, Teng W-F, Chang H-Y, Chien F-M, Liao S-J, Kuo W-F, Chen C-M (2016) Preparation of starch/acrylonitrile-butadiene-styrene copolymers (ABS) biomass alloys and their feasible evaluation for 3D printing applications. Compos Part B Eng 86:36–39
[24] Rutkowski JV, Levin BC (1986) Acrylonitrile–butadiene–styrene copolymers (ABS): Pyrolysis and combustion products and their toxicity—a review of the literature. Fire Mater 10:93–105
[25] Lee H, Lim CHJ, Low MJ, Tham N, Murukeshan VM, Kim Y-J (2017) Lasers in additive manufacturing: A review. Int J Precis Eng Manuf-Green Technol 4:307–322
[26] Kauffman GB (2010) Book Review of Polymer Data Handbook. ACS Publications
[27] Terekhina S, Skornyakov I, Tarasova T, Egorov S (2019) Effects of the infill density on the mechanical properties of nylon specimens made by filament fused fabrication. Technologies 7:57
[28] Cho B-G, McCarthy SP, Fanucci JP, Nolet SC (1996) Fiber reinforced nylon-6 composites produced by the reaction injection pultrusion process. Polym Compos 17:673–681
[29] Mark JE (Hrsg) (2009) Polymer data handbook. Oxford University Press: Oxford ; New York, 2nd ed
[30] Latko-Durałek P, Dydek K, Boczkowska A (2019) Thermal, rheological and mechanical properties of PETG/RPETG blends. J Polym Environ 27:2600–2606
[31] Domb AJ, Kumar N, Ezra A (Hrsg) (2011) Biodegradable Polymers in Clinical Use and Clinical Development: Domb/Biodegradable Polymers. John Wiley & Sons, Inc.: Hoboken, NJ, USA
[32] Hacker M, Mikos A (2009) Foundations of Regenerative Medicine: Clinical and Therapeutic Applications. Academic press, London
[33] Luten J, van Nostrum CF, De Smedt SC, Hennink WE (2008) Biodegradable polymers as non-viral carriers for plasmid DNA delivery. J Controlled Release 126:97–110
[34] Gunatillake PA, Adhikari R, Gadegaard N (2003) Biodegradable synthetic polymers for tissue engineering. Eur Cell Mater 5:1–16
[35] Gunatillake P, Mayadunne R, Adhikari R, El-Gewely MR (2006) Biotechnol Annu Rev
[36] Markstedt K, Sundberg J, Gatenholm P (2014) 3D bioprinting of cellulose structures from an ionic liquid. 3D Print Addit Manuf 1:115–121
[37] Hunt EJ, Zhang C, Anzalone N, Pearce JM (2015) Polymer recycling codes for distributed manufacturing with 3-D printers. Resour Conserv Recycl 97:24–30
[38] Duran C, Subbian V, Giovanetti MT, Simkins JR, Beyette Jr FR (2015) Experimental desktop 3D printing using dual extrusion and water-soluble polyvinyl alcohol. Rapid Prototyp J
[39] Chia HN, Wu BM (2015) Recent advances in 3D printing of biomaterials. J Biol Eng 9:4

[40] Serra T, Planell JA, Navarro M (2013) High-resolution PLA-based composite scaffolds via 3-D printing technology. Acta Biomater 9:5521–5530
[41] Pietrzak K, Isreb A, Alhnan MA (2015) A flexible-dose dispenser for immediate and extended release 3D printed tablets. Eur J Pharm Biopharm 96:380–387
[42] Melocchi A, Parietti F, Loreti G, Maroni A, Gazzaniga A, Zema L (2015) 3D printing by fused deposition modeling (FDM) of a swellable/erodible capsular device for oral pulsatile release of drugs. J Drug Deliv Sci Technol 30:360–367
[43] Kim K, Park J, Suh J, Kim M, Jeong Y, Park I (2017) 3D printing of multiaxial force sensors using carbon nanotube (CNT)/thermoplastic polyurethane (TPU) filaments. Sens Actuators Phys 263:493–500
[44] Kumar R, Singh R, Farina I (2018) On the 3D printing of recycled ABS, PLA and HIPS thermoplastics for structural applications. PSU Res Rev
[45] Rodríguez-Panes A, Claver J, Camacho AM (2018) The influence of manufacturing parameters on the mechanical behaviour of PLA and ABS pieces manufactured by FDM: A comparative analysis. Materials 11:1333
[46] Dey A, Hoffman D, Yodo N (2020) Optimizing multiple process parameters in fused deposition modeling with particle swarm optimization. Int J Interact Des Manuf IJIDeM 14:393–405
[47] Mazzanti V, Malagutti L, Mollica F (2019) FDM 3D printing of polymers containing natural fillers: A review of their mechanical properties. Polymers 11:1094
[48] de Ciurana J, Serenóa L, Vallès È (2013) Selecting Process Parameters in RepRap Additive Manufacturing System for PLA Scaffolds Manufacture. Procedia CIRP 5:152–157
[49] Jerez-Mesa R, Travieso-Rodriguez JA, Llumà-Fuentes J, Gomez-Gras G, Puig D (2017) Fatigue lifespan study of PLA parts obtained by additive manufacturing. Procedia Manuf 13:872–879
[50] Suriyamongkol P, Weselake R, Narine S, Moloney M, Shah S (2007) Biotechnological approaches for the production of polyhydroxyalkanoates in microorganisms and plants — A review. Biotechnol Adv 25:148–175
[51] Hayashi T (1994) Biodegradable polymers for biomedical uses. Prog Polym Sci 19:663–702
[52] Holland SJ, Tighe BJ (1992) Biodegradable polymers. Adv Pharm Sci 6:101–164
[53] Kronenthal RL (1975) Biodegradable polymers in medicine and surgery. Polymers in medicine and surgery. Springer, 119–137
[54] Lee K, Kaplan D (2006) Tissue engineering I: scaffold systems for tissue engineering. Springer, Bd. 102
[55] Gunatillake P, Mayadunne R, Adhikari R (2006) Recent developments in biodegradable synthetic polymers. Biotechnology Annual Review. Elsevier, Bd. 12 301–347
[56] Shim J-H, Lee J-S, Kim JY, Cho D-W (2012) Bioprinting of a mechanically enhanced three-dimensional dual cell-laden construct for osteochondral tissue

engineering using a multi-head tissue/organ building system. J Micromechanics Microengineering 22:085014
[57] Mckeen L (2012) Renewable resource and biodegradable polymers. The effect of sterilization on plastics and elastomers. Elsevier, Amsterdam, The Netherlands. DOI, Bd. 10
[58] Pakkanen J, Manfredi D, Minetola P, Iuliano L (2017) About the use of recycled or biodegradable filaments for sustainability of 3D printing. International conference on sustainable design and manufacturing. Springer, 776–785
[59] Singh AK, Saltonstall B, Patil B, Hoffmann N, Doddamani M, Gupta N (2018) Additive Manufacturing of Syntactic Foams: Part 2: Specimen Printing and Mechanical Property Characterization. JOM 70:310–314
[60] Javadzadeh Y, Hamedeyaz S (2014) Floating Drug Delivery Systems for Eradication of Helicobacter pylori in Treatment of Peptic Ulcer Disease. In: Roesler B (Hrsg) Trends in Helicobacter pylori Infection. InTech
[61] Klemm D, Heublein B, Fink H-P, Bohn A (2005) Cellulose: Fascinating Biopolymer and Sustainable Raw Material. Angew Chem Int Ed 44:3358–3393
[62] Dai L, Cheng T, Duan C, Zhao W, Zhang W, Zou X, Aspler J, Ni Y (2019) 3D printing using plant-derived cellulose and its derivatives: A review. Carbohydr Polym 203:71–86
[63] Zhuang Y, Song W, Ning G, Sun X, Sun Z, Xu G, Zhang B, Chen Y, Tao S (2017) 3D–printing of materials with anisotropic heat distribution using conductive polylactic acid composites. Mater Des 126:135–140
[64] Ronca D, Langella F, Chierchia M, D'Amora U, Russo T, Domingos M, Gloria A, Bartolo P, Ambrosio L (2016) Bone Tissue Engineering: 3D PCL-based Nanocomposite Scaffolds with Tailored Properties. Procedia CIRP 49:51–54
[65] Zhang B, Seong B, Nguyen V, Byun D (2016) 3D printing of high-resolution PLA-based structures by hybrid electrohydrodynamic and fused deposition modeling techniques. J Micromechanics Microengineering 26:025015
[66] Bustillos J, Montero D, Nautiyal P, Loganathan A, Boesl B, Agarwal A (2018) Integration of graphene in poly(lactic) acid by 3D printing to develop creep and wear-resistant hierarchical nanocomposites. Polym Compos 39:3877–3888
[67] Foresti R, Ghezzi B, Vettori M, Bergonzi L, Attolino S, Rossi S, Tarabella G, Vurro D, von Zeppelin D, Iannotta S, Zappettini A, Macaluso GM, et al. (2021) 3D Printed Masks for Powders and Viruses Safety Protection Using Food Grade Polymers: Empirical Tests. Polymers 13:617
[68] Tian X, Liu T, Yang C, Wang Q, Li D (2016) Interface and performance of 3D printed continuous carbon fiber reinforced PLA composites. Compos Part Appl Sci Manuf 88:198–205
[69] Ferreira RTL, Amatte IC, Dutra TA, Bürger D (2017) Experimental characterization and micrography of 3D printed PLA and PLA reinforced with short carbon fibers. Compos Part B Eng 124:88–100

[70] Holländer J, Genina N, Jukarainen H, Khajeheian M, Rosling A, Mäkilä E, Sandler N (2016) Three-Dimensional Printed PCL-Based Implantable Prototypes of Medical Devices for Controlled Drug Delivery. J Pharm Sci 105:2665–2676

[71] Rymansaib Z, Iravani P, Emslie E, Medvidović-Kosanović M, Sak-Bosnar M, Verdejo R, Marken F (2016) All-Polystyrene 3D-Printed Electrochemical Device with Embedded Carbon Nanofiber-Graphite-Polystyrene Composite Conductor. Electroanalysis 28:1517–1523

[72] Gunaratne LMWK, Shanks RA (2008) Miscibility, melting, and crystallization behavior of poly(hydroxybutyrate) and poly(D,L-lactic acid) blends. Polym Eng Sci 48:1683–1692

[73] Arrieta MP, Samper MD, López J, Jiménez A (2014) Combined Effect of Poly(hydroxybutyrate) and Plasticizers on Polylactic acid Properties for Film Intended for Food Packaging. J Polym Environ 22:460–470

[74] Kaygusuz B, Özerinç S (2019) Improving the ductility of polylactic acid parts produced by fused deposition modeling through polyhydroxyalkanoate additions. J Appl Polym Sci 136:48154

[75] Menčík P, Přikryl R, Stehnová I, Melčová V, Kontárová S, Figalla S, Alexy P, Bočkaj J (2018) Effect of Selected Commercial Plasticizers on Mechanical, Thermal, and Morphological Properties of Poly(3-hydroxybutyrate)/ Poly(lactic acid)/Plasticizer Biodegradable Blends for Three-Dimensional (3D) Print. Materials 11:1893

[76] Gonzalez Ausejo J, Rydz J, Musioł M, Sikorska W, Sobota M, Włodarczyk J, Adamus G, Janeczek H, Kwiecień I, Hercog A, Johnston B, Khan HR, et al. (2018) A comparative study of three-dimensional printing directions: The degradation and toxicological profile of a PLA/PHA blend. Polym Degrad Stab 152:191–207

[77] Chen G, Chen N, Wang Q (2019) Fabrication and properties of poly(vinyl alcohol)/β-tricalcium phosphate composite scaffolds via fused deposition modeling for bone tissue engineering. Compos Sci Technol 172:17–28

[78] Esposito Corcione C, Gervaso F, Scalera F, Padmanabhan SK, Madaghiele M, Montagna F, Sannino A, Licciulli A, Maffezzoli A (2019) Highly loaded hydroxyapatite microsphere/ PLA porous scaffolds obtained by fused deposition modelling. Ceram Int 45:2803–2810

[79] Wu C-S, Liao H-T, Cai Y-X (2017) Characterisation, biodegradability and application of palm fibre-reinforced polyhydroxyalkanoate composites. Polym Degrad Stab 140:55–63

[80] Tian J, Zhang R, Wu Y, Xue P (2021) Additive manufacturing of wood flour/polyhydroxyalkanoates (PHA) fully bio-based composites based on micro-screw extrusion system. Mater Des 199:109418

Identifying the optimum tilting angles for solar thermal collectors using four different modelling factors in hungary

Rajab GHABOUR[1], Péter KORZENSZKY[2]
[1]Doctoral School of Mechanical Engineering,
Hungarian University of Agriculture and Life Sciences
[2]Institute of Technology, Hungarian University of Agriculture and Life Sciences

Abstract

Presently, there are many difficulties facing the industrial sector regarding energy and environmental impact because of the usage of fossil fuels in various human activities and their negative impact on the environment, people, and health. Alternative ways are available to everyone and cannot be monopolised as researchers seek renewable energies. On the other hand, the food industry is the fastest-growing globally, especially in developing countries. At the same time, all the world countries face challenges to the continuity of energy supply and the negative impact on all creatures and planet. These countries have renewable energies that can serve as a primary or auxiliary energy source, especially for small milk pasteurisation farms. Pasteurisation aims to reduce the number of harmful pathogenic microorganisms to an acceptable level. This industry requires medium temperatures and heat exchangers to manufacture pasteurised milk, cheese, and other dairy products. Currently, the use of renewable energy in our world today is typical. It is available everywhere and in different forms, but to a lesser degree, within the industrial and production sector. The obstacles depend on many challenges and problems that bind these two together. The most prominent of these problems is the lack of a reference system for hybridising industrial food needs that fluctuate daily or annually with available renewable energy—and second, calculating or measuring the thermal utilisation rate of renewable energy in the industry. In many cases, the temperature and the pasteurisation time are the critical control point (CCP) of food safety. It is necessary to insert buffer storage into the system in the milk factory. Milk storage and heat treatment is a very energy-intensive process. This research goal is to calculate the optimum angle for solar heat for industrial systems existing in Budapest, Hungary. The F-Chart method was used, including four different modelling factors. The supposed industrial process is a pasteurising plant where the demand fluctuates similarly to the solar gain. The results show that the ASHRAE model is closer to reality than the other models. The optimum angle is 63º with 76.58% solar fraction using 20 m^2 for 32.64 GJ demand per annum. The results show that solar thermal energy can be a good potential in central Europe to replace fossil fuels in thermal demands.

Keywords

solar tank, food industry, energy storage, optimum angle, modelling

1. Introduction

The processes in food production, especially water, milk, and Dairy products, are fast-growing, especially in developing countries, which are characterised by many problems, especially the cost of energy and its adverse effects on the environment in the case of usage of traditional sources of fuel . The problem of polluted water in the world is severe, and drinking unsaturated water causes health disasters and sometimes death worldwide. Despite solar energy's tremendous energy and knowing that solar energy in the industry reduces carbon emissions by 65-75% 4. However, the field of application within industrial and food applications is slow because of many obstacles. The most important is to evaluate the feasibility of pre-hybrid projects and determine the optimal points of working parameters. One of the most significant advantages to using the solar energy of the low-temperature pasteurisation system is that it is characterised by uncomplicated inputs, low temperature, ease of control, simple interface, and high reliability. It helps developing countries, especially for the low cost, short payback period, ease of use and low maintenance. Abraham et al have mentioned that the problem of polluted water, especially in the developing world countries, has serious consequences where hundreds of millions of people have no access to safe water, so it causes sickness and even death every year. The authors showed that solar thermal energy could offer a cheap and easy solution with complete pathogens inactivation. Lucentini et al analysed the economic feasibility and technical study of an innovative pasteurising plant in different solar radiation conditions during the year, wherein the processes lost is around 35% of the energy production. Mainly on cleaning the heat exchangers and the floor where the needed temperature is low with a maximum of 70 °C, the solar energy system is designed to cover a part of the plant's thermal yearly energy demand. The estimated cost for providing the service mentioned above for a medium-sized plant is around 38000 $ annually. And for this plant, it was noticed that the payback period was between 10 to 11 years if the natural gas is used and available and five years if the diesel is the only solution, by considering the plant life around 20 years. Panchal et al illustrated the effects on the environment and human being health because of the use of fossil fuel. Milk can be obtained by many animals such as goats, cows, and buffalo, but it can directly be consumed because it contains bacteria and microorganisms. And the solar solution has many advantages: in a remote area, it can be used for better human health and environmentally friendly solution. And it considers a perfect solution where individual farmers produce and deliver small quantities of milk. And the cow, for example, produces 3.1 kg per head in an annual average. Wayua et al have experimented with flat plate solar collectors to heat the water with a low-cost milk pasteuriser and a thickness of 1.5 mm stainless steel. The experiments have made in the northern part of Kenya for 40 litres of raw milk, which was the optimum quantity for the experimental conditions. The milk container used has a capacity of 80 litres with a 50 mm hot water jacket and 38 mm fibreglass insulation. It was observed that the 40 litres of milk required around 1.3 ± 0.5

hours with an interval of the solar intensity of 700 – 1000 W /m^2. As a result, this low-cost solar milk pasteuriser is highly recommended for arid pastoral areas with no grid electricity.

The milk market is a significant income source for the people living there and reduces CO_2 emissions by saving the wood burned. India is one of the largest milk producers, 20% of the total world production and 80 million people work in this sector. Edwin and Sekhar said that the milk industry is a fast-growing business where they face critical problems regarding gas or fuel or environmental aspects. Moreover, solar energy and biomass will be innovative technology used in the rules. This experiment analysed four systems: gas source, biogas, biomass, and solar energy, which shows one of the best results.

Schmitt defined that despite solar energy's tremendous energy. However, industrial and food applications are slow because of many obstacles. The most important is to evaluate the feasibility of pre-hybrid projects dimensioning where the tools and guidelines are required and determine the optimal working parameters' points. This research will classify the integration of solar energy in the food and beverage industry sector. To simplify the choice of the best suitable integration point for the hot water solar system (below 150 °C) in industry. All of these within the critical steps in the feasibility study and assessment is considered one fundamental reason for the slow development of solar energy in the industrial sector. A suggested model illustrates the example of pasteurising methods with the food and beverage industry. According to this model, three different methods for different systems can be used. Where for preheating of fluid streams, flash pasteurisation can be assigned.

Furthermore, for heating and maintaining the temperature of the baths, machinery, or tanks, Spray pasteurising and thermalisation. Allouhi et al admitted that utilising solar energy in various industrial branches has a high opportunity after the high challenge faced by the industrial sector in environmental and energetic terms. In Casablanca, they optimised a centralised solar heating system to provide hot water for industrial purposes and with different levels of temperature and loads. The case study was a milk processing industry where the goal was to find the optimum size solution and the corresponding life cycle cost. As a result of this research, it was found that the 400 m^2 evacuated solar thermal tubes tilted at an angle of 30° and connected to a 2000 litres tank. This solution can reach the highest life cycle, which saves the cost of 179,000 USD per year. Moreover, the annual solar fraction was 41%, and the payback period for this project is 12.27 years and saves 77.23 tons of CO_2 greenhouse emission equivalent annually.

Yildirim and Genc analysed powder milk production's exergy and energy analysis in their paper. Because of its characteristics can be transformed into many other shapes such as cheese, yoghurt, and milk powder. The powder milk production system has pasteurising, evaporation, and spray drying. Furthermore, because the powder milk has the highest shelf time, it can be stored at ambient temperature. It has the highest selling price and the lowest volume, requiring fewer transportation expenses. As a result of this research, it was found that the

evaporator and the heater have a higher improvement impact on the whole system, and the energetic efficiency was 83% (as in Fig. 1.).

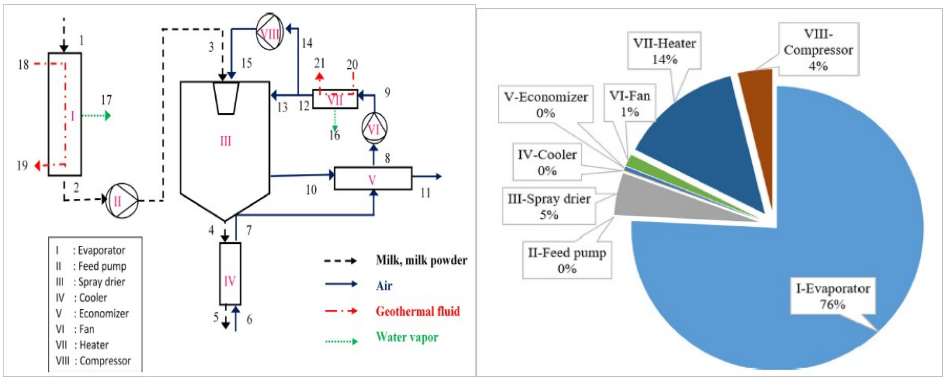

Figure 1. Scheme of the powder industry and the impact ratios of the whole system.

Daneshi et al have studied and estimated packaged fluid milk's carbon footprint (CF) using the life cycle assessment. The goal of this research was to the sources of the emission and how to reduce it. According to IPCC 2006 methodology, a questionnaire was divided on the dairy plant in 2011-2012. As a result, each one kg of corrected fat milk generates 1.57 kg CO_2-eq. Moreover, the main contribution was methane 30%, electricity 14%, diesel 8.9%, manure emission 8.9%, and transportation 8.6%. So, the result was higher in Iran than the EU standard. The potential of using renewable energy, especially solar energy, will significantly reduce emissions. Wallerand et al have optimised the design of solar-assisted energy in the industrial process where the case study was dairy products based on economic and environmental criteria. The researchers illustrated the obstacles facing the integration of renewable energies, such as the time-dependency of resources, storage, and losses. As a result, it was found that the integration of solar energy can significantly reduce the environmental impact of this process with a 65-75% reduction in CO_2-eq emissions. However, this is only combined with an improved heat pump system and heat recovery. These two combinations (heat pump and heat recovery) are in the process to reduce the exergy losses and to enhance efficiency. Also, using a meagre cost, a very low efficiency flat solar collector offers a simple solution that can reduce emissions by about 30 %.

Lucentini et al have presented solar energy's potential in India's heating processes and reduced greenhouse emissions. Many locations and different ambient conditions were tested, also the relationship between the annual performance of the solar heating system and the direct annual irradiance on the total annual performance. As a result, it was found that the dairy sector in India needs 6.4 PJ annually, which can be reduced to 4.5 PJ annually if used solar energy is restricted to the pasteurising stage. Moreover, the corresponding solar

area needed is (1.54-1.83) million m^2 with an average annual solar utilising fraction (0.18-0.32). The reduced CO_2 emission will be around (32–144) thousand tons per year. Manfrida et al studied the potential of using a solar collector with natural circulation in developing countries or emergencies. The system combination consists of a commercial solar collector arranged with a natural circulation system and water compensation. So, there is no electricity needed. The design was tested in different locations and seasons to measure productivity. Depending on the location and year, the system's capability is around 40-80 kg/day/m^2.

In the literature, we did not find any comprehensive study considering the central European climate and specifically Hungary, which illustrates the potential of using solar heat for industrial processes (SHIP). Also, the optimisation methods are missing to identify the best angles considering each case study. Our study will compare four different models (Machler and Iqbal, Parishwad et al, Nijegorogov, and ASHRAE) to identify the optimum tilting angle in Budapest, Hungary, considering the clearness index as a reference. The research also includes a preassumed case study of a dairy factory with annual hot water consumption of 32 GJ.

2. Materials and methods

Design of active systems: f-chart method

Components used in air and water solar systems are standard. These designs are based on a great deal of information and accumulated experience. For residential applications, the cost of a small project does not justify the need for simulation. Then more straightforward "shortcut" methods can be used. So that the design of these simple systems is easy, and it is easier to estimate their thermal performance in the long term. Here, the " f-Chart " method, which applies to heat the medium material to temperatures not less than 20 ° C, will be discussed in the conditions of the residential buildings or their corresponding applications in industrial heat and air conditioning. The load provided through solar energy is the basis for calculations of this method. The secondary variables are the type of collector, storage capacity, liquid flow rate, and heat exchanger size for the load and collector. Thus, this method is the product of many hundreds of thermal simulators of solar energy systems. The conditions of the simulators have varied and changed according to an appropriate number of parameters. Therefore, the resulting final correlations give the F parameter, representing the fraction of the monthly load (for heating and hot water) provided by solar energy as a function of two dimensionless parameters. This method has been developed for three standard configurations. Liquid and air systems for places (hot water) heating and systems for hot water only. Fig. 2. schematic diagram shows the standard heating system using liquid heat transfer fluids.

An anti-freezing liquid is used in the solar collector's loops and the water as a storage medium in this system. In some cases, water can be used directly in solar

collectors and does not need a heat exchanger for the solar collector. At the same time, an auxiliary heater is usually provided for extra energy if the solar reservoir cannot meet the load. The following table illustrates the primary relationships and linkages of the main design factors of this method as in Table 1.

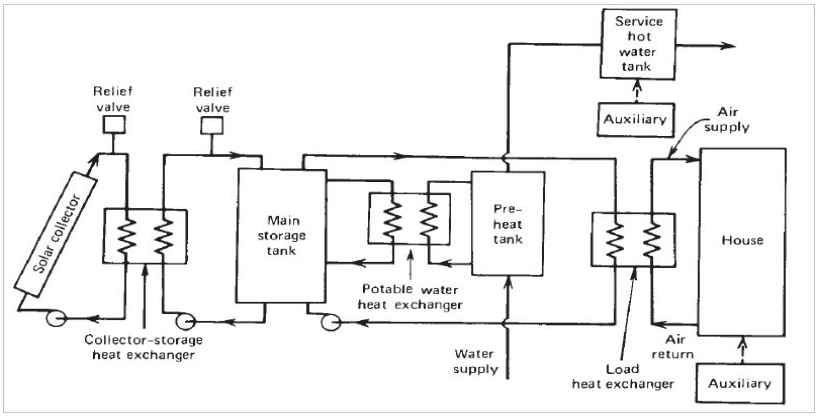

Figure 2. Schematic of standard system configuration using liquid heat transfer and storage media.

Table 1. Ranges of Design Parameters Used in Developing f -Charts for Liquid and Air Systems.

$0.6 \geq (\tau\alpha)_n \leq 0.9$
$5 \leq F'_R A_C \leq 120$ m^2
$2.1 \leq U_L \leq 8.3$ W/m^2 °C
$30 \leq \beta \leq 90$ °
$83 \leq (UA)_h \leq 667$ W/°C

Solar energy is transferred via a heat exchanger to the preheating tank, which provides hot water heated by solar energy to the traditional water heater. The water is heated again to temperatures higher than available if the necessary water temperature is not enough. The dilution valve can keep the tap temperature below a certain degree not to cause damage. It is known that these changes in components do not have a significant impact on system performance.

The use of detailed simulation processes to develop the relationship between the dimensionless variables and the f expression of the monthly fraction of the loads earned from solar energy. The two dimensionless Eq. 1 and Eq. 2 groups are as follows:

$$X = F_R.U_L * \frac{F'_R}{F_R} * \left(T_{ref} - \bar{T}a\right) * \Delta T * \frac{A_c}{L} \quad (1)$$

$$Y = F_R.(\overline{\tau\alpha})n * \frac{F'_R}{F_R} * \frac{(\overline{\tau\alpha})}{(\overline{\tau\alpha})n} * \bar{H}t.N * \frac{A_C}{L} \quad (2)$$

Where:
A_c: collector area (m^2)
F'_R: heat exchanger efficiency factor
U_L: collector overall loss coefficient (W/m^2 °C)
ΔT: total number of seconds in a month
$\overline{T}a$: monthly average ambient temperature (°C)
T_{ref}: empirically derived reference temperature (100 °C)
L: monthly total heating load for space heating and hot water (J)
$\overline{H}t$: monthly average daily radiation incident on collector surface per unit area (J/m^2)
N: days in a month
$(\overline{\tau\alpha})$: monthly average transmittance-absorptance product

Those two equations can be rewritten as the following:

Where F_RU_L and FR $(\tau\alpha)_n$ are obtained from collector test results, The ratio FR'/FR corrects for various temperature drops between the collector and the storage tank. The average air temperature Ta is obtained from meteorological records for the month and location desired, and HT is found from the monthly average daily radiation on the surface of the collector. The calculation of monthly loads L. There is no requirement in the f-Chart development that any particular method is used to estimate the loads. The collector area is AC. Thus, all the terms in these two equations are readily determined. For the configuration within the first system, the fraction of the total monthly load of solar energy and water heating system is given as a function of the X & Y coefficients in the following mathematical relationship Eq. 3:

$$f == 1.029Y - 0.065X - 0.245Y^2 + 0.0018X^2 + 0.0215Y^3 \quad (3)$$

When the storage capacity exceeds 50 litres per square meter of the solar collector area, the annual system performance is insensitive. When the cost of the tank is taken into consideration, the optimum storage capacity is between 50-200 litres per square meter of the solar collector area. The f-Chart method has been developed for a standard storage capacity of 75 litres of water per square meter of solar collector area. Otherwise, coefficient X can be corrected by the following equation to correct the size of the reservoir as in Eq. 4:

$$\frac{X_c}{X} = \left(\frac{actual\ storage\ capacity}{stamdard\ storage\ capacity}\right)^{-0.25} \quad (4)$$

Assuming that the heat exchanger size is reduced, we must increase the storage temperature within the heater tank to continue providing the same amount of heat. From the thermal consideration, the optimal value of this dimensionless number εL*Cmin/(UA)h is infinity even though the system performance depends on this parameter. Moreover, if this ratio is above 10, which is a large number, we can say that it is almost infinite. Furthermore, to undersize, this value due to the reduction of the heat exchanger size will be significant for the values of εL*Cmin/(UA)h less than 1. The practical values usually are between 1 to 3, considering the cost of the heat exchanger.

It is also mentioned that the system depends on the storage capacity of 75 litres per square meter of the collector's area and relies on the distribution of regular use of hot water every day. If there are changes in hot water use from day to day, this can significantly impact performance. One of the assumptions on which this method is based is that the solar thermal insulation of the solar thermal tank is very well insulated. If there is an energy loss in the auxiliary tank, it is not included in the study. Moreover, load losses should be included in the auxiliary tank if this method is used only to provide hot water. The thermal losses within the tank and the mechanical connections are significant if the insulation is not good enough or many connections and brackets mounting. Then it is advisable to study the losses by assuming the tank's temperature is the temperature of the specified water needed Tw. Also, having a Tempering valve on the supply line to mix cold water with hot water from solar energy if the temperature is too high has little effect on the overall output of the solar system.

Calculation steps

- n represents the mean day of the month by starting to count from the first day of the year.
- B factor defined by the equation $B = \frac{360(n-81)}{365}$ dimensionless factor.
- Equation of time represents the difference between the apparent solar time and the theoretical solar time and can be calculated from Eq. 5:
- $ET = 9.87 \sin 2B - 7.53 \cos B - 1.5 \cos B$ (5)
- Solar time ST is the calculation of time based on the position of the sun in the sky and given by the equation $ST = LT + \frac{ET}{60} + \frac{4}{60}(L_S - L_L)$ where L_s is the standard latitude of the position like Hungary 45, but the local one is 47.09, and according to this study, the local time L_T is noon.
- Hour angle expresses the time that is observing the sun from the earth and given by Eq. 6:

$$\omega = 15\ (12 - ST) \tag{6}$$

- The solar azimuth angle is zero always because the panel is directed to the south.
- Eq. 7 defines the angle of declination:

$$\delta = 23.45 \sin(360 \frac{284+n}{365}) \tag{7}$$

- The latitude angle φ is 47.61 for Hungary.
- The zenith angle defines the angle between the observer and the sun and is given by Eq. 8:

$$\theta_z = \cos^{-} 1\ (\sin\delta \sin\phi + \cos\delta \cos\phi \cos\omega) \tag{8}$$

According to ASHRAE calculation, A, B, and C factors represent the beam and diffusive radiation. The factors can be obtained from ASHRAE reference and the same for the other methods in Table 2.

Table 2. Modelling factors

Nijegorodov Factors			Parishwad et al Factors			Machler and Iqbal Factors			ASHRAE Factors		
A	**B**	**C**	**A**	**B**	**C**	**A**	**B**	**C**	**A**	**B**	**C**
1163.00	0.177	0.114	610.00	0.000	0.242	1202.00	0.141	0.103	1230.00	0.142	0.058
1151.00	0.174	0.112	652.20	0.010	0.249	1187.00	0.142	0.104	1215.00	0.144	0.060
1142.00	0.170	0.110	667.86	0.036	0.299	1164.00	0.149	0.109	1186.00	0.156	0.071
1146.00	0.165	0.105	613.35	0.121	0.395	1130.00	0.164	0.120	1136.00	0.180	0.097
1152.00	0.162	0.101	558.39	0.200	0.495	1106.00	0.177	0.130	1104.00	0.196	0.121
1157.00	0.160	0.098	340.71	0.428	1.058	1092.00	0.185	0.137	1088.00	0.205	0.134
1158.00	0.159	0.100	232.87	0.171	1.611	1093.00	0.186	0.138	1085.00	0.207	0.136
1152.00	0.164	0.103	240.80	0.148	1.624	1107.00	0.182	0.134	1107.00	0.201	0.122
1150.00	0.167	0.107	426.21	0.074	0.688	1136.00	0.165	0.121	1152.00	0.177	0.092
1156.00	0.172	0.111	584.73	0.020	0.366	1166.00	0.152	0.111	1193.00	0.160	0.073
1167.00	0.174	0.113	616.60	0.008	0.253	1190.00	0.144	0.106	1221.00	0.149	0.063
1169.00	0.177	0.115	622.52	0.000	0.243	1204.00	0.141	0.103	1234.00	0.142	0.057

- The beam radiation IbN can be generated using Eq. 9:

$$I_{bN} = A \exp(\frac{-B}{\cos}) \quad (9)$$

- The diffusive radiation I_d can be generated from Eq. 10:

$$I_d = C.I_N \quad (10)$$

- The horizontal radiation defined by the equation

$$I_{H=} I_{bN}.cos\,\Theta_z + I_d \quad (11)$$

- Clearness index is the obtained solar irradiance to the ground on a horizontal plane over the extraterrestrial radiation using Eq. 12**.**

$$K_t = \frac{I_H}{I_o} \quad (12)$$

- Eq. 13 can correct the beam irradiance on a tilted plate:

$$R_b = \frac{\cos|\phi-\beta-\delta|}{\cos|\phi-\delta|} \quad (13)$$

- The ratio H_d/H can be obtained where ω_s is lower than 81.4°
- All radiation on a tilted plane can be generated from Eq. 14:

$$\bar{R} = \frac{\overline{H_T}}{\overline{H}} = \left(1 - \frac{\overline{H_d}}{\overline{H}}\right)\overline{R_n} + \frac{\overline{H_d}}{\overline{H}}\left(\frac{1+\cos(B)}{2}\right) + \rho_g\left(\frac{1-c\quad(B)}{2}\right) \quad (14)$$

- According to ASHRAE statistics, the horizontal radiation for the first case is generated in three neighbouring countries, Greece, Germany, and Poland. By taking the nonlinear mean value, we can estimate it from the ASHRAE reference.
- The radiation on the tilted plane can be made by multiplying the horizontal radiation by R.
- The mean ambient degree is taken from the statistic resources of Hungary.
- The needed load of the assumed milking dairy plant.

3. Results and discussion

For any method, there should be assumptions, and in the original development of this method f-Chart, it was necessary to make many assumptions about the system and its performance. Hence these hypotheses are essential and helpful in interpreting the results obtained from this method. The first assumption is that all liquid tanks are connected and thoroughly mixed and preheated. The assumption

can lead to conservative estimates of the long-term performance of the solar system. The second assumption is that all days are considered symmetrical for the noon sun, which is for economic reasons in simulation. It also leads to the conservation of the output of the solar system. If this system is used only to provide hot water, water temperature above the required grade is considered a significant loss. Moreover, the air leakage around the tanks, assuming they are not well insulated, leads to a deterioration in the solar system's performance to below-expected levels.

There are many implicit assumptions within this method, including that the system is well constructed, that the distribution of flow on the solar collectors uniformly, and flow rates as assumed. If these conditions are not met within the solar system, solar system results cannot be predicted using this method. Three steps were used to verify the f-Chart: the first is to compare the detailed simulation process in many sites locations (comparing simulations with experimental results). Second, compare laboratory studies with simulation results using this method. Thirdly, tests on operating systems in the field have also been compared with the f-Chart method. Important information should be added that the weather data or meteorological data used to calculate this method may vary widely with the weather available one year on a given day, resulting in an intrinsic difference between the results and the average data commonly used in the calculations.

The results were compared between f-Chart and the actual results in many sites. Generally, the differences were within 3% in most regions. From the simulating and optimising perspective, we compare the four chosen models with the references using the clearness index factor in Fig. 3.

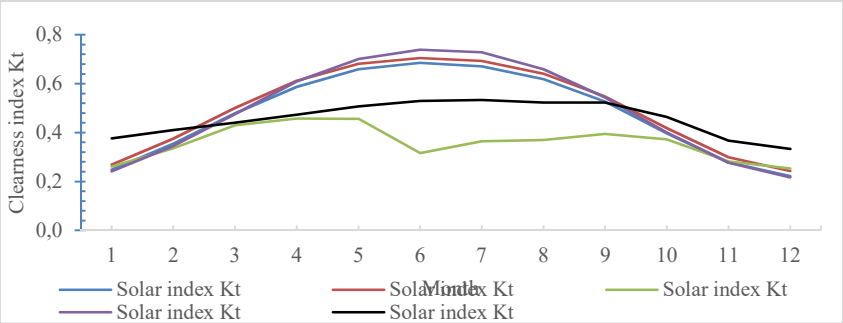

Figure 1. Solar index factor models.

We notice from the figure that the Parishwasd et al is entirely out of the range and Nigegorodov, which is higher than the average and the used one will be ASHRAE. Furthermore, the other method to confirm this result is to compare the long-term statistics with the data gained from this methodology, as in Fig. 4.

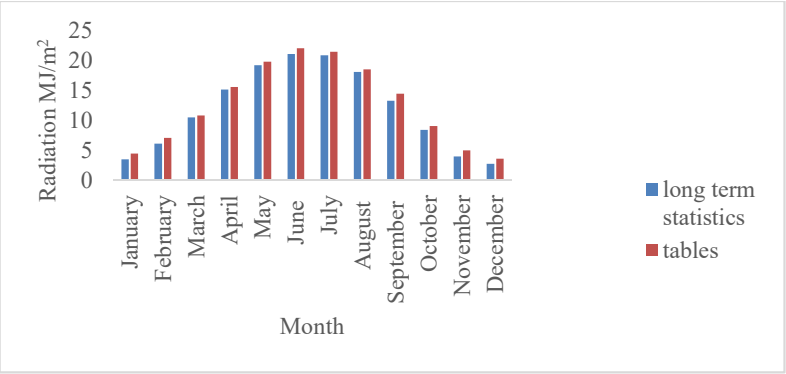

Figure 4. comparing the solar irradiation on a horizontal surface.

The last graph shows that the two results are close, and the error ratio is accepted and less than 6%. The angles for all the models are the same, and as in Fig. 5, it should be noted that these angles are independent of the slope angle and the panel parameters. Moreover, to explain this, we can distinguish it from the following two figures where the first one shows the best angle in winter is 59° while the second one at 63°.

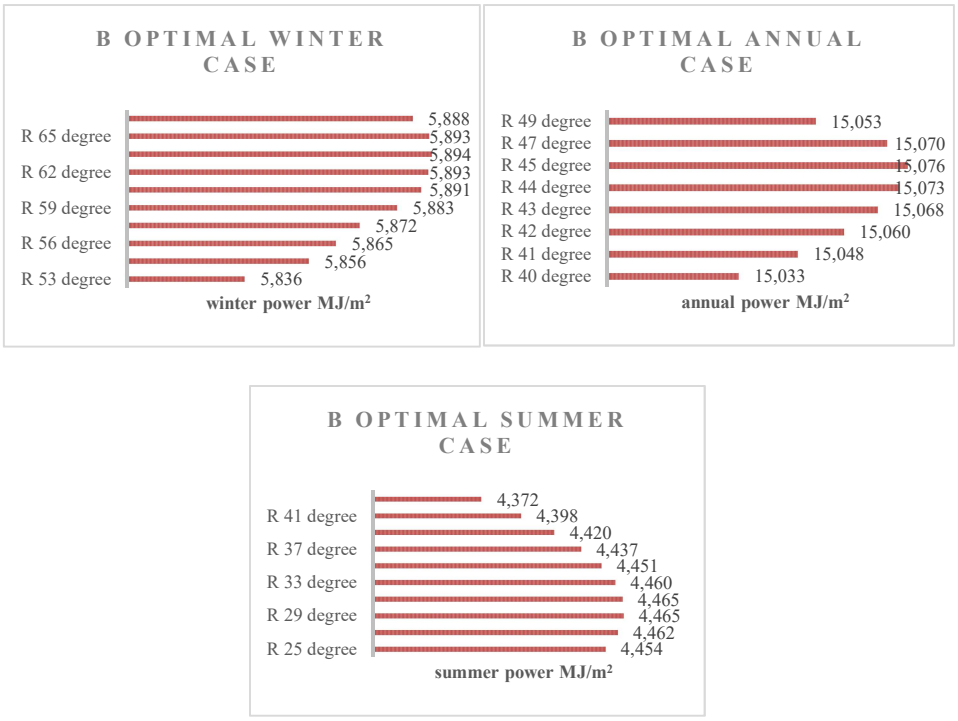

Figure 5. Annual, winter, and summer optimum angle.

Conclusions

Using solar thermal energy for industrial heating purposes can improve competitiveness and lead to environmental saving and economic advancement. It can happen especially in developing countries where usually solar energy is available and abundant. The predesigned solar hybrid systems have many advantages nowadays, especially in developed countries where solar irradiation is usually sufficient. It is known that a significant portion of the energy is used in domestic hot water and industries and can be covered partially or totally with renewable energies such as solar energy. This research predicted the best solar angle considering a solar thermal system with a pasteurising milk enterprise existing in Hungary, considering the daily and monthly fluctuations in the energy demand daily and monthly. The case study consumes more than 32 GJ per annum, and the demands are needed for heat processes. The methodology used to compare four different modelling factors (Machler and Iqbal, Parishwad et al, Nijegorogov, and ASHRAE) to identify the optimum angles during winter, summer, and annual cases. The results show that the ASHRAE model is the closest to reality taking the clearness index as a reference tool. As a result, it was found that 63º, 31º, and 45º are the optimum angles during winter, summer, and annual case studies, respectively. The long-term statistics solar radiations were compared with the ASHRAE model and found matching 94%. The optimum angles match the recommended tilting angles for Budapest, Hungary. The dairy and beverage industries can be a good potential for using the solar thermal system due to the production fluctuation like the monthly solar radiation. The gained energy supposing the winter case of ASHRAE could supply 24.99 GJ, which saves 1.5 million tonnes of CO_2 every year according to EECA (Energy Efficiency and Conservation Authority) and provides more than 76% of the needed demand.

Acknowledgements

This work was supported by the Stipendium Hungaricum Programme and by the Mechanical Engineering Doctoral School, The Hungarian University of agriculture and life sciences, Gödöllő, Hungary.

References

[1] Abraham, J. P., B. D. Plourde, and W. J. Minkowycz (2015) Continuous Flow Solar Thermal Pasteurization of Drinking Water: Methods, Devices, Microbiology, and Analysis, Renewable Energy 81:795–803. doi: 10.1016/J.RENENE.2015.03.086.

[2] Allouhi, A., Y. Agrouaz, M. Amine, S. Rehman, M. S. Buker, T. Kousksou, A. Jamil, and A. Benbassou (2017) Design Optimisation of a Multi-Temperature Solar Thermal Heating System for an Industrial Process, Applied

Energy 206(September):382–92. doi: 10.1016/j.apenergy.2017.08.196.
[3] Daneshi A., A. Esmaili-sari, M. Daneshi, and H. Baumann (2014) Greenhouse Gas Emissions of Packaged Fl Uid Milk Production in Tehran, Journal of Cleaner Production 80:150–58. doi: 10.1016/j.jclepro.2014.05.057.
[4] Duffie, John A., and W. A. Beckman (2001) Solar Engineering of Thermal Processes, 1991.
[5] Duffie, John A., and W. A. Beckman (2013) Solar Engineering of Thermal Processes. Hoboken, NJ, USA: John Wiley & Sons, Inc.
[6] Edwin M., and S. J. Sekhar (2015) Thermal Performance of Milk Chilling Units in Remote Villages Working with the Combination of Biomass, Biogas and Solar Energies, Energy 91:842–51. doi: 10.1016/j.energy.2015.08.103.
[7] Ghabour R., and P. Korzenszky (2020) Mathematical Modelling and Experimentation of Soy Wax PCM Solar Tank Using Response Surface Method, Analecta Technica Szegedinensia 14(2):35–42. doi: 10.14232/analecta.2020.2.35-42.
[8] Ghabour R., and P. Korzenszky (2021) TECHNICAL AND NON-TECHNICAL DIFFICULTIES IN SOLAR HEAT FOR INDUSTRIAL PROCESS, ACTA TECHNICA CORVINIENSIS – Bulletin of Engineering 3(July – September):11–18.
[9] Lucentini M., Vincenzo. N, and L. Rubini (2018) INNOVATIVE MILK PASTEURISING PLANT FED BY SOLAR ENERGY.
[10] Manfrida G., K. Petela, and F. Rossi (2017) Natural Circulation Solar Thermal System for Water Disinfection, Energy. doi: 10.1016/j.energy. 2017.09.132.
[11] Panchal H., R. Patel, S. Chaudhary, D. K. Patel, R. Sathyamurthy, and T. Arunkumar (2018) Solar Energy Utilisation for Milk Pasteurisation: A Comprehensive Review, Renewable and Sustainable Energy Reviews 92:1–8.
[12] Schmitt B (2016) Classification of Industrial Heat Consumers for Integration of Solar Heat, Energy Procedia 91:650–60. doi: 10.1016/J.EGYPRO.2016.06.225.
[13] Sharma A K., C. Sharma, S. C. Mullick, and T. C. Kandpal (2017) Potential of Solar Industrial Process Heating in Dairy Industry in India and Consequent Carbon Mitigation., Journal of Cleaner Production 140:714–24. doi: 10.1016/j.jclepro.2016.07.157.
[14] Wallerand Anna S., M. Kermani, R. Voillat, I. Kantor, and F. Maréchal (2018) Optimal Design of Solar-Assisted Industrial Processes Considering Heat Pumping: Case Study of a Dairy, Renewable Energy 128:565–85. doi: 10.1016/J.RENENE.2017.07.027.
[15] Wayua Francis O., M. W. Okoth, and J. Wangoh (2013) Design and Performance Assessment of a Flat-Plate Solar Milk Pasteurizer for Arid Pastoral Areas of Kenya, Journal of Food Processing and Preservation 37(2):120–25. doi: 10.1111/j.1745-4549.2011.00628.x.
[16] Yildirim N., and S. Genc (2017) Energy and Exergy Analysis of a Milk Powder Production System, Energy Conversion and Management 149:698–705. doi: 10.1016/j.enconman.2017.01.064.

Abrasive wear by experimental methods with three-body abrasive wear testers

Hailemariam SHEGAWU[1], István OLDAL[2] , Gábor KALÁCSKA[2]
[1]Doctoral School of Mechanical Engineering, MATE
[2]Institute of Technology, Hungarian University of Agriculture and Life Sciences (MATE)

Abstract

Abrasive wear occurs when a hard protuberance (asperity) from a material's surface rubs against another, deforming, gouging, or cutting the counter surface. It is critical in a variety of technical applications. The purpose of this paper is to provide a brief summary of the abrasive wear experimental investigation and to lay the foundation for future abrasive wear research. The findings could aid researchers in determining which abrasive wear testing devices and abrasive wear models are most suited.

Keywords

abrasive wear testing devices, abrasive wear models, rubs, wear

1. Introduction

Friction, abrasive wear, fracture, and vibration problems have all been solved thanks to the development of improved tribometer devices and high-quality image scanning electron microscopes. Tribology research has been done to eliminate needless friction, lubrication, and wear. On the other hand, if it is required, they are doing it to better themselves. The science and engineering of interacting surfaces in relative motion is known as tribology. It covers the study and application of friction, lubrication, and wear principles. Abrasive wear occurs when a hard asperity from one material's surface rubs against another, deforming, gouging, or cutting the counter surface. Some of the core theories researchers used to address abrasive wear problems include the Hertz model, Coulomb friction law, Hertz-Mindlin bonding contact model, Rabinowicz's equation, friction energy wear approach, and Archard law. There was research into the effects of load, speed, composition, alloys, composites, temperature, abrasive sizes, abrasive properties, debris layers, microstructure, reinforcement size, mechanical properties, micromechanical, particle motion, grain size, and abrasive wear of rock, soil tool tillage, and sand. The goal of this paper is to give a quick overview of the abrasive wear experimental investigation and to build the groundwork for future abrasive wear studies.

2. Literature review about the experimental study of abrasive wear

Experimental at room temperature

Penagos et al. (Penagos et al., 2017) studied the effect of minor Nb additions utilizing alloys including Mo (at various concentrations), which may make it difficult to identify the role of Nb on abrasive wear resistance using abrasion tests using a Dry Rubber Wheel Abrasion Tester (DRWAT). They employed silica sand material as abrasive, rubber material as wheel rubber, and molybdenum in high chromium cast irons (HCCI) material as sample (pin). They experimented with different levels of wear severity by altering the typical load and abrasive grain size. Materials and methodologies, abrasive wear tests, quantitative metallography, Hardness, wear results, the most severe condition, the intermediate severity condition, and the less severe condition were among the methods used. Conclusion: Even tiny concentrations of Nb and Mo (in combination) can significantly improve HCCI abrasion resistance for low severity conditions (mild wear), resulting in a significant improvement in the cost-benefit ratio for industrial applications. The study's limitations were that it did not address the influence of temperature, did not consider the effects of abrasive particles sticking to the specimen's surface, and did not consider the effect of slip. Using the pin-on-disc test, Okonkwo et al.(Okonkwo et al., 2016) investigated the effects of sliding speed and surface temperature on the wear behavior of an unlubricated mild steel–tool steel contact pair, and abrasive material used oxides. A CSM High-Temperature Tribometer in the ball-on-disc configuration was used to conduct the tribological testing at room temperature (commonly referred to as pin-on-disc tests). Test method, materials, test speed (and interface temperature), friction curve analysis, SEM characterization of the disc surface, ball wear scar, SEM characterization of the worn surfaces of the balls and disc EDX, and profilometry analysis were among the methods used. At the low to moderate sliding speeds and temperatures studied, they discovered a considerable differential in wear response for comparable surface temperature and bulk temperature circumstances. The study's limitations were that it did not address the influence of surface roughness, did not account for load, and did not account for slip. Zafar & Sharma (Zafar & Sharma, 2016) investigated the WC–12Co microwave clads' abrasive and erosive wear performance. Because the load is an important element in wear, three-body abrasive wear studies with silica sand as the abradant were carried out using a dry sand rubber wheel (DSRW) equipment under varied loads. The erosive wear performance of the micrometric (MM) and nanometric (NM) clads was examined using alumina as the erodent in an air-jet erosion (AJE) test setup at ambient temperature. They employed an austenitic stainless steel (SS304) material as a rubber wheel and a specimen constructed of WC–12Co particles as the clad material. Figure 1 shows the abrasive wear test setup with dry sand rubber wheels, and Table 1 lists the test conditions. Figure 2 depicts the air jet erosion test setup for erosive wear tests, while Table 10 lists the test parameters. Materials, cladding process, characterization techniques, abrasive wear testing, erosive wear testing, microstructure observation, clad microhardness analysis, abrasive wear, erosive wear, and subsurface examination were among the methods used. The nanometric clad's average Vickers microhardness (1564 ± 53 HV) was found to be

1.37 times that of the micrometric clad (1138 ± 90 HV). The study had problems in that it didn't account for surface roughness, didn't account for a large number of particles, and didn't include temperature.

Table 1. The parameters test (Zafar & Sharma, 2016).

Testing parameters	Value	Units
Scheme	Dry sand rubber wheel test	–
Abradant	Silica sand	–
Abradant hardness[a]	2100–2600	HV
Abradant particle size	150–355	μm
Abradant feed rate	80 ± 3	g/min
Specimen size	25 × 25 × 7	mm^3
Wheel speed	200 ± 5	RPM
Wheel diameter	240	mm
Normal load	30, 60, 90	N
Total number of revolutions	8000	–
Total linear abrasion	6000	m
Ambient testing temperature	27 ± 3	°C

Table 2. Test parameters test (Zafar & Sharma, 2016).

Testing parameters	Value	Units
Scheme	Air jet erosion test	–
Erodent	Alumina	–
Erodent hardness[a]	1800–2000	HV
Erodent particle size	50 ± 5	μm
Erodent feed rate	5 ± 1	g/min
Erodent velocity	50 ± 3	m/s
Air pressure	1.5 ± 0.2	kg/cm^2
Specimen size	22 × 22 × 5	mm^3
Specimen to nozzle distance	10	mm
Impact angle	30, 60, 90	deg
Total erosion time	20	min
Ambient testing temperature	27 ± 3	°C

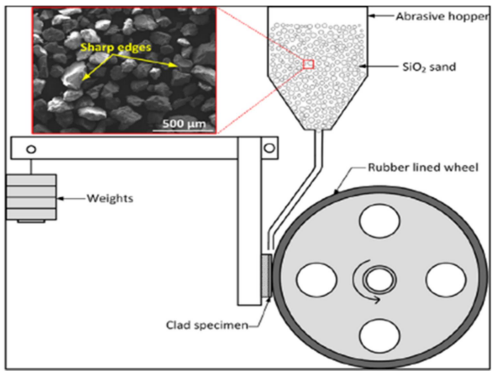

Figure 1. Depicts the setup for abrasive wear test (Zafar & Sharma, 2016).

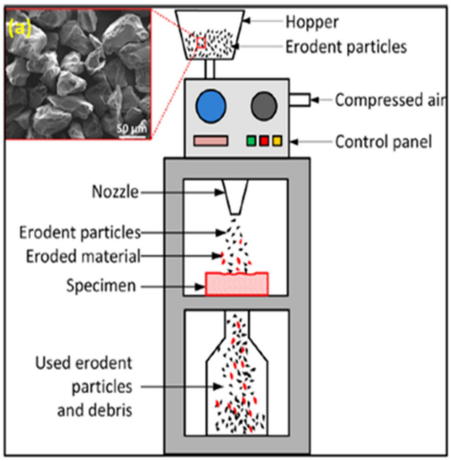

Figure 2. Depicts the setup for an erosive wear test (Zafar & Sharma, 2016).

Experimental at elevated temperature

Varga (Varga, 2017) clarified the formation mechanism of mechanically mixed layers under particular abrasive conditions and forecasted the efficiency of such protective mechanically mixed layers for abrasive applications. As an abrasive, they employed quartz, a disc made of Hardox 400 steel, and a ball (specimen) composed of FeCrC, NiCrW, CoCrWC, and FeCrNbBWC. The abrasion test rigs utilized are shown in Figure 3: a) High-stress abrasion; cyclic impact abrasion, Figure 4: b) solid particle erosion (a*, b*, c*), and Figure 5: c) typical wear scar (a+, b+, c+). The test parameters utilized in various abrasion tests are listed in Table 3. Materials, abrasion testing, microstructure and hardness, high-stress abrasion, impact abrasion, solid particle erosion, and wear processes were among the procedures used. They discovered that impact abrasion had the highest contact severity per abrasive particle, followed by high-stress abrasion and solid particle erosion. The study's weaknesses were that it didn't consider the impact of surface roughness, didn't account for number and particle sizes, and didn't consider slip.

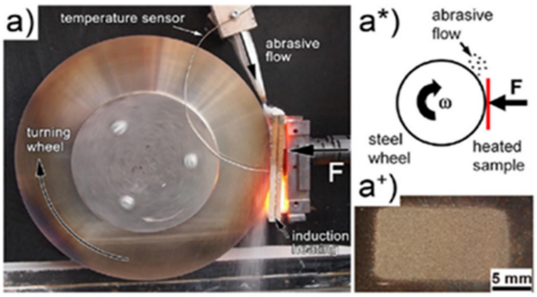

Figure 3. The abrasion test rigs (Varga, 2017).

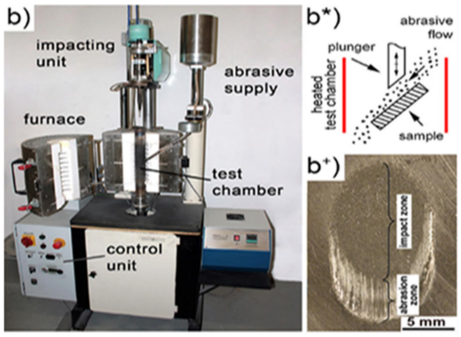

Figure 4. The abrasion test rigs (Varga, 2017).

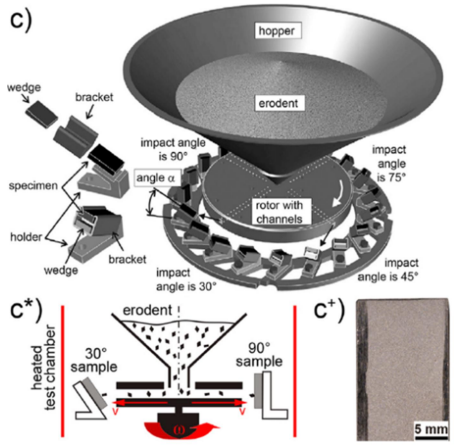

Figure 5. The abrasion test rigs (Varga, 2017).

Table 3. The test parameters used (Varga, 2017).

Parameter	HT-CAT	HT-CIAT	HT-ET
Temperatures	RT, 300 °C, 550 °C	RT, 300 °C, 500 °C, 650 °C, 700 °C	RT, 300 °C, 550 °C, 650 °C
Angle	90°	45°	30°, 90°
Load	45 N	0.8 J/impact	~0.12 mJ/particle at 90° impact
Abrasive	Quartz, 212–300 µm, round	Quartz, 400–900 µm, angular	Quartz, 100–300 µm, angular
Abrasive flow rate	180 g/min	90 g/min	100–150 g/min
Counterbody	Hardox 400 steel wheel	Co-rich high speed steel	–
Velocity	1 m/s	Free fall	80 m/s
Duration	600 m, 10 min	7200 impacts, 60 min	6 kg abrasive, 40–60 min
Wear quantification	Volume loss / sliding distance [mm³/m]	Volume loss / impact [mm³/impact]	Volume loss / abrasive weight [mm³/kg]

Molnar et al. (Molnar et al., 2018) examined the two- and three-body abrasion performance of rubber belts using two well-established normed tests, the ISO 4649 and ASTM G65 tests. The abrasive media used were standardized AFS 50–70 sand from the US Silica firm, which was commercially available conveyor

belts (EPM and SBR), rubber wheel material with an 80 Shore A, and abrasive media. Materials, high-temperature two- and three-body abrasion tests, Micro-mechanical testing by nano-indentation, high-temperature 2-body abrasion, as-delivered hardness development, and aged rubber with temperature were among the procedures used. Temperature distribution in the tribo contact, high-temperature 3-body abrasion, aging effects, surface morphology, wear debris and wear mechanisms, as well as correlations between mechanisms and micro-mechanical testing and contacts, were all covered. Finally, the two established testing procedures use different wear mechanisms to abrade the samples. The study's limitations were that it excluded the effects of particle size and shape, surface temperature, and particle number entering. Varga et al. (Varga et al., 2013) studied tribolayer generation in three materials with varied microstructures in three-body abrasive and impact/abrasive settings at temperatures up to 700°C. A typical dry-sand steel-wheel test equipment was used for the High-Temperature Continuous Abrasion Test (HT-CAT). To examine material behavior under combined impact and abrasive conditions, the High-Temperature Cyclic Impact/Abrasion Test (HT-CIAT) was used. The specimen material (austenitic steel, stainless casting steel with precipitated carbides, and grey cast iron with lamellar graphite and a ferritic–perlitic matrix) was employed for the test, as well as the wheel material (steel) and the abrasive material (Ottawa silica sand). Materials and characterization, hot hardness testing, abrasion testing, impact/abrasion testing, sample preparation, measurement procedure, hardness of materials tested, wear behavior in the abrasive environment, and wear behavior in impact/abrasion environment were among the methodologies employed. They concluded that tribolayer development is influenced by dispersion, size, and structure of hard phases. The study's shortcomings were the absence of the fracturing effect and the absence of the friction effect.

Experimental at both room and elevated temperature

Rahman et al. (Rahman et al., 2019) identified and analyzed the wear mechanisms involved in hot rolling for four HSS roll classes produced by traditional casting (one grade) and additive manufacturing (four grades) (three grades). The friction and wear of one spun cast HSS alloy and three lasers cladded HSS alloys were measured using a CSM-Instruments high-temperature pin on a disc tribometer. They used MC/M2C carbides as an abrasive, a disc made of low carbon steel, and a pin made of laser-clad HSS alloys. Experiment setup and process, materials, analysis tools, microstructure, micro-hardness, friction, wear, and surface topography were among the approaches used. They found that the microstructure of the alloys, particularly the kind, size, and shape of the existing carbides, has a significant impact on the tribological behavior of HSS work roll materials. The study's flaws were that it didn't consider the impact of speed, didn't take into consideration load, and didn't account for slip. Fildes et al. (Fildes et al., 2013) used a ball-on-three-disk (BOTD) test to provide a quick, cost-effective, and accurate estimate of wear and abrasion resistance. This paper examines steel coated with seven different types of nitrides, as

well as unique Cr and Ni plated coatings, as well as uncoated and manganese phosphate coated steel samples. BOTD abrasion tests were performed with a neoprene ball (70 Shore A) and AFS50/70 sand. Modeling the coating using fundamental qualities such as hardness, fracture toughness, and wear resistance can be used to construct performance indicators. The study also found that recently produced AlCrN coatings with stated improved toughness and hardness do provide greater wear resistance, with the multilayer version of the coating providing more wear resistance than the monolayer version. The study's gaps were that it didn't take into account the effect of surface roughness or temperature. Kennedy et al. (Kennedy et al., 2017) looked at the role of third bodies in the wear process (oxide wear debris and tribolayers) and the effect of frictional heating on the wear of Fe30Ni20Mn25Al25. Pin-on-disk wear experiments were conducted utilizing Fe30Ni20Mn25Al25 specimen material, AISI 347 stainless steel disc material, and oxides abrasive material. Materials and methods, the influence of sliding velocity on wear of Fe30Ni20Mn25Al25 against 347SS, TEM inspection, and the influence of wear particles on wear of Fe30Ni20Mn25Al25 against 347SS were among the methods used. When third body wear debris was removed from the disk surface during the wear test, they found that the pin's wear rate was significantly higher. The study's shortcomings included excluding the effects of cracks, surface roughness, and temperature. Using the DUCOM High-Temperature Dry Abrasion tester, Ramadas et al. (Ramadas et al., 2021) evaluated the abrasive wear resistance of laser powder bed fusion 15-5 Precipitation Hardening Stainless Steel in the aged condition (W H900) to that of the traditionally manufactured wrought counterpart (Model: TR-50-HT). Table 4 materials and conditions for three-body dry abrasive wear tests. Material, specimen preparation using laser powder bed fusion, heat treatment procedure, three-body abrasive wear test, and wear track characterization were among the methods used. SEM study of wear tracks, wear processes, comparison of wear resistance of traditional and additive produced specimens was also covered. Micro-cutting and micro-plowing appeared to be the predominant material removal mechanisms, with certain locations showing micro-cracking effect, according to the microstructural characterization of the wear surface. The study's shortcomings included excluding the effects of slip, surface roughness, and temperature.

Hernandez et al. (Hernandez et al., 2015) evaluated the high-temperature three-body abrasive wear behavior of boron steel and two different pre-hardened tool sheets of steel using a high-temperature continuous abrasion machine (HT-CAT) at temperatures ranging from 20 °C to 800 °C. Specimen material included Toolox44 and Toolox33, as well as 22MnB5 boron steel, steel Hardox500 for the disc, and AFS50-70 Ottawa silica sand for the abrasive. Test materials and specimens, test equipment and process, microstructure, hot hardness, and abrasive wear behavior were among the procedures used. They concluded that when the temperature rises, the hardness of all the materials studied decreases. The effects of cracks, surface roughness, and slide were not included in the study's limitations.

Table 4. Lists materials and conditions (Ramadas et al., 2021, p.).

Parameter	Value
Load applied	45 N, 90 N, 130 N
Speed	200 RPM
Number of Revolutions	400 revolutions
Temperature	Room Temperature & Elevated Temperature (300 °C)
Abrasive Used	Quartz sand
Abrasive Particle Size	250–300 µm
Abrasive Flow rate	300 g/min
Wheel type	Chlorobutyl Rubber & Inconel 625
Wheel Dimension	Diameter: 228.6 mm, Width: 12.7 mm
Specimen size	76.2 X 25.4 × 8 mms

3. Aim of the research

The goal of the study is to learn more about advanced technology abrasive wear testing devices, observed microscope devices, manufactured test material procedures, test specimen preparation, experimental setup, and tested procedures. My goal is to learn more about how mass is taken from surfaces and how to lessen the rate of material removal wear:

- To investigate abrasive wear, friction, and fracture used abrasive wear tester devices.
- To look into mechanical and chemical qualities that can help reduce friction, wear, corrosion, and fracture resistance.
- To assess the effectiveness of various methodologies, types of equipment, and testing devices.

4. Abrasive wear experimental setups and procedures

Materials selection

All researchers were first selected abrasive materials, specimens' materials, and disc (rubber) materials to conduct abrasive wear. For example, Hernandez et al. (Hernandez et al., 2015) utilized Toolox44 and Toolox33 specimen materials, as well as 22MnB5 boron steel, steel Hardox500 for the disc, and AFS50-70 Ottawa silica sand for the abrasive, while Kennedy et al. (Kennedy et al., 2015) used Fe30Ni20Mn25Al25 specimen material, AISI (Kennedy et al., 2017). Varga et al. used the specimen material (austenitic steel, stainless casting steel with precipitated carbides, and grey cast iron with lamellar graphite and a ferritic–perlitic matrix) and the wheel material (steel) and abrasive material (Ottawa silica sand) for the test (Varga et al., 2013). Varga (Varga, 2017) used quartz, a disc made of Hardox 400 steel, and a ball made of FeCrC, NiCrW, CoCrWC, and FeCrNbBWC as a specimen. The abrasive media utilized by

Molnar et al. (Molnar et al., 2018) were standardized AFS 50–70 sand from the US Silica firm, commercially available conveyor belts (EPM and SBR), and rubber wheel material with an 80 Shore. Studies with silica sand as the abradant were carried out by Zafar & Sharma (Zafar & Sharma, 2016) utilizing dry sand rubber wheel (DSRW) equipment under various loads. Some of the studies, such as Penagos et al. (Penagos et al., 2017), used silica sand as an abrasive, rubber as a wheel rubber, and molybdenum in high chromium cast irons (HCCI) material as a sample (pin).

Input variables, output variables, and parameters

The input variables, output variables, and parameters used by researchers used summarized as shown below in Table 5.

Table 5. Input variables, output variables and parameters.

Parameters	**Description**
Abrasive wear	Model and experimental
Disc material / rubber wheel	steel, alloy steel or rubber
ball material (specimen)	any engineering material
Abrasive material	Silica, JSC-1AF
Abrasive particle size	(μm)
Abrasive flow rate	(g/min)
Velocity	(m/s)
Temperatures (°C)	(°C)
Atmosphere	Air/Nitrogen Air/Carbon dioxide Vacuum
Angle	(°)
Load	(N) (J/impact) (J/particle)
Duration	m, min impacts, min kg abrasive, min
Wear quantification	[mm³/m] [mm³/impact] [mm³/kg]
contact pressure	(P_a)

Micro-abrasive wear test device

Various three-body abrasive wear tester devices were employed by different researchers.

Hernandez et al. (Hernandez et al., 2015) utilized a high-temperature continuous abrasion machine (HT-CAT), while Ramadas et al. (Ramadas et al., 2021) used the DUCOM High-Temperature Dry Abrasion tester and Kennedy et al. (Kennedy et al., 2017) used Pin-on-disk. Fildes et al. (Fildes et al., 2013) utilized a three-disk ball, Varga et al. (Varga et al., 2013) used dry-sand steel-wheel testing equipment, and Molnar et al. (Molnar et al., 2018) employed ISO 4649 and ASTM G65 tests Varga (Varga, 2017) used high-stress abrasion, cyclic impact abrasion, solid particle erosion, and impact to test quartz, a disc made of Hardox 400 steel, and a ball (specimen) made of FeCrC, NiCrW, CoCrWC, and FeCrNbBWC. Some of the researchers were Zafar & Sharma (Zafar & Sharma, 2016), Okonkwo et al. (Okonkwo et al., 2016), and Penagos et al. (Penagos et

al., 2017) who used dry sand rubber wheel (DSRW) equipment, Okonkwo et al. (Okonkwo et al., 2016) who used the pin-on

Results and conclusions

This paragraph will wrap up publications that used an experimental approach by summarizing the main findings of the study goals, as well as their importance and contribution, will also look into the flaws in the methodology, and give recommendations for further study. The purpose of this paper is to provide a brief summary of the abrasive wear experimental investigation and to lay the foundation for future abrasive wear research. The effect of slip, load, speed, temperature, microstructural, gain size, alloying composition, composite, environmental, mechanical characteristic, metallurgical, surface roughness, and sliding distance discussed by almost all of the researchers working in this abrasive wear field are the key findings and contributions to this research from this methodology. Researchers employed a scanning electron microscope (SEM), transmission electron microscope (TEM), energy-dispersive X-ray spectroscopy (EDS), and electron backscattered diffraction (EBSD) before and after the test to show features on the sample material's internal and external surfaces. They also use a dry rubber wheel abrasion tester (DRWAT), a high temperature-continuous abrasion test, a high temperature-cyclic impact-abrasion test, and a high temperature-erosion test, a home-made device for pin-on-disk wear tests, and ASTM G65 abrasive rig test devices to conduct abrasive wear tests. They also used coulombs law, Archard law, friction energy technique, and Rabinowicz's equation, according to the findings. Excluding all of the following effects, such as temperature, local failure such as damage, breakage, and crack, abrasive particle shape representation of actual abrasive particle shape, abrasive particle velocity, abrasive particle entrance, and motion type, are among the researchers' limitations. Future researchers will use a more advanced way to predict abrasive wear, such as including the effect of slip, surface roughness, sliding distance, temperature, abrasive particle size, characteristics, entrance number, velocity, and motion type to the actual abrasive particle. The important findings, influential factors, legislation, limits, and future study are summarized in this paragraph.

References

[1] Fildes, J. M., Meyers, S. J., Mulligan, C. P., & Kilaparti, R. (2013). Evaluation of the wear and abrasion resistance of hard coatings by ball-on-three-disk test methods—A case study. *Wear*, *302*(1), 1040–1049. https://doi.org/10.1016/j.wear.2012.11.018

[2] Hernandez, S., Hardell, J., Winkelmann, H., Ripoll, M. R., & Prakash, B. (2015). Influence of temperature on abrasive wear of boron steel and hot

forming tool steels. *Wear*, *338–339*, 27–35. https://doi.org/10.1016/j.wear.2015.05.010

[3] Kennedy, F. E., Lu, Y., Baker, I., & Munroe, P. R. (2017). The influence of sliding velocity and third bodies on the dry sliding wear of Fe30Ni20Mn25Al25 against AISI 347 stainless steel. *Wear*, *374–375*, 63–76. https://doi.org/10.1016/j.wear.2017.01.002

[4] Molnar, W., Nevosad, A., Rojacz, H., Adam, K., Henze, H.-J., Ripoll, M. R., & Badisch, E. (2018). Two and three-body abrasion resistance of rubbers at elevated temperatures. *Wear*, *414–415*, 174–181. https://doi.org/10.1016/j.wear.2018.08.015

[5] Okonkwo, P. C., Kelly, G., Rolfe, B. F., & Pereira, M. P. (2016). The effect of sliding speed on the wear of steel-tool steel pairs. *TRIBOLOGY INTERNATIONAL*, *97*, 218–227. https://doi.org/10.1016/j.triboint.2016.01.030

[6] Penagos, J. J., Pereira, J. I., Machado, P. C., Albertin, E., & Sinatora, A. (2017). Synergetic effect of niobium and molybdenum on abrasion resistance of high chromium cast irons. *Wear*, *376–377*, 983–992. https://doi.org/10.1016/j.wear.2017.01.103

[7] Rahman, N. U., Rooij, M. B. de, Matthews, D. T. A., Walmag, G., Sinnaeve, M., & Römer, G. R. B. E. (2019). Wear characterization of multilayer laser cladded high speed steels. *Tribology International*, *130*, 52–62. https://doi.org/10.1016/j.triboint.2018.08.019

[8] Ramadas, H., Sarkar, S., & Nath, A. K. (2021). Three-body dry abrasive wear properties of 15–5 precipitation hardening stainless steel produced by laser powder bed fusion process. *Wear*, *470–471*. https://doi.org/10.1016/j.wear.2021.203623

[9] Varga, M. (2017). High temperature abrasive wear of metallic materials. *Wear*, *376–377*, 443–451. https://doi.org/10.1016/j.wear.2016.12.042

[10] Varga, M., Rojacz, H., Winkelmann, H., Mayer, H., & Badisch, E. (2013). Wear reducing effects and temperature dependence of tribolayer formation in harsh environment. *Tribology International*, *65*, 190–199. https://doi.org/10.1016/j.triboint.2013.03.003

[11] Zafar, S., & Sharma, A. K. (2016). Abrasive and erosive wear behaviour of nanometric WC–12Co microwave clads. *Wear*, *346–347*, 29–45. https://doi.org/10.1016/j.wear.2015.11.003

Authors addresses

[1]Hailemariam, Shegawu, Ph.D. student Mechanical, Institute of Technology, Szent István Campus, MATE
H-2100 Gödöllő, Páter K. u. 1. Hungary abebaw.hailemariam.shegawu@uni-mate.hu
[1]Prof. Dr. Kalácska Gábor, Head of School, Institute of Technology, Szent István Campus, MATE

H-2100 Gödöllő, Páter K. u. 1. Hungary kalacsja.gabor @uni-mate.hu
[1]Prof.Dr. Oldal István, Department of Mechanical, Institute of Technology, Szent István Campus, MATE
H-2100 Gödöllő, Páter K. u. 1. Hungary Buzas.Janos@uni-mate.hu
Contact person
[1]Hailemariam, Shegawu, PhD student Mechanical, Institute of Technology, Szent István Campus, MATE
H-2100 Gödöllő, Páter K. u. 1. Hungary shegawh@yahoo.com

Modelling and simulation of air flow on surface of solar air heater using computational fluid dynamics

Halefom K. ABRHA[1], János BUZÁS[2], István FARKAS[2]
[1]Doctoral School of Mechanical Engineering, MATE
[2]Institute of Technology, Hungarian University of Agriculture and Life Sciences, MATE

Abstract

Nowadays computational fluid dynamics is main tool used for conducting research in different fields mainly used to understand the flow behaviour of given model. The main objective of the recent study was to model and analyse the flow behaviour of solar air heater The simulation was done using ANSYS Fluent 16.2 software with simple algorithm and (k-ε) standard turbulence model. The result of the simulation where attained the minimum convergence criteria for analysed parameters. From the simulation results that the influence of buffers on solar air heaters increases the value of velocity, turbulence (high air circulation), total energy, heat flux and other parameters thus helps also to increase thermal efficiency of the solar air heater.

Keywords

ANSYS 16.2, computational fluid dynamics, solar air heater, (k-ε) standard turbulence

1. Introduction

Computational fluid dynamics is among the power full tools used in recent times by of many researchers in different research areas because it is a fastness and low-cost technique for solving different engineering problems involving fluid flows and heat transfer. It is computer based analysing software used for investigating of flow systems and their related challenges in order to forecast the performance of novel process designs before they are manufactured.

As described and defined by Hirsch (2007) the computational fluid dynamics is a set of approaches that allows us to use a computer to simulate fluid flows numerically. Here term simulation used to describe how we utilize a computer to solve numerically the rules that govern the movement of fluids in or around a material system whose geometry is likewise computer-modelled.

Jiyuan Tu et al. (2008) described the application of computational fluid dynamics as better comprehend the physical events and processes that take place in the flow of fluids around and within the selected objects. It can also apply to dissipation, diffusion, convection, boundary layers, and turbulence processes.

Regardless the type of computational fluid dynamics mostly used for nonlinear flow typically that have no analytic solution. This necessitates the search for numerical solutions to partial differential equations and, in retrospect, appears to undermine the use of linear algebra in the classification of numerical methods.

Karmare and Tikekar (2010) used computational fluid dynamics which saves time and money to examine fluid flow and heat transmission in a solar air heater. Metal ribs of circular, square, and triangular cross-sections with 60 inclinations to the air flow are used to roughen the lower surface of the collection plate. Experimental investigations in the lab were carried out to validate computational fluid dynamics results. The results of the experimental and computational fluid dynamics analyses are found to be in good agreement. The shape of the ribs and their angle of attack were also optimized. Heat transfer is maximized thanks to the square cross-section ribs with a 58-degree angle of attack. Heat transfer is improved by 30% when a square plate was used instead of a smooth surface.

Kumar et al. (2017) used computational fluid dynamics to investigate the fluid flow properties and heat transmission in a ribbed triangle duct (with a 60° apex angle) solar air heater. A three-dimensional model of solar air heater is created, and numerical simulations are performed using a computational fluid dynamics code designed using the finite volume method. The numerical simulations are run on ANSYS Fluent 12.1 software, which is available for purchase. As a result, the numerically projected outcomes are compared to the available findings, and there is a good agreement with a maximum error of 4.04 percent.

Yadav and Bhagoria (2013) were using computational fluid dynamics, the research investigates heat transmission and fluid flow mechanisms in an artificially roughened solar air heater. The ANSYS Fluent 12.1 code is used to do a two-dimensional computational fluid dynamics simulation. The validity of the results is checked by comparing them to the results of previous experiments. The turbulence caused by the tiny diameter of the transverse wire ribs clearly results in a higher increase in heat transmission over the duct. Artificial roughness, on the other hand, leads in increased friction losses.

This paper aims analysing the flow behaviour of solar air heater and select the appropriate turbulence model of a solar collector used to preheat the air for a solar dryer. The initial design of the paper has taken from the Solar Energy Laboratory at the Hungarian University of Agriculture and Life Sciences, Gödöllő, Hungary (Al-Neama and Farkas, 2017, 2019).

2. Experimental and numerical analysis

Experimental investigation

The experiment was conducted at the Solar Energy Laboratory of the Hungarian University of Agriculture and Life Sciences, Gödöllő, Hungary located at 47.59° N, 19.36° E. The data was collected with 10-minute constant time step from 10:00 to 15:00 on August 25, 2017 for five hours. Solar collector external dimensions are 120×50×15 cm length, width and thickness respectively.

Absorbing surfaces are made from copper sheet with 1.5 mm thickness and thermal conductivity 385 W/m K.

The absorber has been made with 18 buffers attached to the absorber with dimensions 10×4 cm length and width respectively and with 25 holes which used to air recirculated from first to second air channel. Buffer's function is increasing air streams length with the absorber surface to improve the useful heat transfer to the air. The space between every two buffers is 17 cm (see Fig. 1) (Al-Neama and Farkas, 2017.)

A solar air heater absorbs incident solar radiations and transforms them into useful heat for heating the collector fluid such as water and air. Solar air heaters, being inherently simple and cheap, are most widely used collection devices. Solar air heaters find several applications in space heating, seasoning of timber and crop drying

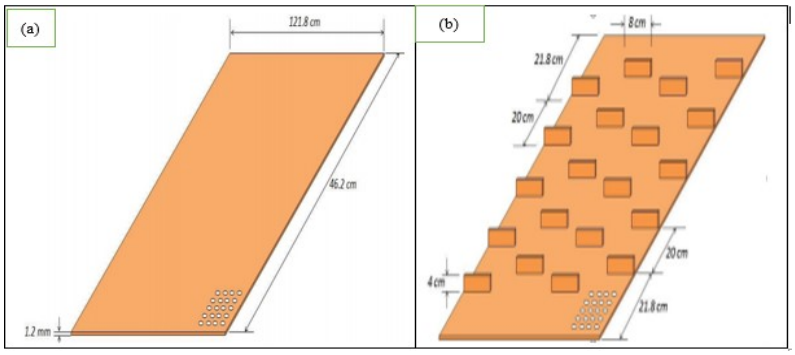

Figure 1. Un-finned absorbing surfaces (a) and horizontally finned absorbing surfaces (b)

Numerical analysis

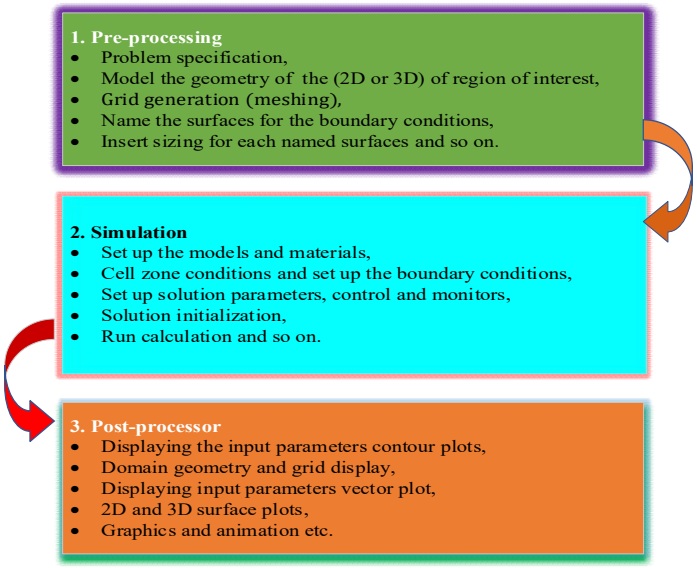

Figure 2. General flow work of computational fluid dynamics (CFD) process

The numerical analysis was done using computational fluid dynamics. The general flow work of CFD process is described below (see Fig. 2).

Developing the geometry

Solar air heater with dimension of 120×50×15 cm length, width and thickness respectively was investigated in the recent study. Solid work 2020 is used to draw the three-dimensional geometry (see Fig. 3) of solar air heater and ANSYS Fluent version 16.2 was used for modelling and simulation of the system.

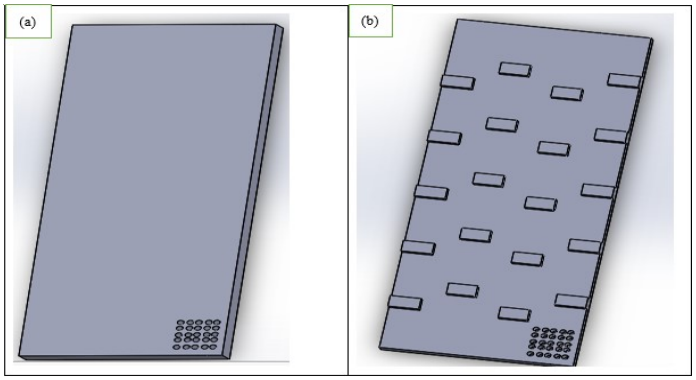

Figure 3. Three-dimensional model of un-finned absorbing surfaces (a) and three-dimensional model of horizontally finned absorbing surface (b) of solar air heaters ready for meshing*2.2.2. Meshing*

Meshing of the domain was done using ANSYS 16.2 with fine grid (see Fig 4).

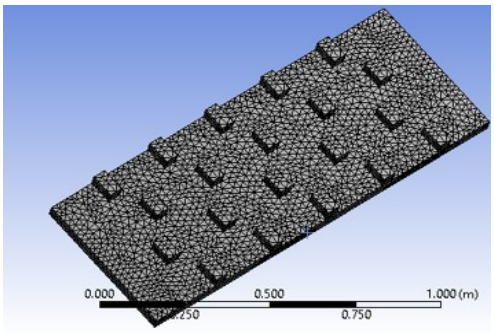

Figure 4. Mesh geometry of solar air heater

Set up the model

The necessary parameters value used for simulation was taken from the experiments which was conducted at Solar Energy Laboratory, Institute of

Technology, Hungarian University of Agriculture and Life Sciences on August 25, 2017. For example, boundary condition the air inlet velocity is 2.5 m/s, average air inlet temperature is 299 K, at the outlet static pressure is fixed at the ambient pressure, turbulent flow type of air behaviour was also considered etc.

As the flow is turbulent, standard (k–ε) model is selected as turbulent model for further analysis of the problem. No slip condition is applied to all the walls. According to the models selected the equations which were going to be solved by continuity equation, energy equation, momentum equation and equation for turbulence.

3. Results and discussions

Convergence criteria

The first-order upwind scheme was chosen for energy and momentum equations. The simple algorithm is chosen as a scheme to couple pressure and velocity; it is more economically efficient and stable than the other algorithms. After setting all necessary input conditions starting modelling, meshing, model selection, material, cell zone specification boundary condition and so on the problem was iterated to solve the governing of continuity, momentum and energy partial differential equations. As shown in Fig. 5 the solution is converged (minimum values reached), when the residuals equation reaches less than 1 x 10^{-2} for *x, y, z* velocity components and 1 x 10^{-4} for (k–ε).

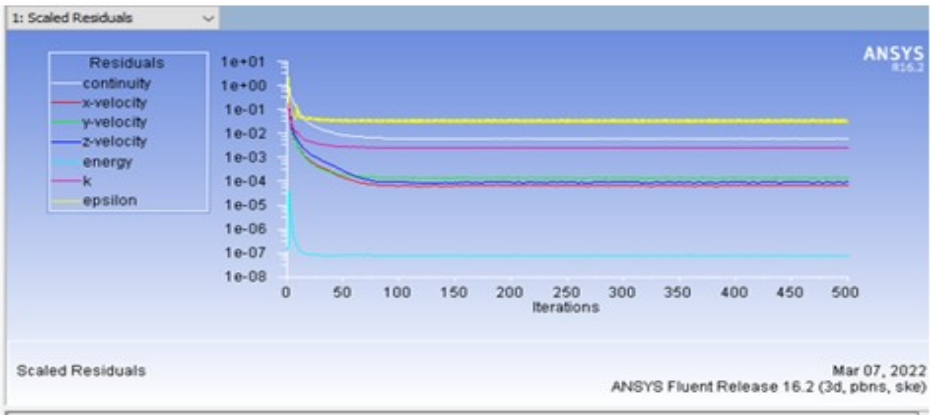

Figure 5. Convergence of the residuals

Temperatures and pressure distribution

Some of the computational results are displayed furthermore. The contour plots of the temperature and pressure distribution obtained from the simulation are displayed in Fig. 6 (a) and (b) respectively. As air passes above absorber the heat exchange takes place from the surface to air. The temperature varies between

299 K and 386 K. The air at end of the surface gets very hot, and this high temperature is sent to drying chamber to dry products placed inside drying chamber due to convection. This primary hot layer mixes with the secondary cold air due to baffles, and heat transfer takes place due to conduction and convection. As a result, the temperature of air close to surface is higher, and goes on decreasing away from the surface up to one third height of the duct.

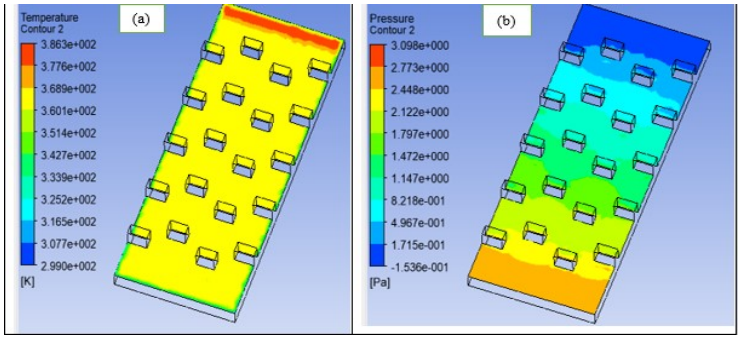

Figure 6. Temperature contour line (a) and pressure contour lines (b)

As shown in Fig. 6 (b) of the above the pressure is high at inlet portion of solar air heater, and gradually decrease (pressure drop) and lower at the outlet of solar air heater. The main reason to drop the pressure is because the flow passes through obstacles (i. e. in this case buffers are subjected to a friction force due to the air's viscosity.

Velocity stream lines

As shown in Fig. 7 shown starting from inlet of the air heater till the outlet of the air heater the presence of fins is clearly seen to have velocity increment. The velocity increment is mainly occurred around the buffers. The function of buffers is mainly to increase air stream length with the absorber surface to enhance the useful heat transfer to the air. Hence the buffers able to create great circulation of air velocity. So, having high velocity helps to facilitate of the air flow process.

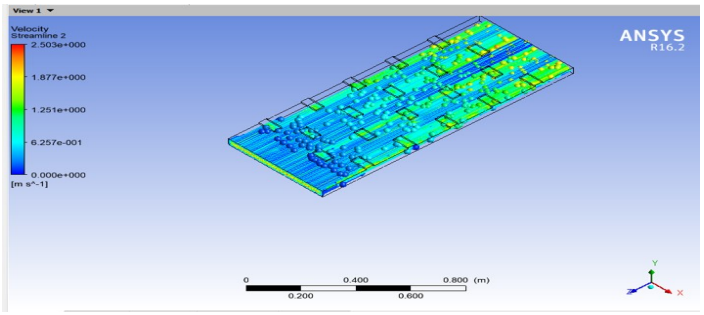

Figure 7. Velocity stream lines and flow of the fluid inside the solar air heater

Turbulent kinetic energy (k) and turbulent eddy dissipation (ε)

The k-epsilon (k−ε) model for turbulence is the most common to simulate the mean flow characteristics for turbulent flow conditions. It belongs to the Reynolds-averaged Navier Stokes (RANS) which gives a general description of turbulence models using two transport equations.

The distribution of turbulent kinetic energy (k) and turbulent eddy dissipation (ε) contour lines are given in Fig. 8 (a) and (b) respectively. As shown in Fig. 8 (a) the air flow has a turbulent kinetic energy throughout the buffers surface of the solar air heater. There is a considerable increase of turbulent kinetic energy in buffers. The dissipation varies between 4.28 x 10^{-2} and 16.55 m^2/s^3.

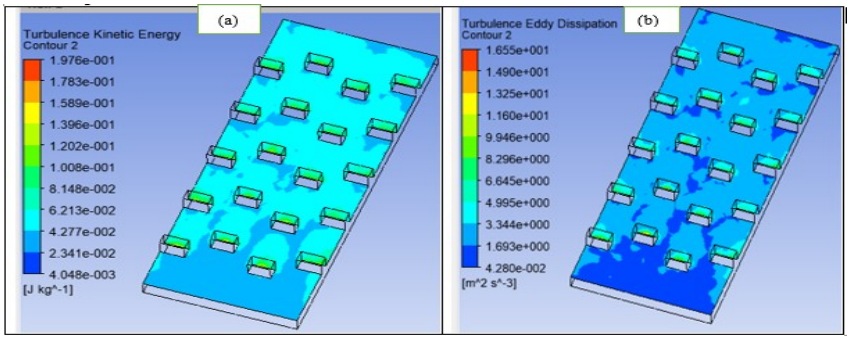

Figure 8. Turbulent kinetic energy (a) and turbulent eddy dissipation (b)

Conclusions

- The simulation was conducted with the use of a commercial computational fluid dynamics program, ANSYS Fluent version 16.2 which solves the Reynolds-averaged Naiver-Stokes (RANS) with two-equation models k–ε turbulence standard model.
- The solutions obtained from simulation of the computational fluid dynamics is with the acceptable range. Thus, the solution was converged (minimum values were reached), when the residuals of the continuity equation and the conservation of momentum equation reach 10^{-2}, for *x, y, z* velocity components: 10^{-4} for (k –ε).
- The pressure was dropped due to the presence of buffers as flow goes from the inlet to outlet.
- From the simulation result the presence buffers on solar air heater indicates that increase the value of, velocity, turbulence (high air circulation), total energy, heat flux etc. and this leads to increase the thermal efficiency of solar air heater.
- Despite some minor variations owing to experimental imperfection computational fluid dynamics is still power full tool, which can be utilized in the future to solve more complex solar collector problems and as means of designing, predicting the flow behaviour, analysing the performance, and optimizing of solar air heater for further manufacturing and development.

Acknowledgements

This work was supported by the Stipendium Hungaricum Programme and by the Doctoral School of Mechanical Engineering, Hungarian University of Agriculture and Life Sciences, Gödöllő, Hungary.

References

[1] Al-Neama, M. and Farkas, I. (2017), Investigation of finned solar air collector performance for drying purposes. R&D in Mechanical Engineering Letters, Gödöllő, Hungary, Vol. 16, pp. 64-72.
[2] Al-Neama M.A., Farkas I. (2019), Thermal efficiency of vertical and horizontal-finned solar collector integrated with forced air circulation dryer for apple as a sample, Drying Technology, Vol. 37, No. 5, pp. 546-558.
[3] Hirsch, C. (2007), Numerical Computation of Internal and External Flows, Volume 1: Fundamentals of computational fluid dynamics (2nd edition). John Wiley and Sons, Ltd.
[4] Jiyuan Tu, Guan-Heng Yeoh, Chaoqun Liu (2008), Computational fluid dynamics, A practical approach, 1-27, Esevier Ltd.
[5] Karmare, S.V. and Tikekar, A.N. (2010), Analysis of fluid flow and heat transfer in a rib grit roughened surface solar air heater using CFD. Solar Energy, 84(3), 409–417.
[6] Kumar, R., Kumar, A. and Goel, V. (2017), A parametric analysis of rectangular rib roughened triangular duct solar air heater using computational fluid dynamics. Solar Energy, 157, 1095–1107.
[7] Yadav, A.S. and Bhagoria, J.L. (2013), A computational fluid dynamics-based heat transfer and fluid flow analysis of a solar air heater provided with circular transverse wire rib roughness on the absorber plate. Energy, 55, 1127–1142.

Reviewing ICE* soot filtration in EATS** laboratory enviroment

Norbert BÍRÓ[1], Péter KISS[2]
[1]IBIDEN Hungary Kft., Technical Center, Test Engineer
[2]Department of Vehicle Technology, Institute of Technology,
Hungarian University of Agriculture and Life Sciences, MATE

1. Introduction

Despite its many advantages, there are several downsides of the diesel engines. Like most fossil fuels, diesel and hydrogen are essential components. In an ideal thermodynamic process, only carbon dioxide (CO_2) and water vapor (H_2O) would be produced in the diesel engine. [13] Factors interfering with ideal conditions: inadequate air-fuel mixing ratio, particle content of intake air, change in combustion temperature, inaccuracy of ignition timing, turbulence in the combustion chamber, non-ideal combustion chamber shape (note: ideal for spherical shape, with centric combustion). Due to these factors, significantly more harmful substances are formed. [1]

In order to reduce the amount of harmful particles in the atmosphere, the European Union began to continuously reduce the amount of harmful emissions to the environment (harmful ambient air load) with standards developed for diesel commercial vehicles in 1990. The most significant of these are nitrogen oxides (NO_x), carbon monoxide (CO), hydrocarbons (HC), and particulate matter (PM), as well as sulfur dioxide (SO_2). (Figure 1) [3]

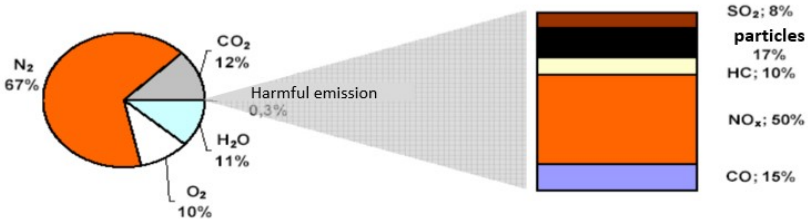

Figure 1. Average exhaust gas composition of diesel engines. [3]

Normally, the nitrogen in the air does not react with the oxygen during combustion, however, as a result of the inhomogeneous combustion characteristic of diesel engines, from a temperature of 1600 °C, the nitrogen already reacts with the oxygen and produces NO_x emissions.

The two main components of NO_x emissions are NO and NO_2. Significantly more toxic NO is slowly converted to NO_2 under normal atmospheric conditions. Road traffic accounts for 40-70 % of anthropogenic NO_x emissions,

of which about 85 % is related to diesel vehicles. [4] Nitrogen oxides also promote the formation of acid rain and smog.

CO is the result of imperfect combustion and is minimal in diesel engines running on high excess air. A colorless and odorless gas, the blood binds to the hemoglobin responsible for transporting oxygen orders of magnitude more than oxygen. It causes concentration problems, slowed reflexes and confusion, and eventually death.

HC emissions can be derived from unburned fuel. It is formed in the engine at lower temperature parts of the combustion chamber due to improperly high temperatures. It contributes to the increase in ground-level ozone, which can cause long-term mental problems in children and several other illness. [5]

As a result of combustion, the particulate emissions (PM) of diesel engines are also significant. These compacted particles (agglomerates) can be formed by the following materials:

- carbon particle,
- dust particles from inadequate air filtration,
- partially burned fuel,
- partially burned lubricating oil,
- ash from fuel and lubricating oil,
- sulphates,
- water molecule,
- metal particles [6].

Due to the many components, the particles are very complex. The materials listed above usually compress into a central carbon core to form particles typically 15-40 nm in size, approximately 90 % of which are smaller than 1 μm. [7] To express the number of particles: a diesel engine emits ~10^{14} particles, which is 3 orders of magnitude higher than the particulate emissions of a gasoline engine. Emissions that are harmful to human health can cause lung and respiratory problems and, according to the current k of science, can cause a major contribution to the development of cancer. [8]

In response to health concerns, more and more stringent emission values have been introduced for new diesel engines worldwide. Current emissions are forcing everyone in the world to continually improve and system-wise, where we need to use and combine advanced engine management in parallel with a variety of sophisticated exhaust after-treatment technologies.

There are several well-functioning exhaust gas treatment technologies for diesel engines today.

The most significant PM reduction technologies:

- diesel oxidation catalyst (DOC),
- diesel particulate filter (DPF),
- closed crankcase ventilation (CCV).

Oxidation catalysts, which were also responsible for the oxidation of hydrocarbons (HC) and CO in early petrol engines, continue to play an important role in diesel engines. Although originally developed to reduce gaseous emissions, they have also been shown to be effective in reducing

particulate emissions, which can be as high as 20-50 % (total particle weight). [8]

Diesel particle filter is also a proven technology. They have a honeycomb structure, with the cell always closed on the opposite side. The filtration thus takes place on the pores of the cell walls. (Figure 2)

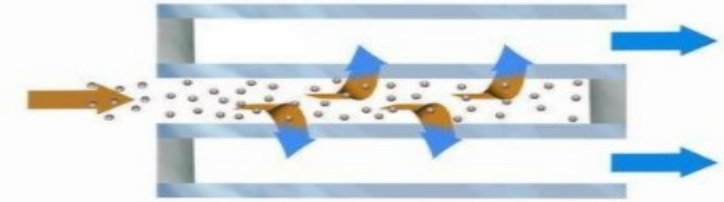

Figure 2. Exhaust gas flow at cell wall pores and accumulation of PM particles. [2]

The two most common raw materials for the particulate filter ceramic body are Cordierite ($2MgO – 2Al_2O_3–5SiO_2$) and silicon carbide (SiC). Cordierite filters are significantly cheaper due to their manufacturing technology, with very good particle filtration properties. This is also true for SiC filters, but this technology is an investment that is offset by its ability to withstand significantly more robust, extreme engine conditions. Today's modern particulate filters, whether Cordierite or SiC, can filter out 99.9% of engine particulate emissions. [1]

2. Equipments and methods:

The test is performed on a dynamometer using a test engine using the following equipments:

- the exhaust gas treatment system to be tested with the associated diesel engine,
- gas concentration measuring device (AVL AMAi60),
- DPF filtration efficiency measuring machines (AVL Particle Counter Plus and AVL Smart Sampler).

The engine brake pad is capable of real vehicle simulation, the gas, brake, clutch and torque converter of an imaginary vehicle are controlled by the simulation software. The engine used for the test was a 4-cylinder 2000 cm^3 EURO5 compliant diesel engine braked by a 220 kW electric brake generator (vehicle acceleration, constant speed travel) or driven (vehicle engine start, vehicle engine brake operation). (Figure 3)

As emission regulations have emerged, there has been a need for equipment that can be used to measure emissions from vehicle engines in a repeatable and comparable way around the world.

In our test room there is an AMAi60 multi-channel continuous emission measuring device from AVL List GmbH. (Figure 4) This equipment uses 2

independent sampling channels to simultaneously measure emissions at 2 different points in the exhaust system (before and after the catalyst). Each channel measures, displays and records the amount of 7 different gas components. The measured gas components are THC (total hydrocarbon), CH_4 (methane), NO_x (nitrogen oxides), NO (nitrogen monoxide), CO_2 (carbon dioxide), CO (carbon monoxide), O_2 (oxygen).

Figure 3. Test cell with measuring equipment. [source: Ibiden Hungary]

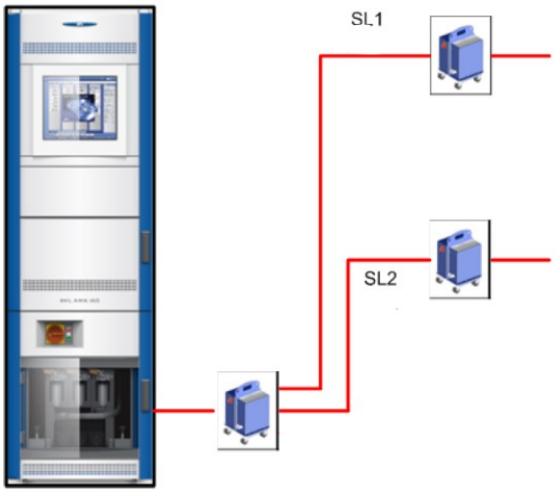

Figure 4. AVL AMAi60 exhaust gas analyzer. [9]

DPF filtration efficiency can be measured and calculated with two devices. One of our devices counts the particle number (PN) emitted by the vehicle. This device is a Particle Counter Plus from AVL List GmbH. Principle of operation: Exhaust gas enters (sample inlet, red marked duct, Figure 5) the primary dilution unit (chopper diluter, PND1) where it is diluted with HEPA filtered compressed

air (blue marked duct, Figure 5). It then passes through a heated tube (channel marked in green, Figure 5) to the evaporator (ET), where the diluted gas is heated to such an extent that all the volatiles evaporate and only the solid particles remain in the diluted sample gas. A second diluent (PND2) is then used to further dilute the sample gas and enter the condensation particle counter (PNC). In PNC, butanol condenses on particles to make the particles larger diameter so that the optics of the equipment can visually detect them. The enlarged particles are then counted based on the scattered light pulses as the particles pass through the laser beam. This makes it possible to determine the number of particles per unit volume (#/cm^3).

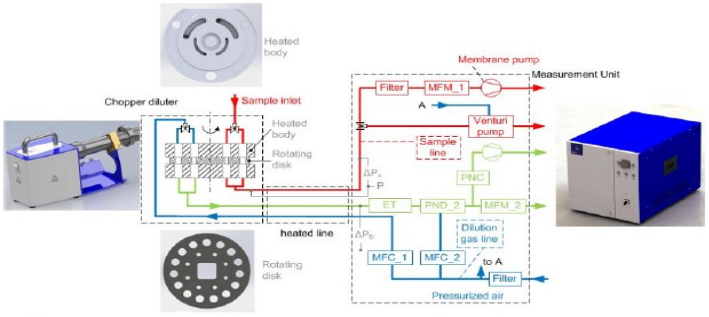

Figure 5. Construction of AVL Particle Counter Plus particle counter. [10]

Another device that measures DPF filtration efficiency uses a gravimetric method, but the Smart Sampler from AVL List GmbH is used to collect particles (diesel soot). With the exception of condensed water, all particles fall into the "PM" category, which is maintained at controlled temperatures of 51.7 °C or less. This device collects these particles on a disc-shaped (47 mm outside diameter) filter paper from the diluted exhaust gas during a vehicle test cycle, the mass of which is measured after conditioning. Because the amount of soot collected is very small, each filter.

Figure 6. Filter paper with particles. [source: Ibiden Hungary]

The only officially approved measurement method for diesel vehicles is the gravimetric method, where the weight of the diluted PM is measured. The sampling system must operate at a constant dilution ratio (Rratio = 300) during the transient cycle, so the amount of gas passing through the filter paper (G_{tot}) must be precisely controlled. In addition, the amount of dilution air (G_{dil}) must be added accurately and quickly for constant dilution. The sample gas mass flow rate (G_p) is calculated from the difference between the mass flow rate on the filter paper and the dilution air mass flow rate. [11]

$$G_p = G_{tot} - G_{dil} \quad (1)$$

The exhaust gas mass flow rate (G_{exh}) of the engine is calculated from the mass of air intake by the engine per unit time (G_{air}) and the mass of fuel consumed per unit time (G_{fuel}) by the test bench computer and forward it to the SPC. (Figure 7) [11]

$$G_{exh} = G_{air} - G_{fuel} \quad (2)$$

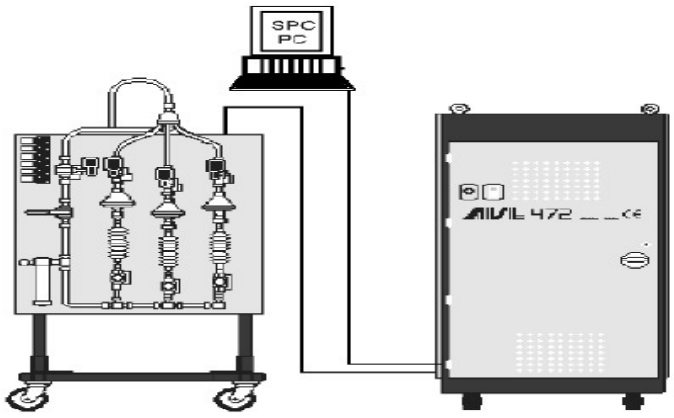

Figure 7. Structure of the AVL Smart Sampler measuring system. [11]

The SPC PC calculates the instantaneous dilution air mass flow rate (G_{dil}) from the exhaust mass flow rate (G_{exh}) from the dilution value (R_{ratio} = 300).

3. Test cycles:

- Particle collection in the DPF filter (preconditioning): EUDC (Extra Urban Driving Cycle),
- Filter efficiency for measurement: NEDC (New European Driving Cycle),
- DPF filter regeneration: DPF regeneration with vehicle engine, post-injection (Post Injection).

Particulate collection: During the 400 second EUDC test cycle, the vehicle travels 6954.9 meters at a maximum speed of 120 km/h. Wait is 39 seconds at idle before and after the start of the cycle for the vehicle engine to warm up or cool down. (Figure 8)

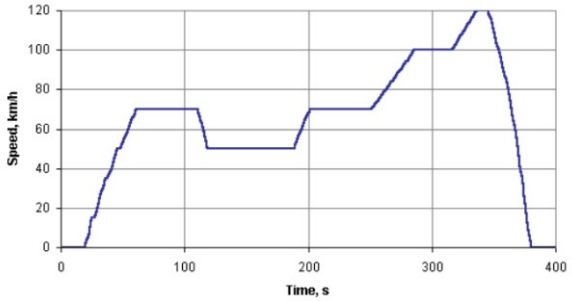

Figure 8. EUDC test cycle flow chart. [12]

Filtering efficiency measurement: The NEDC cycle is a complex cycle consisting of 4 ECE15 cycles and 1 EUDC cycle. The total driving time is 1180 seconds while the vehicle engine is idling for 267 seconds. (Figure 9)

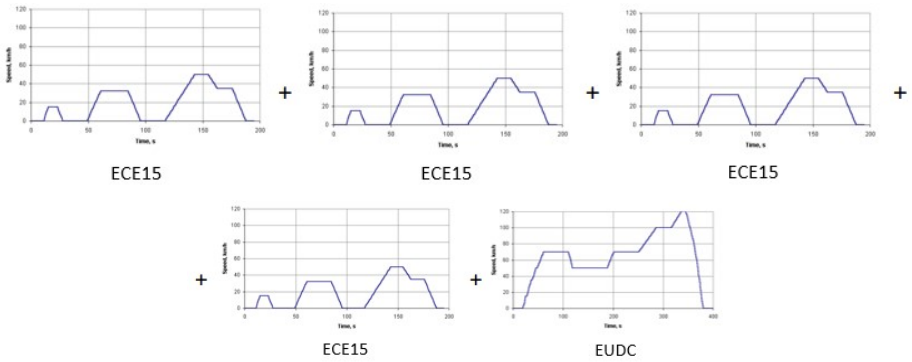

Figure 9. Flow diagram of a NEDC complex test cycle. [12]

Regeneration of the DPF filter: During test periods, the DPF filter must be regenerated (burned out) so that the accumulated diesel particles (diesel soot) burn without residue, or the filter returns to its original state. Therefore, the DPF filter is heated to 650 °C for 30 minutes to allow combustion to take place. This condition is achieved by modifying the engine's fuel injection process. Post injection is used. (Figure 10) Near the end of the stroke (while still burning), fuel is injected into the cylinders before the exhaust stroke, which escapes through the exhaust system into the diesel oxidation catalyst (DOC) and oxidises there

(enough), thereby raising the exhaust gas temperature DPF before filter. This temperature can be adjusted by the amount of fuel injected in the central engine control (ECU) electronics.

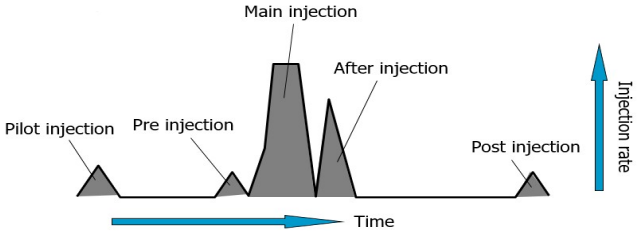

Figure 10. Fuel injection timing diagram. [13]

The Diesel engine uses more air during operation than is needed for perfect combustion (excess air condition), the excess gets out into the exhaust system, and this oxygen helps the DOC to operate, or the DPF to regenerate.

4. Procedure for measuring the change in DPF filtration efficiency:

During continuous measurement series, it is found that the filtration efficiency of DPF reaches the maximum efficiency (99.9 %) after 10-20 hours of operation. This phenomenon is demonstrated in a series of tests in this publication. A series of tests were performed that measure the initial DPF filtration efficiency in the first two steps and then the in-process efficiencies of the increasing particle. (Figure 11)

The amount of particles increases in proportion to the operating hours of the DPF. Thus, it shows the change in filtration efficiency depending on the operating time of the DPF.

DPF Filtration Efficiency experiment steps	
Step	Process
1	NEDC cycle without soot accumulation
2	Active Regeneration
3	NEDC cycle without soot accumulation
4	Active Regeneration
5	NEDC cycle with 1 times soot accumulation
6	Active Regeneration
7	NEDC cycle with 2 times soot accumulation
8	Active Regeneration
9	NEDC cycle with 3 times soot accumulation

Figure 11. Test series to verify the change in DPF filtration efficiency. [source: Ibiden Hungary]

Before step 0, the initial weight of the DPF filter is measured and used as the initial reference weight. After each test period (test step), the weight of the DPF filter is measured and the difference in the initial weight shows the actual weight of the particles remaining in the filter.

Results

During the evaluation of the series of measurements, it became apparent how the initial filtration efficiency of the DPF filter (55%) increases as the operating time progresses. It can be seen that with increasing particle load, the number of particles passing through the DPF filter decreases strongly, so the filtration efficiency increases. (Figure 12)

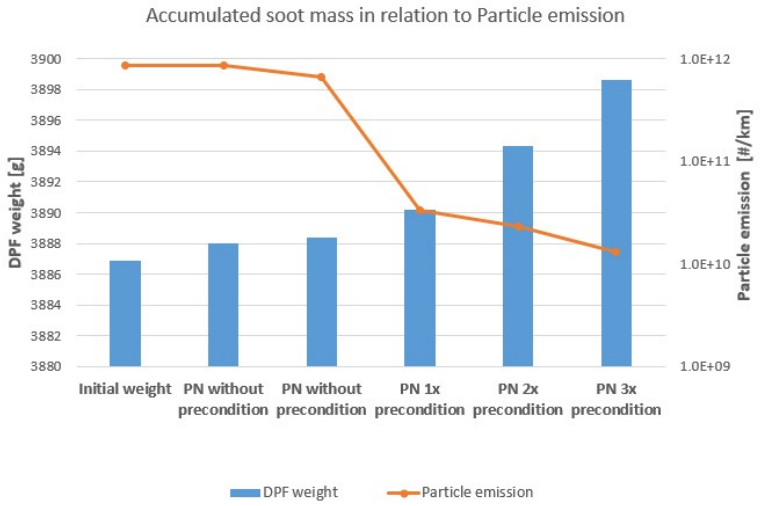

Figure 12. Accunulated soot and particle number.

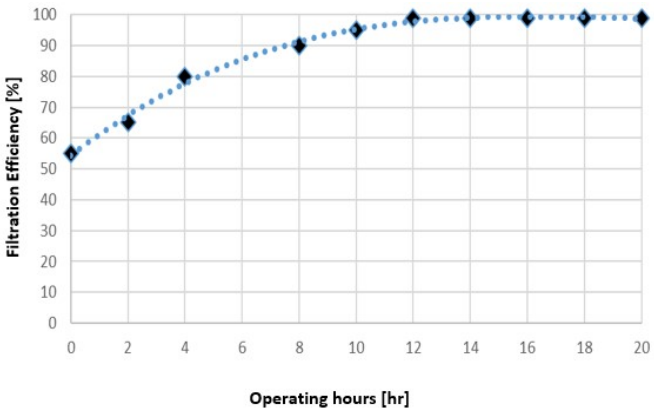

Figure 13. Change of filtration efficiency over operating hours.

Filtration efficiency increases from initial 55 % to final 99.9 % (over 16 hours of operation) as DPF uptime progresses. (Figure 13)

If we further examine the result of Figure 12, we can see that the initial mass of DPF could not be recovered in any way after the tests. That is, there is always a particle (soot) left inside the filter. These soot particles adhered to the DPF filter particles (SiC), thereby reducing flow gaps on the inner surface of the filter. Therefore, the filtration efficiency increased with increasing operating time. (Figure 14)

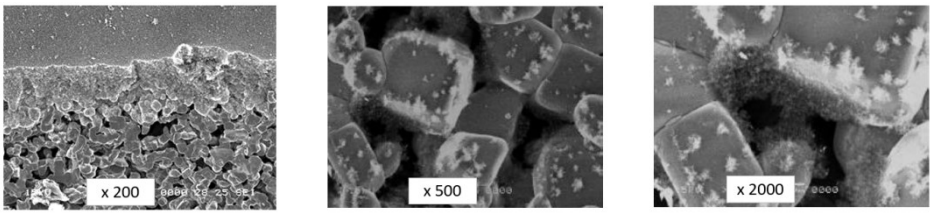

Figure 14. Electron micrograph of the cell wall with the deposited carbon black layer. [source: Ibiden Hungary]

A layer of soot adhering to DPF particles (white layer at the edges of the particles on the electron microscope image, Fig. 14) results in improved long-term filtration efficiency, thereby also helping diesel vehicles to operate more environmentally friendly.

Conclusions/Summary

The test has shown that the DPF filter unit's initial filtration efficiency (55 %) after 16 hours of operation close to 100 % and maintains it for the rest of its life span.

During unlocking the background of this phenomenon, we have discovered that a thin layer of soot adheres to the particles of the filter material (SiC) and narrows the passages and gaps between the particles of the filter substrate, thus increasing the filtration efficiency.

This creates a residual, useful soot layer that cannot be removed by regeneration, so this filtration efficiency can be considered final.

In this experiments with DPF, we have observed a phenomenon which shows the initial filtration efficiency of DPF is lower than the filtration efficiency after a few hours of operation.

Bibliography

[1] Szőllősi D, Bíró N, Kiss P: A dízel részecskeszűrő (DPF) koromszűrési hatékonyságának megállapítása. Mezőgazdasági Technika 2020. szeptember: LXI. Évfolyam 2-5. (2020)

[2] Biró N: Egyedi Adblue befecskendező rendszer tervezése és tesztelése. Diplomadolgozat, Szent István Egyetem (2020) pp. 10-15
[3] Szabó J Z: Gépjárművek üzemanyag ellátó berendezései. Óbudai Egyetem, Mechatronikai és Autótechnikai Intézet, (2013)
[4] Lee T, Park J, Kwon S, Lee J, Kim J: Variability in operationbased NOx emission factors with different test routes, and its effects on the real-driving emissions of light diesel vehicles. Sci Total Environ 461–462:377–385, (2013)
[5] Demers D, Walters G: Guide to exhaust emission control options. BAeSAME, Bristol (1999)
[6] Agarwal AK Biofuels (alcohols and biodiesel) applications as fuels for internal combustion engines. Prog Energy Combust Sci 33:233–271 (2007)
[7] Burtscher H: Physical characterization of particulate emissions from diesel engines: a review. Aerosol Sci 36:896–932 (2005)
[8] Manufacturers of Emission Controls Association. (MECA) - Emission Control Technologies for Diesel-Powered Vehicles. (2007)
[9] AMAi60, User's guide. AT2520E Rev. 2.9 AVL iGEM 1.6 AMA, (12/2016)
[10] APC^{plus} - AVL Particle Counter™ Product Guide. AT2858E, Rev. 14 , (12/2017)
[11] SPC472 SMART SAMPLER INTEGRATION, User´s Guide. AT3198E, Rev. 11, (3/2010)
[12] Dieselnet.com, Standards, Cycles. ECE 15 + EUDC / NEDC
[13] Csankó Cs, Szőllősi D, Bíró N, Kiss P: Dízelmotor NOx kipufogógáz-emissziójának mérése. Mezőgazdasági Technika 2021. szeptember: LXII. Évfolyam 2-5. (2021)

A review of three body abrasive wear by combined finite element method with smooth particle hydrodynamics and discrete element method

Hailemariam SHEGAWU[1], István OLDAL[2] , Gábor KALÁCSKA[2]
[1]Doctoral School of Mechanical Engineering, MATE
[2]Institute of Technology, Hungarian University of Agriculture and Life Sciences (MATE)

Abstract

Abrasive is a material removal technique in which cutting tool hard particles with sharp edges carve scratches and eject chips or wear particles. Abrasive wear is the most common type of roll wear, in which micro plowing and crack initiation happen at the same time, depending on the morphology and hardness of the abrasive particles. It's critical in a variety of engineering settings. The goal of this paper is to give a quick overview of the abrasive wear examination using a combination of finite elements meshed by the smooth particle hydrodynamics method and discrete element method, as well as to establish the groundwork for future abrasive wear research. The findings could aid researchers in choosing the right abrasive wear modeling software and model.

Keywords

abrasive wear, smooth particle hydrodynamics, discrete element method, material removal, wear

1. Introduction

Because of increased technology, complicated problems are now tackled, and one of the most complex phenomena in the world is the wear out of a machine. With the use of advanced technology such as finite element technique with mesh smooth particle hydrodynamics and discrete element method at the contact points or lines, researchers are studying how to develop and evolve in space and time. Subject knowledge is rapidly and continuously evolving for modeling abrasive wear using a combination of discrete element methods and finite element methods with meshed smooth particle hydrodynamics. The kernel function, Hertz model, Coulomb friction law, Hertz-Mindlin bonding contact model, Newton's and Euler's equations, Rabinowicz's equation, friction energy wear approach, and Archard law are some of the fundamental theories researchers utilized to tackle abrasive wear problems. There was research into the effects of load, speed, composition, alloys, composites, temperature, abrasive sizes, abrasive properties, debris layers, microstructure, reinforcement size,

mechanical properties, micromechanical, particle motion, grain size, and abrasive wear of rock, soil tool tillage, and sand. The purpose of this paper is to provide a high-level overview of the abrasive wear experimental investigation and to lay the foundation for future abrasive wear research.

2. Literature review about the combination of discrete element methods and finite element methods with meshed smooth particle hydrodynamics

Modeling of abrasive wear by a couple of discrete elements and finite element mesh with smooth particle hydrodynamic methods

Gui et al. (Gui et al., 2016) investigated the thermal, mechanical, and tribological behaviors of interacting surfaces in a dry slide braking system built of gray cast iron and low metallic friction materials using a finite element technique. The approaches included thermo-mechanical analysis, wear analysis, heat boundary conditions, a hybrid mesh method that combines the advantages of the pure Lagrangian and pure Eulerian mesh methods, and fully coupled thermo-mechanical-wear simulation. Numerical simulations, restrictions, boundary conditions, contact definitions, contact pressure, wear depth, temperature change, and dynamical stress were also included. They discovered that wear has a considerable impact on contact pressure, and that material loss can alter non-uniform contact conditions. The effect of slip and wear type identification was not included in the study because of its limitations. Using a finite element model with a smooth particle hydrodynamic mesh, Duan et al. (Duan et al., 2017a) investigated material removal modes in monocrystal Sic scratching by a single diamond. The main purpose of using FEM was to avoid excessive grid distortions and SPH to tackle boundary concerns. Coupling SPH and FE simulations, experiments, and constitutive equations were among the approaches used. SPH and FEM coupled simulation with diamond grit, stress distribution analysis, effect on maximum width, depth of the groove, and contact force were also included. Figure 1 depicts the SPH and FE in a two-dimensional connection. Scratching monocrystal SiC with a single diamond grit resulted in three removal modes: plastic deformation mode, ductile-brittle transition critical mode, and brittle removal mode, according to the report. The study's limitations included monocrystal SiC isotropy, temperature independence of all physical parameters, minimal heat transfer of workpiece material, and slight elastic deformation on grain.

The purpose of this study, according to Duan et al (Duan et al., 2017b), was to combine finite elements with smoothed particle hydrodynamics to tackle the mesh distortion problem caused by FEM. Monocrystalline silicon carbide and diamond grits were employed as the materials. Definition of scratching kinds, twice-scratching simulation, experimental validation, material constitutive equation, performance parameter, and analysis of twice-scratching simulation findings were among the methods used. Furthermore, analysis of experimental data, comparison of tests and simulations, material damage distribution,

interference mechanism, effect on groove width and depth, and effect on contact force were all included. Figure 2 shows the material damage distribution after scratching (a) section A of the groove, (b) the top view of the groove, (c) the interference region of the lateral fractures, and (d) section B of the groove twice. The length of the lateral cracks and the width of the plastic deformation was used to determine the interference mode. The study's limitations included the absence of cracks, the influence of slip, and the effect of temperature.

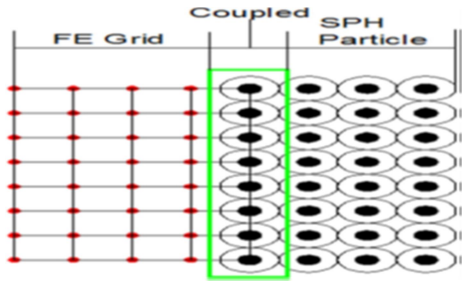

Figure 1. Depicts the SPH and FE in a two-dimensional connection (Duan et al., 2017a).

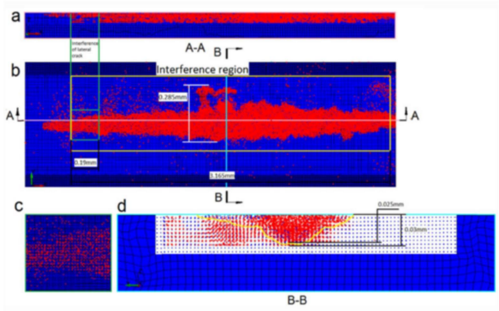

Figure 2. Depicts the material damage distribution following scratching (Duan et al., 2017b).

Modeling of abrasive wear by combined of discrete element method and discrete element method

Phan et al. (Phan et al., 2017) focused on abrasive wear prediction by discrete element method with a specific implementation of abrasive wear. The bond configuration utilized in the 3D EDEM model is shown in Table 1. High-speed steel, oxide (Fe2O3), carbides, mechanical properties of oxide scale, V-rich MC carbides at increased temperatures (650 °C), and the basic principle of DEM were all part of the process. In addition to these, bond configuration determination in the DEM model for oxide at 650°C, tensile test, nanoindentation, and wear calculation on HSS roll were studied. The influence of carbides orientation on wear resistance, effect of scratching tip size on HSS

wear rate, and effect of scratching depth on HSS wear rate were also included. Figure 3 depicts a sample at a given point in time as well as (a) view plane A-A and (b) view plane B-B. Conclusions: As the size of the scratching tip rose, abrasive wear increased linearly. When the scratching depth increased, the wear mass increased as well. Cracks, temperature, and adhesive wear were not taken into account in this investigation.

Table 1. Depicts the bond structure used in the 3D EDEM model (Phan et al., 2017).

Bond Properties	Particles - Particles	Particles - Carbides	Carbides - Carbides
Normal Stiffness (N/m)	6×10^{10}	6×10^{10}	6×10^{16}
Shear Stiffness (N/m)	4×10^{10}	4×10^{10}	4×10^{16}
Critical Normal Stress (Pa)	5×10^{7}	5×10^{7}	5×10^{12}
Critical Shear Stress (Pa)	5×10^{7}	5×10^{7}	5×10^{12}
Bond disc radius (μm)	3	3	3
Coefficient of restitution	0.4	0.4	0.4
Coefficient of static friction	0.8	0.8	0.8
Coefficient of rolling friction	0.5	0.5	0.5
Poisson's Ratio	0.33	0.33	0.33

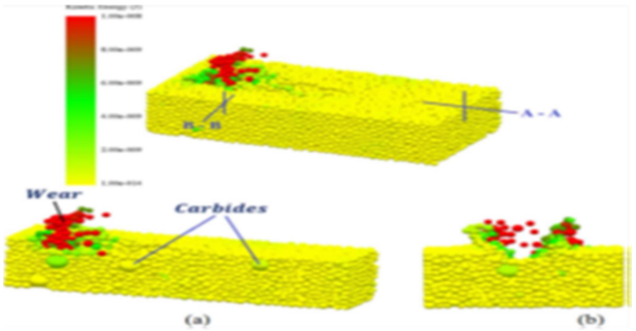

Figure 3. Depicts a sample at a given point in time (Phan et al., 2017).

Perazzo et al. (Perazzo et al., 2019) focused on discrete element method wear rate and wear pattern prediction with the specific implementation of abrasive wear. The model for contact forces is shown in Figure 4. On steel plates that interact with copper ore, discrete elements of the basic equation, temporal integration, contact and particle model, contact detection techniques, and

representation of wear by DEM were among the ways. Additionally, abrasive wear tests, characterization, calibration of bulk solid, grain form, granulometry, repose angle, particle dispersion, and bulk density were included. It was feasible to tell whether the mineral was rolling or sliding on the same material's grain size surface by analyzing the type of wear pattern. The study's limitations ignored the effects of temperature and particle size.

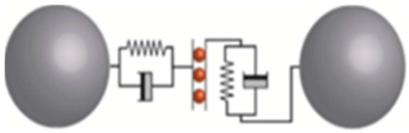

Figure 4. Depicts the contact force model (Perazzo et al., 2019).

Katinas et al. (Katinas et al., 2021) investigated dynamic friction, rolling resistance (particle-sample) sensitivity on wear loss, and friction force-related responses of modeled dry sand rubber wheel test using DEM to compare results with laboratory experiments. The "Rocky DEM" software uses the DSRWT model approach shown in Figure 5. Boron 27 steel, rubber-rimmed steel wheel, and silica quartz sand materials, sample preparation, DSRWT technique, and testing at prescribed load were included in the process. The methodology also includes friction force measurement, worn surface evaluation, wear loss calculations, as well as DEM parameter computations. In addition to the DEM model setup, the statistical analysis of DoE simulation results, the study of simulated DSRWT, and the volume/shear work ratio parameter were also covered. Furthermore, the DSRWT experiment's wear loss, the model under varied lower loads, stress analysis during simulation, wear under constant, progressive volume/shear work ratio (k) parameters, and friction force was studied. They concluded that changing the volume/shear work ratio parameter allowed them to control wear loss. The influence of sand particle motion type, temperature effect, and the presence of oxides were all eliminated from the study due to its limitations.

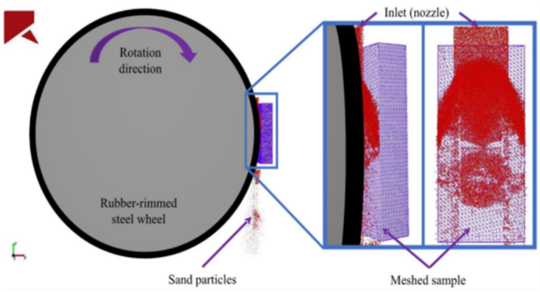

Figure 5. Depicts the DSRWT model the "Rocky DEM" software (Katinas et al., 2021).

Schramm et al.(Schramm et al., 2020) focused on abrasive wear using the discrete element technique and a scratch test with abrasive wear implementation. Figure 6 depicts a step-by-step technique for simulating wear in a tillage operation. Single asperity scratch test, wear simulation, single asperity test, and simulation with geometrical changes was all part of the approach. The soil tillage tool was made up of steel (martensite and bainite) and a diamond tip indenter with a diameter of 200 μm, which corresponds to the soil's average abrasive particle size. This research found that the primary micro-cutting mechanism was detected on tine surfaces in the field under real-world settings. Thermal, chemical, particle size, and particle motion were not included in the restriction.

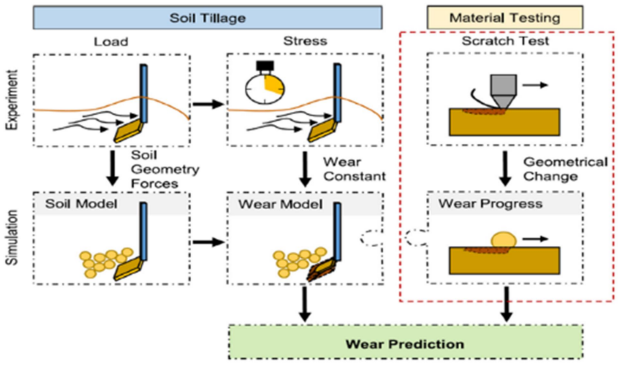

Figure 6. Depicts a wear simulation in the tillage operation (Schramm et al., 2020).

Tekeste et al.(Tekeste et al., 2019) focused on quantifying dimensional wear loss using three 3D scanned and reconstructed cultivator sweeps (new, carbide treated-worn, and untreated-worn), as well as using Discrete Element Modeling to simulate sweep-to-soil interaction for evaluating wear effects on soil forces (draft and vertical) and soil forward failure distance. Simulator-soil interaction, experiment technique, DEM simulation setting, DEM simulation for particle size selection, simulation setup for DEM parametric sensitivity analysis, and data analysis were among the approaches used. DEM model parameter sensitivity, experimental verification, DEM model parameter calibration, optimization, 3D scanned sweeps for dimensional loss measurement, and DEM simulation were all covered. DEM simulation of cultivator sweep-to-soil contact, DEM soil force prediction from worn and fresh cultivator sweeps, DEM anticipated draft forces as a function of tool speed, and DEM soil flow prediction was also included. Figure 7 depicts the velocity profile recovered from EDEM post-processing color mapping of DEM anticipated forward soil failure in front of the cutting tool and depth (A–C). DEM projected forces and the soil failure zone suggested that the carbide-treated-worn sweep performed comparably to new sweep. The

study's limitations included the absence of the effects of temperature, particle size, and soil motion.

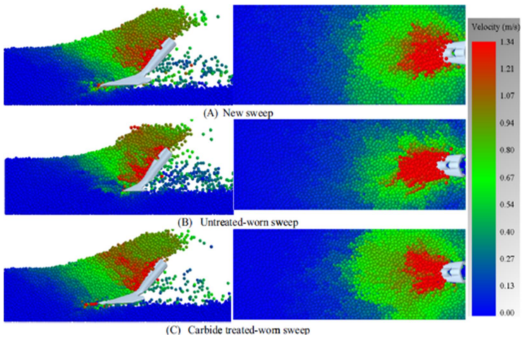

Figure 7. Depicts the DEM's prediction of forwarding soil failure (Tekeste et al., 2019).

Modeling of abrasive wear by combined finite element method with smooth particle hydrodynamic method and discrete element method

Leonard et al. (Leonard et al., 2013) evaluated fretting wear of approximate forecasts utilizing a pair of DEM-FEM. The modulus of elasticity of the semi-infinite domain and the upper cylinder (200GPa), Poisson ratio (0.3), and the coefficient of friction (0.5) were used. Numerical modeling, production of rough surfaces, damage mechanics implementation, modeling of surface roughness effects, and wear modeling utilizing damage mechanics were some of the methods used. The major finding was that a rougher surface causes more wear loss. The study's drawback was that it did not account for the effects of temperature, particle size, and number. Forsström and Jonsén (Forsström & Jonsén, 2016) focused on local failure prediction utilizing a couple of DEM-FEM models with abrasive wear as a special case. Steel grades that came into touch with the granular material found in blast rocks were used. Experimentation, wear drum testing, tipper bodies, numerical modeling, discrete element method, finite element method, and material model were some of the approaches used. Wear computation, tipper body measurements, calibration test, and tipper body unloading validation research were all included. To summarize, the DEM-FEM combination with Archard's wear law could be utilized to model wear behavior in large-scale applications; however, additional effort was required to obtain the absolute wear rate in the structure. The study's weakness was that it did not take into account the effects of temperature, particle size and quantity, and fracture. F. Wang et al. (F. Wang et al., 2020) investigated rock prediction with a combination of FDEM and abrasive machining. During rock cutting, the diamond abrasive interacts with a Fangshan marble rock specimen (whose mechanical parameters were described in Table 2.). The finite element/discrete element approach and the analysis of failure mode for the

cohesive element were among the methodologies used. Abrasive machining models using FDEM, fracture mode, machined surface damage, and cutting forces were also included. Figure 8 illustrates the simulation setup, which includes (a) actual saw cutting, (b) geometric model, (c) mesh and boundary conditions. Figure 9 displays the stress field and chip formation in the abrasive machining process. Conclusions: As the abrasive angle increased, strong compressive stress developed in front of the abrasive as a result of the abrasive's interaction with the material. The study's weakness was that it did not account for temperature, slip, particle size, or the number of rocks.

Table 2. Lists the material characteristics of Fangshan marble (F. Wang et al., 2020).

Properties	value
Density ρ (kg/m^3)	2800
Young's modulus *E* (GPa)	85
Poisson's ratio υ	0.28
Tensile strength σ_t (MPa)	9.5
Shear strength τ (MPa)	20
Compressive strength σ_c (MPa)	160
Fracture toughness in mode I, K_{IC} (MPa·$\sqrt{m}$)	1.3
Fracture toughness in mode II, K_{IIC} (MPa·$\sqrt{m}$)	1.1
Damage stabilization cohesive	1e^{-5}

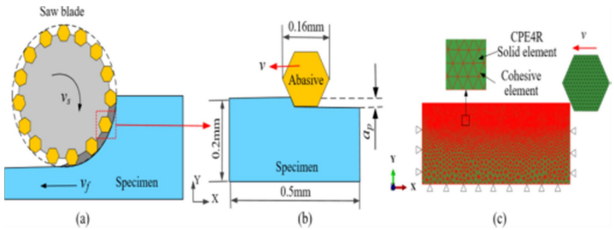

Figure 8. Shows the simulation setup (F. Wang et al., 2020).

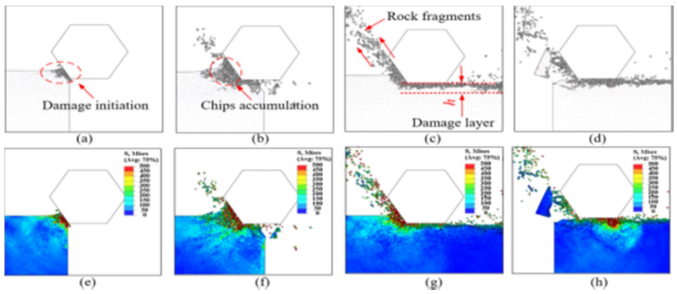

Figure 9. Depicts the stress field and the production of chips (F. Wang et al., 2020).

Leonard et al. (Leonard et al., 2014) investigated the effect of a third body on fretting wear using a mixed finite discrete element technique. As a third body, steel-to-steel material contact with oxides was used. The combined FDE model of the third body, FE model, DE model, DE contact between first bodies, DE contact between first and third bodies were among the approaches presented. DE contacts between third bodies, third body platelets, periodic flow between stiff flat plates, and DE connections between third bodies in Hertzian fretting contacts were also discussed. The findings showed that when the number of particles and platelet size increased, the load borne by the worn slip zone increased in comparison to the unworn stick zone. Temperature, fracture, particle size, and the number of third bodies and platelets were not considered in the study. W. Wang et al. (W. Wang et al., 2014) investigated three-body friction behavior using the FEM–DEM coupling approach. Materials characteristics and model parameters are shown in Table 3. Coupling model and algorithm, model description, coupling algorithm, compression and shearing procedures, coupling programming, and energy analysis were among the approaches covered. Friction coefficient, third-body particle contact state, particle slip rate, particle velocity distribution, particle contact angle, and stress analysis were all included. Figure 11 displays a stress nephogram in the FEM region and a force chain pictured in the DEM region, while Figure 10 shows a model of parallel plates shearing the third body. Conclusions under low pressure, particle velocity changes as energy were exchanged between particles. The study's drawback was that it did not take into account the effects of temperature, crack, particle size, or motion type.

Table 3. The material properties and model parameters (W. Wang et al., 2014).

First-body parameters	Values	Third-body parameters	Values
First-body Young's modulus	100 GPa	Particle number	1200
First-body Poisson's ratio	0.3	Particle mean diameter	40 μm
First-body density	7800 kg/m^3	Particle Young's modulus	1e11 pa
Element size	40*40 μm	Particle Poisson's ratio	0.3
Element number	2500	Particle friction coefficient	0.25
		Particle density	7800 kg/m^3

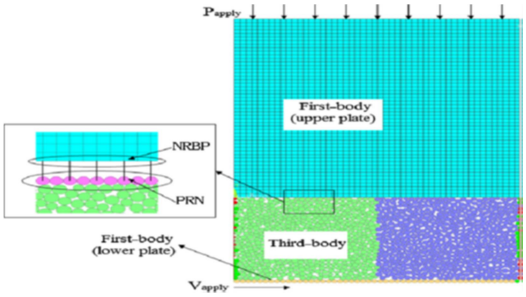

Figure 10. Depicts the model of the parallel plate shearing third body (W. Wang et al., 2014).

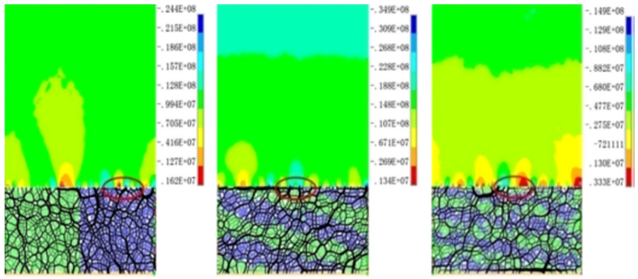

Figure 11. Depicts force chain pictured in the DEM and stress in FEM (W. Wang et al., 2014).

Li et al. (Li et al., 2013) investigated a hybrid finite–discrete technique to study how to anticipate fretting damage behavior in bearing interactions. Third body particles (35Ni4Cr2MoA(E)) and bearing material (GCr15) were employed. FE analysis, FE modeling, FEM simulation throughout the fretting cycle, fretting cycle definition, and risk position determination were among the methods used. Additionally, lateral cut boundaries, sub-model extraction, DE modeling, analysis rebuild sub-model by DEM, the non-degradable model for bearing entity, degradable model liner entity, and non-degradable model for bearing entity were included. Furthermore, contact constitutive model between two adjacent elements, inter-element contacts resultant force, rupture criterion for the parallel-bond model, determine microscopic parameters in DEM, fretting analysis by DEM, define fretting cycle in DEM simulation, multi-axial loading applied non-degradable model were all included. In addition, crack damage analysis, fretting condition crack damage, fretting wear inquiry, detect detached particles, evolution detachment, and ejection particles were all covered. Figure 12 depicts the evolution of ejected and third-body particles using DEM. The study concluded that the wear process was governed by both the detachment and ejection mechanisms and that the third body particles remaining in the contact zone play an important role in the wear process. The study's weakness was that it did not account for the effects of temperature, particle size, or slip.

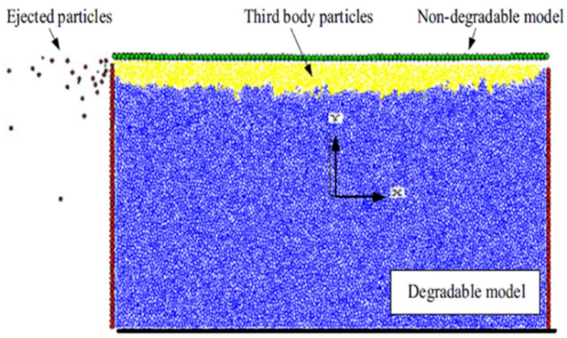

Figure 12. Depicts the evolution of ejected and third-body particles (Li et al., 2013).

3. Aim of the research

The study's purpose is to learn more about advanced technology abrasive wear modeling software, abrasive wear modeling methods, identification of an abrasive wear modeling theoretical model, and various abrasive wear modeling approaches. My goal is to understand more about how mass is removed from surfaces and how to reduce material removal wear rates:

- To investigate abrasive wear, friction, and fracture used abrasive wear advanced software
- To investigate the mechanical and chemical properties that can aid in the reduction of friction, wear, corrosion, and fracture resistance.
- To assess the effectiveness of various methodologies and modeling techniques.

5. Abrasive wear modeling setups and procedures

Materials selection

To undertake abrasive wear, all researchers initially selected abrasive materials, specimen materials, and counter materials. Gray cast iron, oxide, and low metallic friction materials were used by Gui et al. (Gui et al., 2016). Duan et al. (Duan et al., 2017b) employed monocrystalline silicon carbide and a single diamond, while Duan et al. (Duan et al., 2017a) used monocrystalline silicon carbide and diamond grits.

High-speed steel, oxide (Fe2O3), and carbides were employed by Phan et al. (Phan et al., 2017). Steel plates and copper ore were employed by Perazzo et al. (Perazzo et al., 2019). Boron 27 steel, a rubber-rimmed steel wheel, and silica quartz sand components were employed by Katinas et al. (Katinas et al., 2021). Schramm et al. (Schramm et al., 2020) employed a diamond and steel (martensite and bainite).

Steel grades and granular material blast rocks were employed by Forsström and Jonsén (Forsström & Jonsén, 2016). Li et al. (Li et al., 2013) utilized steel material, steel material, abrasive material particles (35Ni4Cr2MoA(E)), and bearing material, while Leonard et al. (Leonard et al., 2014) used steel material, steel material, and oxides (GCr15).

Setups and procedures

The thermo-mechanical analysis, wear analysis, heat boundary conditions, a hybrid mesh method that combines the advantages of the pure Lagrangian and pure Eulerian mesh methods, and fully coupled thermo-mechanical-wear simulation were all part of Gui et al (Gui.'s et al., 2016) setup and procedure.

There were also numerical simulations, constraints, boundary conditions, contact definitions, contact pressure, wear depth, temperature change, and dynamical stress. The setup and process employed by Duan et al. (Duan et al., 2017b) include connecting SPH and FE simulations, experiments, and constitutive equations. Stress distribution analysis, effect on maximum width,

depth of the groove, and contact force were all included in the SPH and FEM coupled simulation with diamond grit. The definition of scratching sorts, twice-scratching simulation, experimental validation, material constitutive equation, performance parameter, and analysis of twice-scratching simulation findings were among the approaches employed by Duan et al. (Duan et al., 2017a). In addition, data analysis, test and simulation comparisons, material damage distribution, interference mechanism, effect on groove width and depth, and effect on contact force were all covered. The setting and approach used by Phan et al. (Phan et al., 2017) include high-speed steel, oxide (Fe2O3), carbides, mechanical properties of oxide scale, and V-rich MC carbides at elevated temperatures (650 °C), and the basic premise of DEM. Bond configuration determination in the DEM model for oxide at 650°C, tensile test, nanoindentation, and wear prediction on HSS roll were all investigated in addition to these. The effects of carbide orientation on wear resistance, scratching tip size on HSS wear rate and scratching depth on HSS wear rate were also studied. On steel plates that interact with copper ore, discrete elements of the fundamental equation, temporal integration, contact and particle model, contact detection approaches, and representation of wear by DEM were among the ways used by Perazzo et al. (Perazzo et al., 2019). Abrasive wear tests, characterization, and calibration of bulk solids were also included, as well as grain shape, granulometry, repose angle, particle dispersion, and bulk density. Simulator-soil interaction, experiment strategy, DEM simulation setting, DEM simulation for particle size selection, simulation setup for DEM parametric sensitivity analysis, and data analysis were among the approaches employed by Tekeste et al. (Tekeste et al., 2019). The following topics were discussed: DEM model parameter sensitivity, experimental verification, DEM model parameter calibration, optimization, 3D scanned sweeps for dimensional loss measurement and DEM simulation. DEM soil force prediction from worn and new cultivator sweeps, DEM expected draft forces as a function of tool speed, and DEM soil flow prediction was also included.

The setup and process used by Schramm et al. (Schramm et al., 2020) included a single asperity scratch test, wear simulation, single asperity test, and simulation with geometrical modifications. The finite element/discrete element technique and the study of failure mode for the cohesive element were among the methodologies employed by F. Wang et al. (F. Wang et al., 2020) in their setup and procedure.

Cutting forces, fracture mode, machined surface damage, and abrasive machining models employing FDEM were all included. Coupling model and algorithm, model description, coupling algorithm, compression and shearing methods, coupling programming, and energy analysis were among the methodologies covered by W. Wang et al. (W. Wang et al., 2014, p.) setup and procedure. The stress study includes friction coefficient, third-body particle contact state, particle slip rate, particle velocity distribution, particle contact angle, and friction coefficient. The non-degradable model was subjected to bi-axial loading. Third body particles (35Ni4Cr2MoA(E)) and bearing material

(GCr15) were used in Li et al (Li .'s et al., 2013) setups and processes. The methodologies employed included FE analysis, FE modeling, FEM simulation throughout the fretting cycle, fretting cycle definition, and risk position determination. Also included were lateral cut boundaries, sub-model extraction, DE modeling, analysis rebuild sub-model by DEM, the non-degradable model for bearing entity, degradable model liner entity, and non-degradable model for bearing entity. Also included was a contact constitutive model between two adjacent elements, inter-element contacts resultant force, rupture criterion for the parallel-bond model, determine microscopic parameters in DEM, fretting analysis by DEM, define fretting cycle in DEM simulation, and multi-axial loading applied non-degradable model.

Results and conclusions

This paragraph will conclude the articles that employed a mix of the finite element with mesh smooth particle hydrodynamics and discrete element methodologies by summarizing the primary findings of the study goals, as well as their value and contribution. will also look into the flaws in the methodology and give recommendations for further study. The goal of this paper is to give a quick overview of the abrasive wear finite element with mesh smooth particle hydrodynamics and discrete element and to build the groundwork for future abrasive wear research. The key finding and contributions to this research from this methodology are the effect of slip, load, speed, temperature, microstructural, gain size, alloying composition, composite, environmental, mechanical characteristic, metallurgical, surface roughness, and sliding distance discussed by almost all of the researchers working in this abrasive wear. Researchers used advanced software and wear loss mass measuring devices before and after. The further finding shows that they are also utilized coulombs law, Archard law, friction energy method, Rabinowicz's equation. The limitations of researchers are excluding all of the following effects such as temperature, local failure such as damage, breakage, and crack, abrasive particle shape representation of actual abrasive particle shape, abrasive particle velocity, abrasive particle entrance, and motion type. Future researchers undertake similar research using a more sophisticated method such as including the effect of slip, surface roughness, sliding distance, temperature, abrasive particles of size, properties, entrance number, velocity, and motion type to the actual abrasive particle to model abrasive wear. In summary, this paragraph's key findings, influence factors, laws, limitations, and future works are presented.

References

[1] Duan, N., Yu, Y., Wang, W., & Xu, X. (2017a). SPH and FE coupled 3D simulation of monocrystal SiC scratching by single diamond grit.

INTERNATIONAL JOURNAL OF REFRACTORY METALS & HARD MATERIALS, *64*, 279–293. https://doi.org/10.1016/j.ijrmhm.2016.09.016

[2] Duan, N., Yu, Y., Wang, W., & Xu, X. (2017b). Analysis of grit interference mechanisms for the double scratching of monocrystalline silicon carbide by coupling the FEM and SPH. *INTERNATIONAL JOURNAL OF MACHINE TOOLS & MANUFACTURE*, *120*, 49–60. https://doi.org/10.1016/j.ijmachtools.2017.04.012

[3] Forsström, D., & Jonsén, P. (2016). Calibration and validation of a large scale abrasive wear model by coupling DEM-FEM: Local failure prediction from abrasive wear of tipper bodies during unloading of granular material. *Engineering Failure Analysis*, *66*, 274–283. https://doi.org/10.1016/j.engfailanal.2016.04.007

[4] Gui, L., Wang, X., Fan, Z., & Zhang, F. (2016). A simulation method of thermo-mechanical and tribological coupled analysis in dry sliding systems. *Tribology International*, *103*, 121–131. https://doi.org/10.1016/j.triboint.2016.06.021

[5] Katinas, E., Chotěborský, R., Linda, M., & Kuře, J. (2021). Sensitivity analysis of the influence of particle dynamic friction, rolling resistance and volume/shear work ratio on wear loss and friction force using DEM model of dry sand rubber wheel test. *Tribology International*, *156*, 106853. https://doi.org/10.1016/j.triboint.2021.106853

[6] Leonard, B. D., Ghosh, A., Sadeghi, F., Shinde, S., & Mittelbach, M. (2014). Third body modeling in fretting using the combined finite-discrete element method. *International Journal of Solids and Structures*, *51*(6), 1375–1389. https://doi.org/10.1016/j.ijsolstr.2013.12.036

[7] Leonard, B. D., Sadeghi, F., Shinde, S., & Mittelbach, M. (2013). Rough surface and damage mechanics wear modeling using the combined finite-discrete element method. *Wear*, *305*(1), 312–321. https://doi.org/10.1016/j.wear.2012.12.034

[8] Li, W., Huang, Y., Fu, B., Cui, Y., & Dong, S. (2013). Fretting damage modeling of liner-bearing interaction by combined finite element – discrete element method. *Tribology International*, *61*, 19–31. https://doi.org/10.1016/j.triboint.2012.11.019

[9] Perazzo, F., Lohner, R., Labbe, F., Knop, F., & Mascaro, P. (2019). Numerical modeling of the pattern and wear rate on a structural steel plate using DEM. *MINERALS ENGINEERING*, *137*, 290–302. https://doi.org/10.1016/j.mineng.2019.04.012

[10] Phan, H. T., Tieu, A. K., Zhu, H., Kosasih, B., Zhu, Q., Grima, A., & Ta, T. D. (2017). A study of abrasive wear on high speed steel surface in hot rolling by Discrete Element Method. *TRIBOLOGY INTERNATIONAL*, *110*, 66–76. https://doi.org/10.1016/j.triboint.2017.01.034

[11] Schramm, F., Kalácska, Á., Pfeiffer, V., Sukumaran, J., Baets, P. D., & Frerichs, L. (2020). Modelling of abrasive material loss at soil tillage via scratch test with the discrete element method. *Journal of Terramechanics*, *91*, 275–283. https://doi.org/10.1016/j.jterra.2020.08.002

[12] Tekeste, M. Z., Balvanz, L. R., Hatfield, J. L., & Ghorbani, S. (2019). Discrete element modeling of cultivator sweep-to-soil interaction: Worn and hardened edges effects on soil-tool forces and soil flow. *Journal of Terramechanics*, *82*, 1–11. https://doi.org/10.1016/j.jterra.2018.11.001

[13] Wang, F., Liu, S., & Ji, K. (2020). Numerical study on abrasive machining of rock using FDEM method. *Simulation Modelling Practice and Theory*, *104*, 102145. https://doi.org/10.1016/j.simpat.2020.102145

[14] Wang, W., Liu, Y., Zhu, G., & Liu, K. (2014). Using FEM–DEM coupling method to study three-body friction behavior. *Wear*, *318*(1), 114–123. https://doi.org/10.1016/j.wear.2014.06.023

Trends in material selection for mechanical seals

Péter Marcell KISS, Gábor KALÁCSKA
Institute of Technology, Hungarian University of Agriculture and Life Sciences (MATE)

Abstract

The mechanical seal was invented in 1923 by George J. Cooke. At that time it was called Cooke seal, and was first used in refrigeration compressors. Since then, mechanical seals got very important roles in sealing systems, and nowadays these seals and seal systems are one of the most expensive parts in the pump equipment. Manufacturers and distributors are constantly developing and improving the properties and characteristics of the seals, to earn better density and longer lifecycle. These improvements are significantly affect the costs of the planning, manufacturing and assembly of the seal. This paper describes the structural and conceptual operation of the mechanical seals and introduces the applied seals in the agriculture and pump technology.

Keywords

Mechanical seal, Carbon, Ceramic, Silicon Carbide, Tungsten Carbide

1. Introduction

Mechanical seal is an end-face device used on a rotating shaft to control fluid's leakage and keep contaminants out. It prevents the fluid from leaking through a device, which is most often a centrifugal pump. The mechanical seals are located in the pumps stuffing box or in its seal chamber. This is the area where the pump shaft connects to an electrical motor, and we have to control or stop the leakage. The basic concept of mechanical seals requires two surfaces. One surface has to be stationary, while the other one must rotate. This concept is the basics of all mechanical seals, but in few things, such as arrangement of the seal, secondary seal and gasket types and ring materials can be different from each seals. A mechanical seal has five main parts. These are the mating ring, primary ring, spring mechanism, drive mechanism and the secondary seals. Mating ring is the stationary and the primary ring is the rotating part of the seal. Companies are using different mating ring and primary ring face materials depending on the pumped fluid, to reduce wear, and generated heat while the seal is operating. Spring mechanism offsets the change due to the wear, which is important to keep the system sealed. Rotating and stationary parts both require drive mechanism, to induce or prevent rotation. In some cases, the secondary seals provides enough drive force to act as a drive mechanism. Secondary seals are the O-rings and gaskets. These have different profiles depending on, what is the

pumped liquid, and what are the specifications of the pumps operation. (MAYER, Ehrhard 2013)

A mechanical seals were not designed to stop leakage but to control them. These seals are controlling leakage radially between the stationary and rotating components, by limiting the flow of fluid between the two surfaces. Mechanical seals are operating on a thin fluid film at a high rotating speed. This thin fluid film moves from the higher pressure side, to lower pressure side between the rotating and stationary faces. Mechanical seals must allow for axial motion to compensate for wear, bearing clearances thermal growth, and for radial and axial deflections. These deflections are mostly due to hydraulic loads on pumps. In the seal chamber, there can be variable factors such as, change in rotating speed, temperature and pressure, which influence the operation of the seals. Due to these factors, mechanical seals need to be able to adjust automatically for these variable circumstances.

2. The review

There are many pumps used in the agriculture, especially for transporting and lifting various liquids. These liquids can be water, fertilizer or fertilizer water mixture. The pH value of the manure can be acidic or alkane. Depending on, what kind of pH value liquid we would like to transport or lift, we have to apply the adequate mechanical seal. It depends on the pumped fluid's chemical and physical properties, how we have to do the selection of seal faces, metal components and secondary seals in accordance with specifications, to be resistant to most type of corrosion. The most common used material is carbon, ceramic, silicon carbide, tungsten carbide. The other group of seal faces would be the coated type seals. (Huebner M. 2005)

Carbon

Carbon is the basis of all organic products, that's why it is one of the most common element on earth. Carbon is used in mechanical seals with preference, because they are stable and self-lubricating. Self- lubricating materials are a new generation of materials to minimize friction and wear over high temperature range between seal faces. These materials are using the benefit of incorporated solid-lubricating compounds.

Nowadays the most commonly used mechanical seal face combination is a high duty mechanical carbon and a reaction bonded or alpha sintered silicon carbide. G.A Jones from University Salford, (JONES, G. A. 2004) did an experiment, regarding dry running mechanical carbon wear. The purpose of his experimental procedure was, to better understand the tribological-dynamics of the carbon graphite surface film and film forming processes. He used an Amsler friction and wear testing machine, where the pads were manufactured from alpha- and bonded sintered silicon carbide, and the rotating cylinders were manufactured from mechanical carbon. In the experiment procedure the

mechanical carbon cylinders were rotating at a constant surface velocity 0.5 m/s. The load was continuously increased in the first experiment until the contact instability. He did two test runs per every type of material combination and experiment. He did 3 experiments, first one was the determination of PV (pressure x velocity), second experiment was a measurement under constant conditions, and in the third one he tested the influence of the silicon carbide surface. From each test run he got information on PV performance, and provided a PV profile. In addition, information was obtained on friction coefficient of the different surfaces, the wear rate, the generated frictional heat, and the role of carbon graphite contact films in the generated performance profile. The analysis and result in this research have contributed to the knowledge and understanding of tribological behaviour of mechanical carbon seals. At the end of the experiment they have developed analysis and tools that could be useful to the mechanical seal designer and the materials technologist. In the hydraulic pump industry mechanical carbon used in a mixture of amorphous carbon and graphite. The physical properties of the mixture depends on the percentage of each material.

HIRANI, H. et al. examined the friction and wear of carbon–graphite face seal under dry, water and steam conditions. They summarized that tribological performance depends on pressure, rotating speed, mating and primary ring surface and presence of water pressure. Then ran on the test setup carbon-graphite rings. There were 3 experiments, first with dry running condition, second with water lubrication, ant the third one with steam lubrication. They calculated the wear loss by measuring the weight of the mechanical seals. Often weight loss was less than 1 mg after 1000 cycles, so they did at least 10,000 rotation. After the dry condition measurement, they could see, that the initial friction was higher compared to the measured friction after 5000 cycle. The possible reason for this reduction is the initial breakdown of surface structure of carbon–graphite into wear debris. This resulted a soft, and low strength surface layer between the two faces. To summarize the results, they identified that the seals, the primary and the secondary seal lost their weight by 0.16 μg.

In the second experiment, the primary and the secondary seal was operated in 0.5MPa saturated steam environment. They operated for 50,000 cycles under steam lubrication. Compared to the dry running measurement, it could be stated, that the wear rate was here much higher. Interesting to mention, that only a very little number of particles remained separated, and large number of particles got accumulated. The maximum weight loss in steam lubricated condition was 1.9 μg per rotation.

Three cases were considered to evaluate the performance of the seals under water lubrication. In Case 1 0.5MPa steam pressure was supplied to the rotary seal. In Case 2 the rotary joint was completely filled with water. In Case 3 less water was added to the rotary joint, just the lowest point of the seal touched the water, so the seal could operate under water vapour conditions. From the measurements, they determined, that the maximum seal wear occurred under Case 2 condition, while the minimum under Case 3. This is because excessive

quantity of water tries to remove the carboy layer, what would form under dry operation. As a result this effect increases the wear rate between the two seal faces. (HIRANI, H. 2009)

Ceramic

Ceramics are non-metallic nonorganic materials that usually applied on high temperature processing. These materials have high hardness, stiffness, low thermal expansion and very good wear resistance. Due to these properties, ceramic is a very popular seal material for pumping high temperature fluid. Thermal water which has a higher temperature is used in agriculture to sprout plants. However this type of mechanical seal, ceramic is not a very common applied seal face material in the agriculture. (HUEBNER M 2005)

Silicon Carbide

Metal carbides are often used as wear materials in sliding contact applications, such as mechanical seal faces. They have excellent and high wear resistance, hardness and corrosion resistance. They are used in pump industry with different coatings such as Silicon Carbide. (CARROLL, B., et al. 2003)

Silicon carbide consist of one silicon atom and one atom of carbon. This results an extremely strong and stable bond over wide range of temperatures and chemical applications. It is abrasion resistance, corrosion resistance and thermal shock resistance. Next to these advantages it has a high hardness and modulus. On the other hand, it is very difficult to manufacture in different shapes, which would be important for component design. (Pascal Déprez, et al. 2009) made an experiment in 2009, about Application to the Characterization of Carbon-Silicon Carbide Tribological Couples of Automotive Water Pump Seals. The investigated primary rings were thermohardening from a resin base and a specified mixture of graphite, coke, antimony and zinc stearate. The tested mating rings were sintered porous silicon carbide.

There were five different studied factors:

- primary ring variant (carbon 1, 2),
- normal load (1, 5 daN),
- surrounding (dry, lubricated),
- mating ring finishing (3µm),
- rotational frequency (50 rad/s, 400 rad/s).

During the test, the temperature of the friction surface and the liquid in the container were measured on 50Hz frequency. The experiment was recorded after 10 hours of operation, and from the records, they could determine the dynamic friction coefficient and the wear of the carbon primary ring. From the data collected during the experiments, significant factors and interactions between the factors could be identified. A nonlinear regression method can be also used to develop a predictive mathematical model to optimize performance outputs. On Figure 1 we can see the main effects of the five studied factors. On Figure 1 we can see the degree of the effect of a factor. The bigger deviation from horizontal axis means the stronger effect of the friction. However, the most significant

factor after the 10 hour operation is the environment. It affects the most, the coefficient of dynamic friction. It is important and interesting to note, that the coefficient of dynamic friction is larger with the carbon 1 primary ring, then with the carbon 2. This is probably due to a lower hardness of the carbon 2 then the carbon 1. The knowledge in this experiment gained, allows the optimization of new pair of materials for dynamic sealing applications. The effects of five factors and their interactions were examined in this study, where they determined the optimal conditions and the best friction couple of material to apply in dynamic sealing system.

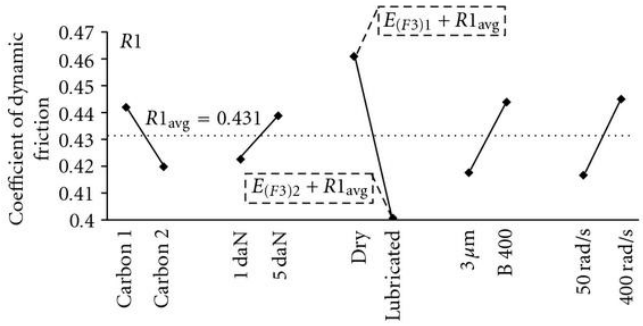

Figure 1. Main effects on the coefficient of dynamic friction.

The capacity of the specific load can be increased if a lubricant is used to separate the mating and the primary ring to reduce wear. Exterior elements, such as dust, or grease can influence the behaviour lifetime and reliability of the tribological system. (ZHAO, X. et al. 2014)

Tungsten Carbide

Tungsten carbide is one of the most employed materials, known for its hardness and strength. Pumping corrosive fluid has a serious chemical wear, especially for Co-bonded tungsten seals. This can be avoided by using a more corrosive-resistant material, Ni. (PIRSO et. Al 2004) S. Shankar, at el. did an experiment, with tungsten carbide stationary ring and rotating carbon ring. This kind of application is very common in the pump industry too. For the experiment, they used two seal faces, both faces were diamond polished, and the roughness of the rings were 0.03 to 0.04 μm. They applied eco-friendly lubricants such as vegetables oil or oils extracted from seeds. The lubricants were mixed with 1 wt.%, 3 wt.% and 5 wt.% of boric acid powder, and well mixed with the oils.

The rotary seal was fitted to the top of the test rig, and pressed onto the stationary seal. The stationary seal was fixed to the lower chamber, while a spring mechanism maintained the pressure between the two faces. The spindle, which hold the rotary seal was powered by a motor, which was controlled by a

variable frequency driver, this allowed the team to provide uniform torque at all speed. All the test were carried out with atmosphere air, temperature 31 °C and humidity 55%. From 100N to 500N (in step of 100) load was applied on the seals during the experiment.

The lubricant flowed over sliding faces, and was controlled by a throttle vane. Each running period had a running-in cycle, which took 3600s. After this running-in, the load was varied. From the recorded seal face temperature, friction coefficient and friction torque they got diagram in function of friction coefficient an actual load. Figure 2 and Figure 3 shows the variation of frictional coefficient for the applied vegetable oils combined with boric acid powder.

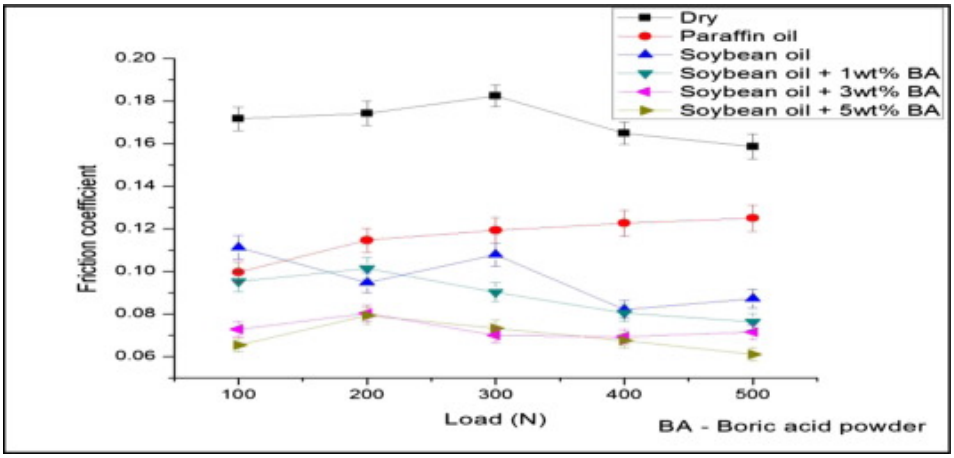

Figure 2. The frictional coefficients or pure and BA-soybean lubricants.

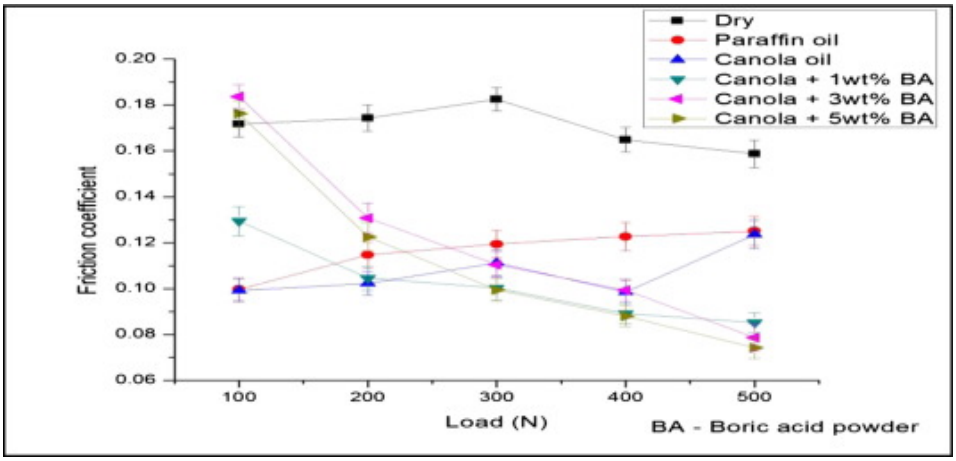

Figure 3. The Frictional coefficient of pure and BA-canola lubricants.

At the unlubricated condition, for dry running-in test, the start frictional coefficient was low. Later, in absence of lubricants, there were asperity interactions, between the two seal faces resulting wear, which increased the friction coefficient. On the other hand, two vegetable oils, canola and soybean had shown better frictional characteristics, as they were expected.

At the 100N load, the starting friction was high, because the soybean oil firm has not formed yet. It took about 200s, until the film formed. In stabile state the formed film's frictional coefficient was $\mu = 0.1113$, while for the canola oil, the formed oil film's frictional coefficient was $\mu = 0.099$. The soybean oil lubrication resulted a better and lower frictional values. For the initial 100N load, the vegetable lubricants mixed with boric acid powder showed better frictional performance, than the pure canola or soybean oils. The reason for this decrease in friction was that a hybrid tribofilm is formed from the lubricating vegetable oil and boric acid powder. Overall they made a conclusion, that boric acid powder can be used with vegetable oils eco-friendly, to reach lower frictional coefficient. Because the vegetable lubricant formed a thin tribofilm between the seal faces, it had shown a better frictional performance, compared to unlubricated condition. (SHANKAR S. et al. 2016)

Metal carbides are often used as wear materials in sliding contact applications, such as mechanical seal faces. They have excellent and high wear resistance, hardness and corrosion resistance. They are used in pump industry with different coatings such as SiC.

Conclusions

- From the above detailed investigations, the following conclusions can be drawn:
- Material selection for mechanical seals of pumps used in the agriculture has to be adequate for corrosion-, wear- and heat resistance. With these properties, the mechanical seal has to provide the control of the leakage.
- Most commonly used materials for seal faces are: Carbon, Silicon Carbide and Tungsten Carbide. The best solution for water transport duties is Silicon Carbide material selection. If the water is mixed with fertilizer, which can be alkane or acidic, then Silicon Carbide coated by Nickel is a possible solution.
- Tungsten Carbide can be used to transport any medium, but since this is the most expensive solution, engineers always go for proper material selection.
- Boric acid powder can be used with vegetable oils eco-friendly, to reach lower frictional coefficient under operation.

Acknowledgements

[1] HUEBNER M. Material selection for mechanical seals, 2005.
[2] MAYER, Ehrhard. Mechanical seals. Butterworth-Heinemann, 2013.

[3] JONES, G. A. On the tribological behaviour of mechanical seal face materials in dry line contact: Part I. Mechanical carbon. Wear, 2004, 256.3-4: 415-432.
[4] CARROLL, B., et al. Effect of humidity on the tribological properties of carbide-derived carbon (CDC) films on silicon carbide. Tribology Letters, 2003, 15.1: 51-55.
[5] HIRANI, H.; GOILKAR, S. S. Formation of transfer layer and its effect on friction and wear of carbon–graphite face seal under dry, water and steam environments. Wear, 2009, 266.11-12: 1141-1154.
[6] DÉPREZ, Pascal, et al. Friction and wear studies using taguchi method: application to the characterization of carbon-silicon carbide tribological couples of automotive water pump seals. Advances in Materials Science and Engineering, 2009, 2009.
[7] ZHAO, Xingyu, et al. Frictional performance of silicon carbide under different lubrication conditions. Friction, 2014, 2.1: 58-63.
[8] PIRSO, Jüri; LETUNOVITŠ, Sergei; VILJUS, Mart. Friction and wear behaviour of cemented carbides. Wear, 2004, 257.3-4: 257-265.
[9] SHANKAR, S., et al. Experimental study on frictional characteristics of tungsten carbide versus carbon as mechanical seals under dry and eco-friendly lubrications. International Journal of Refractory Metals and Hard Materials, 2016, 54: 39-45.

Titanium alloys application in 3D printing in the field of biocompatible materials

Varun VASHIST[1], Zoltán SZAKÁL[2], István OLDAL[2]
[1]Doctoral School of Mechanical Engineering,
Hungarian University of Agriculture and Life Sciences, MATE
[2]Institute of Technology, Hungarian University of Agriculture and Life Sciences, MATE

Abstract

In our review paper we discuss about titanium and its alloys which are used in biomedical applications, their suitability, properties that make titanium alloys fit for biomedical applications. This review paper classifies some important titanium alloys which are safe and fit to be used as implant devices. We have classified titanium alloys into different classes and have discussed their advantages. This review paper also focusses about the additive manufacturing techniques that are best suitable for fabrication and production of titanium alloys to be used as implant materials. Various parameters and angles have been discussed which affect the fabrication of titanium alloys during electron beam melting and selective laser melting.

Keywords

Titanium Alloys, Biomaterials, Additive manufacturing, Electron Beam Melting, Selective Laser Melting

1. Introduction

As the growing population of the aged people is increasing, the older and aged population demanding replaced failed tissue with artificial instruments is increasing. Metallic biomaterials have been identified to replace failed tissue / organ till now. Some of the important metal materials that have been use are stainless steels, cobalt alloys, titanium and its alloys. Titanium and its alloys are emerging as frontrunner bioimplant material due to their excellent properties such as high strength and excellent corrosion resistance. The difficult machining and exorbitant cost of material removal arising from conventional manufacturing process are the two main hindrances with regard to the potential applications of titanium alloys as implant devices. Additive manufacturing has evolved in past few years as of the best futuristic non-conventional manufacturing process. This technique is ideal for creation of customized devices, where intricate complex three-dimensional object could be produced. Additive manufacturing helps to develop parts without geometric constraints and, at a faster rate without any high economic cost factor.

2. Titanium and Its Alloys

Titanium and its alloys have higher specific strength which makes them perfect choice for biomedical applications. Titanium is considered to be biocompatible due to its low electrical conductivity which adds to electrochemical oxidation of titanium leading to the formation of a thin passive oxide layer. The oxide layer ultimately leads to higher resistance to corrosion [1]. In biomedical applications titanium and its alloys are used as implant materials and they substitute failed hard tissue. They find their application in a number of medical implant materials like hip joint, cardiac valve artificial knee joints, bone plates fracture fixation screw, artificial hearts, pacemakers. Many titanium alloys are mainly used these days, most prominent being Ti64Al4V. But his alloy has certain limitations in permanent implant applications where this alloy has a toxic effect due to vanadium and aluminum when they are released. So therefore, the research has progressed and researchers have now been focusing vanadium and aluminum free alloys for biomedical implant devices. Some of the new alloys include Ti6Al7Nb, Ti13Nb-13Zr, Ti12Mo-Zr. In many institutions and universities across the globe researches and experimentation have been done on titanium alloys in the past 50 years. Research has demonstrated that perfect biocompatibility of titanium is mainly due to its partnership with its oxides. Cp-Ti which is the commercially pure titanium is preferred as finest biocompatible metallic material due to its surface properties which causes rapid buildup of stable inert oxide layer [2]. Titanium and their alloys have been found out to be perfect replacement for stainless steel and Co-Cr alloy as both stainless steel and Co-Cr alloy are being used biomaterials in implant devices. Titanium alloys have low young modulus and this is the prime reason for their extensive application as biomaterials.

Due to their lower young modulus, they are perfect to display inhibiting bone resorption and increasing good remodeling as load transfers through both implants and bone when young's moduli of both materials is closely matched. [2-5]

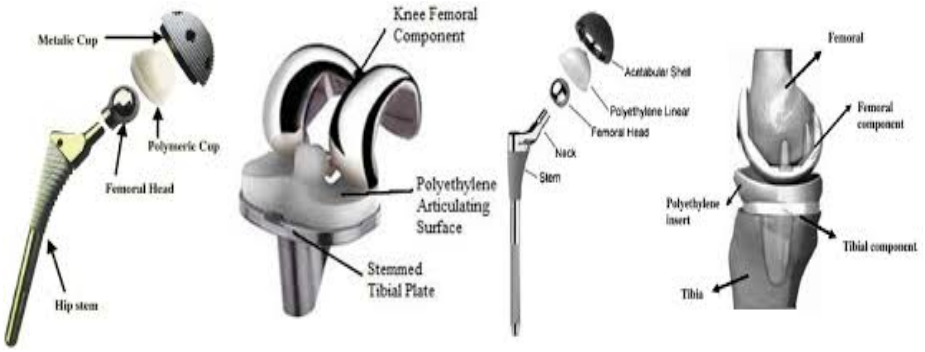

Figure1. Schematic diagrams displaying Titanium alloys biomedical implants

Lower density of titanium alloys is another reason for their preference over other biomaterials. 4.5g/cc is the density of titanium alloys which is nearly half that of the stainless steel and Co-Cr alloy (6). Titanium alloys are generally classified into α type, (α +β), β type alloys as per their primary constitution phases. The α type titanium alloys consist of single phase α – microstructures. The β type alloys have single phase β microstructures. The (α+β) type titanium alloys have double phase (α+β) microstructures. The α and β phases are hexagonal closely packed and body centered cubic structures and latter having lower atomic density. Among the three types α, (α+β) and β Ti alloys, the β alloys have the low young's modulus. The β – type Ti alloy have started gaining much importance and attention of the scientists to produce Ti alloys with a low young's modulus [7,8]. Also, despite portraying lower young's modulus β- type Ti alloys display good cold workability and higher strength [9,10,11,12,13]. The strength of β – type titanium alloys can be increased simultaneously having lower young's modulus by cold working after solution treatment as high ratio cold working is possible in β – type titanium alloys [14].

Low Modulus Titanium Alloys

The Ti alloys which have lower modulus for biomedical applications are β- type alloys which contains nontoxic elements. Low modulus β-type Ti alloy developed at first for the field of biomedical application was Ti-13Nb-13Zr [26]. The alloys Ti-12Mo-6Zr-2Fe (TMZF) [27], Ti-15Mo [28], Ti-16Nb-10Hf (Tiadyne 1610) [29], Ti-13Mo5Zr -3Al [30], Ti35.3Nb-5.1Ta-7.1Zr (TNTZ) [31], and Ti-29Nb-13Ta-4.6Zr (TNTZ) [32] were also developed early. And from now on mainly low modulus β- type Ti alloy are being developed and also have been nurtured in the past. For some while low modulus β- type Ti alloy consisting of cheaper elements like Fe, Cr, Mn, Sn Al are being favored to lower the consumption of costly elements like rare metals Nb, Ta, Mo, Zr. Some of the examples of these alloys include Ti-10Cr-Al [33], Ti-Mn [34], Ti-Mn-Fe [35], Ti-Mn-Al [36], Ti -Cr-Al [37], Ti-Sn-Cr [38], Ti-Cr-Sn -Zr [39], Ti (Cr, Mn)-Sn [40] and Ti-12Cr [41].

Improvement of Strength and Endurance Factors of Low Modulus β- Type Titanium Alloys.

In solutionised conditions the lowest young's modulii for β- type Ti alloy can be attained. For β- type Ti alloys strength and fatigue resistance like fatigue strength in solutionised condition is weak compared to that of (α+β) type Ti alloys for biomedical applications eg. Ti6Al-4VELI. So particularly, increase in strength and fatigue of β- type Ti alloys is important in biomedical areas of usage. Conventional severe cold working like severe cold rolling, severe cold swagging [42], special plastic deformation like equal channel angular processing [ECAP][43], accumulative roll bonding [ARB][44] and high-pressure torsion

[HPT] are very useful in in improving strength of β – type Ti alloys and at the same time keeping a lower young's modulus. For TNTZ, its tensile strength increases with increasing cold working for cold swagging. For TNTZ, tensile strength increases with increasing rotation number during HPT. After Hpt there is a gradual increase in strength of TNTZ because of increase in density of dislocation and refinement of microstructure. While Fatigue strength / dynamic strength of TNTZ when exposed to severe cold rolling has been found out to not be impacted and improved when compared to that TNTZ subjected to solution treatment while tensile strength is significantly improved [45]. Hence forth fatigue strength of β- type Ti alloy is not improved by conventional severe cold working or severe plastic deformation. With the help of aging treatment static and dynamic strengths can be improved significantly [46]. Aging treatment takes into account secondary phases such as α and ω phases within β matrix of β type Ti alloys, thereby resulting in precipitation hardening. Also, young's modulus value increases to a value similar to that of Ti6Al-4VELI [47]. When aging treatment is controlled, it helps young's modulus to be kept below 80 GPa, which nears to the highest value among β – type Ti alloy but it is still lower than that of (α+β) type Ti alloys with an increase in static and dynamic strength. By introducing small number of secondary particles like the ceramic particles such as Tib dynamic strength can be increased.[48]

Alloy Elements in Titanium Alloys in The Field of Biomedical Implant Devices
The research and development of alloys of titanium in biocompatible materials has started very recently. The elements which are observed to be non-toxic and non -allergic with the help of reported data of cell viability of pure metals [49], polarization of resistance and tissue compatibility of pure metals, representative metallic biomaterials [50] and allergic properties of pure metals [51] are chosen as alloying elements for titanium. Nb, Ta, and Zr are chosen safe alloying elements to titanium, also Mo, Sn are considered as safer elements for living body. So, the titanium alloys which are considered suitable biomaterials are:

- Ti-Zr system, (b) Ti-Mo system (c) Ti-Ta system (d) Ti-Ta-Zr system (e) Ti-Nb-Hf system
- Ti-Nb-Zr system (g) Ti-Nb-Sn system (h) Ti-Nb-Ta-Zr system (i) Ti-Fe-Ta system (j) Ti-Mo-Zr-Sn system (k) Ti-Sn-Nb-Ta system (l) Ti-Mo-Zr-Fe system (m) Ti-Mo-No-Si system (n)Ti-Mo-Ga system (o) Ti-Mo-Ge system (p) Ti-Mo-Al systems [52-57]

3. Three-Dimensional Printing of Titanium Alloys

Titanium production is disturbed by high cost in conventional manufacturing process and bad workability for complex shape productions.[15]. The non-conventional production process such as the 3D printing or rapid prototyping or additive layer manufacturing is the technique which provides better design flexibility and good economical options for producing products that have

complex geometries with a high precision of size [16]. The 3D printing or layer manufacturing possesses a hub of technologies that have emerged in the last decade. In 3D printing material is added one cross section layer at a time to produce the part. [17]. All 3D printing techniques first starts from the formation of a 3-dimensional computer aided design model which may be formed in a cad system. The 3D cad model is converted into standard STL file format. Cad file model which constitutes the geometry of the part is formed and once it's optimised CAD file is then sliced numerically into the layer thickness machine will build in. When it is transferred to 3D printing machine software and loaded to 3D printing machine thereby leading to a file-based build to begin. Material layers are laid down successively with each layer corresponding to different shape [18]. There are various processes of additive fabrications in use in the 3D printing manufacturing such as the liquid based processes, powder-based processes, solid based processes. Various rapid prototyping technologies are being used till date such as Stereolithography (SLA), Fused Deposition Modelling (FDM), Selective Laser Sintering, Digital Light Processing, Electron Beam Melting, Selective laser melting. In our review paper we are concerned about reviewing electron beam melting, selective laser melting which are the foremost and best technologies to produce and fabricate Titanium and its alloys.

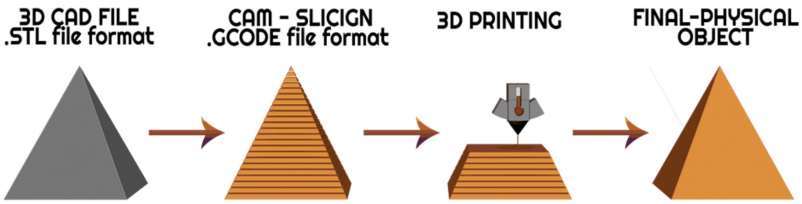

Figure2. Showing process of 3D printing from design to printing

Electron beam melting

For fabrication of metallic biomaterials this additive manufacturing technique is mainly preferred. It creates components by melting the metal powder layer by layer through the help of a magnetically directed electron beam upto 3KW in a high vacuum atmosphere. [19]. And this is the potential reason that is best preferred titanium and its alloys implants. To optimise the surface finish of final part is one of the main challenges of using EBM for production of surgical implants and it is linked mainly with EBM processing parameters such as beam current, part orientation and powder particle size. It is a well-known and accepted fact that surface topology of biomedical implant affects the biocompatibility as it affects the cell attachment proliferation and differentiation. The quality and usage of biomedical implants and their biocompatibility is highly dependent on initial interaction between surfaces of implants and

biological environment [20].

The EBM consists of various process parameters such as:

- Beam Power
- Beam Scanning Velocity
- Beam Focus
- Beam Diameter
- Beam Line Spacing
- Plate temperature
- Pre Heat Temperature
- Contour strategies
- Scan Strategies

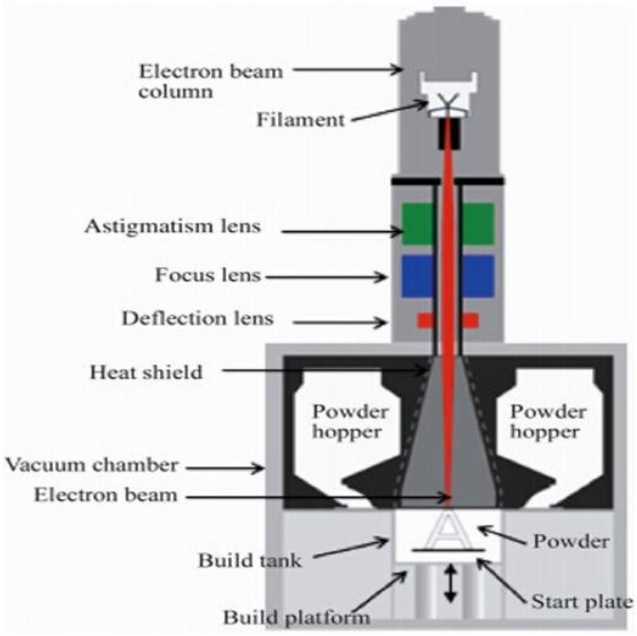

Figure 3. Schematic Diagram showing Electron Beam Melting Process

The perfect use of process parameters is more tricky than Selective Laser Melting process. So only fewer materials are used for EBM process such as the Ti grade 2, Ti6Al4V, Inconel 718, CoCrMo [21]. The EBM is a slow process and cost of part is very high. Electron beam melting takes place in a vacuum atmosphere unlike inert atmosphere during the Selective Laser Melting process. Therefore, oxidation of part is usually avoided. Also, any adsorbed gases along the surface of powder particles does not causes creation of porosity in the EBM process. So, it is best to avoid process alloys that have volatile constituents such as Zn, Mg, Pb, Bi etc. Brittle materials can also be processed by EBM which cannot be processed by in SLM. Brittle materials such as intermetallic have poor

thermal expansion and contraction behaviours. Upon cooling of these materials at a faster rate from their melting points/ solidifying range they may solidify quickly and also at the same time they are unable to accommodate the internal stresses as a result of solidification process thereby leading to crack formation also referred to as solidification cracks. On the other hand, Selective Laser Melting process has high cooling rates, so brittle materials display formation of solidification of cracks. Whereas in EBM process, cooling rate can be decreased rapidly by increasing temperature of powder bed.

Selective Laser Melting

This is also one of the powder bed fusion based additive manufacturing process used to produce metallic parts. [22,23]. SLM process employs a fibre of laser heat source. SLM usually contain four important process parameters which are:

- Laser power
- Scan Speed
- Hatch spacing
- Layer thickness

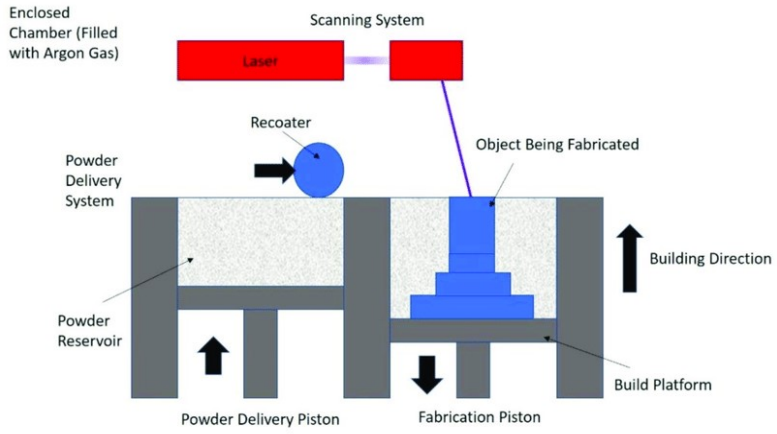

Figure 4. Schematic diagram showing Selective laser melting Process

Usually, this process uses high scanning speeds and high thermal gradients which lead to higher cooling rates. Higher cooling rate leads to non-equilibrium microstructure, thereby needing heat treatment for some specific applications. Build chamber in SLM process is regularly flushed with inert gas to decrease the oxygen. Usually, layer thickness lies in the range of 20-100µm. This technique can be used for processing of standard materials such as Ti6Al4V, 316L, 17-4PH, 15-PH, hot work steels, cobalt based and nickel-based alloys. [24]. Selective laser melting offers range of advantages such as:

- It offers wide material range
- It is capable to tune properties during part processing

- Increased functionality
- Cost reduction and ability to produce near net shaped components which are ready to use.

Selective Laser Melting also has certain disadvantages:

- Slower speed due to process speed limitations.
- Acute size restrictions
- High Power usage
- Initial Costs are very high.
- To make best use of process parameters is time consuming.
- Powder handling is somehow complex and parts produced might have rough surfaces.[25]

Conclusion

Titanium alloys have emerged as frontrunner in biomedical implants owing to their higher specific strength and higher biocompatibility when compared to other materials. New titanium alloys have currently evolved in biomaterial field such Ti6Al17Nb, Ti13Nb-13Zr. Lower young modulus and lower density of titanium alloys are among the prime reasons for extensive applications of Ti alloy in biomedical field. β type titanium alloys exhibit lower young's modulus, good cold workability, higher strength and they are much in focus of the researchers and scientists to produce Ti alloys implant devices. Aging treatment is best suited to increase the dynamic and fatigue strength of the β type Ti alloys and also it helps to keep young's modulus at a lower level below 80 Gpa. Also, furthermore additive manufacturing processes are the best suited for fabrication and production of Ti alloys for implant devices due to better design flexibility and economic factors. Electron beam melting and Selective laser melting are the two techniques of 3D printing for fabrication of Ti alloys. But it can also be concluded from the above study that selective laser melting is the best process to be used for production of Ti alloys in biomedical devices due to their wide material range and cost reduction factors.

References

[1] "Biocompatibility of Advanced Manufactured Titanium Implants-A Review", Alfred T. Sidambe, Materials 2014, 7, 8168-8188; doi:10.3390/ ma7128168

[2] Elias, C.N.; Lima, J.H.C.; Valiev, R.; Meyers, M.A. Biomedical applications of titanium and its alloys. *JOM* **2008**, *60*, 46–49.

[3] Niinomi M, Hattori T, Morikawa K et al (2002) Development of low rigidity β-type titanium alloy for biomedical applications. Mater Trans 43(12):2970–2977

[4] Sumitomo N, Noritake K, Hattori T et al (2008) Experiment study on fracture fixation with low rigidity titanium alloy – plate fixation of tibia

fracture model in rabbit. J Mater Sci Mater Med 19:1581–1586
[5] Niinomi M, Nakai M, Hieda J (2012) Development of new metallic alloys for biomedical applications. Acta Biomater 8:3888–3903
[6] Park JB, Lakes RS (1992) In: Biomaterials: an introduction. Plenum Press, New York
[7] Niinomi M (2013) Titanium alloys with high biological and mechanical biocompatibility. J Jpn Soc Bone Morphometry 23(1): S59
[8] Nakai M, Niinomi M, Zhao XF et al (2011) Self-adjustment of Young's modulus in biomedical titanium alloys during orthopaedic operation. Mater Lett 65:688–690
[9] M. Niinomi, Cyto-toxicity and fatigue performance of low rigidity titanium alloy, Ti–29Nb–13Ta–4.6Zr, for biomedical applications, Biomaterials 24 (2003) 2673–2683.
[10] K.K. Wang, L.J. Gustavson, J.H. Dumbleton, Microstructure and properties of a new beta titanium alloy, Ti–12Mo–6Zr–2Fe, developed for surgical implants, in: S.A. Brown, J.E. Lemons (Eds.), Medical Applications of Titanium and Its Alloy, ASTM STP 1272, 1996, pp. 76–87
[11] A.K. Mishra, J.A. Davidson, R.A. Poggie, P. Kovacs, T.J. FitzGerald, Mechanical and tribological properties and biocompatibility of diffusion hardened Ti–13Nb–13Zr—a new titanium alloy for surgical implants, in: S.A. Brown, J.E. Lemons (Eds.), Medical Applications of Titanium and Its Alloy, ASTM STP 1272, 1996, pp. 96–113.
[12] D. Kuroda, M. Niinomi, H. Fukui, A. Suzuki, J. Hasegawa, Heat treatment processes and mechanical properties of new b-type biomedical Ti–29Nb–13Ta–4.6Zr alloy, Tetsu-to-Hagane 86 (2000) 610–616.
[13] Y.L. Hao, M. Niinomi, D. Kuroda, K. Fukunaga, Y.L. Zhou, R. Yang, A. Suzuki, Aging response of the Young's modulus and mechanical properties of Ti–29Nb–13Ta–4.6Zr for biomedical applications, Met. Mater. Trans. A 34A (2003) 1007–1012.
[14] M. Niinomi, T. Hattori, K. Morikawa, T. Kasuga, A. Suzuki, H. Fukui, S. Niwa, Development of low rigidity b-type titanium M. Niinomi / Science and Technology of Advanced Materials 4 (2003) 445–454 453 alloy for biomedical applications, Mater. Trans. 43 (2002) 2970–2977.
[15] Froes, F.H. Titanium powder metallurgy: A review—Part 1. *Adv. Mater. Process.* **2012**, *170*, 16–22.
[16] Van Noort, R. The future of dental devices is digital. *Dent. Mater.* **2012**, *28*, 3–12.
[17] Ivanova, O.; Williams, C.; Campbell, T. Additive manufacturing (AM) and nanotechnology: Promises and challenges. *Rapid Prototype. J.* **2013**, *19*, 353–364.
[18] Al-Bermani, S.S.; Blackmore, M.L.; Zhang, W.; Todd, I. The origin of microstructural diversity, texture, and mechanical properties in electron beam melted Ti-6Al-4V. *Metall. Mater. Trans. A* **2010**, *41A*, 3422–3434
[19] Ponader, S.; Vairaktaris, E.; Heinl, P.; Wilmowsky, C.V.; Rottmair, A.; Körner, C.; Singer, R.F.; Holst, S.; Schlegel, K.A.; Neukam, F.W.; *et*

al. Effects of topographical surface modifications of electron beam melted Ti-6Al-4V titanium on human fetal osteoblasts. *J. Biomed. Mater. Res. A* **2008**, *84A*, 1111–1119.

[20] ARCAM Electron Beam Melting of Metals. Available online: http://www.arcam.com/technology/electron-beam-melting/materials/ (accessed on 19 January2021).

. [21] F. Abe, K. Osakada, M. Shiomi, K. Uematsu, and M. Matsumoto, The Manufacturing of Hard Tools from Metallic Powders by Selective Laser Melting, J. Mater. Process. Technol., 2001, 111, p 210–213

[22] S.M. Gaytan, L.E. Murr, E. Martinez, J.L. Martinez, B.I. Machado, D.A. Ramirez, F. Medina, S. Collins, and R.B. Wicker, Comparison of Microstructures and Mechanical Properties for Solid and Mesh Cobalt Base Alloy Prototypes Fabricated by Electron Beam Melting, Metall. Mater. Trans. A, 2010, 41A, p 3216–3227.

[23] E. Brinksmeier, G. Levy, D. Meyer, and A.B. Spierings, Surface Integrity of Selective-Laser-Melted Components, CIRP Ann. Manuf. Technol., 2010, 59(1), p 601–606

[24] Prashanth, K.G.; Scudino, S.; Eckert, J. Defining the tensile properties of Al-12Si parts produced by selective laser melting. *Acta Mater.* **2017**, *126*, 25–35.

[25] Mishra AK, Davidson JA, Poggie RA, Kovacs P, Fitzgerald TJ. Mechanical and tribological properties and biocompatibility of diffusion hardened Ti–13Nb–13Zr – a new titanium alloy for surgical implants. In: Brown SA, Lemons JE, editors. Medical applications of titanium and its alloys, ASTM STP 1272. West Conshohocken, PA: ASTM International; 1996. p. 96–116.

[26] Wang KK, Gustavson LJ, Dumbleton JH. Microstructure and properties of a new beta titanium alloy, Ti–12Mo–6Zr–2Fe, developed for surgical implants. In: Brown SA, Lemons JE, editors. Medical applications of titanium and its alloys, ASTM STP 1272. West Conshohocken, PA: ASTM International; 1996. p. 76–87

[27] Wang K. The use of titanium for medical applications in the USA. Mater Sci A1996; 213:134–7.

[28] Steinmann SG, Mausli PA, Szmukler-Moncler S, Semlitsch M, PohlerHintermann HE, Perren SM. Beta-titanium alloy for surgical implants. In: Froes FH, Caplan I, editors. Titanium ’92, science and technology. Warrendale, PA: TMS; 1993. p. 2689–96

[29] Ahmed T, Long M, Silvestri J, Ruiz C, Rack HJ. A new low modulus, biocompatible titanium alloy. In: Blenkinsop PA, Evans WJ, Flower HM, editors. Titanium ’95, science and technology, vol. II. London: Institute of Metals; 1996. p. 1760–7

[30] Kuroda D, Kawasaki H, Hiromoto S, Hanawa T. Development of new Ti–Fe–Ta and Ti–Fe–Ta–Zr system alloys for biomedical applications. Mater Sci Eng C2005; 25:312–20.

[31] Hatanaka S, Ueda M, Ikeda M, Niinomi M. Isothermal aging behavior in Ti–10Cr–Al alloys for medical applications. Adv Mater Res 2010;89–91:232–7.

[32] Ikeda M, Ueda M, Kinoshita T, Ogawa M, Niinomi M. Influence of Fe content of Ti–Mn–Fe alloys on phase constitution and heat treatment behaviour. Mater Sci Forum 2012;706–709:1893–8
[33] Ikeda M, Ueda M, Matsunaga R, Niinomi M. Phase constitution and heat treatment behaviour of Ti–7 mass% MN–Al alloys. Mater Sci Forum 2010;654–656:855–8.
[34] Ikeda M, Sugano D. The effect of aluminium content on phase constitution and heat treatment behaviour of Ti–Cr–Al alloys for healthcare applications. Mater Sci Eng C 2005; 25:377–81
[35] Ashida S, Kyogaku H, Hosoda H. Fabrication of Ti–Sn–Cr shape memory alloy by PM and its properties. Mater Sci Forum 2012;706–709:1943–7.
[36] Murayama Y, Sasaki S. Mechanical properties of Ti-Cr-Sn-Zr alloys. Bull Niigata Inst Tech 2009; 14:1–8.
[37] Kasano Y, Inamura T, Kanetaka H, Miyazaki S, Hosoda H. Phase constitution and mechanical properties of Ti–(Cr, Mn)–Sn biomedical alloys. Mater Sci Forum 2010;654–656:2118–21.
[38] Nakai M, Niinomi M, Zhao XF, Zhao XL. Self-adjustment of Young's modulus in biomedical titanium alloy during orthopaedic operation. Mater Lett2011; 65:688–90.
[39] Niinomi M, Fukui H, Hattori T, Kyo K, Suzuki A. Development of high biocompatible titanium alloy. Mater Jpn 2002; 3:221–3.
[40] Valiev RZ, Islamgaliev R, Alexandrov IV. Bulk nanostructured materials from severe plastic deformation. Prog Mater Sci 2000; 45:103–89
[41] Saito Y, Utsunomiya H, Tsuji N, Sakai T. Novel ultra-high straining process for bulk materials development of the accumulative roll-bonding (ARB) process. Acta Mater 1999; 47:579–83.
[42] Zhilyaev AP, Langdon TG. Using high-pressure torsion for metal processing: fundamentals and applications. Prog Mater Sci 2008; 53:893–979.
[43] Niinomi M. Titanium alloys for inhibiting bone atrophy. In: Pignatello R, editor. Biomaterials science and engineering. Shanghai, China: Intech; 2011.p. 249–68
[44] Niiinomi M. Fatigue performance and cyto-toxicity of low rigidity titanium alloy, Ti–29Nb–13Ta–4.6Zr. Biomaterials 2003; 24:2673–83
[45] Hao YL, Niinomi M, Kuroda D, Fukunaga K, Zhou YL, Yang R, et al. Aging response of Young's modulus and mechanical properties of Ti–29Nb–13Ta–4.6Zr for biomedical applications. Metall Mater Trans A 2003; 34:1007–12
[46] Song X, Niinomi M, Nakai M, Tsutsumi H, Wang L. Improvement in fatigue strength while keeping low Young's modulus of ab-type titanium alloy through yttrium oxide dispersion. Mater Sci Eng C 2012; 32:542–9.
[47] H. Kawahara, S. Ochi, K. Tanetani, K. Kato, M. Isogai, Y. Mizuno, H. Yamamoto, A. Yamaguchi, Biological test of dental materials. Effect of pure metals upon the mouse subcutaneous fibroblast. Starin L cell in tissue culture, J. Jpn. Soc. Dent. Apparat. Mater. 4 (1963) 65–75

[48] S.G. Steinemann, Corrosion of surgical implants—in vivo and in vitro tests, in: G.D. Winter, J.L. Leray, K. de Groot (Eds.), Evaluation of Biomaterials, John & Sons, Bristol, 1980, pp. 1–34.
[49] P.J. Uggowitzer, W.-F. Ba¨hr, M.O. Speidel, Metal injection molding of nickel-free stainless steels, Adv. Powder Metall. Part. Mater. 3 (1997) 18.113–18.121.
[50] M. Niinomi, Recent research and development on titanium for biomedical applications in Japan, JOM 51 (1999) 32–34.
[51] K. Nitta, S. Watanabe, N. Masahashi, H. Hosoda, S. Hanawa, Ni-free Ti–Nb–Sn shape memory alloys, in: M. Niinomi, T. Okabe, E.M. Taleff, D.R. Lesuer, H.F. Lippard (Eds.), Structural Biomaterials for the 21st Century, TMS, 2001, pp. 25–34
[52] Y. Daimatsu, A. Yamamoto, H. Hosoda, S. Miyazaki, Shape memory characteristics of Ti–Mo–Ga for biomedical applications, Proc. Fall Meet. Jpn Inst. Met., 2001, p. 401.
[53] H. Hosoda, A. Yamamoto, S. Miyazaki, Mechanical properties of Ti– Mo–Ge shape memory alloy for biomedical applications, Proc. Fall Meet. Jpn Inst. Met., 2001, p. 401
[54] H. Hiromoto, F. Mizuno, T. Hanawa, C. Kuroda, H. Hosoda, K. Wakashima, S. Miyazaki, Polarization behavior of Ti–Mo–Al shape memory alloy in simulated body liquid, Proc. Annu. Meet. Jpn Inst. Met., 2002, p. 443.
[55] M. Ikeda, Y. Nakamura, N. Takahama, Effect of Zr contents on heat treatment behaviours and phase constitution of Ti-50 mass% Ta–Zr alloy, Proc. Annu. Meet. JIM, 2003, p. 130.
[56] T. Maeshima, T. Eto, H. Uchiyama, K. Uchiyama, M. Nishida, Development of Ti–Sc–Mo shape memory alloy, Annu. Meet. JIM, 2003, p. 134
[57] M. Niinomi, Recent research and development on titanium for biomedical applications in Japan, JOM 51 (1999) 32–34.

Flame retardancy testing of polymers: a review

Pál KUN[1], Gábor KALÁCSKA[2]
[1]Department of Chemistry, Institute of Mathematics and Natural Sciences,
Hungarian University of Agricultural and Life Sciences, MATE
[2]Institute of Technology, Hungarian University of Agriculture and Life Sciences (MATE)

Abstract

One of the challenges facing companies manufacturing and processing plastics is to ensure that their products meet increasingly stringent fire, environmental and health and safety requirements while maintaining the functional properties guaranteed in different industries. This article analyses the flame retardancy of polymers in the light of additives, test methods and standards, and results.

Keywords

polymer; polyamide; polylactic acid; flame retardancy; montmorillonite; carbon nanotubes; UL-94; flame retardant additives; thermal expansion; ignition time; halogen-free; graphite; phosphorus compounds; E/E industry;

1. Introduction

Plastics are organic compounds. They contain carbon and hydrogen atoms, which burn well. Polyamides also contain oxygen atoms, which further increase their combustibility.

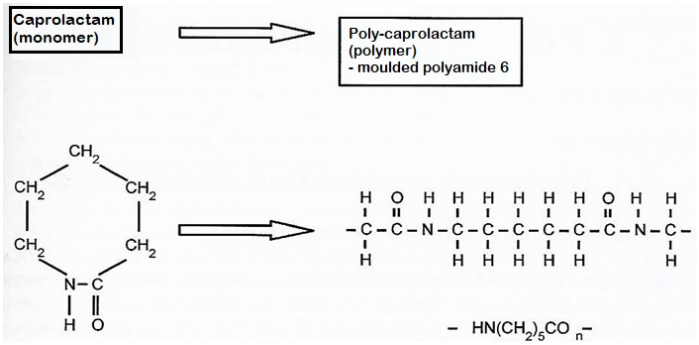

2. Figure. Polyamide 6 polymerization during casting (2)

Increasing the flame resistance of plastics is an essential goal from the outset, because it reduces the extent of the damage that occurs, even by slowing the

spread of fire. In the past, many types of halogenated additives were used in flame retardants. In line with changes in social conditions, there has been a growing aversion to halogen additives (mainly because of the health risks), which has put products containing them at a competitive disadvantage.

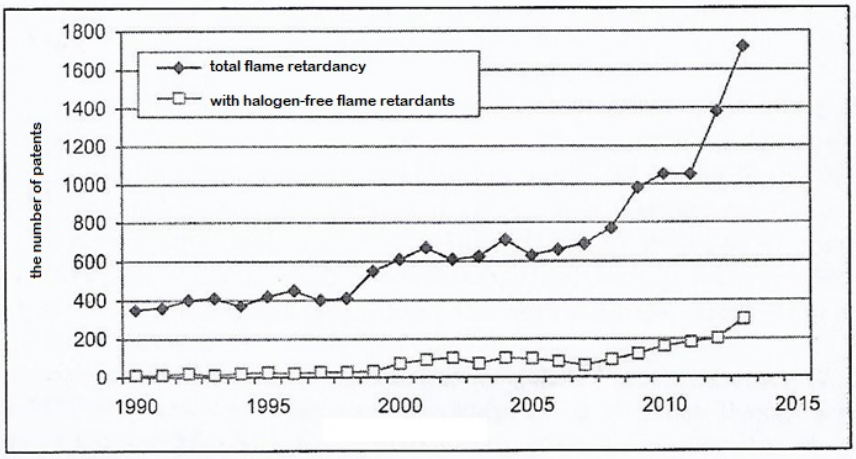

3. Figure. Patent claims filed and patents granted for reduced flammability plastics 1990-2013

The effect of flame retardant additives depends on the duration and intensity of the ignition effect. It is expected that they do not react with the raw material during processing, they must not be toxic and their products must not be dangerous. The following additives are used to improve flame resistance (Pál 2006): *chromium compounds, bromine compounds, crystal water containing materials, phosphorus compounds, aluminium hydroxide, magnesium hydroxide, coke-forming defoamers.*

Halogen compounds bind free radicals produced during combustion, thus slowing or extinguishing combustion. The mechanism of action of aluminium or magnesium hydroxide is based on the fact that they release water at the temperature of combustion, which is an endothermic reaction, i.e. they reduce the energy of the environment. A further energy reduction is caused by the evaporation of the water produced.

One of the new materials for combustion inhibition is montmorillonite (Pál 2006, Hao 2006). Montmorillonite is a clay aggregate that is modified by increasing the distance between the clay layers to the point where the polymer can penetrate between the layers.

Phosphorus is the most common flame retardant additive in polyamides. Phosphorus compounds promote decomposition and cause charring. They prevent the oxygen content of the air from coming into contact with the combustible parts of the material. They also have the effect of promoting the formation of water and non-combustible gases.

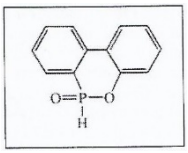

4. Figure. One phosphorous-containing flame retardant,
DOPO (9,10-dihydro-9-oxa-10-phospho-phenanthrene-10-oxide),
has the formula (7)

A composite made from carbon nanotubes can also have variable combustibility properties. The thermal conductivity of carbon nanotubes can be as high as 6600 [W/mK], the highest of any currently known material (Du 2007). The magnitude of the thermal conductivity is significantly affected, usually reduced, by the associated materials in addition to the carbon content, which explains why the thermal conductivity of the composite is significantly lower than that which would result from the thermal conductivity of carbon nanotubes (Du 2007). Kashiwagi (2002) mixed multi-walled carbon nanotubes into a polypropylene (PP) base matrix and found that they significantly reduced thermal expansion and were at least as effective as montmorillonite.

2. Burn test according to UL-94

The test system has two measurement arrangements. For the measurements rectangular test specimens (120±0.5; 10±0.2; 4±0.2) are used. In the first test arrangement, the test specimens are held horizontally and two marks are made on one surface at 25 [mm] and 105 [mm].

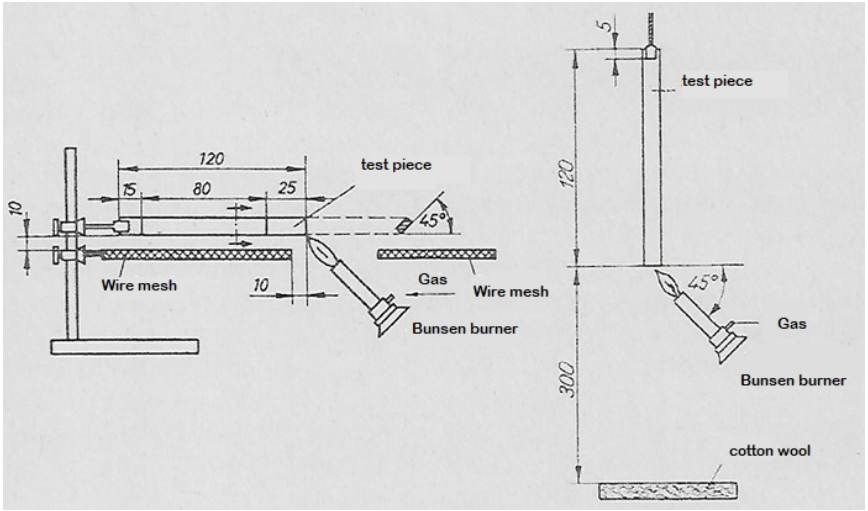

5. Figure. UL-94 horizontal and vertical measurement layout (1)

Ignition is carried out with the Bunsen burner set at 25 [mm] for 30 [s]. Measure the time between the two marks for the plastic to burn. If all five test pieces burn all the way through, the flame spread rate is calculated from the equation $v = 80 \times t^{-1}$ [mm/min] and the test piece is rated HB.

If any of the test pieces do not burn out, the remaining 5 test pieces shall be tested in the vertical type. The test piece is then burned for only 10 [s], which can be repeated if necessary. Based on the burn time, specimen dripping and glowing, the plastics can be classified as V-2, V-1 and best V-0 - if they do not meet these criteria, they are also classified as HB.

The UL-94 standard distinguishes four types of combustion categories. For V-0 and V-1, materials have very limited combustion and do not ignite their surroundings. For a V-2 rating, the test specimen will not burn in a horizontal arrangement. Also in a vertical arrangement, burning is limited, but dripping is allowed. HB - worst burn rating - is given to a plastic that burns continuously in the horizontal orientation or extinguishes, but has no limited burning in the vertical orientation. (1)

3. Results

Mátyás Andó (2010) (1) in his Ph.D. thesis divided the HB group into two parts. He indicated with HB-A if the specimens burned out in the horizontal arrangement and with HB-B if the specimens burned out during the tests but did not yet meet the V-2 conditions. In his tests, he found that the combustion properties deteriorated with increasing montmorillonite content. At 1 and 3% montmorillonite content, horizontal specimens burn through at a rate of about 16 [mm/min]. At a montmorillonite content of 6%, the combustion process changes significantly. The combustion products drip less frequently and therefore burn with a much higher flame. The combustion rate is reduced compared to lower additions because the molten plastic does not drip off and covers the base material. The combination of less frequent dripping and higher flame results in much larger droplets being separated from the test piece, so the dripped portion burns longer. The altered combustion properties can be explained by the fact that montmorillonite's good thermal conductivity means that heat is not only transferred to the air, but also more efficiently to the parts that are not yet burning. The polyamides drip during combustion, i.e. a significant amount of energy is released from the system with the dripped part, which does not contribute to further higher combustion intensities. The dripping also causes montmorillonite to leave the system, so that the intensity can only be limited by the dripped part, which is no longer taken into account in the UL test. Therefore, the main effect of the additive in the tests is to preheat and accelerate the combustion process. At a montmorillonite content of 6%, the viscosity of the plastic droplet increases, so that the burning plastic droplet can only drip off the test piece later, but then a much larger droplet is removed.

Montmorillonite content [%]	Group signal	Comment
0	HB-B	drip as 2 [s]
0,5	HB-B	drip as 2 [s]
1	HB-A	drip as 2 [s], 16,4 [mm/min]
3	HB-A	drip as 2 [s], 16 [mm/min]
6	HB-A	Drip less often, 14,8 [mm/min]

6. Figure. Combustion characteristics of samples containing montmorillonite (1)

The faster combustion observed in the montmorillonite samples does not contradict the findings of the heat release tests, but it does contradict the conclusions drawn from them. On this basis, the combustion inhibition of polyamide 6 (PA6) is impaired by montmorillonite, i.e. its use is not recommended to improve the combustion properties of this base material.

Andrea Toldy 2010 (5): She and her colleagues reviewed the commercially available phosphorus additive and reactive flame retardants, their fields of application and compared them with a reactive phosphorus flame retardant (TEDAP), which also acts as a crosslinking component in epoxy resins. The aim was to develop a flame retardant carbon fiber reinforced epoxy resin composite that meets both mechanical and flammability requirements. The flame retardancy is favourably affected when phosphorus containing degradation products are present in both the gas phase and the solid phase. They have succeeded in achieving a decisive reduction in the heat emission of the samples produced during combustion and have achieved a self-extinguishing V-0 grade. Although combustion inhibition generally deteriorated the mechanical properties of the epoxy resins, the design of coated composites was able to maintain the load-bearing capacity of the composite at a level close to the reference.

Sample name	UL-94 (classification)	UL-94 (classification)
TPS Ref	HB	HB
TPS Flax	HB	HB
TPS-Flax-ADHF	HB	HB
TPS-GF	V-1	V-1
TPS-GF-Flax	HB	HB
TPS-GF-Flax-ADHF	V-0	V-0

7. Figure. UL-94 flammability test results for flame retardant biocomposites

Lujza Szabó and colleagues (2013) (4) investigated the flame retardancy potential of a fully degradable starch-based natural fibre-reinforced biocomposite. In order to reduce the combustibility of the thermoplastic starch (TPS) matrix material, phosphorus containing polyol was used to soften the starch. The flame retarded starch matrix was reinforced with cut flax fibres. In

order to increase the flame resistance of the reinforcing fibres, a thermotex surface treatment with a phosphorus containing compound (ammonium dihydrogen phosphate) was applied. The biodegradable composite obtained showed significant improvements in both mechanical and flammability properties. It has been classified V-0 (self-extinguishing) according to UL-94 flammability standard, its LOI has been increased to 34 and the heat emitted during combustion has been halved.

Sample name	LOI
TPS Ref	22
TPS Flax	22
TPS-Flax-ADHF	29
TPS-GF	34
TPS-GF-Flax	30
TPS-GF-Flax-ADHF	32

8. Figure. Oxygen index measurement results for combustion inhibited biocomposites

Sample name	Combustion residues (%)
TPS Ref	4
TPS Flax	8
TPS-Flax-ADHF	22
TPS-GF	20
TPS-GF-Flax	22
TPS-GF-Flax-ADHF	26

9. Figure. Comparison of the amount (%) of combustion residues obtained after the Cone Calorimeter test

Katalin Bordácsné Bocz (2016) (3) investigated the flame retardancy potential of multilayer self-reinforced composites made of polypropylene and recycled polyolefins, and self-reinforced composites produced by injection moulding. In all cases, a foaming flame retardant additive system based on ammonium polyphosphate (APP) was used in the matrix material of the composites to reduce the flammability of the composites, which are entirely made of polypropylene (PP).

In multilayer self-reinforced composites, a specific synergistic flame retardant effect was observed as a result of the physical interaction between APP-based flame retardant and highly oriented PP fabrics.

It was found that the significant shrinkage of highly oriented PP fibers upon heating plays a key role in the self-extinguishing behaviour of self-reinforced PP composites with surprisingly low flame retardant content (only 9%). In both the horizontal and vertical tests, the elongation of the melted specimens due to shrinkage and thus the formation of new polymer surfaces was clearly observed. More dense carbon surfaces are formed, which effectively act as a barrier to heat and mass transfer, resulting in immediate extinction of the flame.

For injection moulded self-reinforced polypropylene composites, the synergism demonstrated between the continuous oriented fibers and the foaming flame retardant additive system in short fiber reinforced sheets was only moderate. It is concluded that the length, orientation and structure of the reinforcing fibers are key parameters for the combustibility properties of self-reinforced flame retarded composites.

The flame retardancy of thermoplastic starch (TPS) composites reinforced with natural fibres was also investigated. The combination of flame-retardant plasticizer and flame-retardant natural fibers has been shown to be a promising option for the production of flame-retardant biodegradable TPS composites and was further investigated in polytartaric acid (PLA)-based composites.

Polylactic acid (PLA) is one of the most intensively researched biodegradable polyesters. New phosphorus containing multifunctional additives for the flame retardancy of natural fibre reinforced PLA/TPS biocomposites have been prepared. To produce flame retarded TPS, a phosphorus containing polyol, glycerol phosphate (GP), was used to plasticize the starch. The modified starch had an increased charring effect in PLA, resulting in PLA/TPS blends with reduced flammability. A new reactive surface treatment agent (PSil) was prepared to exploit the phosphosilicon synergism in the treatment of flax fibres.

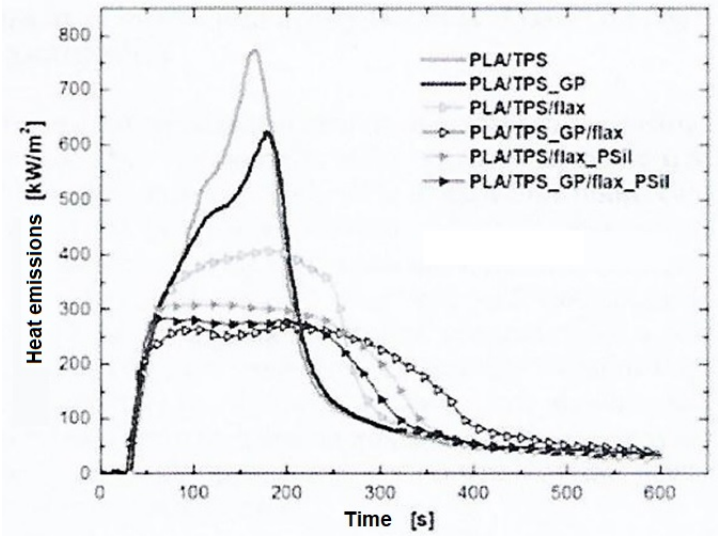

10. Figure. Heat release curves of PLA/TPS based composites (3)

The oxygen index of both PLA/TPS and PLA/TPS-GP blends decreased when associated with untreated flax fibres. The adverse wicking characteristic of fibrous materials was completely eliminated when the fibres were surface treated with the synthesised phosphosilane. In the case of the bio-fibres, a high degree of charring was achieved (47% char residue at 500 [°C] in TGA) without a significant reduction in the thermal stability of the cellulosic fibres. When the flame retardant plasticizer was combined with PSil-treated flax fibres, a 30% reduction in the maximum heat release was achieved compared to the reference biocomposite.

The 0.65% phosphorus content of the plasticizer and the fiber treatment agent proved to be insufficient to obtain self-extinguishing composites. However, when applied, only 10% APP was sufficient to achieve the V-0 category and an oxygen index of 33 v/v%.

Beáta Szolnoki (2018) (6) Investigated the environmentally friendly flame retardancy of bio-based epoxy resin composites. For the preparation of the bioepoxy matrix, sorbitol polyglycidyl ether (SPE) was crosslinked. Four cross-linking components were used: 4,4 - diaminodiphenylmethane (DDM); 3,3-dimethyl-4-4 -diaminodicyclohexylmethane (T-58); triethylenetetamine (TETA); N,N,N -tris(aminoethyl)phosphoric acid triamide (TEDAP). APP, RDP (resorcinol bis(diphenylphosphate)), red phosphorus (RP); ammonium salt of DOPO-acid (DXA) and melamine salt of DOPO-acid (DXM) as flame retardant additives.

One of the conclusions of the study is that 3% phosphorus input is necessary to achieve the best V-0 grade.

The other major experience is the combination of combustion inhibitors. Red phosphorus can work in solid phase. The ammonium salt of DOPO acid works in the gas phase according to the manufacturer's specifications, and the P-containing radicals produced from the molecule react with the hydrogen and hydroxide radicals responsible for the propagation of combustion to slow down the spread of the flame. In contrast, in the case of DXM, there is also a significant solid phase effect due to the melamine, which is a salt of DOPO acid. It was found that adequate flame retardancy (V-0) is achieved when the solid and gas phase effects are balanced.

The use of flame retardants in plastics is growing steadily worldwide at 3-4% per year, with above average growth in the automotive industry and increasing demand in the electrical and electronics (E&E) industry. (16)

Newer high molecular weight or polymeric flame retardants are gradually displacing low molecular weight compounds which are prone to migration, and halogen-free flame retardants are also expected to be successful. (16)

Brominated flame retardants, still widely used worldwide, are only really effective when mixed with synergistic antimony trioxide (ATO). The traditional flame retardant for polystyrene foam was hexabromocyclododecane (HBCD), but the EU chemical legislation REACH has classified this chemical as a substance of very high concern (SVHC). To replace HBCD, they wanted to develop a flame

retardant that would not harm the environment and health, preferably contain no halogen, be no more expensive than HBCD, but have a similar flame retardant effect and not alter the original properties of the foam. (7)

Lanxsess has launched polyamide 6 (PA 6) and polybutylene terephthalate (PBT) polyester compounds with halogen-free flame retardants. They have a flammability rating of V-0 according to UL-94, high long-term heat resistance, favourable creep strength and low corrosion tendency. Made of glass-fiber reinforced PBT composite, the product has met the stringent filament-wire test for the flammability of plastic components. (17)(20)

Modern flame retardants prefer to use oligomers or polymers instead of low molecular weight additives because they have less impact on the properties of the matrix material and are less leachable and less migratory. Good results have been obtained with derivatives of monophosphinic or phosphoric acids, especially when they are incorporated into the polyamide molecular structure by covalent bonding. The flammability of such combinations is significantly reduced even with very low phosphorus contents of <1%. (18)

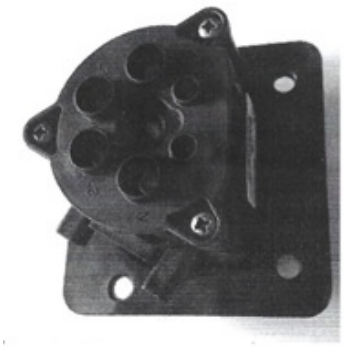

11. Figure. Connector for charging electric vehicles made from Radici's Radiflam A PA66 RV250HF

Radici Perfomance Plastik, a division of the Italian-based Radici Group, manufactures engineering plastics, mainly for the encapsulation of electrical devices, which are resistant to high temperatures, even in thin-walled devices. They have to withstand lead-free soldering temperatures. The range includes halogen-free and phosphorus-free PA6 PA66 types. Radiflam's AFR brand of unfilled PA66 achieves UL-94 grade V-0 in 0.4 [mm] thickness. (19)

Increasingly, sustainability, including the use of renewable bio-based raw materials and the recycling of waste, is becoming a focus of product development. (14) The development of flame resistance is an important issue in the recyclability of flame retardant polyamides. Clariant has shown in studies with the Fraunhofer LBF Institute and PINFA member companies that the flammability of glass-fibre polyamides containing the halogen-free flame

retardant Exolit OP 1400 does not change after repeated recyclization. The reciclates also meet the requirements of UL-94 V-0. (21)

The development of electrical and electronic equipment in the E&E market is creating new requirements. Solvay offers its PA compounds containing halogen-free flame retardants for the production of very small electrical and electronic components. Their latest generations meet UL-94 V-0 requirements at thicknesses as low as 0.4 [mm] and can therefore be used effectively for miniaturisation of smart electrical systems such as smart current sensors and protection switches.

Conclusions

- The issue of flame retardancy needs to be addressed in a complex way, as flame retardant additives also alter other properties of plastics - usually by impairing tribological properties. This is why it is important to continuously improve and regulate testing methods.
- In technical development, it is worth further reflecting on the fact that additives should preferably be obtained from natural sources; this will help to increase cost-effectiveness and reduce environmental and health damage.
- Further exploring and developing the mechanisms of action of halogen-free flame retardants is a constant task, as the range of requirements for plastics and thus the technical, health and environmental demands on flame retardants is constantly expanding.
- It is important to better understand and incorporate new chemical technologies, both in production and in recycling (e.g. chain extension - chain shortening... miniaturisation... chemical bonding issues, spatial issues in the structure of plastics...)
- For sustainability, production safety, users are looking for PA6 types. Manufacturers are also adding new products for the automotive and E/E industries.(21)
- A huge body of knowledge has been built up on plastics. The role of education and training is a priority. Symbiotic cooperation between countries is needed.

The aim of this review is to summarise in a nutshell the subject of polymer flame retardancy. The studies are all aimed at improving the properties of materials and take into account environmental and health protection issues. The work is ongoing and has no end in sight.

Bibliography

[1] Andó M. (2010):Műszaki műanyag kompozitok fejlesztése mezőgazdasági gépészeti alkalmazásokhoz Ph.D értekezés
[2] Kalácska G. (2017):Műszaki polimerekről gépészmérnököknek
[3] Bordácsné Bocz Katalin (2016):Környezetbarát égésgátolt polimer kompozi-

tok fejlesztése. Ph.D összefoglaló Magyar Kémiai Folyóirat /2016/1.szám/.
[4] Szabó Lujza (2013):Lenszál erősítésű termoplasztikus keményítő kompozitok égésgátlási lehetőségeinek vizsgálata. /Magyar Textiltechnika 2013./4./
[5] Dr. Toldi Andrea – Szolnoki Beáta – Czeller Anna :Égésgátolt szénszál-erősítésű kompozitok fejlesztése repüléstechnikai alkalmazásokhoz Műanyag és Gumi 2010. 47.évfolyam 10.szám
[6] Szolnoki Beáta: Bioalapú epoxigyanta kompozitok környezetkímélő égésgátlása Magyar Kémiai Folyóirat 124. évfolyam 1-2. szám 2018.
[7] Műanyagipari Szemle (2015./3.):Égésgátlás, korszerű, környezetkímélő adalékokkal. p. 9.-20.
[8] Műanyagipari Szemle (2016./2.):Nyolcvanéves a poliamid – múlt és jelen. p. 3.-8.
[9] Műanyagipari Szemle (2016./3.):Hogyan zabolázható meg a mai műanyagok éghetősége? p. 43.-52.
[10] Műanyagipari Szemle (2016./5.):Fokozottan hőálló és mérsékelten égő poliamidok. p. 12.-19.
[11] Műanyagipari Szemle (2016./5.):Műszaki adatlapok csapdái 1. p. 19.-23.
[12] Műanyagipari Szemle (2016./5.):Adalékanyagok újdonságai. p. 23.-30.
[13] Műanyagipari Szemle (2016./6.):Műszaki adatlapok csapdái. 2. p. 11.-15.
[14] Műanyagipari Szemle (2016./6.):Másodlagos (újra feldolgozott) műanyagok tulajdonságainak javítása adalékanyagokkal. p. 32.-39.
[15] Műanyagipari Szemle (2018./1.):Új nagy hőállóságú műanyagok. p. 3.-9.
[16] Műanyagipari Szemle (2018./5.):Valódi újdonságok az égésgátlásban. p. 24.-34.
[17] Műanyagipari Szemle (2019./1.):Égésgátolt kompaundok igényes autóipari és elektronikai alkalmazásra.
[18] Műanyagipari Szemle (2019./2.):Új égésgátlók és új csökkentett éghetőségű műanyagok az építőipar az E/E ipar és a szálgyártás számára. 1.rész
[19] Műanyagipari Szemle (2019./3.):Új égésgátlók és új csökkentett éghetőségű műanyagok az építőipar, a szálgyártás és az E/E ipar számára. 2.rész
[20] Műanyagipari Szemle (2019./3.):Halogén – és vörösfoszformentes égésgátlók poliamidokhoz a Lanxesstől.
[21] Műanyagipari Szemle (2020./3.):Felsőbb osztályba lép a poliamid.

Fuzzy control and its applications

Piroska VÍG[1], István SZABÓ[2], Norbert SCHREMPF[2], Antal VERES[1],
Zoltán SEBESTYÉN[1], Péter KORZENSZKY[2]
[1]Institute of Mathematics and Basic Science,
Hungarian University of Agriculture and Life Sciences, MATE
[2]Institute of Technology, Hungarian University of Agriculture and Life Sciences, MATE

Abstract

With advances in science and technology, there are more and more opportunities to solve challenging problems. At the same time, it is becoming increasingly important to pay more attention to energy efficiency and environmental sustainability in tackling fundamental challenges. An essential part of engineering problems is when some regulation needs to be implemented. It is also essential to find the most optimal solution by taking advantage of these new opportunities in solving such tasks. In addition to traditional control methods, fuzzy control is a new option. The concept of fuzzy logic is based on human reasoning and natural actions. This article reviews fuzzy control's essence and main features and its specific applications.

Keywords

process control, fuzzy logic, fuzzy applications, food industry

1.Introduction

We encounter controls in countless areas of our lives. Control is a closed-loop whose task is to keep a given characteristic constant. The system uses feedback and responds to a change measured by a sensor (Márton, 2019). A general control loop consists of the process and the technical means to control it (Figure 1).

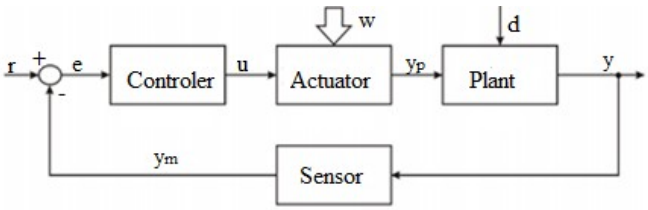

Figure 1. Main parts of the control

where:
- u_p – plant input,

- y – plant output,
- y_m – measured output,
- r – reference signal,
- e – control error,
- u – control signal,
- d – disturbance,
- w – the impact of the intervention on the system.

Care should be taken in selecting the right controlled characteristics for the regulatory purpose, considering possible disturbances and selecting characteristics that can be modified or altered. The task of the control algorithm is to determine the actuator input as a function of the sensor output and the setpoint so that the process output follows the setpoint despite the various disturbances affecting the system.

Several theoretical description methods are possible for conventional control: differential equations in the time domain, transfer functions in the Laplace domain, and frequency functions in the frequency domain. The choice of controllers depends mainly on the process and the purpose of the control.

The control would be ideal if the controlled characteristic were at a corresponding value to steady-state and transient states setpoints. However, this is not possible in practice due to the time-delayed elements of the regulation. The closer a regulation is to the ideal, is more complex and more expensive it is. Consequently, it is a self-evident requirement to find a reasonable compromise between the goodness of regulation and simple structure (Mizsey, 2012; Kóczy, Tikk, 2000).

In the most commonly used traditional regulations, the physical laws describing the relationship between variables are known and are used. The most common here are the proportional (P), integrating (I), differentiating (D) terms and the PI, PD and PID controllers obtained by their parallel connection. In the case of these controls, the controlled system or the process will be modelled.

In contrast, a novel control mode is artificial intelligence-based fuzzy control, which aims to incorporate human expertise into the control algorithm. Thus, in this regulation, an expert's thinking process model is used in the regulation.

Often only incomplete, inaccurate, uncertain information is available, in which case fuzzy systems offer a suitable alternative. The advantage of fuzzy control is that fuzzy control models can be developed without special knowledge of control theory, using the associated, approximately known input-output pairs defined by a fuzzy rule.

The setting uses quasi-optimal algorithm tuning, always resulting in an approximate model. Therefore, it is worth considering using a fuzzy model for systems for which an accurate analytical model cannot be established, or the model would be very complex.

2. The fuzzy logic control

Fuzzy logic

The most critical principles in traditional computing (conventional computing) are accuracy, certainty, and rigour. In contrast, soft computing uses the human

brain as a model. The thought process humans use effectively is described in mathematical formulas and attempts to achieve traceability, robustness and a better connection with reality (Zadeh, 1994).

The types of soft calculations and the possibilities inherent in their application are reviewed in Table 1. Hybrid systems (neuro-fuzzy, neural network and genetic algorithm, fuzzy logic, and genetic algorithm) that combine these advantageous properties are often used, possibly even combined with physically-based models, for more efficient handling and more reliable performance.

Table 1. Systems using soft computing

System	Application area
neural network	learning, pattern recognition, adaptation, system identification
fuzzy system	dealing with inaccuracies, approximate conclusions, rule-based systems, counting words
genetic algorithm	optimisation

Fuzzy logic represents information like regular communication and concludes it like human inference. Instead of binary logic, it uses values between 0 and 1, introducing membership functions (characteristic function) and linguistic variables based on them. In order to conclude, he formulates rules of the 'If-Then' type. Figure 2 shows an example of a characteristic function.

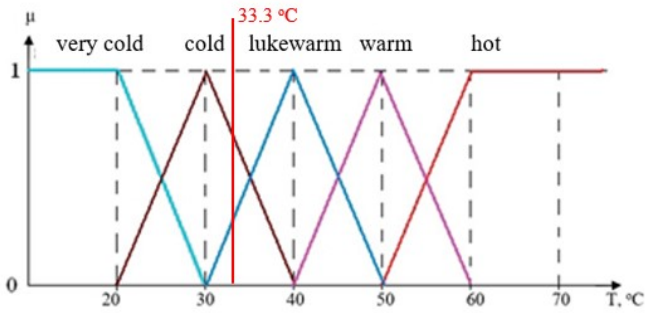

Figure 2. Example for, the fuzzy characteristic function of temperature

Zadeh introduced linguistic variables (fuzzy sets) in 1973 to describe systems of high complexity. However, these, with the if-then rules, were complex and computationally intensive due to their high dimension. Mamdani further developed the idea in 1975; in his simplified model, he used a kind of section of k, 1-dimensional relation projections instead of k-dimensional relations, which significantly reduced the computational requirements.

Main parts of the fuzzy control system

Rules: A set of if-then rules that describe how a system works. These rules can be derived from theoretical and practical knowledge by analysing a controlled process or learning (e.g., using a neural network's learning capabilities).

Unit of fit: compares the history of the rule base with the current observation; based on the similarity, a value between 0 and 1 is determined, which represents the degree of fit (in the example, a temperature of 33.3°C is cold with a value of 0.7 and lukewarm with a value of 0.3).

Firing rule: If the intersection of history and observation is a non-empty set (cold and lukewarm in the example in Figure 2), then consequences modified according to the degree of fit are entered into the inferential unit.

Inference unit: Combine the consequences of the firing rules in the rule base with the degree of fit as a weight. In Mamdani's method by the minimum, Larsen's method by the multiplier. The output of the inference unit is usually a fuzzy quantity.

Defuzzification unit: A fuzzy output set is represented by a single number (defuzzification) as its most characteristic feature element. The output of the main defuzzification methods is the centre or edge kernel, the centre of the area under the membership function, or the characteristic value of the centroid of the area under the function (Retter, 2006). The scheme of fuzzy control is shown in Figure 3.

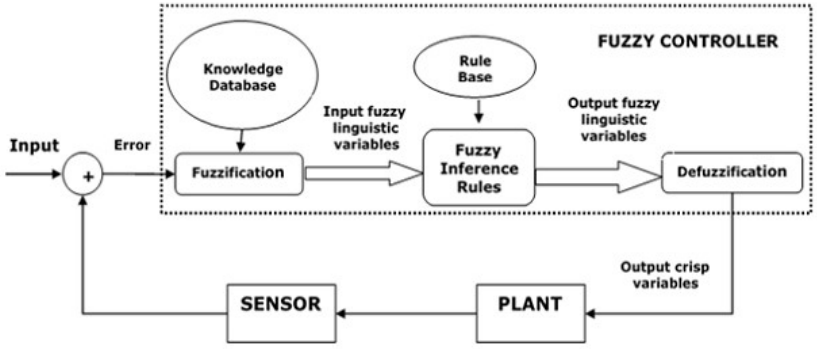

Figure 3. Elements of fuzzy control

Steps for designing the fuzzy control system:

- Definition of input and output variables.
- Specify the ranges of values of input and output variables.
- Partitioning of input and output value ranges (partitioning of spaces). The possible values of each language variable are partitioned or partialised to cover the basic set of values for the variable. It is required that there is positive membership information for each possible input value. The more language terms a fuzzy partition contains, the less expressive the language

tags will be. A reasonable trade-off between accuracy and linguistic expressiveness must be sought in the number of fuzzy sets used.
- Formulate rules between input and output values.
- Choice of membership functions (μ) for input and output linguistic variables. These can be monotonic, triangular, trapezoidal, Gaussian, bell-shaped, etc. The choice can be based on empirical and expert knowledge or learning and self-organising methods. The membership functions can be used to determine the degree of fit.
- Inference (inference) unit design. This design work is a central part of the fuzzy model. It includes inference (implication), composition (composition) selection and interpretation of linking norms. The design requires an individual, problem-specific solution. It may be that two or more rules are fired for a given input. This may even be the case for two or more rules whose consequences (actions) are different, possibly contradictory. This is not a problem, and each is properly taken into account in the weighting. The higher the degree of fit of a rule, the greater its effect on the output.
- Choice of defuzzification strategy.

The control steps are illustrated graphically in Figure 4.

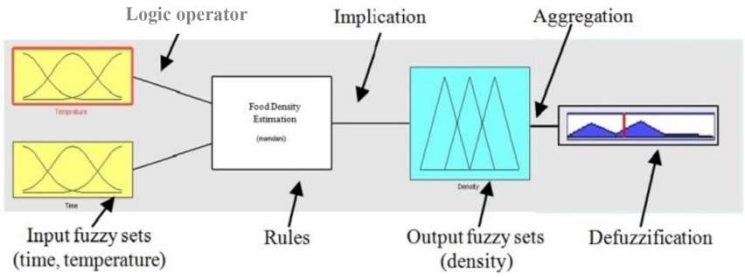

Figure 4. Outline of fuzzy control of a baking process with MATLAB notation

In the previous example, based on the temperature and the time elapsed since the start of frying, the model determines the fuzzy function of frying, which can be used to control frying after defuzzification.

Advantages, disadvantages of fuzzy control

In summary, Fuzzy Logic Control is relatively cheaper in performance than model-based or other controllers. At the same time, it is more robust than PID controllers because of its ability to cover a wide range of operating conditions. They can be easily customised, emulate human deductive reasoning, and are more reliable and efficient than conventional control systems.

However, along with the advantages, they also have disadvantages; they require much data, cannot be used for many more or fewer cases than existing data, require high human expertise, and the rules need to be updated over time.

Fuzzy control is appropriate for any control where physics-based control is difficult or non-existent to implement or where energy efficiency is a concern.

3. Main application areas of fuzzy control

There are several fields where the fuzzy logic system uses:

- Automobile and other vehicle subsystems, such as automatic transmissions, ABS and cruise control (e.g. Tokyo monorail). Elevators.
- Air conditioners, cameras, digital image processing, such as edge detection.
- Rice cookers, dishwashers, washing machines and other home appliances.
- Video game artificial intelligence.
- Language filters on message boards and chat rooms.
- Pattern recognition, e.g. in remote sensing, hydrometeor classification algorithms for polarimetric weather radar and mineral deposit estimation.
- Fuzzy logic has also been incorporated into some microcontrollers and microprocessors.

Several parameters have to be considered in parallel in the food industry, so the food industry is an important application area. A single sensory property, such as colour or texture, can be related to significant quantities recorded by the human brain. The food industry must produce products that meet fixed standards by processing variable raw materials, so regulating food-related processes is a complex, nonlinear process in which variables are linked. For example, in addition to temperature changes during the heating or cooling process, changes at the biochemical (nutrient, colour, aroma, etc.) and microbiological levels must also be considered. During treatment, the moisture content of food fluctuates continuously, affecting the taste, texture, nutrient concentration, and physical properties such as density, thermal and electrical conductivity, specific heat, viscosity, permeability, etc. The many variable parameters make it essential to apply fuzzy logic in the food industry.

Fuzzy logic can be used with great success in 3 main areas: it contributes to sensory analysis (Vivek et al., 2020; Kaushik et al., 2015; Chakraborty et al., 2015), a valuable tool for regulating food-related processes and research related to food quality. (Perrot et al., 2005).

In his book excerpt, Alghannam (2012) provides an overview of articles using fuzzy logic control in food processing and details the steps for designing a fuzzy controller. For simple fuzzy systems modelling, starting the control design with a PID controller and then replacing it with an equivalent linear fuzzy controller is suggested. In the next step, it is recommended to make this controller nonlinear by fine-tuning.

4. Results and discussion

The importance of the topic is underlined by the fact that the concept of fuzzy is present in almost every aspect of our lives. The wider spread of practical applications and a more precise mathematical background are the main directions for further developing the theory. (Fodor and Baets, 2007) At the same time, hardware and software development are also encountered in practice. (Thareja et al., 2009).

The importance of the field is emphasised by several journals (Fuzzy Sets and Systems, Advances in Fuzzy Systems, International Journal of Fuzzy Systems, Journal of Fuzzy Extension & Applications, International Journal of Fuzzy Logic and Intelligent Systems, Journal of Intelligent & Fuzzy Systems, International Journal of Fuzzy System Applications, etc.) Several organisations offer the possibility to publish results in this field: the International Fuzzy Systems Association, The European Society for Fuzzy Logic and Technology, the World Federation of Soft Computing, and Magyar Fuzzy Társaság. These societies also play an essential role in establishing contacts between research groups.

Conclusions

Our work has given an overview of the essence of fuzzy control and its main applications. Numerous scientific articles can be read both in the application and to establish the theoretical background. Based on these results, it can be said that fuzzy logic is an approach to our environment, the processes in our environment, that is easy to understand, flexible, and tolerant of inaccurate data, similar to the human brain decision-making strategy.

Concerning food, fuzzy models can model the complex nonlinear behaviour of any sensory test, thus helping to objectively evaluate foods and being a practical option for regulating food processes and helping for food quality issues.

Acknowledgements

Project no. 2020-1.1.2-PIACI-KFI-2020-000151 has been implemented with the support provided by the Ministry of Innovation and Technology of Hungary from the National Research, Development and Innovation Fund, financed under the 2020-1.1.2-PIACI KFI funding scheme.

References

[1] Alghannam A.R.O. (2012) Design of a Simple Fuzzy Logic Control for Food Processing, in Trends-in-Vital-Food-and-Control-Engineering, ed. Eissa A.A., IntechOpen
https://www.intechopen.com/books/trends-in-vital-food-and-control-engineering

[2] Chakraborty S, Rao P.S., Mishra H.N. (2015) Response Surface Optimisation of Process Parameters and Fuzzy Analysis of Sensory Data of High Pressure-Temperature Treated Pineapple Puree, J Food Sci. vol. 80(8), pp.1763-75., DOI: 10.1111/1750-3841.12967.

https://pubmed.ncbi.nlm.nih.gov/26220205/
[3] Fodor J., De Baets B. (2007), Uninorm basics, in: P.P. Wang, D. Ruan, E.E. Kerre (Eds.), Fuzzy Logic—A Spectrum of Theoretical & Practical Issues, Springer, 2007, pp. 51–66.
[4] Kaushik N., Rao P.S., Mishra H.N. (2015) Application of fuzzy logic technique for sensory A review, Thermal treatment, Innovative Food Science & Emerging Technologies, Volume 32, pp. 70-78. https://www.sciencedirect.com/science/article/abs/pii/S1466856415001629
[5] Kóczy T. L., Tikk D.: Fuzzy systems, Typotex Kiadó, 2000
[6] Márton L, Fehér Á. (2019) Control Engineering Laboratory Guide, Scientia Kiadó http://real.mtak.hu/108910/1/Iranyitastechnika_REAL.pdf
[7] Mizsey P. (2012): Process Control Systems, Typotex Kiadó https://oszkdk.oszk.hu/storage/00/00/59/44/dd/1/Folyamatir-rendszerek_videok_nelkul.pdf
[8] Perrot, N. Ioannou, I., Allais, I., Curt C., Hossenlopp J., Trystram, G.(2005) Fuzzy concepts applied to food product quality control: A review, Fuzzy sets and systems, Vol. 157, No. 9 https://dl.acm.org/doi/abs/10.1016/j.fss.2005.12.013
[9] Retter Gy.: Fuzzy, neural, genetic, chaotic systems, Akadémiai Kiadó, Budapest, 2006
[10] Thareja V., Montcalm M. and Bolic M.(2009), Configurable Fuzzy Logic Coprocessor for Small Scale Food Preparation, Soft Computing Applications'09 3rd International Workshop, 7, pp. 229-234.
[11] Vivek K., Subbarao K.V., Routray W, Kamini N.R., Dash K.K. (2020) Application of Fuzzy Logic in Sensory Evaluation of Food Products: a Comprehensive Study, Food and Bioprocess Technology, Vol. 13, pp. 1–29 https://link.springer.com/article/10.1007%2Fs11947-019-02337-4
[12] Zadeh L.A. (1994): Fuzzy logic, neural networks and soft computing. Communications of the ACM, 37, pp. 77-84.

Assessment of Ploughing Stability

Jozef RÉDL[1], Juraj MAGA[2], Pavol FINDURA[2], Gábor KALÁCSKA[3], Davood KALANTARI[4], Jozef BANGO[1]

[1]Institute of Design and Engineering Technologies, Faculty of Engineering, Slovak University of Agriculture in Nitra

[2]Institute of Agricultural Engineering, Transport and Bioenergetics, Faculty of Engineering, Slovak University of Agriculture in Nitra

[3]Institute of Technology, Hungarian University of Agriculture and Life Sciences (MATE)

[4]Department of Farm Machinery, Faculty of Agricultural Engineering, Sari Agricultural Science and Natural Resource University, Iran

Abstract

To improve the process of soil irrigation we designed and applied the original methodology based on rigid body vibration. The goal of this article is the design and application of methodology aimed to assessment of the stability of the ploughing process of topsoil and design a new stability criterion hypothesis. The methodology based on the experimental measurements of the plough accelerations during the ploughing operation in three-dimensional movement. The numerical integration method Runge-Kutta 4th order were applied for transformation of measured accelerations of plough. The used plough was a product of Pottinger Company and used type was Servo 6.50 Plus 7 for medium-deep ploughing. The measurement device was Analog Devices ADXL345 digital accelerometer. The simple model of loaded plough was created. The mathematical model is based on the differential equation $m \cdot \frac{d^2x}{dt^2} + c \cdot \frac{dx}{dt} + k \cdot x = 0$. The model was excited with the experimental functions of acceleration and velocity with real time function. The damping and stiffness parameters of flotation wheel were appropriate chosen. The stability of the ploughing process was evaluated by stability criterion designed from ideal parameters of ploughing stability with consideration of the semi-real model parameters. For mathematical procedures we were used the software MathWorks Matlab and programing language Microsoft Visual C# 2010 Pro.

Keywords

ploughing stability, soil tillage, tool vibrations, numerical integration,

1. Introduction

Nowadays is the major effort of the political authorities aimed on the reduction of the carbon emission. The agriculture is one of the biggest producer of the

carbon emission through the agricultural machines. Tractors in process of tillage and harvest machines produce the majority of exhalations. To reduce the production of exhalation the most manufacturer searching the way to optimize the fuel consumption through the optimization the efficiency of used agricultural tools especially the ploughs. Guul-Simonsen et al., 2010, have analyzed the genealogy of design, improving and production of ploughs in northern Europe. Their study is based on 165 publications from 1771 to 2001 and covers the main parameters in relation to energy requirement, wear, ploughing result and crop yield. The study concludes that the features of greatest potential are changes of the ploughing depth and of the shape and surface characteristics of shares and other lower plough body parts. Study also analyzing the standards DIN and ASAE. Influence of soil moisture content on the traction performance of a 78-kW agricultural tractor during plow tillage were investigated by Kim et al., 2021. The soil moisture content has an influence in various tractor traction performance factors such as traction coefficient and tractive efficiency. The tire is the transmitter of the power between the ground and machine to realize the agro technical operation. Determination of stiffness and damping coefficient of tractor front tyres in non-rolling conditions was investigate by Babu et al., 2016. The tyre is the link between the road and the chassis of a vehicle. It has, therefore, an important role in the transmission of the tractive and braking forces and it influences the ride and the road stability of the vehicle. The many researcher investigated the relationship between the energy consumption and the efficiency of agro technical operation. They are mostly focused on the optimizing the tool geometry parameters and improving the tillage systems. Moitzi et al., 2013, investigated the energy consumption in cultivating and ploughing with traction improvement system and consideration of the rear furrow wheel-load in ploughing. Chávez et al.,2015, investigated the vertical tillage parameters to optimize energy consumption. The objective of his study is the assessment of different chisel plow body arrangements using different settings of the most important operating parameters for tillage work in order to optimize energy consumption for vertical tillage. The influence of different operating parameters of tillage tools on the performance in cultivation practice must be considered before applying deep plowing for a more efficient use of energy. The most relevant factor on the biochemical processes in soil is the optimal set up the tillage parameters and fertilization. These aspects were investigated by Hury et al., 2020. The aim of their research is to assess the effect of cultivation systems and varied nitrogen fertilization doses on yield and yield components of two cultivars and one strain of winter spelt. The method of cultivation (conventional vs. reduced tillage) did not show differences for the four analyzed yield components and SPAD of winter spelt. The influence of soil tillage or soil cultivation on the efficiency of the photosynthetic apparatus in maize leaves (Zea mays L.) has been investigated by Stępień-Warda, 2020 where declared that the cultivation of maize in no-tillage farming systems has become increasingly important in recent years, due to the observed climate changes and the increasing droughts. Such a cultivation system has a positive effect on the physicochemical and biological properties of the soil, but above all allows for greater retention of water available to plants. The aim of the research

was to assess the effect of the method of soil preparation for sowing maize grown in monoculture. The research showed that the applied tillage system had a significant impact on the parameters of chlorophyll fluorescence and the yielding of maize, while the weather conditions, especially rainfall, were also of great importance. The ploughing as a part of grassland renovation investigate by Gawel et al., 2019. It compares two ways of renovating grassland: A – after ploughing and B – after superficial disturbance of the soil to the depth of 5 cm with a compact harrow. The many points of view of importance of ploughing were analyzed. The ploughing playing an important role in soil cultivations, increasing the soil fertility and helping the biochemical process in soil with increasing the soil fertility.

2. Materials and methods

Experimental site

Characteristics of the experimental ground: soil type was brown-clay soil on proluvial-dusted sediments. The specific gravity of the soil ranges from 2.6 to 2.63 $t.m^{-3}$, the porosity is 45-48% in the topsoil and 42% in the subsoil. Humus content is medium (1.95 - 2.28%), pH KCl is 4.76 - 5.56.

Tillage variants in interaction with the incorporation of post-harvest plant residues were:

- medium deep ploughing (0.20 - 0.25 m) with incorporation of post-harvest residues,
- medium deep ploughing (0.20 - 0.25 m) without incorporation of post-harvest residues,
- deep ploughing (0.25 - 0.3 m) without incorporation of post-harvest residues,
- plating (0.12 - 0.15 m) with incorporation of post-harvest residues,
- plating (0.12 - 0.15 m) without incorporation of post-harvest residues.

Figure 1. Ground before ploughing

The ground dislocation in near of village Veľké Zálužie in Nitra region in 13 km in Nort-West direction. The raw soil depicted in Figure 1 and the cultivated

soil is depicted in figure 2. The provided ploughing was a deep ploughing and was realized on November.

Figure 2. Ground after ploughing

Accelerations and soil moisture measurement

For measurement of plough vibration has been used an Eval - ADXL 345, (Analog Devices, 2021) data acquisition board. The board measured accelerations in the XYZ axes. Measured data has been recorded to the MiniSD card. The relevant direction for us was the accelerations in X axis and Z axis directions. The data from SD card has been saved in text format with time duration and values in mV for each direction.

Figure 3. Eval - ADXL 345Z-DB

Figure 4. Moisture sensor

We were used a Moisture Meter HH2 to measure the soil moisture that was ploughed during the experiments (Figure 4.). The HH2 hygrometer from Delta-T is a device that is mobile in nature and displays the measured data directly on the integrated display. The moisture meter reads outputs from ThetaProbe sensor type ML2x). The average moisture of soil in 10cm depth was 25.42 % before ploughing.

Figure 5. Mounted device on plough frame

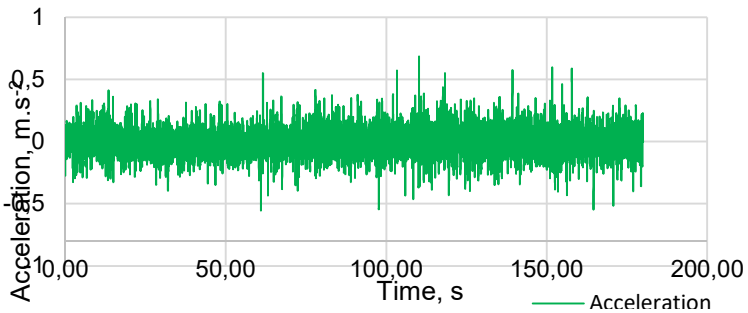

Figure 6. Acceleration in Z-axis direction

Tractor implement combinations

Figure 7. Full mounted 2x7 mouldboard plough with 182kW 4WD tractor

The agro technical operation has been realized with Tractor Fendt 824 and mounted plough Pöttinger Servo 6.50 Plus. To degrees the contact area the soil with mouldboard shares the slat mouldboard was chosen. For this type of semi-heavy soil is the best option. The plough parameters are in table 1.

Table 1. (www.pottinger.com)

Parameter	**Value**	**Unit**
Manufacturer	POTTINGER Landtechnik GmbH	
Type	Servo 6.50 Plus 7	
Total weight W	3410	kg
Units distance	1.02	m
Units count	7	

Signal processing and numerical integration

Acceleration processing

For processing the accelerations, it has been created the program Datahander in Microsoft Visual C# NET 2010 Pro language by authors, Figure 8. The loaded data from ADXL device, has been loaded into the program Datahandler and processed. The sample from the experimental recording is showed in Table 2.

Table 2. Data sample ADXL 345Z-DB

No.	Time	x	y	z
0	00:00:00:089	44	43	186
1	00:00:00:090	47	58	150
2	00:00:00:090	16	65	249
3	00:00:00:090	22	71	286
4	00:00:00:090	21	87	224

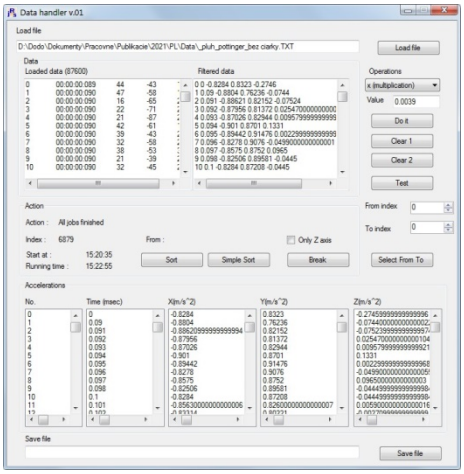

Figure 8. Data handler software

The program separating each column from original file and recalculated the time to second into the simplest format. The ADXL 345Z-DB device recording values in real time with time difference 1/128 s. For this reason, in different times which are going consecutive has the same value of accelerations in different time. The program filtering these irregularities for chosen time difference by user.

Matlab filter

As defined in the Matlab description, the discrete FIR Filter block independently filters each channel of the input signal with the specified digital FIR filter. The block can implement static filters with fixed coefficients, and time-varying filters with coefficients that change over time. The Matlab offers the signal processing algorithms in script as follows:

```
filtertype = 'FIR';
Fs = 1/60;  % Frequancy
N = 3;       % Order of filter
Fpass = 1/(10*60*60); % filter pass band
Fstop = 1/(2*60*60);  % filter stop band
Rp = 0.8; % Passband ripple
Astop = 150; Stop band attenuation
LPF = dsp.LowpassFilter('SampleRate',Fs,...
                                'FilterType',filtertype,...
                                'PassbandFrequency',Fpass,...
      'StopbandFrequency',Fstop,...
                                          'PassbandRipple',Rp,...
      'StopbandAttenuation',Astop);
   Output = step(LPF, xd); % Output- filtered data
```

Numerical integration

For purpose of accelerations and velocities processing we were used the Runge-Kutta 4th order method in the next form, (Rédl, 2010):

$$Y_j = Y_{j-1} + \frac{\Delta t}{6}\left(k_1 + 2k_2 + 2k_3 + k_4\right), \tag{1}$$

where:

$$\begin{aligned} k_1 &= f\left(x_{j-1}, Y_{j-1}, \ldots, {}^{n}Y_k\right), \\ k_2 &= f\left(x_{j-1} + \frac{\Delta t}{2}, Y_{j-1} + \frac{\Delta t}{2}.k_1, \ldots, Y_k + \frac{\Delta t}{2}.k_1\right), \\ k_3 &= f\left(x_{j-1} + \frac{\Delta t}{2}, Y_{j-1} + \frac{\Delta t}{2}.k_2, \ldots, Y_k + \frac{\Delta t}{2}.k_2\right), \\ k_4 &= f\left(x_{j-1} + \Delta t, Y_{j-1} + \Delta t.k_3, \ldots, Y_k + \Delta t.k_3\right). \end{aligned} \tag{2}$$

For numerical integrations we were designed an algorithm in the MS Visual C#. NET 2010 Pro environment based on the equations (1) and (2). The used algorithm is the part of the software RKTest as published by Redl, 2010. The designed source code has the next structure:

```
for(int j=1;j<=jcount-1;j++) {
    for(int i=1;i<=icount-1;i++) {
        rk_arr_out[i,j]= rk_arr_out[i-1,j]+dti.RK_Step;
       k1=rk_arr[i-1,j];
       k2=rk_arr[i-1,j]+(rk_arr[i,j]-rk_arr[i-1,j])/2;
       k3=k2;
       k4=rk_arr[i,j];
       rk_arr_out[i,j]=rk_arr_out[i-1,j] +((dti.RK_Step/6)*
                    *(k1+(2d*k2)+(2d*k3)+k4)); } }
```

The `rk_arr_out[i,j]` variable is multidimensional. The $i-th$ dimension indicating the dataset to be integrated and $j-th$ dimension indicating the integrated functions. The time differences for numerical integration was set for $\Delta t = 1.10^{-3}$ second = `dti.RK_Step` variable.

3. Results

Mathematical model

For the mathematical model we consider the initial conditions as follows:

- the plough frame construction is substituted with simple rectangular steel beam,
- the total weight of plough were substituted with uniform loading, which load the beam on full length of beam,

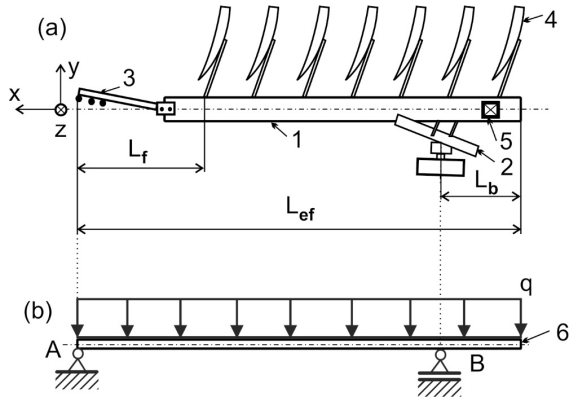

Figure 8. Model of plough
L_f-frontend distance, L_{ef}-effective length, L_b-back distance,q-uniform loading, 1-plough frame, 2-flotation wheel frame with damper, 3-three-point linkage connection frame, 4-mouldboard, 5-acceleration measurement device, 6-beam model

- the shape dimensions irregularity of the plough were substituted with effective length L_{ef} (Figure 8 (a)),
- the tractor three point linkage was modelled with rotational join (Figure 8 (b)),
- the flotation wheel connection was modelled with roller join (Figure 8 (b)),
- the distance between acceleration sensor and flotation wheel is neglected,
- the admissible load of flotation wheel is equal to reaction in point **B**,
- during the maneuver occurs no obstacles hidden in the soil.

From free-body diagram and static condition of equilibrium we solved the reaction at point **B**. The equation has the next form:

$$R_B = \frac{q \cdot L_{ef}^2}{2 \cdot \left(L_{ef} - L_b \right)}, \tag{3}$$

where: $q = \frac{W}{L_{ef}}$.

The parameters used in equation (3) and reaction in point B are in the table 3. Parameter W_B is used load on the flotation wheel in mass-stiffness-damper model.

Table 3. Model parameters

Parameter	Value	Unit
L_f	3	m
L_{ef}	10.14	m
L_b	1.02	m
q	3299	$N.m^{-1}$
R_B	18595.6	N
W_B	1859.57	kg

Parameters L_f, L_{ef}, L_b were measured on the plough.

Plough movement results

The simple model alternative is the transformation the measured acceleration with acceleration device. For the numerical integration we were used the algorithm described in the equation (1), (2) and C# program. With one integration of x-axis of the acceleration we get the plough velocity in the machine moving direction. With second integration of acceleration of z-axis direction we get the dislocation of the positions of the acceleration device mounted on the plough frame. The ploughing velocity is depicted in the figure 9. The average ploughing velocity was 3.11 $km.h^{-1}$. The total time of the processed data was 180 second. The change of the dislocations of the acceleration device and the plough mainshare are depicted in the figure 10.

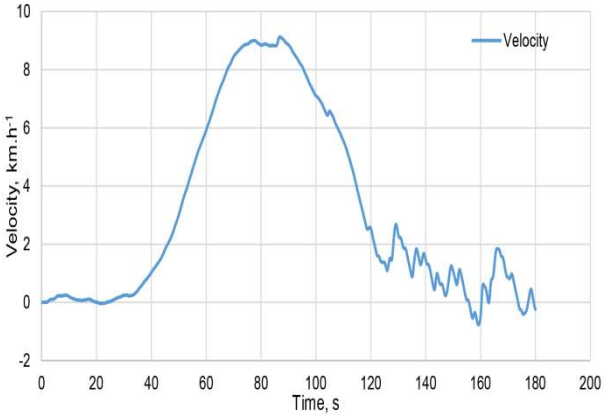

Figure 9. Plough moving velocity in x direction (filtered)

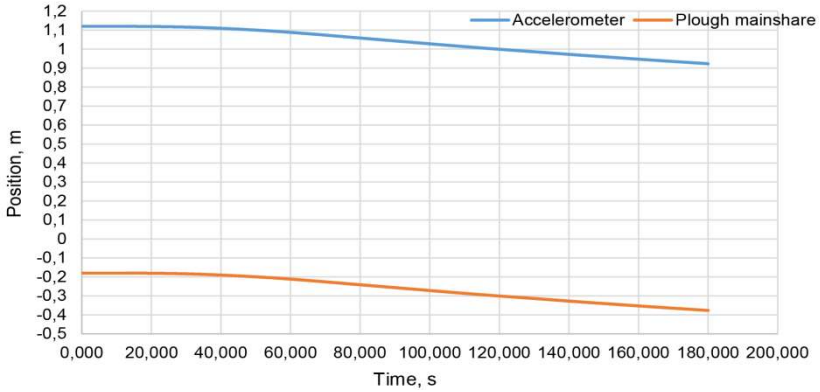

Figure 10. Accelerometer and plough mainshare positions (filtered)

The agro technical operation was the deep ploughing. The mainshare pruning into the topsoil is depicted in the Figure 10. The chart form is shapeless and continuous with semi-linear character because in the model is not included the vibration factors from flotation wheel. The start position is the begging of the ploughing process. The mainshare height from the ground in the starting position depending on the plough settings provided by operator. The ploughing depth depending on the planed agro technical operations. The ploughing depth is mentioned above in this article.

Damping and stiffness of model

To achieve the most significant result, we has been created the simple mass-spring-damper model. The flotation tire (Figure 11) was modeled with mass-spring damper model depicted in Figure 12. The main point of this model is, that we were exited the mathematical model with measured acceleration and solved velocity with numerical integration.

Figure11. Flotation wheel

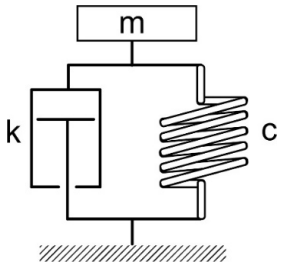

Figure 12. Mass-damper-spring model

The stiffness parameter was solved by equation (4) as follows:

$$k = \frac{W}{R - R_S}, \tag{4}$$

where:

R – tire diameter =0.511m,

R_S – static diameter of tire=0.455m,

k - stiffness =530 N.m^{-1}.

The damping parameter was chosen in value C=3.5 N.s.m^{-1} as recommended Lines,1991. The differential equation of mas-spring-model has the next form:

$$m \cdot \frac{d^2x}{dt^2} + c \cdot \frac{dx}{dt} + k \cdot x = 0 \tag{5}$$

.

For computer processing we rewrite the equation (5) in the next form:

$$x(t)_i = -\frac{m}{k} \cdot \left(\frac{d^2x}{dt^2} \right)_i - \frac{c}{k} \cdot \left(\frac{dx}{dt} \right)_i \tag{6}$$

where:

$x(t)_i$ - displacement function in the x-axis direction in i[th] index,

m- mass weight of plough,

$\left(\frac{d^2x}{dt^2}\right)_i$ - second derivative of displacement in i[th] index, obtained from experiment,

$\left(\frac{dx}{dt}\right)_i$ - first derivative displacement in i[th] index, obtained from numerical integration of the second derivative of the displacement.

The equation (6) was solved with simple program written in Visual C#. The results of positions of the excited model are in figure 13. For the usual convention we let the form of equation (5) intact and not substituted the variable x with z which indicating the z-axis direction and displacement for this axis. The allowed tyre loading W_T=2735 kg. The tire type is BKT Flotation 500/45 R 22.5 (https://www.bkt-tires.com/) and tire pressure was 208 kPa.

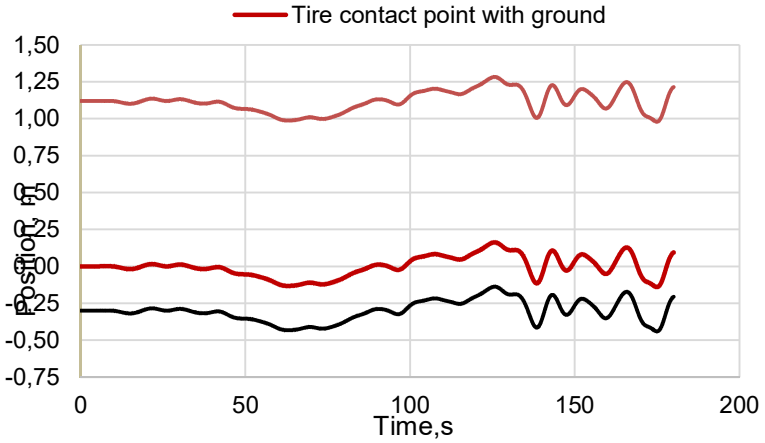

Figure 13. Positions of mainshare, tyre contact point and accelerometer, actuated with ride vibrations

Stability criterion hypothesis

In general form the quality of the ploughing process is defined as function of more variables. But we had consider that in our case we are evaluated the stability of ploughing process. The main condition of stability of ploughing is conservation the dislocation of the plough mainshare in defined ploughing depth. If we define the stability criterion for ideal state ($_{is}SC$) we get:

$$_{is}SC = const. = d_P \text{ in any case,} \tag{7}$$

where d_P is the ploughing depth in m.

For the semi-modelled state, we should define the criterion as the next:

$$_{ml}SC = f\left(a_x(t), a_y(t), a_z(t), TP, DP, TF\right) \text{ in any case,} \tag{8}$$

where:

- $a_x(t), a_y(t), a_z(t)$ are the time depending accelerations functions with respect to the x,y,z directions, where x is the moving direction, y is the side interference and z is the ploughing depth directions,
- TP are the flotation tire parameters,
- DP is the additional damping from hydraulic damper.
- TF is the terrain flatness factor.

The acceleration in the x direction depending on the velocity controlled by operator or automatic speed controller. Recommendation for ploughing is to keep the velocity constant. Considering this option, we could define:

$$\text{if } v(t)_x = const., \text{ then } a_x(t) = \frac{dv(t)_x}{dt} = 0. \tag{9}$$

If we consider that the construction of the plough frame with additional object is mounted on the rear of the tractor in three-point linkage, the applied joints are partly denied the dislocations in the directions which are perpendicular on the moving direction. The mass of tractor and body of the plough are largely absorbed side disturbance and the automatic hydraulic damping system compensate the side disturbance in cooperation with safety system of plough. For this reason, we could neglecting the $a_y(t)$ variable in equation (8) and also if we are neglecting the influence of damper we got:

$$_{m}SC = f\left(a_z(t), TP, TF\right). \tag{10}$$

With mentioned assumptions above, we could define the general form stability criterion as follows:

$$SC_{\%} = \left[1 - \left(\frac{1}{n}\sum_{i=1}^{n}\left|-_{i}SC - _{m}SC_{(i)}\right|\right)\cdot TF\right]\cdot 100, \tag{11}$$

where: n is the count of samples, i is the iteration index, $TF = 1$ (Deng Y., et al 2017) because the ground slope gradients are under 10 deg. From the realized simulation on designed model, we get the value $SC_{\%}$=94%.

4. Discussion

Analyzing the plough stability is the most investigated parameter of the ploughing process. The applied methodology is rare and the stability criterion

hypothesis is in the process of investigation during the project VEGA 1/0102/21 lifetime. Bulgakov et al.,2017, investigated the set-up and parameters of the ploughing unit with a front-mounted plough basing on the theoretical investigation of the stability of its motion in the horizontal plane. The methods of research include obtaining the amplitude and phase-frequency response characteristics of the dynamic system in order to analyze the stability of its motion under the action of external statistically random perturbations. The ploughing unit's motion stability substantially improves in case of higher air pressure in the tyres on the tractor's front and rear wheels. The similar research of the plough stability has been investigated by Bulgakov et al.,2021. They designed and analyzed the results from field tests on ploughing units based on a modular draft device (MDD) and this module consists of an energy module and a technological module. Applied MDD in ploughing process and compared to a 4WD tractor with a 6WD wheel arrangement offered a greater stability of the ploughing depth. The other research published by Ivanovs et al., 2018, investigated the ploughing aggregate, operating according to the "push-pull" scheme, and it has satisfactory path indicators. The path variations of the furrow laid by this aggregate are of a low-frequency nature. Arrangement of the supporting wheel of the frontal plough outside the furrow and its movement across an undeveloped agro phone does not lead to the deterioration in the steering ability of the explored ploughing aggregate. The archived results were evaluated and compared by the normalized spectral density of investigated parameters. The other research published by Lobachevski, 2021, investigated the ploughing quality and energy consumption depending on plough bodies' type. They research results for designed plough construction achieved the allowed change ploughshares installation angles relative to the furrow line from 25 to 55º. Optimal ploughshares angle to the furrow line obtained 45…50º. The traction resistance force of the plough equipped with helicoidally bodies was measured 6...8% lower than cultural bodies and 3...4% lower than cylindroid ones at tractor speed 2.5…3.0 $m \cdot s^{-1}$. The ploughing process were investigated from many aspects. Our research fulfill the mentioned results. The average optimal ploughing from our experiment is equal with Lobachevski, 2021. The other results published by Bulgakov et al,. 2017, 2021and Ivanovs et al., 2018, partly applied the mathematical modeling by without the excitation the model with experimental functions. The additional devices mounted between plough and tractor is interesting idea but manipulating and operating issues could occur during the duty. We do not recommend this solution.

Conclusions

The mathematical model based on mass-spring-damper of ploughing process has been designed. The values of accelerations were measured by ADXL 345 acceleration sensor which was mounted on the plough body. For data processing we were designed the software Datahandler in Microsoft Visual C# language. The

Matlab software were used for experimental data filtering with RIF filter. The mass-spring-damper were based on the parameters of flotation tire of the plough. Stiffness of the tire was evaluated and damping of tire were appropriate chosen. The model was excited by function of acceleration and velocity in z axis direction measured in real time during the ploughing process. The average moisture of soil in 10cm depth before ploughing was 25.42 %. The ploughing was the deep ploughing in the depth 30cm. To reduce the sliding resistance the soil with mouldboard the slat mouldboard was chosen. The type of soil was brown-clay soil, which is average heavy soil. We designed the stability criterion hypothesis to evaluate the stability of ploughing process. The hypothesis is still under investigation in the project VEGA 1/0102/21. From realized simulation we get the stability of ploughing process which was 94%. The largest part on the degreasing the stability was the soil type, soil moisture, terrain unevenness and vibration of the plough. The obstacles were not found on the terrain. The average velocity of the ploughing was 3.11 $km.h^{-1}$ and the maximal velocity reached the 9 $km.h^{-1.}$ The total time of the maneuver was 180 second.

Acknowledgements

This article was created with the support of the Research Funding Agency of the Ministry of Education, Science, Research and Sport of the Slovak Republic, project VEGA 1/0102/21 'Reducing chemical loads and degradation of agricultural and forestry soils by selecting appropriate agri-technology with regard to climate change.'

References

[1] Analog Devices. Evaluation Board User Guide UG-065
https://www.analog.com/media/en/technical-documentation/user-guides/UG-065.pdf
[Accessed :28.05.2021]
[2] Babu B H., Kumar D A., Srigiri D. 2016 Determination of stiffness and damping coefficient of tractor front tyres in non-rolling conditions. International Journal of Agricultural Science and Research 6(2) p. 43-52
[3] BKT Flotation tire parameters. https://www.bkt-tires.com/
[Accessed :28.05.2021]
[4] Bulgakov V., Adamchuk V., Nadykto V., Kistechok O., Olt J., 2017 Theoretical research into the stability of motion of the ploughing tractor. Agronomy Research 15(4), 1517-1529, 2017
https://doi.org/10.15159/AR.17.069
[5] Bulgakov V., Pascuzzib S., Adamchukc V., Ivanovsd S., Pylypakaa S. 2019. A theoretical study of the limit path of the movement of a layer of soil along the plough mouldboard Soil & Tillage Research 195, 104406
[6] Bulgakov V.,Nadykto V.,Ivanovs S., Dukulis I. 2021 Improving the performance of a ploughing tractor by means of an auxiliary carriage with

motorized axle. Journal of Agricultural Engineering 52(1)
[7] Deng Y., Wilson J. P., Bauer B. O. 2007. DEM resolution dependencies of terrain attributes across a landscape, International Journal of Geographical Information Science, 21:2, 187-213, DOI: 10.1080/13658810600894364
[8] Gaweł E., Grzelak,M. 2019 The impact of grassland renovation on sward composition and quality under organic farming conditions. Polish Journal of Agronomy 2019, 39, 35–43
[9] Guul-Simonsen F., Jørgensen M.H., Have H., Håkansson I. (2002)Studies of Plough Design and Ploughing Relevant to Conditions in Northern Europe. Acta Agriculturae Scandinavica, Section B — Soil & Plant Science, 52:2, 57-77, DOI: 10.1080/090647102321089800
[10] Hury,H., Stankowski S, Jaroszewska, A, Michalska B, Gibczyńska M. 2020.The effect of tillage system and nitrogen fertilization on yield and yield components of winter spelt cultivars (Triticum aestivum ssp. spelta L.). Polish Journal of Agronomy 2020, 41, 11–19
[11] Chávez M A R., Campos Magaña S G., Zapata M C, López J A L., Piña N C. 2015 Vertical tillage parameters to optimize energy consumption. Agric Eng 17(4) p. 130-140
[12] Ivanovs S., Bulgakov V., Adamchuk V., Kyurchev V.4, Kuvachov V. 2018 Experimental research on the movement stability of a ploughing aggregate, composed according to the "push-pull" scheme. INMATEH - Agricultural Engineering 56(3) p. 9-16
[13] Kim W,S., Kim Y J., Park S U., Kim Y S. 2021. Influence of soil moisture content on the traction performance of a 78-kW agricultural tractor during plow tillage. Soil & Tillage Research 207, 104851
[14] Lines J A. 1991. The Suspension Characteristics of Agricultural Tractor Tyres. Doctor of Philosophy Thesisi.Cranfield Institute of Technology Silsoe College. p.138 https://core.ac.uk/download/pdf/19209307.pdf
[15] Lobachevsky Y P., Liskin I V., Panov A I., Aldoshin N V., Plyaka V I., Lylin N A. 2021. Ploughing quality and energy consumption depending on plough bodies type IOP Conf. Series: Materials Science and Engineering 1030, 012154. IOP Publishing. doi:10.1088/1757-899X/1030/1/012154
[16] Matlab FIR Filter Design. https://www.mathworks.com/help/signal/ug/fir-filter-design.html
[Accessed :28.05.2021]
[17] Moitzi G., Haas M., Wagentristl H., Boxberger J., Gronauer A. 2013 Energy consumption in cultivating and ploughing with traction improvement system and consideration of the rear furrow wheel-load in ploughing Soil & Tillage Research 134,p 56–60
[18] Rédl, J. 2010. Design of scientific application for science and research. VES SPU Nitra. P.146
[19] Stępień-Warda, A. 2020 Effect of soil cultivation system on the efficiency of the photosynthetic apparatus in maize leaves (Zea mays L.) Polish Journal of Agronomy 2020, 43, 57–62

Plans, measurement methods and challenges for the remote measurability of alpha-emitting materials in the context of the EMPIR 2020 RemoteAlpha project

István Róbert NIKOLÉNYI[1], Zoltán GÉMESI[2]
[1] Institute of Mathematics and Basic Science,
Hungarian University of Agriculture and Life Sciences, MATE
[2] Hungarian University of Agriculture and Life Sciences, MATE

Abstract

The principle of radioluminescence measurement method and its deployment strategies for remote detection of alpha-emitting radionuclides are presented. The importance of the method is that it overcomes the shortcomings of conventional detectors, which must be positioned very close to the surface (within the range of alpha particles) due to the short range of a few centimeters of alpha particles in air. We give an overview of the EMPIR 19ENV02 RemoteAlpha project and present some results from previously published work on optical detection of alpha particles. We briefly address also some technical aspects related to mounting the optical system on a UAV.

Keywords

alpha particles, remote detection, radioluminescence, UV-C , CCD-based imaging

1.Introduction

The importance of the remote measurability of radioactive materials has risen to outstanding levels due to the shocking world political events of today. Nuclear power plants face a specific military threat that intimidates the public and greatly increases the risk of radioactive release into the environment, as decommissioned reactors may overheat and damage the casing in the absence of heat dissipation. [Aszódi, 2022]. Military acts anticipate the so-called the use of dirty bombs as well.

The essence of the operation of these bombs is that after the operation of the bomb, the charge, which is a purely alpha-emitting radioactive substance, radioactively contaminates the target area. The alpha particle is the atomic nucleus of the Helium atom, made up of two protons and two neutrons. They are the biggest threat to the human body. Due to its high mass and charge, its specific ionizing ability is 20 times that of beta, X-ray and gamma rays, which directly destroy human tissues. (Molnár et al, 2008]. At the same time, its range

in the air is only a few centimeters, essentially a thin sheet of paper or a leaf already absorbs and shadows it. This poses a particular danger because a direct detector connection is required to detect its presence, so it may go unnoticed for a long time. The dangers of spreading through the human body are well illustrated by A.V. Litvinenko's poisoning story , the one of the late Russian intelligence officer with Po-210 alpha radiation also. [Molnár et al, 2008].

In the event of a reactor accident, alpha-emitting substances may also be released into the environment, as in the case of Chernobil [Broda et al, 1989] and Fukushima [Morihita et al, 2019]. In the latter case, alpha-emitting Pu-238 contamination was also detected inside the reactor building, with beta-emitters Cs-137 and Sr-90 accounting for the largest proportion of total contamination. The difficulties of direct detection as well as the decontamination work of the staff are well illustrated by the use of the smear papers to wipe dirt off the floor (Figure 1.)

It is also important to mention that due to the change in attitudes towards nuclear power plants, humanity wants to meet the growing demand for energy in the future with more and more renewable energy sources and therefore to decommission a significant part of nuclear power plants. Radioactive monitoring of these decommissioning processes is also essential. Based on all these "…Instrumentation and methods therefore need to be developed which overcome the shortcomings of traditional detectors and that will allow remote detection of alpha particles in the environment, reducing risk to personnel, detection costs and time. …"(Publishable Summary for 19ENV02 RemoteALPHA, EURAMET)

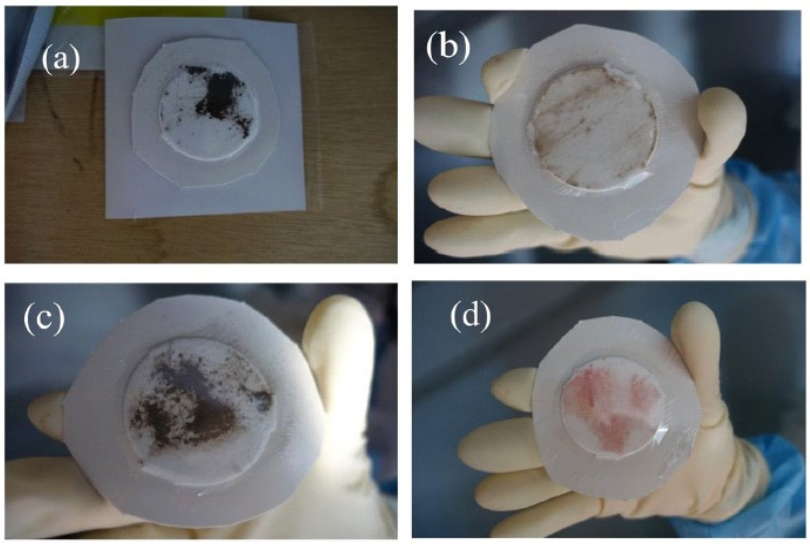

Figure 1. The usage of the smear paper in the reactor building of Fukushima (Morihita et al, 2019)

In this paper, we briefly present the main objectives, principles and implementation ideas of the EMPIR 2020 RemoteAlpha 19ENV02 project for the remote real-time measurability of alpha emitting materials (RemoteAlpha, 2020).

RemoteALPHA is a collaborative project between 8 EU institutions namely

Physikalisch-Technische Bundesanstalt (PTB, Braunschweig) in Germany- the leader of the project- and national metrology offices (NMIs) such as the Horia Hulubei National Institute of R&D for Physics and Nuclear Engineering (IFIN-HH) in Romania and the Hungarian Government Office of the Capital City Budapest (BFKH) and other participants namely Alfa Rift Oy (Finland), Gottfried Wilhelm Leibniz Universität Hannover (Germany) Szent István University (Hungary, now it has changed and its new name: Hungarian University of Agriculture and Life Sciences, MATE), Tampere University Foundation sr (Finland) Universitat Politècnica de Catalunya (Spain).

The structure of the article is as follows: we first describe the principles of the method and the scientific results that underlie them, and then touch briefly on the laboratory results and the ideas for installation on the drone, the latter with the help of only an illustrative photographs.

2. Principles of remote measurability

The principle of remote measurement is optical and based on the detection of the UV light. The basics of the method rely on the Baschenko's fundamental results [2004], among other publications. Alpha-emitting materials can excite or ionize ambient air molecules and emit UV light during excitation, which can be measured remotely with optical devices (photodetector, photomultiplier tube, monochromator, UV lens, spherical mirror, etc.). The author obtained the following optical spectrum for this secondary optical phenomenon, called atmospheric alpha-radioluminescence at normal atmospheric pressure at 20 ° C.

The main spectral lines are at 316, 337, 358, 380 nm and at 391 and 428 nm respectively. The former group can be identified by molecular nitrogen and the latter by ionized nitrogen, i.e. the main emitter is molecular nitrogen. What makes Baschenko's result special is that in addition to the Pu-238 alpha emitter (3.7×10^7 Bq), Co-60 gamma emitters with 5 times higher activity (18.5×10^7 Bq) were also present during the detection. Nevertheless, only the alpha-emitting part was observed in the optical image, i.e. the detection took place from a distance of 30 meters with a large gamma-emitting background! Detection outdoors is made difficult by several orders of magnitude UV backgrounds from solar radiation. Irradiance of sunlight and the brightness of the peaks of nitrogen radioluminescence are in the order of (2-8) * 10^{-2} (W / cm^2 nm) and 10^{-10} -

10^{-7} (W / cm^2 nm) respectively for sources within the 3.7×10^7 and 3.7×10^{10} Bq (mCi-Ci) [Baschenko, 2004].

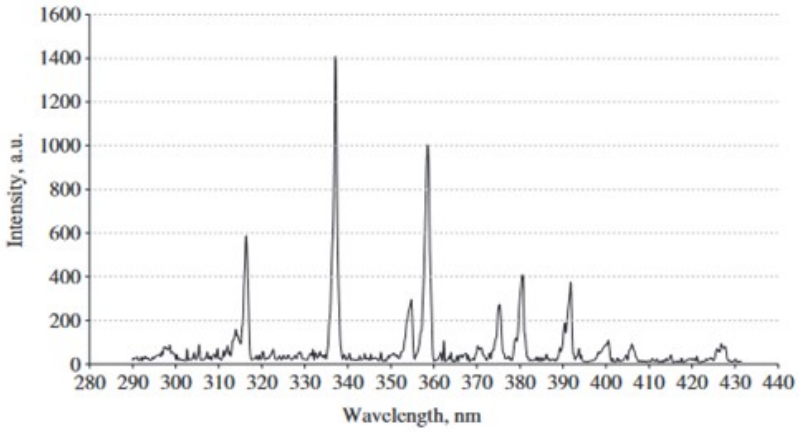

Figure 2. The athmosheric alpha-radioluminescent spectrum measured by Baschenko under standard conditions

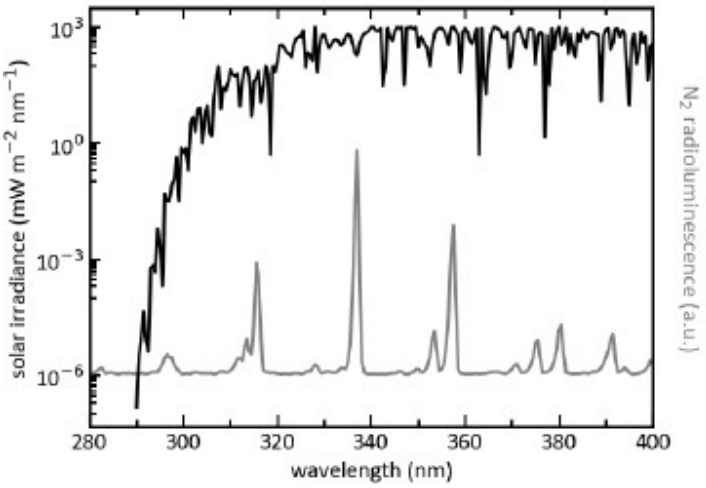

Figure 3. Adapted from [Kerst, Toivonen, 2018] Spectrum of sunlight reaching the earth's surface (black) contrasted with the radioluminescence of N2 (gray) in the wavelength range 280 nm – 400 nm. The solar irradiance (AM1.5 Global tilt) is displayed on a logarithmic scale, while the N_2 emissions are shown on a linear scale. At wavelengths longer than 290 nm the solar irradiance spectrally overlaps with the radioluminescence of N_2.

Direct measurement of the 337 nm radioluminescent line of nitrogen, according to PTB researchers, is based on the following conceptual layout and the caption of the figure and is possible.

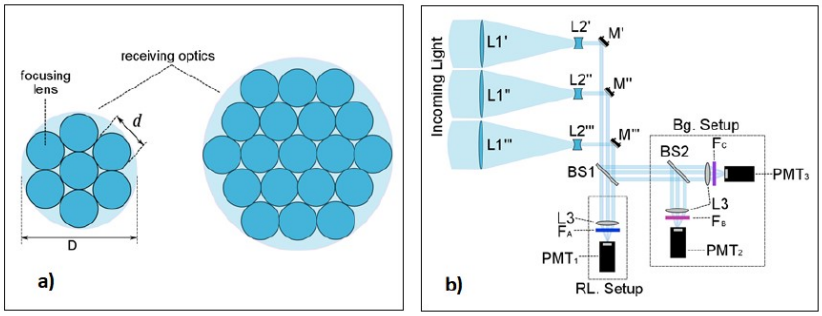

*Figure 4.„ ...*Front view of the receiving optics. Commercial focusing lenses (UV grade fused silica), each with a diameter of d=75 mm (focal length can be selected in accordance with the setup size) are arranged in a close-packed arrangement of diameter D. **(b)** Side view of the optical setup for detection of alpha-radioluminescence. The setup consists of telescopes (L1-L2) which reduce the diameter of the incoming beam, beamsplitters (BS1 and BS2) which steer the incoming beam towards the radioluminescence (RL) and background (Bg.) setups, lenses (L3) which focus the beam onto photomultiplier tubes (PMT1, PMT2 and PMT3) and interference filters (FA, FB and FC) which select specific colors of the incoming light. …" Adapted from Krasniqi, Röttger, (2018)

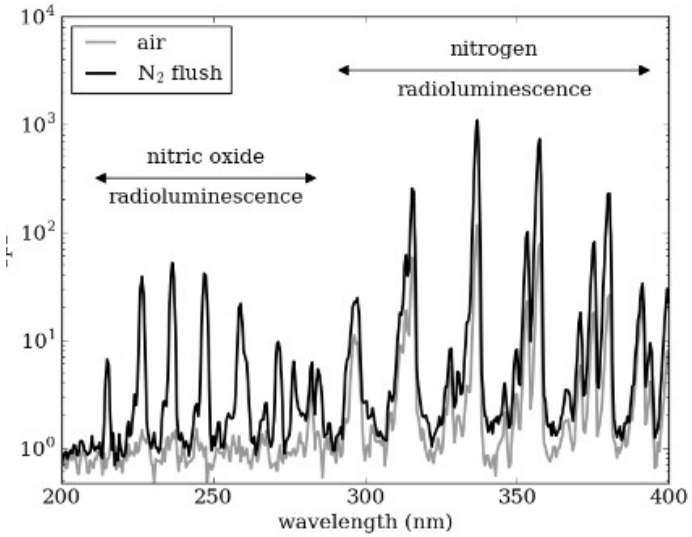

Figure 5. „…The intensity of nitric oxide (NO) radioluminescence in the solar blind region created by the presence of an alpha emitting source is strongly dependent on the atmosphere around the emitter. Increasing the concentration of N 2 allows the light yield of NO fluorescence to reach detectable values…." Adapted from [Kerst et al, 2017).

The essence of this is that the UV background of solar radiation at 337 nm can be estimated from the range B (325-335 nm) and C (345-355 nm) below the peak, in which there is no part of the radioluminescent spectrum. Another possibility is based on a more detailed analysis of the radioluminescent spectrum: there is a weak peak in the so-called solar-blind range below 300 nm.

Here, as the name suggests, the UV background of solar radiation drops to near zero. According to the basic result of Kerst and coworkers [Kerst et al, 2017], by flushing the ambient air with N_2 in the vicinity of the alpha radiation source, the amount of radioluminescence in the solar blind range may increase by an order of magnitude due to the nitric-oxide (NO) present.

The fundamental result of Kerst's doctoral work [2019] is the central element of the project which states that "… .replacing the air around an alpha emitter with a mixture of 50 ppm of NO in N_2 amplifies the production of ultraviolet light by more than two orders of magnitude. The technique is shown to render the detection resistant to influences of daylight…. ".

The laboratory result of the project was based on this method, which is described in the next section after some previous results in the literature.

3.Laboratory results

As mentioned earlier, detection is done by optical means. The most promising version of this is CCD camera-based methods, in which alpha emitting materials are photographed. In this regard, two preliminary results are presented. The first CCD-based image of an Am-241 source with 30 kBq activity was taken by Lamadie et cowerkers [Lamadie et al. 2005].

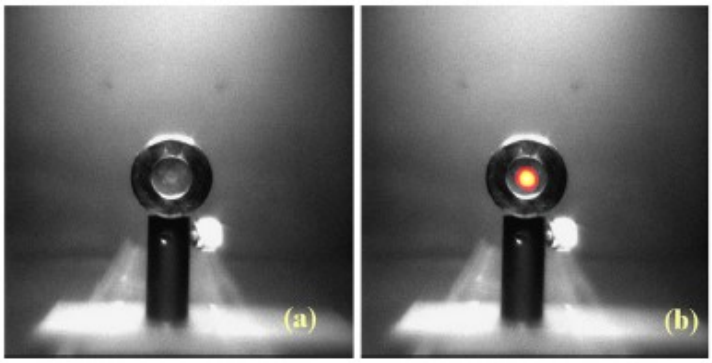

Figure 6. Adapted from [Lamadie et al, 2008]: (a) Visible-light image alone and (b) with a superimposed enhanced false-color image of a 30 kBq Am source.

The shot was taken from a distance of 60 cm in complete darkness. The optical measuring system consisted of an objective lens (consisting of convergent silica lenses with a focal length of 23.5 mm) and a CCD camera with a 25 ° field of view.

The results of Kerst et al. (2018) were an important step towards practical applications. The authors reconstructed two possible real cases using the so-

called electron-multiplying charge-coupled device (EMCCD) method. One concerns a possible crime scene scenario, in which the presence of a radioactive source is presumed, but the locations of objects should not be changed. The images were taken from a distance of 1 meter from two Am-241 sources with 35.9 ± 0.9 and 12.8 ± 0.3 MBq activity placed on the table. The other is the imaging an Am-241 source also located inside a radioactive hot cell through a lead window. Hot cells are used in the nuclear industry as well as in medicine to check the condition of spent nuclear fuel rods and to process medical isotopes.

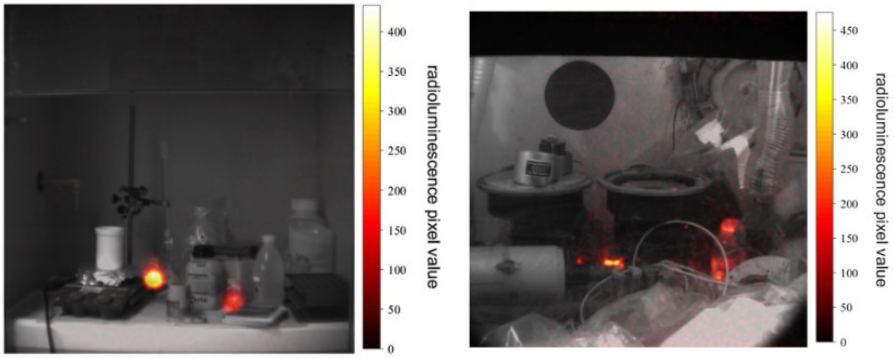

Figure 7. [Adapted from Kerst et al, 2018] (left) Detection of the alpha radioactive sources (left) in the cases of the crime scene scenario and (right) in the hot cell placing.

The radioluminescent spectrum was in the range of 280-430 nm, mainly in the range of 300-400 nm. With this procedure, the total image acquisition time for the crime scene scenario was 10 min, for the hot cell imaging it was 1 h. As in the previous case, the images were taken in complete darkness. These results clearly demonstrate the importance of optical detection of radioluminescence, namely that it allows the rapid identification of alpha sources from a safe distance, thus protecting the staff and the measurement system itself from the contamination. Relying on the already mentioned Kerst and coworkers's results for the solar blind range, researchers in the RemoteAlpha project have taken a significant step toward the detectability under daylight conditions [Krasniqi et al., 2021, previously published by Ivanov et al. 2011.measurement under daylight].

Krasniqi and coworkers studied the effect of nitric oxide on the extension of the activity limit at the levels of two technologies:

- CCD (ICCD) camera based imaging system (where the wide field of view (FOV) imaging system consists of two lenses of focal light f = 100 and 35 mm and a diameter of 2 inches joined to an image intensifier ICCD camera with UV-C filter pass-band of 270 nm), and
- scanner-based photomultiplier (PMT) detection system (based on narrow FOV Galilean type telescope having objective lens of diameter 100 mm and

UV-C filter of pass-band 260 nm with a PMT of cesium-telluride photocathode)

The effect of NO on the extension of the measuring range easy to read from the following images of Figure 8., where from a distance of 40-53 cm first an extended Am-241 source of 32 MBq activity, and surface of 1x 5 cm^2 was detectable but a smaller source of activity 3.7 MBq source without NO addition was not yet detectable, but this activity was already detectable in steel chamber adding NO of at a concentration of NO 50 ppb (µg / L) with flushing the quartz window with a scientific grade N_2 at a rate of 5 L/min. (Fig.8. top right). By increasing the concentration (3ppm = 3 mg / L), the limit of measurement could be reduced to 9.9 kBq, activity of the source of a smoke detector (Fig. 8. bottom left).

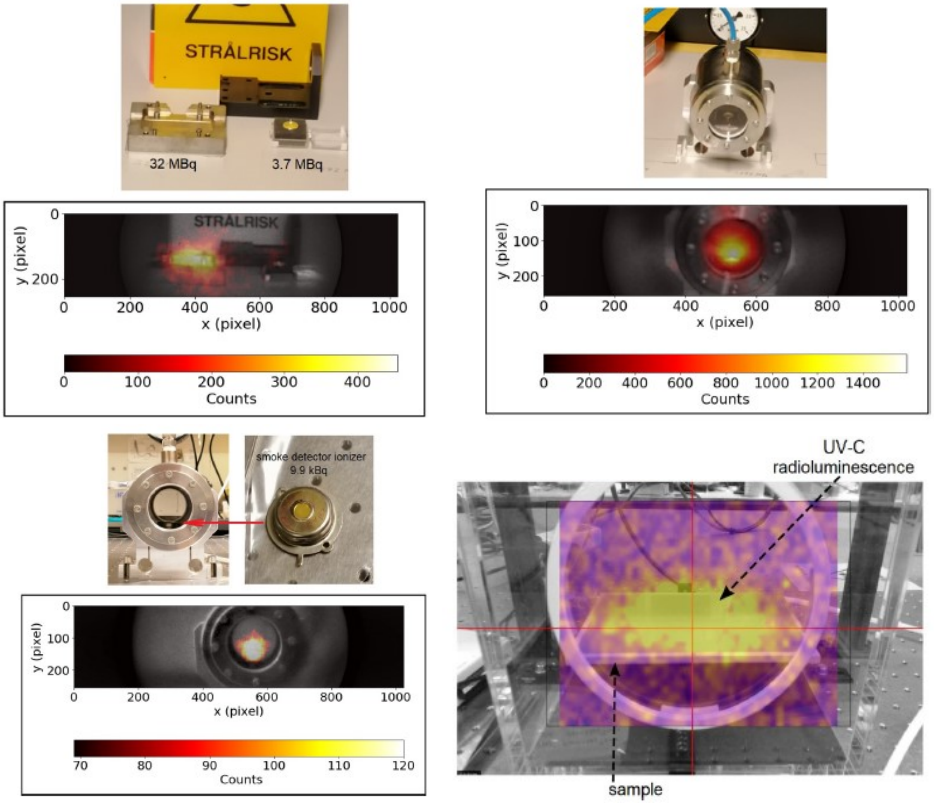

Figure 8. [adapted from Krasniqi et al, 2021.] UV-C radioluminescent CCD-based images of alpha sources with different activities resp. scanner based image. Top left: 32 MBq extended 1x 5 cm^2, next to it: 3.7 MBq, bottom left of the smoke detector ionization source with 9.9 kBq activity. Bottom right is a scanner-based image with a surface activity of 1.5 Bq / cm^2, a total activity of 330 Bq, and a surface area of 19.1 x 11.9 cm^2 composed of isotopes U-234, U-235, and U-238 from a distance of 0.4 m. The value of the detected specific activity is the lowest among the previously known activities measured by UV-C radioluminescence.

4. Plans to install the optical system on the drone

The original goal of the RemoteAlpha project is to install a radioluminescent optical detection system on a drone or a multi-rotary-wing unmanned airborne vehicle. To do this, the distance to the source detection system must be increased by increasing of the diameter of the receiving optics according to the quadratic inverse law of the measuring distance which can be seen in Figure 9. For example the initial distance of 0.5 m can be quadrupled to 2 meters by using four times larger diameter of receiving optics.

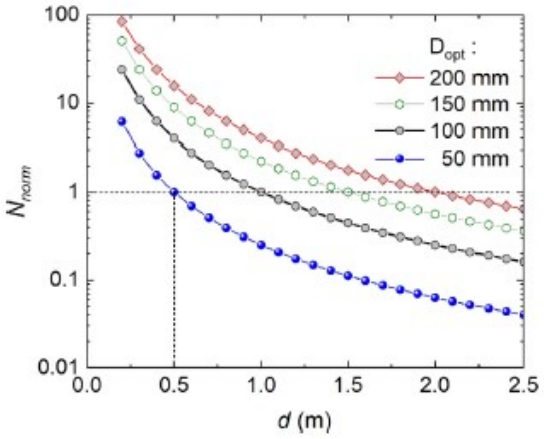

Figure 9. Normalized count number versus source- detektor distance at four diameter of receiving optics. (Krasniqi et al, 2021)

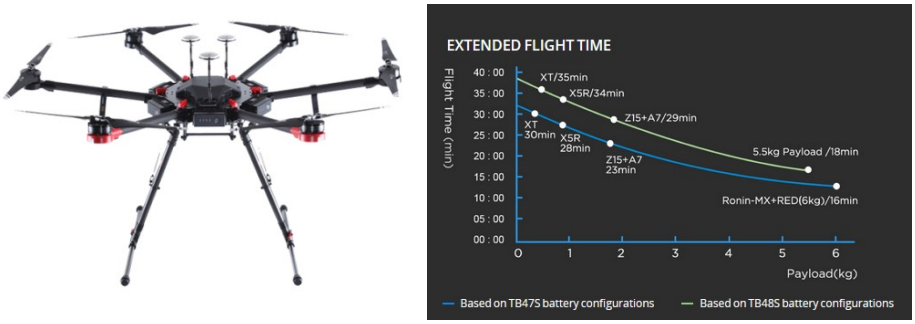

Figure 10. Illustration the DJI Matrice 600 Pro drone and its extended flight time characteristics based on the battery configurations (Adapted from: https://store.dji.com/hu/product/matrice-600-pro?site=brandsite&from=buy_now_bar and https://www.dji.com/hu/matrice600-pro)

Using the diameter of 200 mm at a distance of 0.5 m, the already measurable activity can be 700 Bq. According to the authors, "… optical

detection systems based on aluminum paraboloid reflectors are light weight and, therefore, even reflectors with diameters as large as 500 mm can be easily accommodated into a robotic vehicle, drones or tripod systems". " Here now, without detailing, we would like to illustrate only by a photograph the choosen type of the drone (DJI Matrice 600 Pro) which is the most suitable to install the optical system and has essential advantages for planning the flights thanks to its extended flight time and the 5km long-range transmission.

5. Other objectives

Further objectives of the project are developing and establishing SI traceable calibration procedure, calibration systems and novel portable calibration standards for this new *novel*-type radioluminescence detector systems and a very challenging feasibility study on the posssible use of a laser-induced fluorescence spectroscopic method for the detection of alpha emitters. This latter one is based on the resonant Raman scatterings on the alpha particle generated N_2^+ ions.

We intend to report on these extremely interesting objectives in a subsequent publication.

Conclusions

The radioluminescent measurement method is a very effective tool for safe, remote detection in all cases where the use and storage of alpha-emitting materials (hot cells, criminal scenes, nuclear facilities) becomes necessary or release to the environment may occur. The addition of nitric oxide significantly increases the radioluminescent signal by an order of magnitude compared to natural air. This has been demonstrated in two technologies, at CCD-based and scanner-based ones. The latter had the lowest specific activity known to date. The detector-source distance can be increased by increasing the size of the receiving optics. The idea of installing a radioluminescent optical system on a drone is well-founded.

Acknowledgements

This project 19ENV02 RemoteALPHA has received funding from the EMPIR programme co-financed by the Participating States and from the European Union's Horizon 2020 research and innovation programme. 19ENV02 RemoteALPHA denotes the EMPIR project reference. The authors express their

thanks to Dr.Faton Krasniqi – leader of the EMPIR 19ENV02 RemoteAlpha project- for his comments on the manuscript.

References

[1] Aszódi A. (2022): https://aszodiattila.blog.hu/2022/03/10/a_csernobili_telephely_elvesztette_a_kulso_villamosenergia-ellatasat_milyen_hatasa_lehet_ennek)

[2] Molnár, Á., Vincze, Á., Solymosi, J.(2008): Consequences and elimination of an "dirty bomb" attack with an alpha emitter (in Hungarian), Sugárvédelem, I. Evf. 1.szam pp. 21-29

[3] RemoteALPHA, Remote and real-time optical detection of alpha-emitting radionuclides in the environment, (2020): https://www.euramet.org/researchinnovation/search-research-projects/details/project/remote-and-real-timeoptical-detection-of-alpha-emitting-radionuclides-in-the-environment/.)

[4] Morihita, Y., Torii, T., Usami, H., Kikuchi, H., Utsugi, W.Takahira, S. (2019): Detection of alpha particle emitters originating from nuclear fuel inside reactor building of Fukushima Daiichi Nuclear Power Plant, Scientific Reports DOI: 10.1038 / s41598-018-36962-4.)

[5] Broda, R, Kubica, B, Szeglowski, Z, and Zuber, K. (1989): Alpha emitters in Chernobyl hot particles. Germany: N. p., 1989. Web

[6] Baschenko, S.M. (2004): Remote optical detection of alpha particle sources, J. Radiol. Prot. 24 (2004) 75.

[7] Kerst, T.(2019): Optical Stand-Off Detection of Alpha Radiation in Nuclear Facilities (Ph.D. thesis), Tampere University, Tampere, Finland, Tampere University Dissertations 129.

[8] Kerst, T., Johan Sand, J. Ihantola, S.,Peräjärvi, K., Nicholl, A.,Hrnecek, E. Toivonen, H. · Juha Toivonen, J.(2018): Standoff alpha radiation detection for hot cell imaging and crime scene investigation, Optical Review https://doi.org/10.1007/s10043-018-0413-8

[9] Lamadie, F., Delmas, F., Mahe, C., Gironcs, P., Le Goaller, C.,Costes, J.R. (2005).: Remote alpha imaging in nuclear installations: new results and prospects. IEEE Trans. Nucl. Sci. **52**(6), 3035–3039

[10] Ivanov,O.P.,Stepanov, V.E., Smirnov, S.V. , Volkovich A. G.(2011): Development of method for detection of alpha contamination with using UV-camera ''DayCor'' by OFIL, in: Nuclear Science Symposium and Medical Imaging Conference, NSS/MIC, IEEE, Valencia, 2011, pp. 2192–2194.

[11] Krasniqi, Faton S.; Kerst, Thomas; Leino, Martti; Eisheh, Jens Tarek; Toivonen, Harri; Röttger, Annette; Toivonen, Juha (2021) : Standoff UV-C imaging of alpha particle emitters, Nuclear Inst. and Methods in Physics Research, A 987 (2021) 164821

[12] Krasniqi, F.S., Röttger, A. (2018): Remote and real-time optical detection of alpha-emitting radionuclides in the environment, Draft, Physikalisch-Technische Bundesanstalt, Bundesallee 100, 38116 Braunschweig, Germany
[13] Institute of Energy Technologies (INTE), Technical University of Catalonia (UPC) (2022): M18 Meeting of 19ENV02 RemoteAlpha Project, ppt.

Monitoring the preservation of apples in a domestic fridge

Salma KASSEBI[1], Rajab GHABOUR[1], Péter KORZENSZKY[2]
[1]Doctoral School of Mechanical Engineering, Hungarian University of Agriculture and Life Sciences, MATE
[2]Institute of Technology, Hungarian University of Agriculture and Life Sciences,

Abstract

In the past, consumers almost consumed the fruit near its place of production. Still, thanks to advances in post-harvest and marketing technologies, fresh fruit is transported to distant locations and eaten a few or several days after harvest. The refrigerator is an essential link in the cold chain since it is required for the optimal preservation of the most perishable goods and assures their availability throughout the year. To halt or decrease bacterial development, consumers should keep fruits and vegetables at optimum temperatures and humidity. Bacteria may reproduce every 20 minutes in unfavourable temperature circumstances, such as between 5 and 60°C. This study examines the temperature variation caused by on/off behaviour in apples of various sizes stored in a small to medium storage refrigerator. The refrigerator's great height also contributes to the heat dispersion. ANSYS compares all of the measured parameters to the simulated computations. Colour sensors in a small-scale residential refrigerator are used to assess the impact of the open-close door on the crisp apple flavour and aesthetic criteria. Compared to the non-convection model, the findings demonstrate that the convection mode model is closest to the real-time experiment. The five-day colour measurement does not show a significant difference. The lowest level of the three-shelf refrigerator, on the other hand, exhibited a significant temperature differential.

Keywords

Apple, ANSYS, Temperature, Colour

1. Introduction

Vast apples are harvested annually; in 2020, about 11.9 million tons in the European Union. (USDA, 2021). Considering that consumption does not follow mass production and people consume the fruit all around the year, storing is the best solution and can get more profit if sold out of the season. Also, in countries where large amounts of this fruit cannot be locally cultivated due to expenses or climate conditions, they have to import it. Therefore, cooled cargo containers are needed (Farkas et al., 2019). The main parameter for storing the harvested production is to be picked correctly and stored appropriately. Stored apples need

to be harvested at the minimum maturity point and the storing period varies a lot according to the cultivar species, from 1-2 weeks to 3-6 months. If the storing period is exceeded, the apple starts to develop an off flavour because the fruit starts to feed on the sugar, starch, and acid content after losing the nutrients from the tree. The good storing apple depends on the cultivars, maturity picking stage, how soon the fruit was cooled, and finally, the storing conditions (temperature and humidity). Where the appropriate conditions are from 0 to 5 °C with a 90-95 humidity ratio and with 0.2% loss of moisture per month,

If the humidity is inaccurate, apples will be dehydrated and shrivelled (Naeve et al. 2008). Many household and commercial refrigeration methods need to improve the thermal behaviour of food in order to ensure the shelf life of fresh or stored food. Estimating the best solution must be done by comparing the simulation results with the experiments and understanding its risk. Garrido et al. (2010) measured a ham slice in 33 domestic refrigerators in Spain. After just three days of two storage temperatures, 5 and 9, the ham reaches a dangerous level of pathogens. Also, they focus on building a colour model graph where the appropriate position of the shelf can be determined. Many approaches have focused on the energetic aspects; however, thermal distribution and airflow are essential (Ding et al. 2004). The appropriate temperature condition will result in better storage (Brown et al., 2014). Better interior designs are needed since the temperature variation is prejudiced in the fridge (Gupta et al., 2007).

Refrigeration represents a share of around 28% of all electricity usage in domestic scenarios. This number used can be intensified or diminished by refrigerator efficiency and its open-close door dynamic throughout time. An experiment in Bangladesh revealed that opening a refrigerator door can increase energy consumption by 7-30%, depending on the frequency of the opening (Hossen Khan et al., 2014; Géczi et al., 2019). Another research conducted in Malaysia corroborates this conclusion; the scholars found an increase of 40% in energy usage in an open-door refrigerator (Hasanuzzaman et al. 2008). This process also impacts the compressor's on-off cycling; as shown in the same study, it is increased by 2-5 times, increasing loss in the refrigeration system and, therefore, decreasing refrigerator lifespan and increasing hazardous waste. In addition, the fluctuation of inside temperature can lead to lower food quality, which is the investigation point for this present study.

In this paper, we aim to analyse the temperature fluctuation of the apple fruits (core and shell) due to the motor is on/off working behaviour in the domestic fridge environment and the influence of the apple rigidity and colour. The specific goals are ANSYS simulation of thermal distribution, measuring the actual temperature of the apples (core and shell), compare results from ANSYS simulated calculation and actual data. The resulting apple fruit will be measured according to colour measurement based on the green and yellow dyes on the apple's skin. In usual conditions of temperate zones, harvested apples do not need precooling; however, if the apple's temperature is high, it must be precooled quickly. (Ghabour et al., 2021)

2. Experimental

In order to experiment were used the following materials: a small-scale storage fridge (Gorenje) with nominal power 73W; an electrical clamp meter (Chauvin Arnoux); a power monitor socket type "EM 231"; data logger, type Almemo 2590-9; and temperature sensors NiCr-Ni type.

The scale storage fridge has three roof levels, a small drawer, a freezing compartment and the specifications. The electrical consumption of the fridge is measured by the electrical clamp meter, working as an amperage of the fridge's socket, which will be multiplied by the average voltage to determine the final power consumption.

The power consumption was determined by obtaining the results of the power monitor, which shows the voltage, amperage, and the Phi angle and calculated as in Equation 1.

$$P = I \cdot U \cdot \cos(phi) = 0.58 \cdot 230 \cdot 0.54 = 72.04 \text{ W} \quad (1)$$

The data was stored and transferred to the data logger with a large graphical display and eight input channels, as in Figure 1. The temperature sensors are NiCr-Ni type measures from –200.0 to +1370.0°C with a 0.1K accuracy rate.

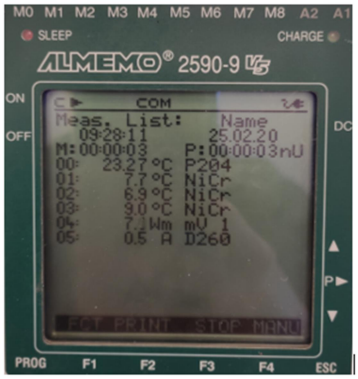

Channel	Description
M0	Ambient temperature outside the fridge
M1	T_1 at the top roof of the fridge
M2	T_2 at the lower roof of the fridge
M3	T_3 at the middle space of the drawer
M4	Q_hf the heat flux on the side wall of the fridge
M5	I_current the electrical current of the power consumption imported from the clamp meter

Figure 1. Almemo data logger 2590-9 and temperature sensor NiCr-Ni type

The measurements were performed in the food technology laboratory at the Hungarian University of Agriculture and Life Sciences for two days and a half continuously, with step one reading per minute.

3. Results and discussion

The actual measurement data revealed the behaviour of fluctuation, which is repeated frequently for all the measured parameters; therefore, 12 hours of 16 repeated cycles were taken since it is representative of all the data as in Figure 2.

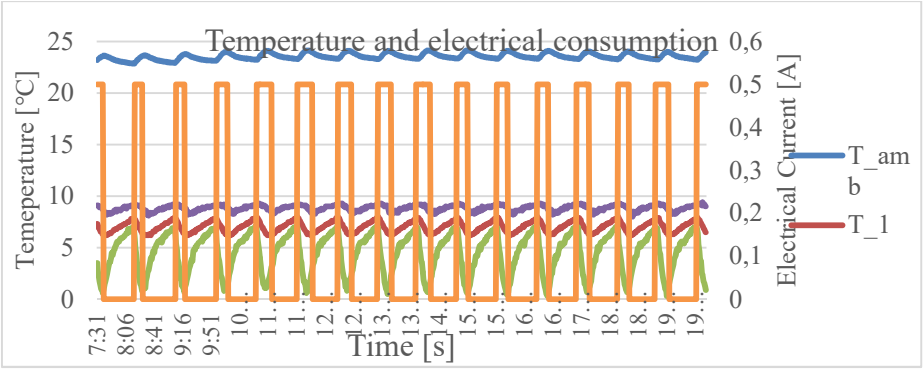

Figure 2. Thermal and electrical performance of the fridge

The noted results regarding T_1 and T_3 (upper roof and drawer) were stable and consistent with less than 2℃ difference between maximum and minimum and the electrical consumption matching the on-off working period of the compressor motor. The unusual data was regarding the T_2 (lower roof), where the fluctuation in the temperature was high for more than 7℃. The well-known advice regarding food storing that the coolest part shall be above the drawer is correct regarding the obtained results. However, the fluctuation was more than three times higher than the fluctuation in the other two spots, so deciding to store such fruits like apples in the lowest part was not recommended because of the temperature fluctuation and exceeding the appropriate storing temperature limit of 5℃.

The maximum, minimum, and average rates are also listed in Table 1. The difference between maximum and minimum in T_1, T_3, and T_amb, are 2, 1.4, and 1.28℃, respectively. At the same time, T_2 has the highest difference by 7.1℃, which shows the importance of this case since if the average temperature was only considered as 4.17℃ it will be a good choice. This fluctuation may affect the stored items, mainly shelf time and colour changes.

Table 1. Maximum, minimum, and average parameters' rate.

	T_1	**T_2**	**T_3**	**T_amb**	**Q_hf**	**I_current**
Max	8	7.2	9.4	24.14	13.1	0.5
Min	6	0.1	8	22.86	4.9	0
Average	6.976	4.37	8.82	23.48	7.762	0.12

The measurement is compared to a simulation process using the ANSYS simulation program. Since the measurement concern is thermal with time, the Transient thermal process was chosen. The apple item was added to the material library as in Table 2. The chosen size of the apple is 5 cm mounted on the lowest

roof which has a fluctuation between 7.2 and 0.1 °C with starting temperature of 22 °C supposed as room temperature. The literature determines the heat convection coefficient as 3.28 W/m^{2}K (Inan et al., 2000; Laguerre et al., 2012).

Table 2. Apple specifications

Density	960	kg/m^3
Isotropic thermal conductivity	0.406	W/m·K
Specific heat	1760	J/kg·K
Diameter	5	cm

The simulation results are different; the first assumes that the apple's shell temperature is the same as the surrounding temperature, which means no conviction is happening, while the conduction between the shell and the core is the primary phenomenon. The second method uses a heat convection coefficient of 3.28 W/m^{2}K. The two methods show different results, where the convection makes more realistic results, as in Figure 3. The C labelled graphs mean using convection, while NC means no convection. The measurement duration is 7 hours for six on-off cycles till it is stable, where it is noted that the core temperature reaches 4.58°C and the shell 4.54°C for the convection results.

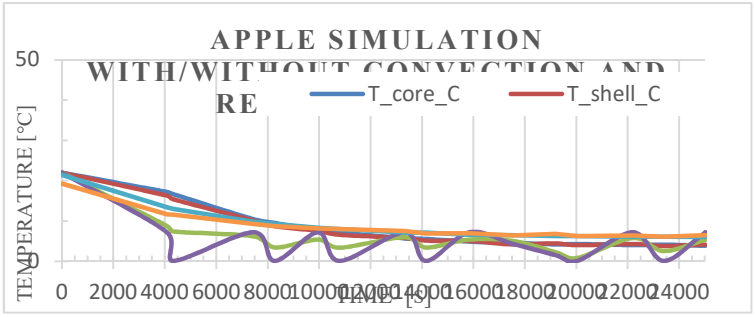

Figure 3. Simulation results with and without convection compared to an actual experiment

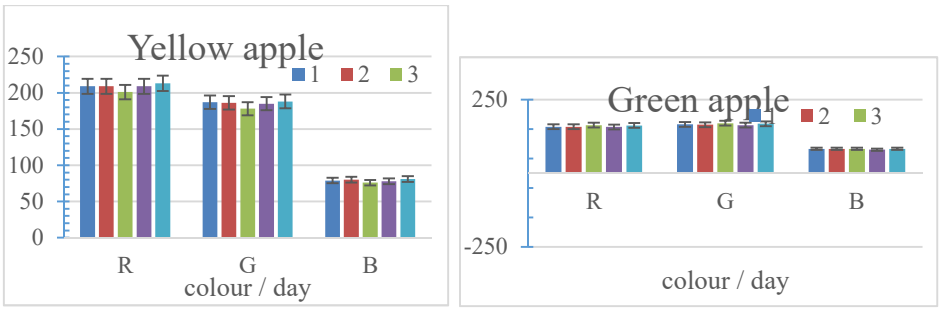

Figure 4. Colour specification of both samples

While in terms of colour, as shown in Figure 4, there is no significant change in colour components over five consecutive days for both samples. In the case of short-term storage, the colour specification of green or yellow apples does not change dramatically under the specified temperature and humidity conditions.

Conclusions

People aim to store their food for a specific period to consume it out of its season. Apple fruits are harvested and stored from one season to another, ensuring their availability throughout the year. The main question is how long we can store our apple in a domestic fridge, and what is the actual temperature of the core and shell of the fruit compared to the fridge temperature. In this paper, we made 60 hours of an actual experiment on two types of apples (yellow and green) to measure their actual temperature. Meanwhile, we conducted a simulation using the ANSYS program with two approaches, with and without conviction. The results show that the conviction model is closer to the actual experiment. After that, we conducted five days of colour measurement to check the changing in the red, green, and blue factors in the apple's skin. Nevertheless, it shows that the colour components remain relatively the same during the experiment.

Acknowledgements

This work was supported by the Stipendium Hungaricum Programme and by the Mechanical Engineering Doctoral School, The Hungarian University of agriculture and life sciences, Gödöllő, Hungary.

References

[1] Brown, T., N.A. Hipps, S. Easteal, A. Parry and J.A. Evans (2014), Reducing domestic food waste by lowering home refrigerator temperatures. International Journal of Refrigeration, 40, 246–253.
[2] Ding G.L., H.T. Qiao, Z.L. Lu (2004), Ways to improve thermal uniformity inside a refrigerator, Applied Thermal Engineering, 24, 1827–1840.
[3] Farkas Cs., L. Fenyvesi, K. Petroczki (2019), Multiple linear regression model of golden apple's failure characteristics under repeated compressive load, Potravinarstvo Slovak Journal of food sciences volume 13., 793–799.
[4] Garrido V., I. García-Jalón, A.I. Vitas (2010), Temperature distribution in Spanish domestic refrigerators and its effect on Listeria monocytogenes growth in sliced ready-to-eat ham. Food Control, 21, 896–901.
[5] Géczi G., Dodog Z., Székely L., Veres A (2019), Examining the effect of the door opening on the operation of the domestic fridge, Researched Risk

Factors of Food Chain, ISBN: 9789632697758, 127-130.
[6] Ghabour R., S. Kassebi, P. Korzenszky, (2021), Simulation and experiment of apple fruits in domestic fridge, Hungarian Agricultural Research: Environmental Management Land use Biodiversity 30, pp.11-14.
[7] Gupta J.K., M. Ram Gopal, S. Chakraborty (2007), Modeling of a domestic frost-free refrigerator. International Journal of Refrigeration, 30, 311–322.
[8] Hasanuzzaman M., R. Saidur, H.H. Masjuki (2008), Investigation of energy consumption and energy savings of refrigerator-freezer during open- and closed-door condition. Journal of Applied Sciences, 8, 1822–1831.
[9] Hossen Khan, M.I., H.M.M. Afroz (2014), An Experimental Investigation of Door Opening Effect on Household Refrigerator; the Perspective in Bangladesh. Asian Journal of Applied Sciences, 7, 79–87.
[10] Inan, C., T. a Newell, N. Egrican (2000), Heat and Mass Transfer through a Domestic Refrigerator and Evaluation of Evaporator Performance under Frosted Conditions 61801.
[11] Laguerre O., M.H. Hoang, D. Flick (2012), Heat transfer modelling in a refrigerated display cabinet: The influence of operating conditions, Journal of Food Engineering, 108, 353–364.
[12] Naeve L., P. A Domoto (2008), Harvesting and storing apples, In: Cooperative Extension Service, U.S. Department of Agriculture, Iowa State University of Science and Technology, Ames, Iowa
[13] USDA Foreign Agricultural Service/4 December 2021, Global Market Analysis
(https://downloads.usda.library.cornell.edu/usda-esmis/files/1z40ks800/736675268/8910kv534/fruit.pdf)